The Energetics and Environments of *Swift* Gamma-Ray Bursts

Thesis by

S. Bradley Cenko

In Partial Fulfillment of the Requirements

for the Degree of

Doctor of Philosophy
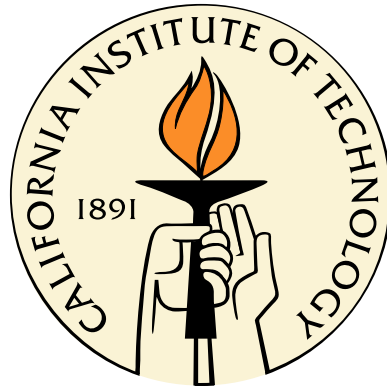
California Institute of Technology

Pasadena, California

2009

(Defended June 4, 2008)

Acknowledgements

Though only my name appears on the title page, the work that follows would not have been possible without the support of my co-workers, friends, and family. While I will take the blame for any errors in this text, I would at the very least like to thank by name some of those who made the last six years both enjoyable and fulfulling.

For most of my graduate studies I have had both the blessing and the curse of having two academic advisors: Professors Fiona Harrison and Shri Kulkarni. Though stylistically quite different, I could not have asked for a better pair to match my temperment. Shri was a constant source of enthusiam, energy, and ideas, while Fiona was always there with a keen eye for detail and a vital sense of perspective. Because of them I was given the tools and support necessary to attack an interesting problem and the freedom to do so in my own unique way — no graduate student could ever ask for any more.

In addition to Shri and Fiona, the entire GRB group at Caltech (and beyond) offered a stimulating working environment in which to pursue my research. It has been a pleasure to be surrounded by such talented and motivated people, and I want to thank them all for their expertise, patience, and friendship. Though by no means an exhaustive list, I want to mention Alicia Soderberg, Edo Berger, Mansi Kasliwal, Brian Cameron, Paul Price, Eran Ofek, Arne Rau, Avishay Gal-Yam, Dae-Sik Moon, Dale Frail, and in particular Derek Fox and thank them for all of their help over the years.

I came into the GRB field at a particularly opportune time, with the launch of the *Swift* γ-Ray Burst Explorer in 2004 November. *Swift* continues to provide new surprises and discoveries even to this very day. I want to thank the entire *Swift* team

for building such a wonderful instrument, and in particular Dr. Neil Gehrels and the NASA Graduate Student Research Program for funding much of my research.

Traveling to Palomar Observatory to conduct follow-up GRB observations was always something I looked forward to, and this is in large part due to the wonderful people who work there. I want to thank the entire staff at Palomar for all of your effort over the last few years; without you all, the P60 project never would have gotten off the ground to begin with.

I have been a Resident Associate on campus for the last four years, and the residents of Fleming House have managed to keep me on my toes for much of that time. I have greatly appreciated being a part of such a community, and I want to thank not only the Flems but everyone else affiliated with the RA program for a wonderful experience.

My friends at Caltech and beyond have provided an endless reservoir of support throughout my stay here. At Caltech I would like to thank (among others) Megan Eckart, Robert Ward, Marie-Hélène Rousseau, Dan Busby, James Maloney, Keiko Yoshida, Andrew and Meredith Beyer, Jon Eguia, John Keith, and in particular Christie Canaria for such a memorable time. I will miss you all very much as I head off to Berkeley.

Finally, I would not be where I am today without the tremendous sacrifices of my family. I cannot thank you enough for your love and support.

Abstract

For their short durations, γ-ray bursts (GRBs) are the most electromagnetically luminous objects in the universe. In this thesis, I use these fascinating objects, both as signposts, indicating the presence of an ultra-relativistic (Lorentz factor $\Gamma \sim 10^2$–10^3) outflow from a newly born stellar mass black hole, and as lighthouses, illuminating the circumburst ($r \sim 1\,\mathrm{pc}$) and inter-stellar ($r \sim 1\,\mathrm{kpc}$) media along the line of sight.

In Part I, I describe my efforts to automate the Palomar 60 inch telescope (P60), the primary instrument on which much of this thesis is based. Designed to capitalize on NASA's recently launched *Swift* γ-Ray Burst Explorer, P60 now routinely provides moderately fast ($\Delta t \lesssim 3\,\mathrm{min}$) and sustained ($R \lesssim 23\,\mathrm{mag}$) observations of GRB afterglows and other optical transients.

Part II focuses on the geometry and energetics of some of the best-sampled events in the *Swift* era. I find both GRB 050820A and GRB 060418 are an order of magnitude more energetic than pre-*Swift* events, with a total energy release in excess of $10^{52}\,\mathrm{erg}$. Both GRBs are therefore members of an emerging class of "hyper-energetic" events, suggesting a much broader energy distribution then previously thought and challenging current massive star progenitor models.

Finally, in Part III I study the environments of long-duration GRBs. The massive star progenitors should leave an imprint on the GRB environment, both on the pc scale as a wind from mass loss of the outer envelope, and on the kpc scale from the dense, dusty disk where massive stars form. Interestingly, I demonstrate that GRB 070125 exploded in a halo environment, suggesting at least some massive stars form far way from the disk of their host. By comparing the X-ray and optical light curves from a sample of 29 GRBs, I find nearly half show evidence for suppressed

optical emission. I attribute this to dust absorption in the host galaxy, consistent with a massive star origin for long-duration GRBs.

Contents

List of Figures

List of Tables

Chapter 1

Introduction and Overview

γ-ray bursts (GRBs) are brief ($\Delta t \sim 0.1$–100 s), intense ($F_\gamma \sim 10^{-5}$–10^{-7} erg cm^{-2}), flashes of high-energy (1 keV–10 MeV) radiation. Discovered serendipitously by the *Vela* satellites in the late 1960s (Klebesadel et al., 1973), GRBs result from collision-less shocks within an ultra-relativistic, collimated outflow. As the shock expands, the kinetic energy of the outflow accelerates electrons in the circumburst medium. The resulting broadband (radio–X-ray), long-lived ($\Delta t \sim$ days to weeks) synchrotron radiation is known as the afterglow. At least two extragalactic populations appear capable of producing GRBs: long-duration ($\Delta t \gtrsim 2$ s) events are associated with massive star core-collapse, while short-duration ($\Delta t \lesssim 2$ s) GRBs are likely associ-ated with an older stellar population. In this chapter, I provide a brief introduction to GRBs, primarily in the context of the relativistic fireball model and the result-ing synchrotron afterglow emission. I conclude with a brief overview of the results presented in the remainder of this thesis.

1.1 Observed Properties of the Prompt γ-Ray Emis-sion

Figure 1.1 displays the high-energy light curves of a sample of GRBs (Bonnell et al., 1997). Upon first glance, the most striking feature is the marked diversity — no two light curves look exactly alike. The durations in Figure 1.1 are representative of

the observed GRB population as a whole, with t_{90}[1] values ranging from $\lesssim 100\,\mathrm{ms}$ to $\gtrsim 10^3\,\mathrm{s}$. In fact the observed extreme values are likely artifacts of instrumental time resolution and triggering algorithms.

Another feature evident in nearly all light curves in Figure 1.1 is rapid variability. In fact many GRB light curves show statistically significant variations on all sampled time scales (as low as tens of ms). If relativistic effects are neglected, causality arguments would constrain the physical size of the emitting region to $R < c\delta t \approx 3 \times 10^8\,\mathrm{cm}$, comparable in size to the radius of Earth ($R_\oplus = 6.378 \times 10^8\,\mathrm{cm}$).

The high-energy spectra of GRBs are non-thermal. Most events are well fitted by a power-law spectrum with an exponential cutoff at energies of a few hundred keV (Band et al., 1993). Like durations, the observed cutoff values can span over many orders of magnitude, dropping as low as the X-ray bandpass in some cases (the X-ray flashes, or XRFs; Heise et al., 2001).

The launch of the Burst Alert and Transient Explorer (BATSE) on-board the *Compton Gamma-Ray Observatory* (CGRO) in 1991 allowed for the first time detailed population studies by providing degree-sized localizations for thousands of GRBs (Paciesas et al., 1999). It was thus determined that GRBs were distributed isotropically on the sky, and the luminosity function ($\log N - \log S$: number as a function of peak flux) showed clear deviations from the $S^{-3/2}$ power-law required for a bounded Euclidean space (Meegan et al., 1992). Both findings argued strongly in favor of a cosmological origin for GRBs (Paczynski, 1986), although a Galactic model in the extended halo (e.g., high-velocity neutron stars; Li & Dermer, 1992) could not be ruled out entirely until the detection of afterglow emission (Section 1.3).

Finally, observations with BATSE revealed the first evidence of two distinct sub-populations of GRBs. The observed duration distribution is bimodal, with a cutoff value at $t_{90} \approx 2\,\mathrm{s}$ (Figure 1.2; Norris et al., 1984; Kouveliotou et al., 1993). Furthermore, the observed duration shows a strong correlation with spectral hardness, as those events with the most high-energy photons also had the shortest durations

---

[1]The duration calculation for a background-subtracted light curve is not particularly well defined. I adopt here the standard measure in the field, t_{90}, which is defined as the interval over which 90% of the total background-subtracted counts are observed.
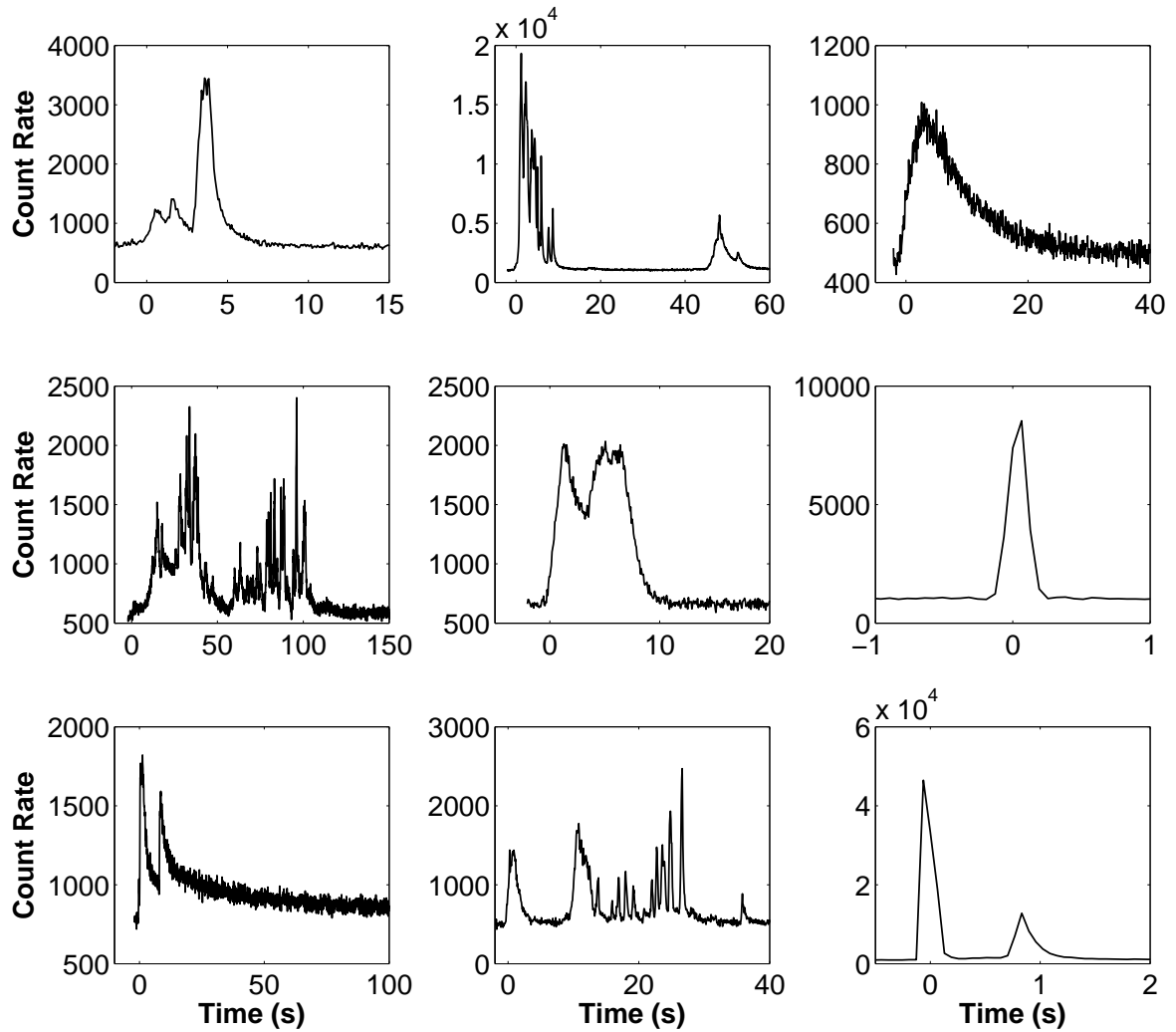
Figure 1.1 — GRB high-energy light curves. Plotted here is the count rate in all four BATSE energy channels (30 keV – 2 MeV) as a function of time. Note the large diversity in shape and duration, as well as the rapid variability seen in many bursts.
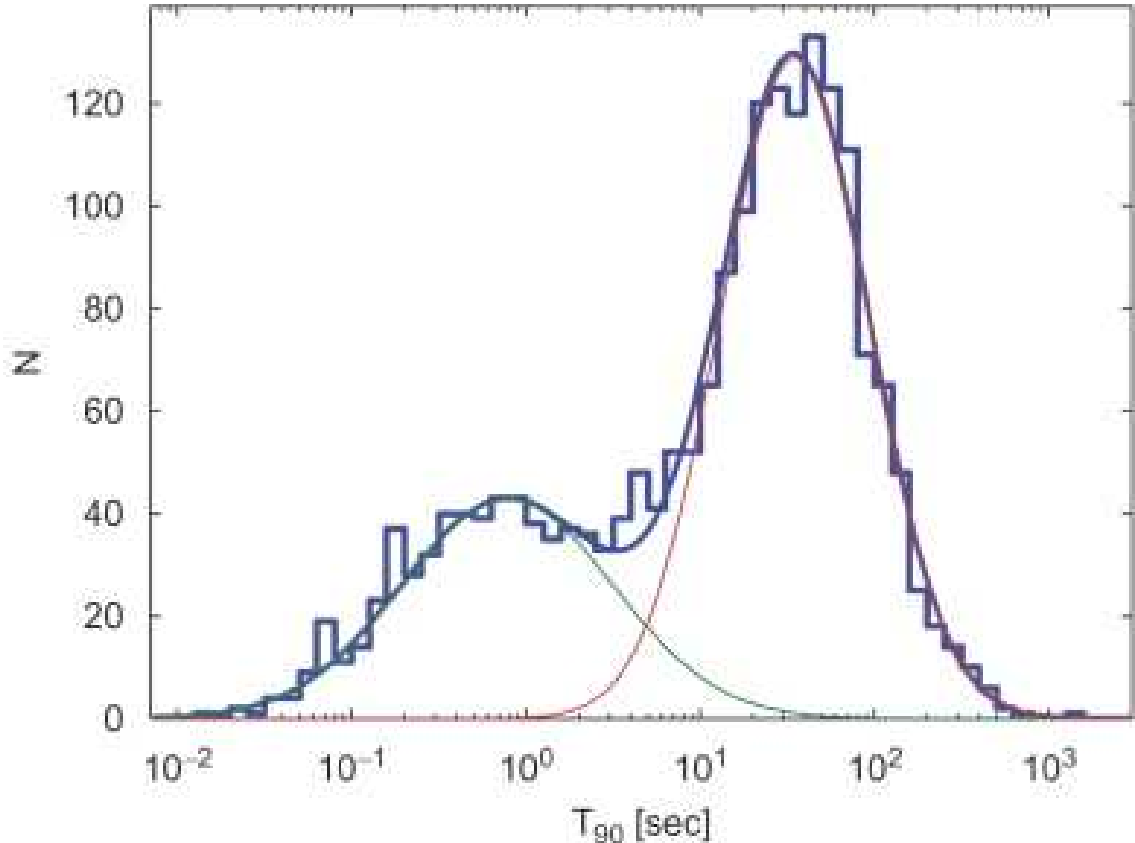
Figure 1.2 — Bimodal duration distribution of BATSE GRBs. The decomposition into two log-normal distributions, as determined by Horváth (2002) (*thin solid lines*), together with the sum of the two distributions (*thick solid line*), are shown here superposed on the observed histogram. From Nakar (2007).

(Qin et al., 2000). The two populations are often referred to as short-hard ($t_{90} \lesssim 2\,\mathrm{s}$) and long-soft ($t_{90} \gtrsim 2\,\mathrm{s}$) bursts. For the remainder of this thesis, unless otherwise specified, I will be discussing primarily long-soft GRBs.

1.2   The GRB Paradigm: Relativistic Fireball Model

Armed solely with the facts about the prompt emission presented in Section 1.1, it is nonetheless possible to gain remarkable insight into the GRB phenomenon. The short time scale variability requires γ-ray production in a compact emission region: a so-called astrophysical "fireball" (Cavallo & Rees, 1978). As originally envisioned, a fireball should be opaque due to $e^- - e^+$ pair creation. Photon pressure would cause

the fireball to expand and cool until the energy spectrum is degraded below the pair production threshold, and a thermal spectrum would emerge once the outflow became optically thin (Goodman, 1986; Paczynski, 1986).

We know, however, that GRB spectra are non-thermal, and the resolution to this "compactness problem" forms the foundation of our current understanding of GRBs. The optical depth for pair creation is given by (e.g., Piran, 2005):

$$\tau_{\gamma\gamma} = \frac{f_{e^\pm}\sigma_T 4\pi d^2 F_\gamma}{m_e c^2 R^2} \tag{1.1}$$

where $f_{e^\pm}$ is the fraction of photons above the pair production threshold energy (i.e., $2m_{e^\pm} = 1.02\,\mathrm{MeV}$), σ_T is the Thomson cross section, d is the distance to the burst, and F_γ is the GRB fluence. Assuming GRBs lie at cosmological distances ($d \sim 10^{28}\,\mathrm{cm}$) and using typical fluence and radius measurements from BATSE ($F_\gamma \sim 10^{-7}\,\mathrm{erg\,cm^{-2}}$, $R \approx c\delta t \sim 3 \times 10^8\,\mathrm{cm}$), we find an optical depth of $\tau_{\gamma\gamma} \approx 10^{15}$. All photons with $E > 1.02\,\mathrm{MeV}$ would create pairs, and the emergent spectrum would be thermal.

To resolve the compactness problem, we invoke ultra-relativistic expansion of the fireball toward the observer. If we consider an outflow with Lorentz factor Γ [$\Gamma \equiv (1 - (v/c)^2)^{-1/2}$], the size of the emitting region will increase by a factor of Γ^2: $R \approx \Gamma^2 c\delta t$. Additionally, observed photons have been blue-shifted by a factor of Γ, so the fraction above the pair production threshold in the fireball rest frame decreases by a factor of $\Gamma^{-2\alpha}$, where α is the power-law spectral index of the prompt emission. For observed values of $\alpha \approx 2$, we require $\Gamma \gtrsim 100$ in order for the fireball to be optically thin ($\tau_{\gamma\gamma} < 1$) and thus produce the observed non-thermal spectra.

We consider here two possible mechanisms to generate the prompt γ-ray emission from the ultra-relativistic fireball outflow (Figure 1.3). If the outflow contains baryonic material, the kinetic energy of these entrained baryons can be converted to radiation via dissipation in shocks, either internally, through instabilities within the outflow (Narayan et al., 1992; Rees & Meszaros, 1994; Paczynski & Xu, 1994), or externally, by sweeping up the circumburst medium (Rees & Meszaros, 1992). The observed durations and variability time scales suggest internal shocks as the likely
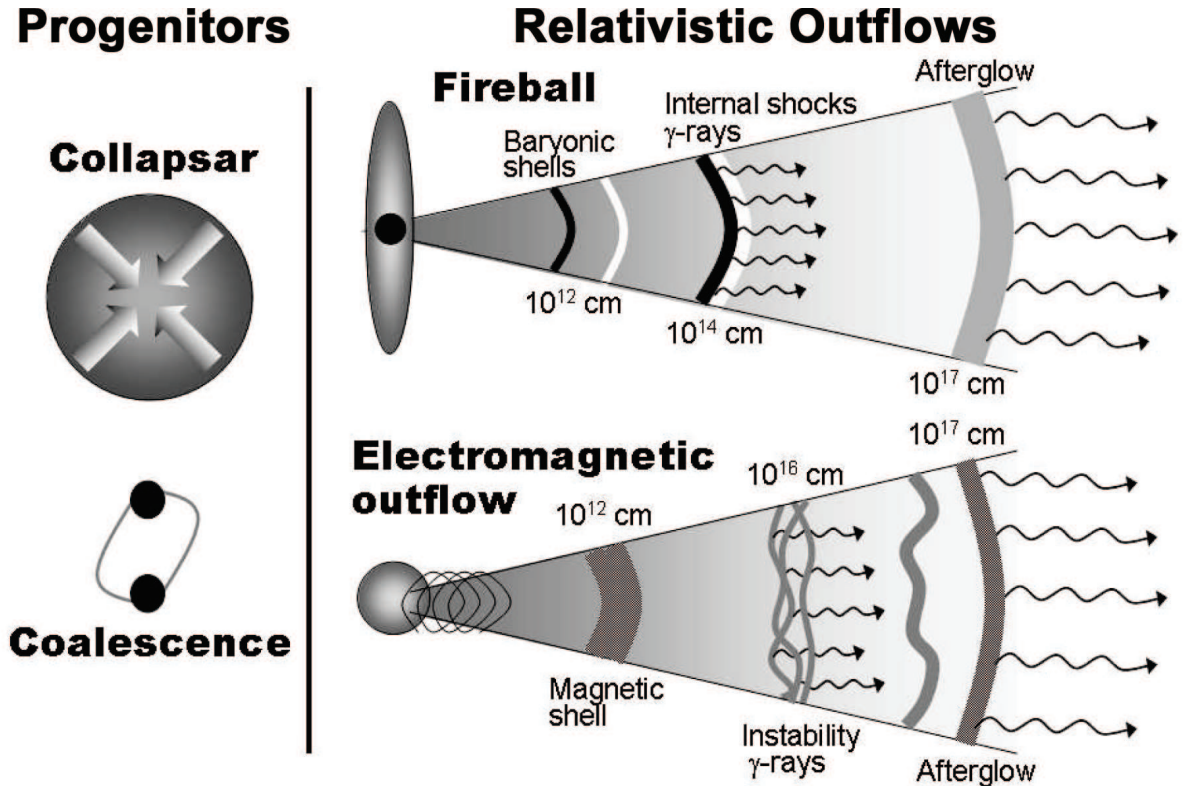
Figure 1.3 — The GRB paradigm: an ultra-relativistic fireball outflow. Shown on the left are the two leading progenitor models for GRBs. There is now strong evidence linking the core-collapse of a massive star to long-duration GRBs (Section 1.4). Coalescence of two degenerate compact objects (neutron star-neutron star or neutron star-black hole) is thought to be the leading candidate for short-duration GRB progenitors. In both cases, accretion onto the newly formed black hole generates a highly collimated, ultra-relativistic outflow. If the outflow contains an appropriate amount of baryons, collisionless shocks within the outflow (i.e., internal shocks) generate the prompt γ-ray emission. Alternatively, for an electromagnetically dominated outflow, instabilities within the outflow could be the source of GRBs. In both cases, long-lived, broadband afterglow emission results when the the outgoing shock accelerates electrons in the circumburst medium, causing them to emit synchrotron radiation.

source of GRB emission (e.g., Piran, 2005 and references therein). It is important to note, however, that the Lorentz factor of the outflow and the efficiency of conversion of kinetic energy of the baryons to γ-rays depend sensitively on the fraction of entrained baryons (Cavallo & Rees, 1978; Goodman, 1986; Shemi & Piran, 1990). The capture of too many baryons will produce only a mildly relativistic outflow with a low γ-ray conversion efficiency. This is know as the "baryon loading" problem.

Alternatively, the outflow could also be electromagnetically dominated (e.g., Usov, 1992; Lyutikov & Blandford, 2003; Figure 1.3). In this case, γ-ray production is caused by instabilities in a relativistic magnetic outflow. One advantage of this model is that it does not require the large circumburst magnetic field invoked to explain the observed afterglow emission (Lyutikov & Blandford, 2003). However, in its current state, it is difficult to observationally discriminate between these two models for the outflow.

1.3 The Key to the Puzzle: Afterglow Emission

A natural consequence of the relative inefficiency in converting the kinetic energy of the outflow into γ-ray radiation is the production of long wavelength emission as the outflow sweeps up and shocks the ambient circumburst medium. Given the long-lived, fading nature of this emission, these counterparts have been dubbed "afterglows" (Figure 1.3).

After many unsuccessful attempts (due primarily to the long time delay in obtaining follow-up observations), the first X-ray (Costa et al., 1997), optical (van Paradijs et al., 1997), and radio (Frail et al., 1997) GRB afterglows were detected in 1997. Unlike the prompt emission, afterglow radiation was confirmed to be both broadband (radio–X-ray) and smoothly variable. As an example, I display the X-ray, optical, and radio light curves of the afterglow of GRB 060418[2] in Figure 1.4.

To explain the afterglow emission, we consider a relativistic shell of material propa-

---

[2]It is customary to name GRBs after the UT trigger date, appending letters for those days on which more than one GRB was discovered. Thus the third GRB discovered on 2010 January 1 would be referred to as GRB 100101C.
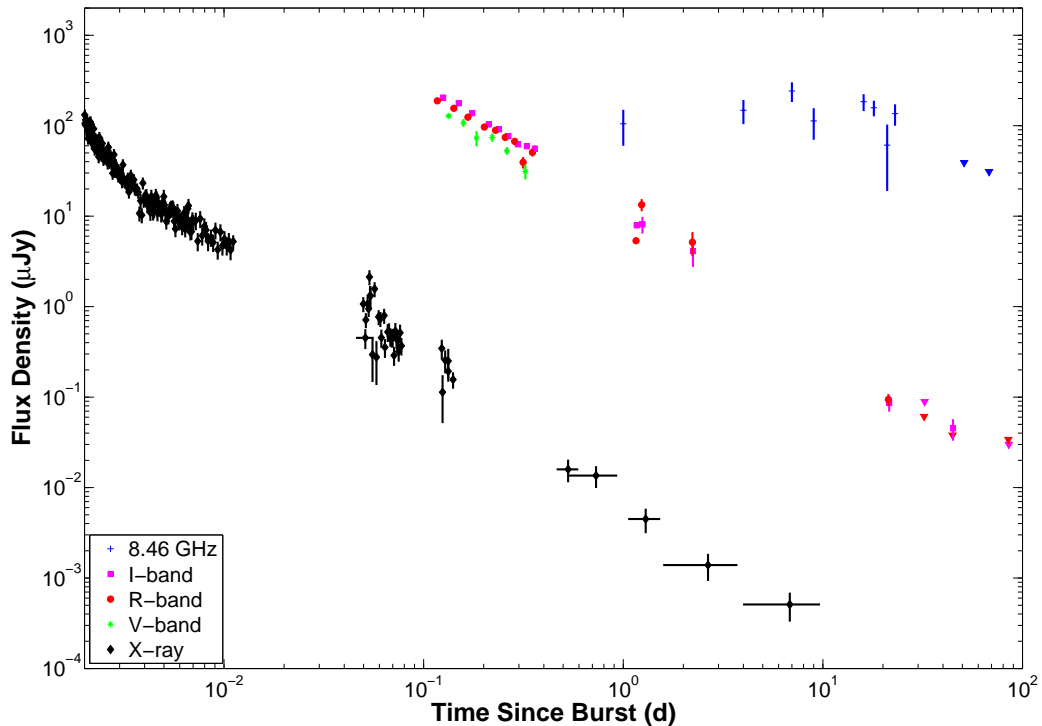
Figure 1.4 — Broadband afterglow of GRB 060418. Afterglow emission is broadband, long-lasting, and lacks the short time scale variability seen from the prompt emission. All three band passes (X-ray, optical, and radio) can typically be well fitted as a series of broken power-laws.

gating into the undisturbed circumburst medium. The shell will decelerate once it has swept up a circumburst mass of M/Γ, where M and Γ are the mass and Lorentz factor of the outgoing shell, respectively. For typical values of $\Gamma_0 \approx 100$ and $E_{\mathrm{KE}} \approx 10^{51}$ (Section 1.5), and assuming a circumburst particle density of $n \approx 1\,\mathrm{cm}^{-3}$, the deceleration begins at a radius of $r \approx 10^{17}\,\mathrm{cm}$.

At the intersection of the relativistic outflow and the ambient circumburst medium, a shock front forms. The densities at the shock front are so low that the mean free path for collisions is larger than the size of the system. Either magnetic fields or plasma waves play the role normally assigned to collisions; in this sense the shocks are "collisionless". Assuming the unshocked circumburst medium is cold, then conservation of mass, energy, and momentum across the shock front requires (Blandford

& McKee, 1976):

$$n_2 = 4\Gamma_2 n_1$$

$$e_2 = 4\Gamma_2 n_1 m_p c^2$$

$$\Gamma_s^2 = 2\Gamma_2^2 \tag{1.2}$$

where $n_{1,2}$ and $e_{1,2}$ are the number density and energy density, measured in the local rest frame of the unshocked (subscript 1) and shocked (subscript 2) material. Γ_2 is the Lorentz factor of the fluid just behind the shock, and Γ_s is the Lorentz factor of the shock front (both measured in the frame of the unshocked circumburst medium).

To calculate the emitted spectrum, we follow the formulation of Sari et al. (1998). In the shocked circumburst material, we assume electrons are accelerated to a power-law distribution of energies, $N(\Gamma_e) \propto \Gamma_e^{-p}$ (Fermi, 1949), with a cutoff at low energy given by Γ_m. To mask our ignorance of the detailed microphysics of the shock process, we further assume that a constant fraction of the total energy is imparted to the electrons (ϵ_e) and magnetic field (ϵ_B):

$$e_e = \epsilon_e e = 4\Gamma_2^2 \epsilon_e n_1 m_p c^2 \tag{1.3}$$

$$e_B = \epsilon_B e = B^2/8\pi = 4\Gamma_2^2 \epsilon_B n_1 m_p c^2. \tag{1.4}$$

The minimum electron Lorentz factor can then be written as:

$$\Gamma_m = \epsilon_e \left(\frac{p-2}{p-1}\right) \frac{m_p}{m_e} \Gamma_2. \tag{1.5}$$

The accelerated post-shock electrons, in the presence of a magnetic field, will emit synchrotron radiation (Rybicki & Lightman, 1979). The resulting spectrum will be a broken power-law, with the exact shape determined by the relative ordering of three critical frequencies: ν_a, the frequency where self-absorption becomes significant $[\tau(\nu_a) \equiv 1]$; ν_m, the frequency corresponding to the minimum energy electron $[\nu_m \equiv \nu(\gamma_m)]$; and ν_c, the frequency above which electrons cool efficiently via radiation. For most times of interest, $\nu_a < \nu_m < \nu_c$ (i.e., the slow cooling regime). Integrating over

the electron distribution yields:

$$F_\nu \propto \quad \nu^2 \qquad ; \nu < \nu_a \qquad (1.6)$$

$$\nu^{1/3} \qquad ; \nu_a < \nu < \nu_m \qquad (1.7)$$

$$\nu^{-(p-1)/2} \quad ; \nu_m < \nu < \nu_c \qquad (1.8)$$

$$\nu^{-p/2} \qquad ; \nu > \nu_c. \qquad (1.9)$$

A plot showing the spectra resulting from all possible orderings of ν_a, ν_m, and ν_c is shown in Figure 1.5 (Granot & Sari, 2002).

The hydrodynamic evolution of the shock depends on the density profile of the circumburst medium, as well as the angular profile of the outflow (i.e., collimated or isotropic). Consider first an isotropic outflow expanding into a constant density $(\rho \propto r^0)$ medium. This scenario is also referred to as an inter-stellar medium (ISM). Assuming adiabatic expansion, the flux density will scale as (Sari et al., 1998):

$$F_\nu \propto \quad t^{1/2} \qquad ; \nu < \nu_a \qquad (1.10)$$

$$t^{1/2} \qquad ; \nu_a < \nu < \nu_m \qquad (1.11)$$

$$t^{3(1-p)/4} \quad ; \nu_m < \nu < \nu_c \qquad (1.12)$$

$$t^{(2-3p)/4} \quad ; \nu > \nu_c. \qquad (1.13)$$

Alternatively, if we eliminate the electron distribution index p from the above equations, we find a characteristic relation between the temporal and spectral indices in each spectral regime known as a "closure relation" (Price et al., 2002):

$$\alpha = \quad \frac{\beta}{4} \qquad ; \nu < \nu_a \qquad (1.14)$$

$$\frac{3\beta}{2} \qquad ; \nu_a < \nu < \nu_m \qquad (1.15)$$

$$\frac{3\beta}{2} \qquad ; \nu_m < \nu < \nu_c \qquad (1.16)$$

$$\frac{3\beta-1}{2} \qquad ; \nu > \nu_c. \qquad (1.17)$$
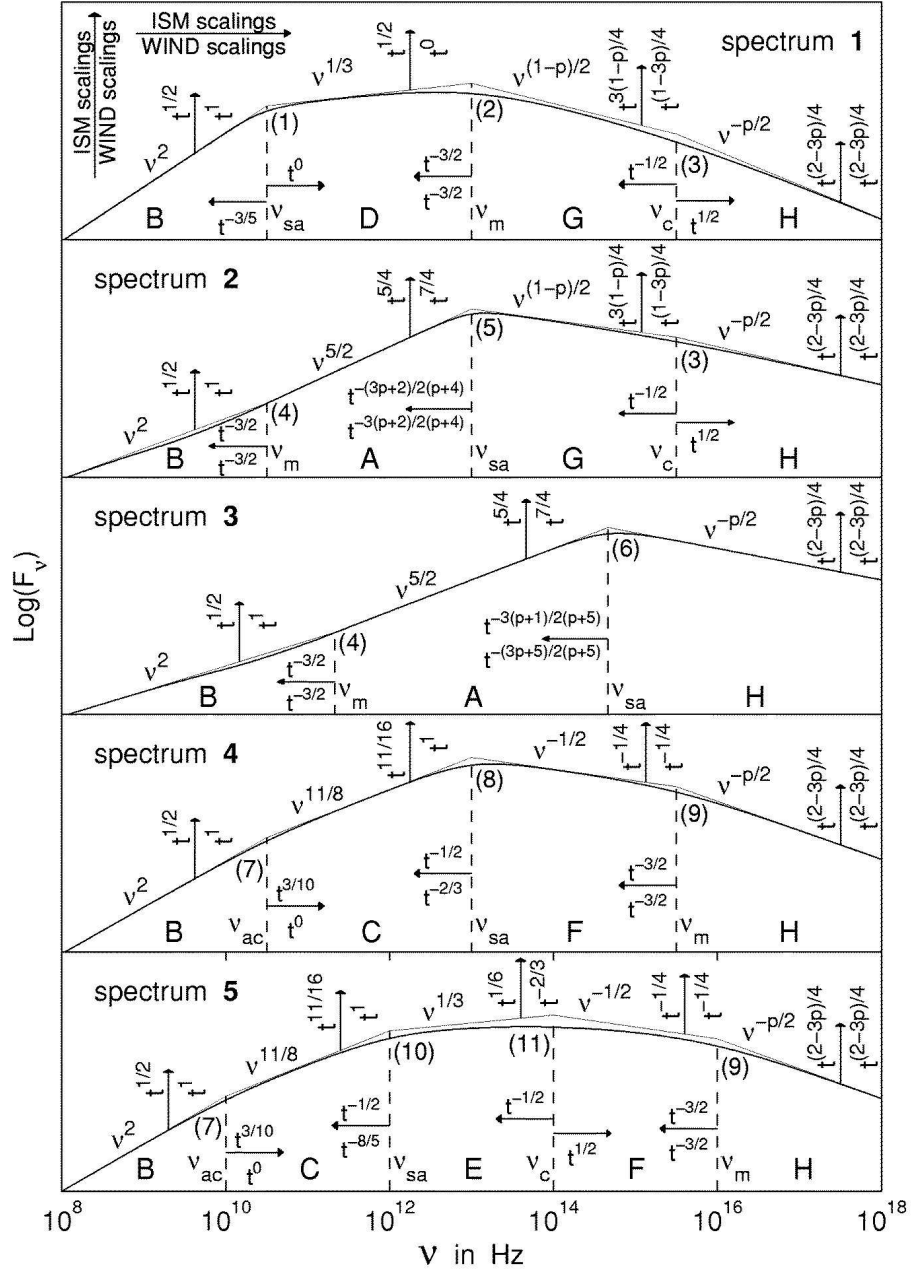
Figure 1.5 — Synchrotron spectra from GRB afterglow emission. The predicted spectrum is a broken power-law, with the exact shape depending on the relative ordering of the three critical frequencies: ν_a, ν_m, and ν_c. Typical afterglow observations are made when $\nu_a < \nu_m < \nu_c$ (*top panel*). Scalings of the flux density (*vertical arrows*) and critical frequencies (*horizontal arrows*) with time are indicated for the case of constant density and wind-like circumburst profiles. From Granot & Sari (2002).

The long-soft class of GRBs, however, is thought to arise from the deaths of massive stars as they collapse to form black holes (Section 1.4; Woosley, 1993). In the late stages of evolution, massive stars are stripped of their outer envelopes in a wind, leaving behind a signature $\rho \propto r^{-2}$ density profile that should be discernible in the afterglow light curve. The analogous temporal decay indices for an isotropic outflow expanding into a wind-like medium are (Chevalier & Li, 2000):

$$F_\nu \propto \quad t^1 \qquad ; \nu < \nu_{\mathrm{a}} \tag{1.18}$$

$$t^0 \qquad ; \nu_{\mathrm{a}} < \nu < \nu_{\mathrm{m}} \tag{1.19}$$

$$t^{(1-3p)/4} \quad ; \nu_{\mathrm{m}} < \nu < \nu_{\mathrm{c}} \tag{1.20}$$

$$t^{(2-3p)/4} \quad ; \nu > \nu_{\mathrm{c}}. \tag{1.21}$$

The derived closure relations are:

$$\alpha = \quad \frac{\beta}{2} \qquad ; \nu < \nu_{\mathrm{a}} \tag{1.22}$$

$$\frac{3\beta+1}{2} \quad ; \nu_{\mathrm{a}} < \nu < \nu_{\mathrm{m}} \tag{1.23}$$

$$\frac{3\beta+1}{2} \quad ; \nu_{\mathrm{m}} < \nu < \nu_{\mathrm{c}} \tag{1.24}$$

$$\frac{3\beta-1}{2} \quad ; \nu > \nu_{\mathrm{c}}. \tag{1.25}$$

The above temporal decay indices and closure relations (Equations 1.10–1.25) are only valid for a spherically symmetric outflow. GRBs, however, are thought to be beamed events (Section 1.5). At early times, observers only notice emission from a narrow cone (opening angle $\theta \sim \Gamma^{-1}$) due to relativistic beaming. As the shock slows, however, lateral spreading of the jet becomes important, and the observer eventually notices "missing" emission from wider angles (Rhoads, 1999; Sari et al., 1999). This hydrodynamic transition manifests itself as an achromatic steepening in the afterglow light curve, with an expected post-jet break decay proportional to t^{-p}.

The power of afterglow observations is that they allow us to infer fundamental properties of the outflow (E_{KE}, θ, ϵ_e, and ϵ_B) and the circumburst medium (n and the density profile) from relatively straightforward observations. The primary drawback,

however, is that our estimates of the physical parameters are often limited by our model uncertainties, which can be quite difficult to determine. The methods used to translate afterglow observations into physical parameters are discussed in more detail in Section 1.5.

1.4 Massive Star Progenitors and the Environments of GRBs

Until now, I have not mentioned the source powering the relativistic outflow. The nature of this central engine is almost entirely lost in the process of converting the kinetic energy of the outflow into γ-rays. The sub-arcsecond positions provided by afterglow detections, however, have nonetheless allowed us to unambiguously identify the central engines powering long-duration GRBs: massive star core-collapse (Woosley, 1993).

The most compelling evidence in support of the GRB-supernova connection comes from observations of the closest ($z \lesssim 0.3$) events (Woosley & Bloom, 2006). At late times, as the emission from the afterglow fades, it is sometimes possible to observe the effects of radioactive decay from the ^{56}Ni produced during core-collapse. In four cases (GRB 980425: Galama et al., 1998; GRB 030329: Stanek et al., 2003; Hjorth et al., 2003b; GRB 031203: Gal-Yam et al., 2004; Malesani et al., 2004; and GRB 060218: Pian et al., 2006; Modjaz et al., 2006) spectroscopy during this phase revealed broad-lined features indicative of fast-moving but sub-relativistic ($v \lesssim 10,000\,\mathrm{km\,s^{-1}}$) ejecta. In all four cases the spectra were classified as Type Ib/c supernovae, which are believed to result from the core collapse of the most massive stars ($M \gtrsim 20\,M_\odot$; Filippenko, 1997). As an example, we plot our spectroscopic observations of SN 2006aj, associated with GRB 060218, in Figure 1.6.

At $z \gtrsim 0.3$, supernovae are too faint, redshifted, and absorbed to be routinely detected with current facilities. Observations of the environments of GRBs, however, are consistent with a massive star origin. Because of their relatively short lifetimes
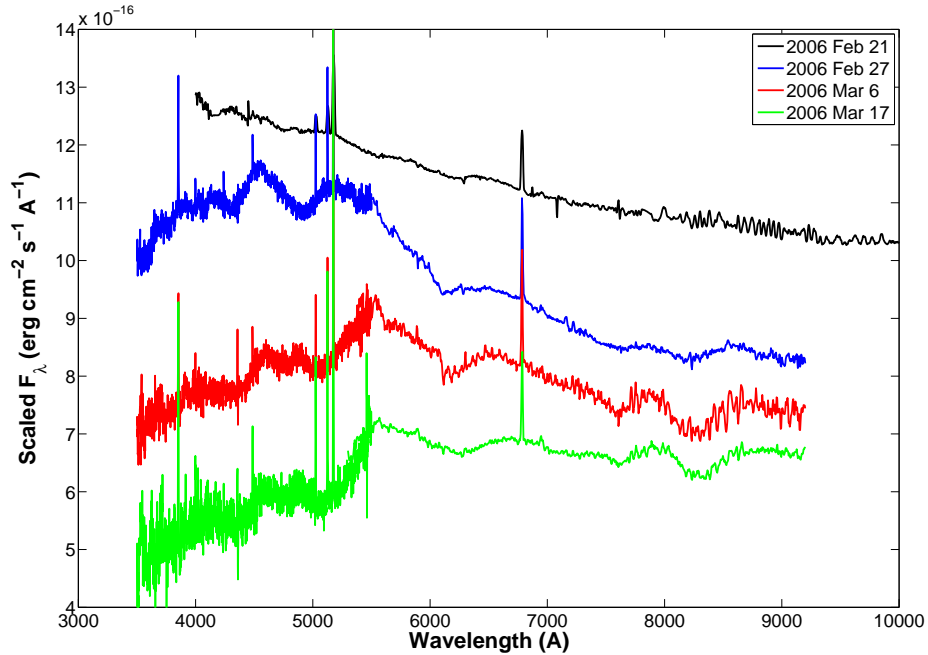
Figure 1.6 — Evolution of SN 2006aj associated with GRB 060218. The initial spectrum was taken on 2006 February 21, three days after the GRB, and is dominated by featureless, power-law afterglow emission (the bright emission lines are from the host galaxy and are unrelated to the GRB/SN). At later times, as the afterglow fades, broad-lined humps and valleys begin to emerge. Because of the lack of H and He, SN 2006aj was classified as Type Ic SN. Type Ic SNe are believed to result from the core-collapse of the most massive stars ($M \gtrsim 20 M_\odot$; Filippenko, 1997).

($\lesssim 20 \, \text{Myr}$), massive stars don't have time to venture far from the dense disks in which they formed. As a result, GRB host galaxies form a population of irregular, blue galaxies (Floc'h et al., 2003) with exceptionally large rates of specific star formation (star formation per unit mass; Christensen et al., 2004). Within their hosts, GRBs are preferentially located in the innermost regions, tracing the blue light from hot young stars even more closely than ordinary (i.e., non-relativistic) core-collapse supernovae (Bloom et al., 2002; Fruchter et al., 2006).

Absorption spectroscopy of bright GRB afterglows is therefore ideally suited to probe the dense regions where stars are being formed. The ISM along GRB sightlines has therefore yielded some of the largest neutral hydrogen column densities seen outside the Milky Way. The observed median value, $\langle \log N(\text{H I}) \rangle = 21.6 \, \text{cm}^{-2}$ (Jakobsson

et al., 2006a), is comparable only to the densest class of quasar (QSO) sightlines, the so-called damped Ly-α systems (DLAs; Wolfe et al., 2005). Because QSOs sample gas according to cross section, they are much more likely to probe the outer regions of galaxy halos (e.g., Prochaska et al., 2007b).

The massive star progenitors of long-duration GRBs should affect the local (pc scale) circumburst density as well as the global (kpc scale) ISM environment. Massive stars shed large portions of their outer H and He envelope in the late stages of evolution through stellar winds. The resulting circumburst density profile ($\rho \propto r^{-2}$ for a constant mass loss rate) should be detectable from the temporal evolution of the broadband afterglow (Section 1.3). Unlike spectroscopy of the dense ISM, however, demonstrating a wind-like environment on pc scales has proven challenging. Broadband modeling of the best-sampled afterglow light curves seems to rule out a wind-like medium for a substantial fraction of events (Yost et al., 2003; Panaitescu & Kumar, 2001). Explaining this discrepancy is still an open question in the GRB field.

The origin of short-hard GRBs remains one of the outstanding questions in the field. Several recent events have been associated with elliptical galaxies with little signs of ongoing star formation (GRB 050509B: Gehrels et al., 2005; Bloom et al., 2006; GRB 050724: Berger et al., 2005b; Barthelmy et al., 2005b), suggesting an older stellar population. The leading candidate is a coalescing degenerate binary system (neutron star-neutron star or neutron star-black hole; Eichler et al., 1989). Confirmation of this hypothesis, however, would likely require detection of a non-electromagnetic signal (i.e., gravitational waves), and may therefore be some time off in the future.

1.5 GRB Energetics: Collimation and Distribution

With the discovery of the first GRB afterglows in 1997, it became possible for the first time to directly measure the distance scale to these events. Optical spectroscopy of the bright afterglow of GRB 970508 revealed a strong metal absorption system at $z = 0.835$, firmly establishing the cosmological nature of long-duration GRBs (Metzger et al., 1997). Even for those events without bright optical afterglows, optical spectroscopy of the host galaxy often yields bright emission lines and hence a redshift determination.

With a distance in hand, we can convert GRB fluences to energies, the most fundamental parameter for any explosion. The implied energy release for the brightest GRBs was truly astounding, in some cases approaching 10^{54} erg, the rest mass energy of a neutron star (Kulkarni et al., 1999a). Such tremendous luminosities are difficult to explain even in the context of massive star collapse.

The resolution of this "energy catastrophe" lies in the geometry of the outflow. GRBs are now widely believed to be collimated explosions (Rhoads, 1999; Sari et al., 1999). At early times, when the Lorentz factor of the shock is larger than the inverse of the outflow opening angle, θ, relativistic beaming causes the outflow to appear isotropic. As the shock decelerates, however, observers begin to see more and more of the outflow. Finally, when $\Gamma \sim \theta^{-1}$, observers begin to notice "missing" emission from wide angles (Figure 1.7).

This hydrodynamical transition manifests itself as an achromatic steepening in the afterglow light curve, and convincing evidence for such a transition has been seen in several cases (Figure 1.8; Harrison et al., 1999). Measuring the time of this "jet break" allows for a determination of the opening angle, as the two are directly related by (Frail et al., 2001):

$$\theta = 0.057 \left(\frac{t_j}{1\,\mathrm{d}}\right)^{3/8} \left(\frac{1+z}{2}\right)^{-3/8} \left(\frac{E_{\gamma,\mathrm{iso}}}{10^{52}\,\mathrm{erg}}\right)^{-1/8} \left(\frac{\eta_\gamma}{0.2}\right)^{1/8} \left(\frac{n}{0.1\,\mathrm{cm}^{-3}}\right)^{1/8}. \quad (1.26)$$
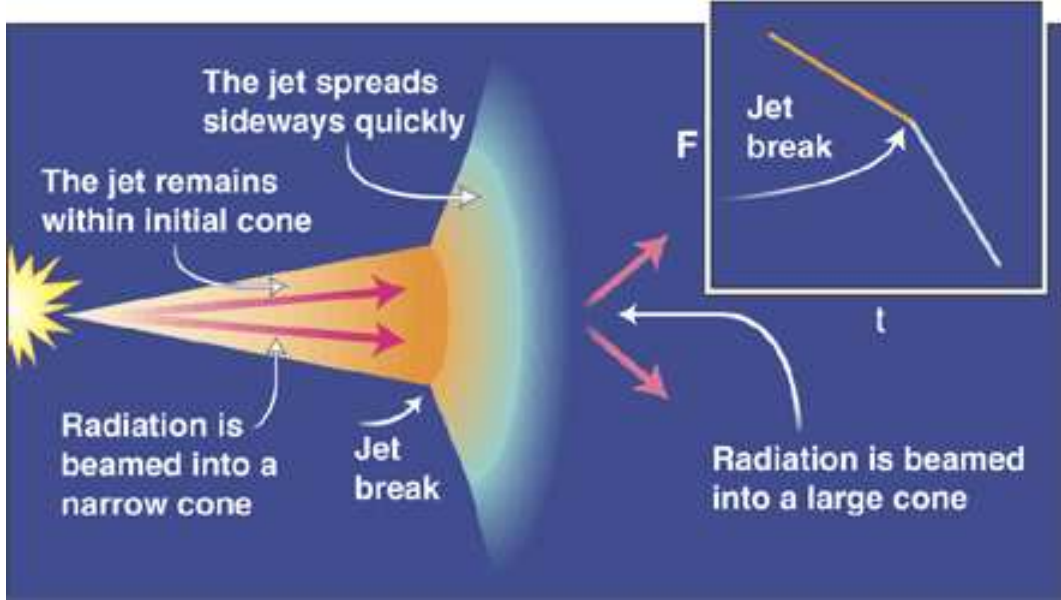
Figure 1.7 — Jets in GRBs. At early times, radiation is beamed into a narrow cone, and the light curve evolution appears isotropic. When the Lorentz factor of the outflow approaches the inverse opening angle, the jet begins to spread laterally and the observer notices missing emission from wide angles. This transition is visible as an achromatic steepening in the light curve known as a jet break. From Piran (2002).

Here t_j is the jet break time, $E_{\gamma,\mathrm{iso}}$ is the isotropic prompt energy release, η_γ is the efficiency in converting kinetic energy to γ-rays, and n is the circumburst density.

Based primarily on jet breaks observed in the optical and radio bandpasses, most GRBs appeared to be highly collimated ($\theta \sim$ a few to tens of degrees). Correcting for the narrow opening angles, the prompt γ-ray energy release (E_γ) was found to cluster around 10^{51} erg, similar to the electromagnetic energy release from SNe (Figure 1.9; Frail et al., 2001). This was an extremely important result in the field, as it offered the hope that GRBs, like Type Ia supernovae, may be used as standard candles to constrain the cosmology of our universe.

As noted previously, only a fraction of the initial outflow kinetic energy is dissipated internally to generate the prompt emission. The remainder propels a shock outward into the circumburst medium, generating the broadband afterglow emission[3]. Given that internal shocks are predicted to be relatively inefficient ($\eta_\gamma \approx 10\%$;

---

[3]In fact, GRBs may emit energy through a variety of channels, from non-relativistic ejecta (i.e., SN) to non-electromagnetic emission (gravitational waves, neutrinos). Here I will concern myself
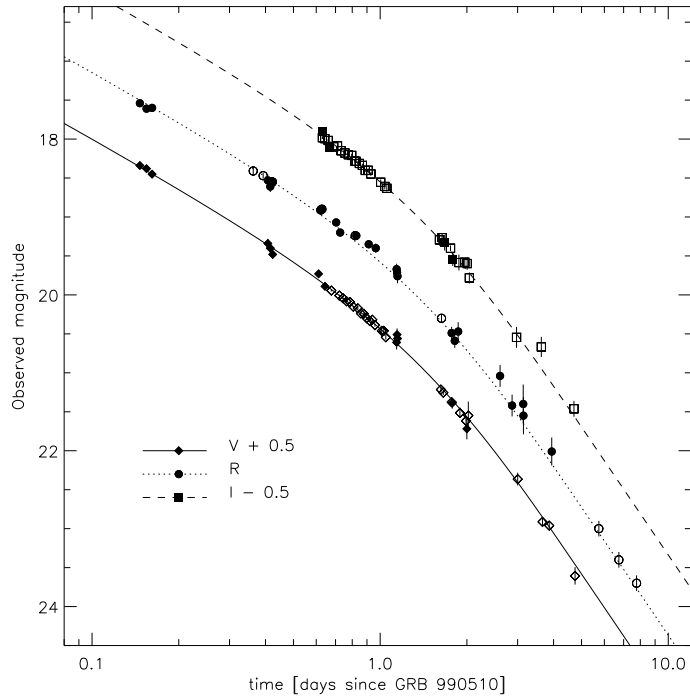
Figure 1.8 — Achromatic steepening of the light curve of GRB 990510. By determining the time of this jet break transition, it is possible determine the degree of collimation of the outflow (Equation 1.26). With narrow opening angles (4.6° for GRB 990510), determining the degree of collimation is required for an accurate determination of the total energy release. From Harrison et al. (1999).

Kobayashi et al., 1997; Daigne & Mochkovitch, 1998), constraining this outflow kinetic energy (E_{KE}) is just as important to understand the central engine as E_γ.

Accurately determining E_{KE} is not nearly as straightforward as measuring E_γ, as only a fraction of the shock energy is converted to afterglow emission. Instead it is necessary to rely on comparing observations to theoretical predictions for afterglow emission (i.e., afterglow modeling).

Robust afterglow modeling requires broadband observations of the afterglow over the entire course of its evolution, as well as accurate predictions for the afterglow flux. Throughout this work, I make use of the multi-parameter fitting software developed by Yost et al. (2003). The theoretical models include corrections for electron radiative losses as well as inverse Compton emission (Sari & Esin, 2001), and therefore represent

predominantly with relativistic output of the central engine, as this is what differentiates a GRB from an ordinary SN.
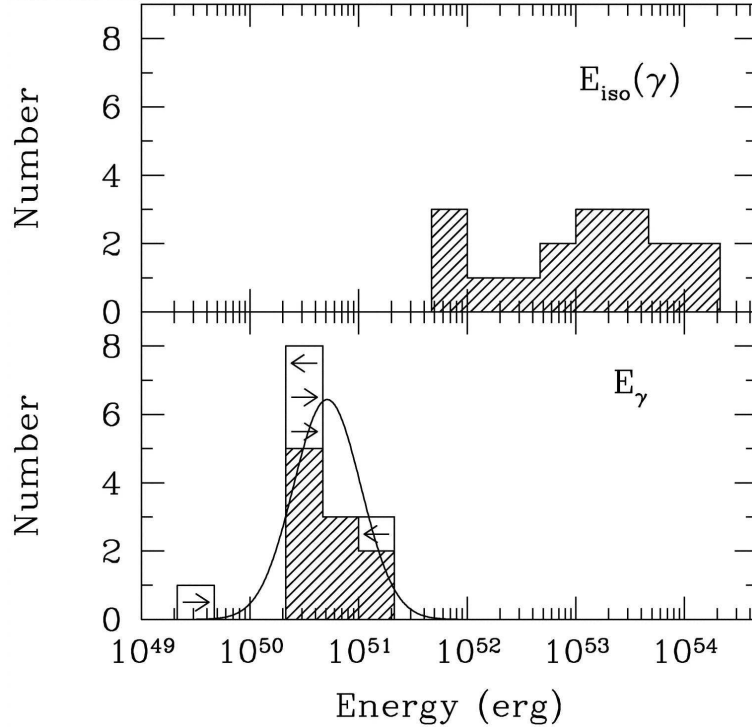
Figure 1.9 — Collimation-corrected prompt energy release in GRBs. The top panel shows the isotropic prompt energy release ($E_{\gamma,\mathrm{iso}}$) from a sample of pre-*Swift* GRBs. After applying the collimation correction (*bottom panel*), the true prompt energy release (E_γ) is tightly clustered around 10^{51} erg. From Frail et al. (2001).

our most detailed understanding of afterglow physics. These models still undoubtedly suffer from large and unknown uncertainties. However, together with the broadband (X-ray through radio) data sets presented here, this work represents some of our most detailed examinations of GRB afterglow emission to date.

1.6 The *Swift* γ-Ray Burst Explorer

Progress in the field of GRBs has come predominantly through two means: 1) new satellite missions capable of providing more accurate localizations for larger numbers of GRBs with smaller delay times; and 2) follow-up afterglow observations at earlier times, with larger telescopes, and/or in new regimes of the electromagnetic spectrum. Much of the work in this thesis builds off discoveries made by the *Swift* γ-Ray Burst Explorer, the latest NASA satellite dedicated to GRB science (Gehrels et al., 2004).

Table 1.1.   *Swift* Instrument Overview

Instrument	Effective Area	Detector	Field of View	Localization Accuracy	Energy Range
BAT	$5200\,\mathrm{cm}^2$	CdZnTe	$2\,\mathrm{sr}$	$\approx 3'$	$15 - 150\,\mathrm{keV}$
XRT	$135\,\mathrm{cm}^{2\,\mathrm{a}}$	XMM EPIC CCD	$23 \times 23'$	$\approx 3''$	$0.2 - 10\,\mathrm{keV}$
UVOT	$30\,\mathrm{cm}^{\mathrm{b}}$	Intensified CCD	$17 \times 17'$	$\approx 0.3''$	1700 - 6500 Å

[a]Measured at $1.5\,\mathrm{keV}$.

[b]Mirror diameter.

For this reason, I outline the salient characteristics of *Swift* below.

Launched in November 2004, *Swift* has three instruments on board: the wide-field (2 sr) Burst Alert Telescope (BAT; Barthelmy et al., 2005a), a hard X-ray (15–150 keV) coded-mask imager; the X-ray Telescope (XRT; Burrows et al., 2005a), a 2– 10 keV X-ray imaging telescope, and the Ultra-Violet/Optical Telescope (UVOT; Roming et al., 2005), providing imaging from 1700–6500 Å. The BAT currently provides $\approx 3'$ localizations for ≈ 100 bursts each year. Meanwhile, the XRT and UVOT "swiftly" slew to BAT-discovered GRBs, typically beginning observations of the afterglow within 100 s of the burst. Initial results from all three instruments are relayed to ground-based observers in real-time (i.e., time lag of only seconds) so that they may coordinate observations of the afterglow as well. The relevant characteristics of all three *Swift* instruments are outlined in Table 1.1.

1.7   Thesis Overview

The GRB field has matured considerably since the discovery of the first afterglows only a decade ago. As discussed in this introduction, a general picture has emerged, what I refer to as the relativistic fireball model (Figure 1.3), with the following key components:

- A compact central engine, capable of generating an ultra-relativistic outflow ($\Gamma \gtrsim 100$). We know at least some (if not all) members of the long-soft class of GRBs are powered by a massive star undergoing core-collapse.

- Shocks and/or instabilities within the ultra-relativistic outflow, which generate the short-lived, non-thermal flashes of high-energy radiation we know as GRBs.

- Accelerated electrons in the shocked circumburst medium, responsible for the long-lived, broadband afterglow emission.

- A high degree of collimation, which, after incorporating into energy estimates, results in a relatively narrow distribution of GRB energy release: $E \sim 10^{51}$ erg.

Building off the unique opportunity heralded by the launch of *Swift*, this thesis attempts to address two fundamental issues in GRB studies: 1) What is the true distribution of opening angles and collimation-corrected energy releases from *Swift* GRBs? and 2) Are the environments of *Swift* GRBs, both locally (i.e., the circumburst medium) and globally (i.e., the host galaxy ISM) consistent with a massive star origin?

The centerpiece of this thesis is the robotic Palomar 60 inch telescope (P60), which I introduce in Chapter 2. I took a lead role in converting P60 from a classically scheduled, night-assistant-operated telescope into a fully automated facility dedicated to transient astronomy. The workhorse of the GRB group at Caltech, P60 now routinely responds to *Swift* GRB triggers immediately following (and in some cases even during) the prompt γ-ray emission, providing an unprecedented multi-color glimpse into the poorly understood early afterglow phase. Unlike most robotic facilities, however, P60 is large enough to observe afterglows for days or even weeks, enabling detailed multi-color studies to investigate the geometry, energetics, and environments of *Swift* GRBs.

Chapters 3 and 4 are devoted primarily to the study of GRB energetics. Chapter 3 focuses on the P60-discovered afterglow of GRB 050820A, one of the most detailed broadband data sets in the *Swift* era. *Swift* triggered on a faint precursor (several hundred seconds before the bulk of the prompt emission), allowing us to obtain contemporaneous X-ray and multi-color optical observations during the GRB itself. Following the X-ray, optical, and radio light curves for months, I measure a total

energy release (E_γ and E_{KE}) in excess of 10^{52} erg, suggesting the true GRB energy distribution may be much broader than previously imagined.

Building off this result, I provide detailed broadband light curves for GRB 050525A and GRB 060418 in Chapter 4. Using the multi-parameter fitting software developed by Yost et al. (2003), I model the observed light curves for both events in order to infer the fundamental physical properties of the outflow. I find that GRB 060418, much like GRB 050820A, is an over-energetic outlier compared to the pre-*Swift* sample. I define a new class of "hyper-energetic" GRBs, with total energy release in excess of 10^{52} erg, and discuss the repercussions of the existence of such events on progenitor models and GRB cosmology.

In Chapter 5, I use both absorption spectroscopy and afterglow modeling to study the environment of GRB 070125 on both the pc and kpc scales. GRB 070125 appears to have occurred in an environment unlike any previous GRB, far away from the disk of its host (and hence far away from the bulk of massive star formation). I speculate the resolution may lie in triggered star formation in a tidally stripped region caused by galaxy mergers and interactions, suggesting that GRBs may be relatively unique probes of star formation in such extreme environments at high redshift.

In Chapter 6, I turn my attention from individual events to consider properties of the entire population of *Swift* optical afterglows. I construct a sample of 29 *Swift* GRB afterglows with P60 coverage beginning less than an hour after the burst, an order of magnitude increase over pre-*Swift* samples. I find that a significant fraction (50%) of *Swift* GRBs show a suppressed level of optical afterglow flux relative to the X-ray, the so-called "dark bursts." Contrary to previous studies, our multi-color P60 data allows me to show that in fact most of this suppression is caused by dust extinction in the GRB host galaxy, consistent with what one would naively expect from a system with a massive star progenitor.

Not surprisingly, the studies in this thesis have raised many new questions, particularly with regards to the GRB energy distribution. I conclude in Chapter 7 with a summary of the major results, as well as a look forward to future studies of GRB energetics and environments.

Part I

The Palomar 60 Inch Automation Project

Preamble

In order to take advantage of the unique opportunities offered by the launch of *Swift*, in 2004 we converted the Palomar 60 inch telescope (P60) from a classical night-assistant-operated telescope to a fully automated facility dedicated to γ-ray burst (GRB) and other transient follow-up. Like other small, robotic telescopes then in existence, P60 is capable of automatically responding to transient alerts, providing an unprecedented multi-color glimpse into the crucial minutes immediately following (and in some cases even during) the prompt γ-ray emission. Furthermore, P60 is currently one of the largest robotic optical facilities in the world. It is therefore capable of providing multi-color imaging of GRB optical afterglows for days or even weeks after the trigger. In this sense P60 was designed to bridge the gap between the earliest rapid-response observations and deep, late-time imaging and spectroscopy on the world's largest telescopes.

In the chapter that follows, I outline the design requirements, hardware and software upgrades, and lessons learned from the roboticization process. The chapter is largely based on an article published in *The Publications of the Astronomical Society of the Pacific* (Cenko et al., 2006a), with an updated discussion of non-GRB science and the future of P60.

Chapter 2

The Automated Palomar 60 Inch Telescope

S. Bradley Cenko[a], Derek B. Fox[b], Dae-Sik Moon[a], Fiona
A. Harrison[a], S. R. Kulkarni[c], John R. Henning[d], C. Dani Guzman[d],
Marco Bonati[d], Roger M. Smith[d], Robert P. Thicksten[d], Michael
W. Doyle[d], Hal L. Petrie[d], Avishay Gal-Yam[c], Alicia M. Soderberg[c],
Nathaniel L. Anagnostou[e], and Anastasia C. Laity[e]

[a]Space Radiation Laboratory, MS 220-47, California Institute of Technology, Pasadena, CA 91125

[b]Department of Astronomy & Astrophysics, 525 Davey Laboratory, Pennsylvania State University, University Park, PA 16802

[c]Department of Astronomy, Mail Stop 105-24, California Institute of Technology, Pasadena, CA 91125

[d]Caltech Optical Observatories, Mail Stop 105-24, California Institute of Technology, Pasadena, CA 91125

[e]Infrared Processing and Analysis Center, Mail Stop 100-22, 770 South Wilson Avenue, Pasadena, CA 91125

Abstract

We have converted the Palomar 60 inch (1.52 m) telescope from a classical night-assistant-operated telescope to a fully robotic facility. The automated system, which has been operational since 2004 September, is designed for moderately fast ($t \lesssim 3$ minutes) and sustained ($R \lesssim 23$ mag) observations of γ-ray burst afterglows and other transient events. Routine queue-scheduled observations can be interrupted in response to electronic notification of transient events. An automated pipeline reduces data in real-time, which is then stored on a searchable Web-based archive for ease of distribution. We describe here the design requirements, hardware and software upgrades, and lessons learned from roboticization. We present an overview of the current system performance as well as plans for future upgrades.

2.1 Introduction

The field of optical transient astronomy has matured to produce numerous important scientific discoveries in recent years. Type Ia supernovae (SNe) have been used as standard candles to produce Hubble diagrams out to $z \sim 0.5$, providing evidence that the expansion of the universe is accelerating (Riess et al., 1998; Perlmutter et al., 1999). Observations of the broadband afterglows of long-duration ($t > 2$ s) γ-ray bursts (GRBs) have revealed an association with the deaths of massive stars (Galama et al., 1998; Stanek et al., 2003; Hjorth et al., 2003b). The discovery of the first afterglows and host galaxies of short-duration ($t < 2$ s) GRBs (Gehrels et al., 2005; Bloom et al., 2006; Hjorth et al., 2005; Fox et al., 2005) has possibly revealed a new class of GRB progenitors: compact binary coalescence (Eichler et al., 1989).

As interest in the field has steadily grown, new, more powerful methods of identifying optical transients have been developed. The *Swift* γ-Ray Burst Explorer (Gehrels et al., 2004) is currently providing ~ 100 prompt GRB localizations per year, an order-of-magnitude improvement over previous missions. Planned wide-angle, high-cadence surveys with large facilities, such as Pan-STARRS (Panoramic Survey Telescope and

Rapid Response System; Kaiser et al., 2002) and LSST (Large Synoptic Survey Telescope; Tyson, 2005), promise to overwhelm our current follow-up capability, providing hundreds of variable optical sources each night.

Dedicated, robotic, medium-aperture (1–3 m) telescopes have the opportunity over the next few years to play a crucial role in this field. Like small-aperture (< 0.5 m), robotic facilities, they can respond autonomously to transient alerts, providing observations at early times. And given the relative abundance of such telescopes, it is entirely feasible to focus predominantly on transient astronomy. However, like larger telescopes (> 5 m), interesting events can be followed for longer durations and in multiple colors. In this sense robotic, medium-aperture facilities can act to bridge the gap between the earliest rapid-response observations and deep, late-time imaging and spectroscopy.

To this end, we have roboticized the Palomar 60 inch telescope (P60). As a dedicated, robotic facility, the P60 is capable of responding moderately fast ($t \lesssim 3$ minutes) to transient alerts. With the increased event rate of *Swift*, the P60 is providing observations of the poorly understood early afterglow phase (Figure 2.1). Additionally, as a 1.5 m telescope, the P60 can continue the sequence of observations longer than most robotic telescopes. As Figure 2.2 shows, one day after the burst, most afterglows have faded below $R = 20$; however, for days or even weeks after that, they remain at levels of $R < 23$ accessible to P60 photometry.

In this work, we first outline the high-level design requirements of a robotic system optimized for observations of transient sources (Section 2.2). Section 2.3 provides the details of the automation procedure, including both the hardware and the software efforts. Section 2.4 describes the current system performance (as of 2006 May), which will primarily be of use for those interested in observing with the P60. Finally, in Section 2.5, we conclude with a summary of P60 science highlights to date and discuss the future of P60 as part of the Palomar Transient Factory (PTF).
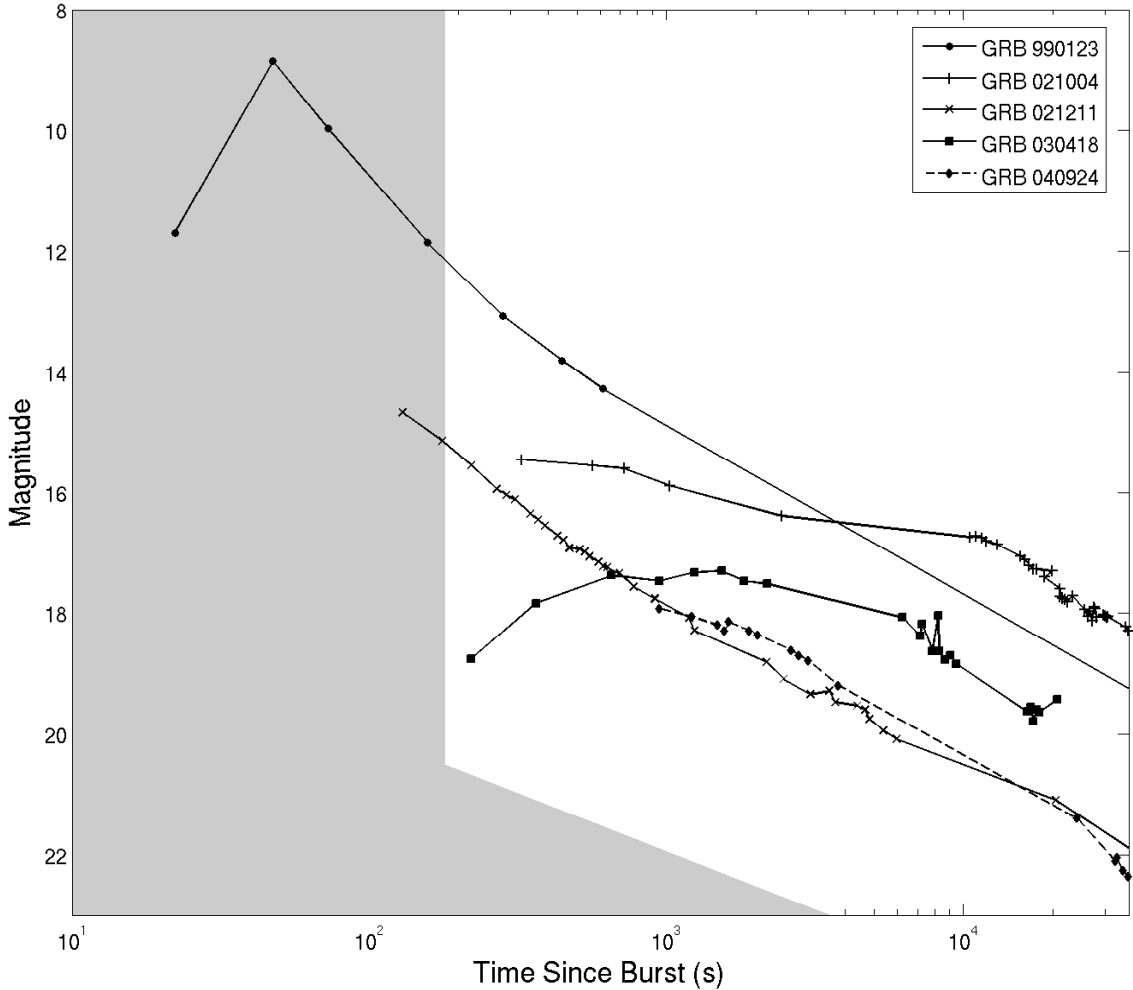
Figure 2.1 — Early afterglows of pre-*Swift* GRBs and P60 response capabilities. Regions with a white background are accessible for automated P60 observations: $t \gtrsim 3$ minutes, $R \lesssim 23$ mag. With only a handful of examples, the early optical afterglows of pre-*Swift* GRBs show a marked diversity. GRB 990123 (Akerlof et al., 1999) and GRB 021211 (Fox et al., 2003a; Li et al., 2003) exhibit the fast t^{-2} early-time decay indicative of adiabatic evolution of the reverse shock. On the other hand, GRB 021004 (Fox et al., 2003b; Holland et al., 2003; Pandey et al., 2003) shows a distinctive slow $t^{-0.4}$ decay that likely signifies continuing energy input to shock regions. Reverse shock emission from GRB 030418 (Rykoff et al., 2004) was not seen; the optical peak at $t = 0.4$ hours is due to the forward shock component. As a proof of concept, P60 discovered the optical afterglow of GRB 040924 (Fox & Moon, 2004; Li et al., 2004; Hu et al., 2004; Silvey et al., 2004; Khamitov et al., 2004). The early time behavior is quite similar to that of GRB 021211.
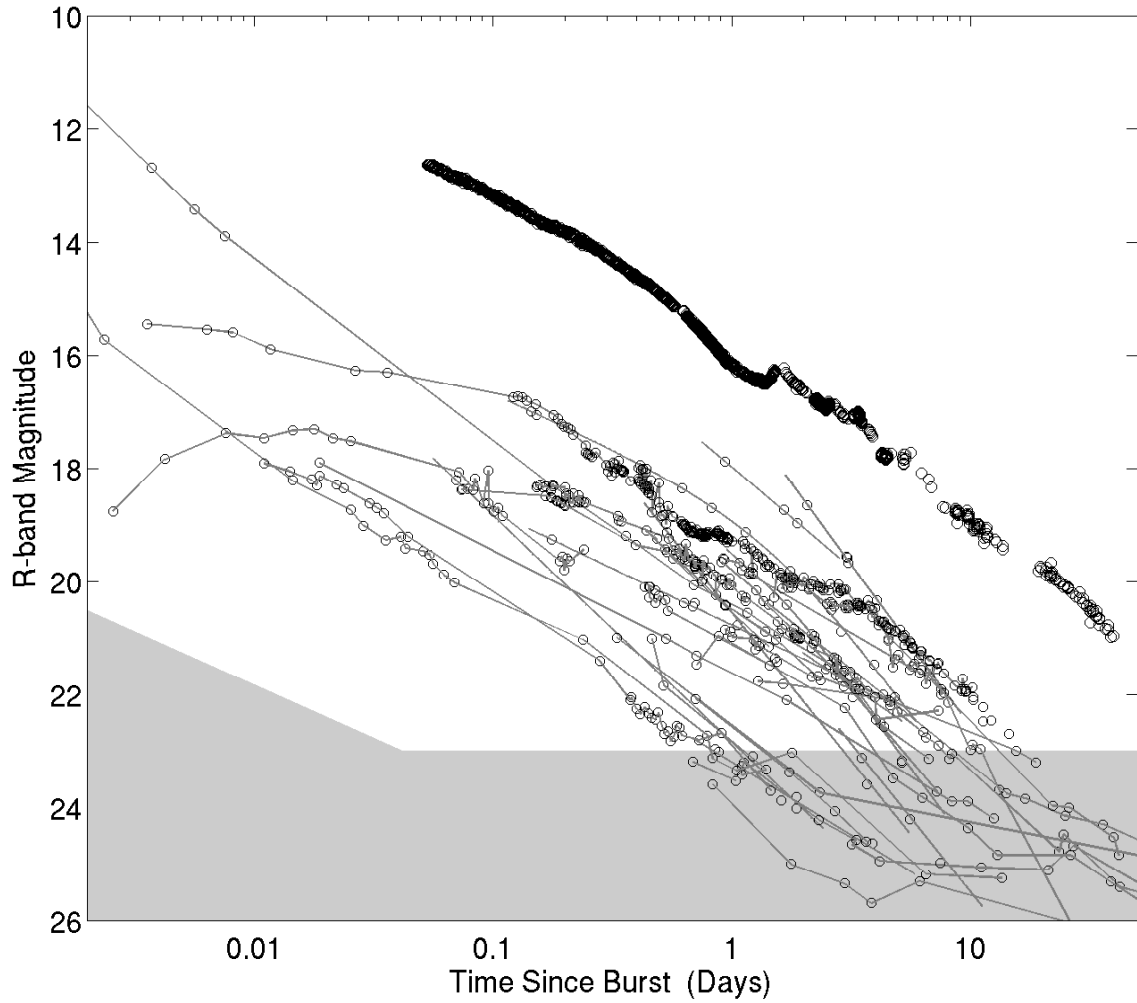
Figure 2.2 — Late-time light curves of pre-*Swift* GRB afterglows. The gray shaded region displays the phase space inaccessible to automated P60 observations. Observations of most afterglows require > 1 m class facilities after the first night; investigation of optically-extinguished ("dark") or high-redshift bursts require such facilities merely to register detections or collect physically interesting upper limits.

2.2 General Design Considerations

Designing a robotic system for transient astronomy presents a unique set of challenges from both a hardware and a software perspective. It is necessary to create an intelligent system that can reliably handle the roles usually provided by the observer and night assistant at a standard facility (e.g., Genet & Hayes, 1989).

Given our scientific objectives, we identified following system requirements for the Palomar 60 inch automation project:

1. **Automated transient response in $\lesssim 3$ min** — GRB afterglows are predicted to decay in time as a power-law ($F_\nu \propto t^{-\alpha}$) with index $\alpha \approx$ 1–2, depending on whether the emission is dominated by the forward ($\alpha_{\mathrm{FS}} \approx 1$; Sari et al., 1998) or reverse ($\alpha_{\mathrm{RS}} \approx 2$; Sari & Piran, 1999a) shock. For (optically) bright bursts, rapid response enables studies of the afterglow at its brightest, shedding light on the poorly understood early afterglow phase (Figure 2.1). For the fainter bursts, rapid response is required simply to obtain a detection or even a meaningful upper limit (Figure 2.2). Our desired response overhead is limited primarily by the telescope slew time.

2. **CCD Readout in < 30 s** — Given the expected power-law behavior, densely-sampled observations are necessary to accurately characterize the early afterglow decay. And since our current system is not equipped with an automated guider, deep observations must be broken down into many individual exposures (and hence many accompanying readouts). Given typical values for our telescope slew (3 minutes) and exposure (1–3 minutes) times, we determined a readout time < 30 s would not significantly affect our sampling rate or efficiency.

3. **Photometry from the near ultra-violet to the near-infrared (NIR)** — GRB redshifts can be estimated photometrically by modeling afterglow spectral energy distributions (SEDs). Ly-α absorption in the inter-galactic medium (IGM) causes a steep cutoff in the SED, the location of which indicates the afterglow redshift (Lamb & Reichart, 2000). To constrain as large a spectral range

as possible ($2 \lesssim z \lesssim 6$), we require coverage over the entire optical bandpass (Figure 2.3). The ideal solution would be a multi-band camera, providing simultaneous imaging in multiple filters. The cost of either purchasing or building such an instrument, however, was too high for our first generation of operations. Instead, we employ a 12-position filter wheel, with coverage spanning from Johnson U ($\lambda_c = 3652\,\text{Å}$) to Sloan z' ($\lambda_c = 9222\,\text{Å}$).

4. **Intelligent observation oversight** — Like a virtual night assistant, a centralized source of information is required to effectively manage nightly observations (i.e., telescope, weather, and instrument status information). Under ideal conditions, this is not a difficult task. More challenging, however, is implementing a robust capability to intelligently respond to adverse conditions.

5. **Queue scheduling system for standard mode** — Since not all of the telescope time is devoted to rapid-response GRB observations, a scheduler is needed to handle standard scientific observations, as well as calibration images. We chose to implement a queue-scheduler, as it is capable of providing real-time management of observations (i.e., targets can be submitted to the queue at any time) with a minimal amount of daily oversight (night-to-night memory ensures that there is no need to write daily target lists). Furthermore, a queue-scheduler is ideally suited for long-term monitoring of transient objects; SNe and GRBs can be left in the queue for regular monitoring on time scales of weeks or even months.

6. **Automated, real-time (< 2 minutes) data reduction** — Real-time data reduction is necessary for several reasons. First and foremost, feedback is required for standard system oversight commonly performed by observers present at the telescope. Focusing is the simplest example. Second, rapid identification of optical counterparts is critical for intelligent follow-up observations. High-resolution absorption spectroscopy in particular requires a rapid turn-around with large facilities. Finally, properly handling the large amounts of data produced on a nightly basis requires that data reduction be fully automated.
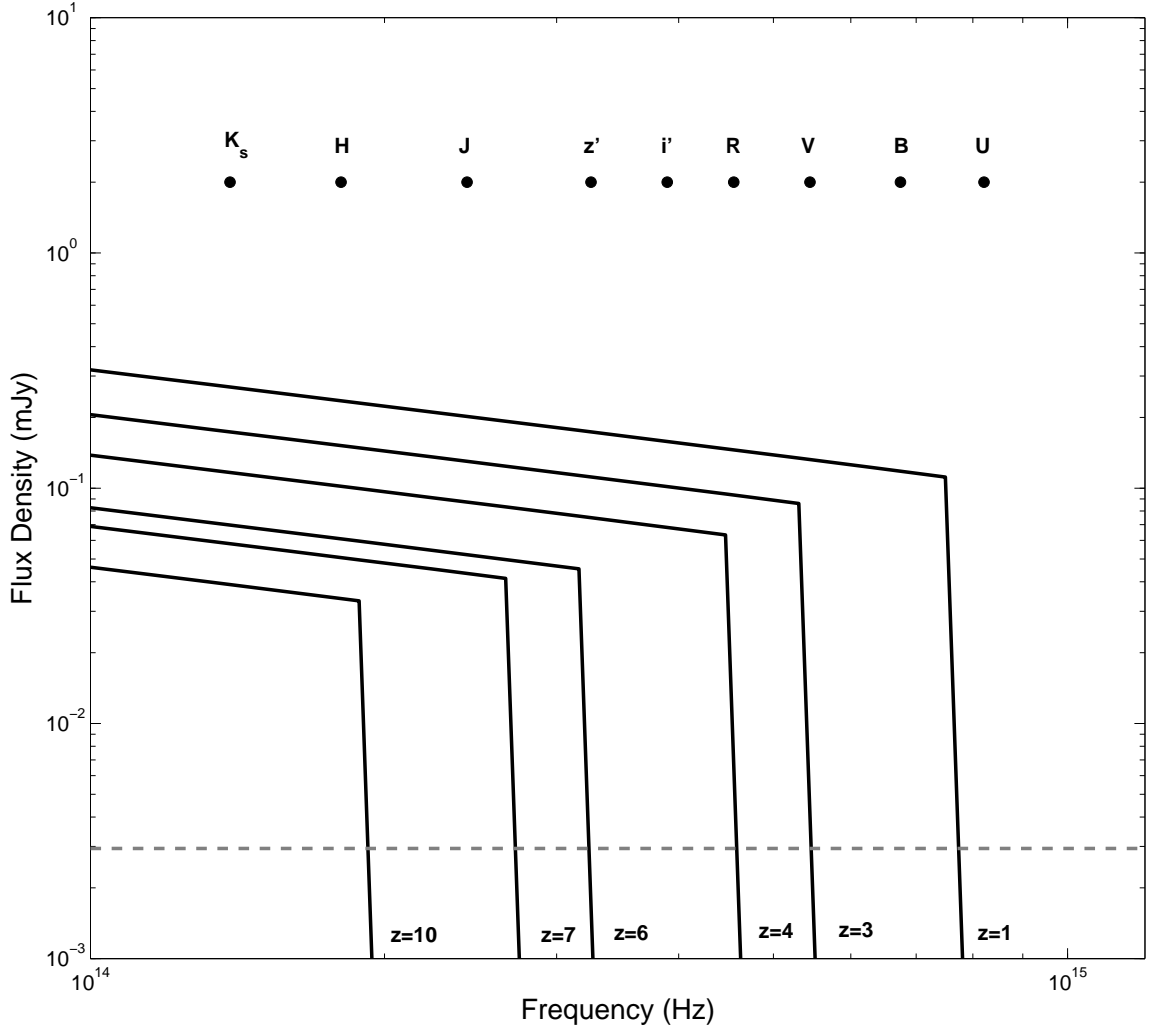
Figure 2.3 — Optical/NIR SEDs of GRB afterglows as a function of redshift. These SEDs are models of the afterglow of GRB 990510 1 hr after the burst (Panaitescu & Kumar, 2001), viewed at redshifts ranging from $z = 1$ to $z = 10$. The P60 R-band sensitivity (1 hr integration, $R \approx 23$ mag) is shown as a dashed line, extended to all frequencies for reference. The central wavelengths of the broadband filters on the P60 are drawn above the spectra, as well as the standard $JHK_{\rm s}$ NIR filter set. Ly-α absorption in the IGM causes the steep cut-off in the afterglow spectra, which can be used to estimate the redshift of GRB afterglows photometrically (Lamb & Reichart, 2000).

7. **Fully searchable, web-based data archive** — The average P60 data rate, including daily calibration files, is ~ 5 GB per night. Furthermore, with our queue-scheduling system, science images are obtained for a large number of users (~ 10) on most nights. We therefore opted for a high-capacity, fully searchable data archive for ease of data storage and distribution.

2.3   Automation Procedure

In Section 2.2 we outlined the design requirements for the automated system. Here we describe the techniques we have used to meet these requirements in a more thorough manner.

2.3.1   New CCD and Electronics

The previous P60 CCD took almost three minutes to read out, unacceptably long given our desired response time of $\lesssim 3$ minutes. Furthermore, the camera was only accessible via a local MicroVAX terminal, making automated observations impossible. To meet our design requirements, we chose to build a new camera using the latest San Diego State University controller, Generation III electronics (SDSU-III; Leach & Low, 2000). This system is capable of better performance than an off-the-shelf product, with the trade-off being that a significant time investment was required for development and testing. In the following two sections, we describe the new electronics (Section 2.3.1.1) and the software used to control the camera (ArcVIEW; Section 2.3.1.2).

2.3.1.1   SDSU-III Electronics

The telescope was equipped with a new SITe 2K $\times$ 2K back-illuminated CCD. While we have not measured the quantum efficiency of the new device, our observations indicate its quantum efficiency is comparable to that of the previous camera (which was an identical SITe 2k $\times$ 2k CCD). For reference, we include a quantum efficiency
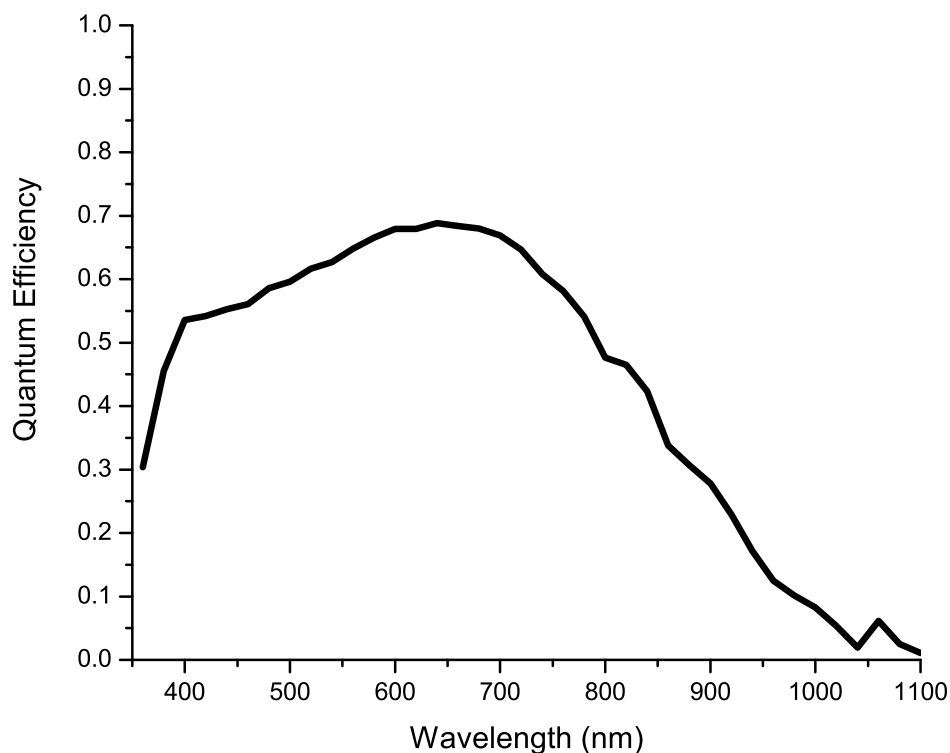
Figure 2.4 — Previous P60 CCD quantum efficiency. While we have not measured the quantum efficiency of the new P60 CCD, it is identical in design to the previous version shown here. Observations made with both detectors indicate a comparable overall performance.

plot from the old CCD in Figure 2.4.

The new CCD is controlled by an SDSU-III controller (Leach & Low, 2000). The new controller contains a faster optical link than the Generation II system, as well as a newly designed timing board. The system is capable of reading out four channels in parallel. However, to reduce costs and simplify fabrication, we currently utilize only two amplifiers for readout.

Temperature sensors were placed in thermal contact with the CCD and the dewar neck and can, as well as on board the electronics. These sensors are capable of triggering an alarm under abnormal conditions, for example when the dewar runs out of liquid nitrogen and begins to warm.

Table 2.1. New P60 CCD and Electronics Capabilities

Property	Amplifier 1	Amplifier 2	Full Chip
Array Size	2048×1024	2048×1024	2048×2048
Pixel Size (μm)	$\cdots$	$\cdots$	24
Plate Scale (arcsec pixel^{-1})	$\cdots$	$\cdots$	0.378
Field of View (arcmin)	12.9×6.5	12.9×6.5	12.9×12.9
Gain (e$^-$ ADU^{-1})	2.2	2.8	$\cdots$
Read Noise (e$^-$)	5.3	7.8	$\cdots$
Dark Current (e$^-$ s^{-1})	10^{-3}	10^{-3}	$\cdots$
Charge Transfer Efficiency	$> 99.999\%$	99.999%	$\cdots$
Full Well Capacity (e$^-$)	130,000	140,000	$\cdots$
Bias Level (ADU)	610	445	$\cdots$
Saturation Limit (ADU)	50,000	45,000	$\cdots$

In addition to the standard full-frame readout mode, two additional capabilities have been implemented. Using the region-of-interest (ROI) functionality, we can read out only a subsection of the chip. This is particularly important for small GRB error circles, helping to improve both the sampling rate and efficiency of our system. Additionally, the ability to manipulate charge independent of the readout ("parallel shift") greatly decreases the time required for a focus loop. This has been of utmost importance, given the difficulties we have encountered maintaining system focus throughout the night (see Section 2.4.3).

The relevant characteristics of the new camera are outlined in Tables 2.1 and 2.2. The P60 camera was the first developed under an engineering scheme designed to standardize enclosures and cabling for new instruments on the mountain. The lessons learned have been extended to future instruments being developed for Palomar Observatory.

2.3.1.2   Instrument Control System: ArcVIEW

The software used to control instrument operation is called ArcVIEW, a package that was developed at the Cerro Tololo Inter-American Observatory and Caltech. It is based on Labview (interfaces and communication) and C (real time data processing and drivers API [application programming interface]).

Table 2.2. P60 CCD Readout Time

Fraction of Array	Sky Size (arcmin)	Readout Time (s)
Full	12.9×12.9	24
1/2	6.5×12.9	18
1/4	6.5×6.5	10

The ArcVIEW architecture consists of a set of software modules that can be loaded or unloaded dynamically to control different processes. The core of the software receives commands and passes them to the appropriate module for processing. A translation layer built into the system allows for transparent hardware control (i.e., the standard command set available to the user is independent of the details of the hardware being controlled).

ArcVIEW commands are sent as plain ASCII strings passed through raw sockets. Graphical user interfaces (GUIs) are not needed to control the system; however, some of them are provided in order to handle data taking, filter movements, telescope control system (TCS) commands, and low-level engineering commands in a user-friendly way.

Besides the normal command/response channel, ArcVIEW contains an optional asynchronous message channel, that allows the system to send asynchronous alarm messages (temperatures, power supplies, etc.), callbacks, or event messages to the connected client. Using this extra channel it is possible to perform simultaneous actions (e.g., moving the telescope while reading out the array).

The final output of the system is an image (or sequence of images) written in FITS format and containing user-defined header information. The two P60 amplifiers are read out and stored as a multi-extension FITS file.

We have chosen a modular design for our major software components, as illustrated in Figure 2.5. Each component acts independently, with a well-defined communication protocol between the different modules. This design makes software upgrades easier, allows for a clean division of labor and responsibilities, and guarantees a more

P60 Software Overview
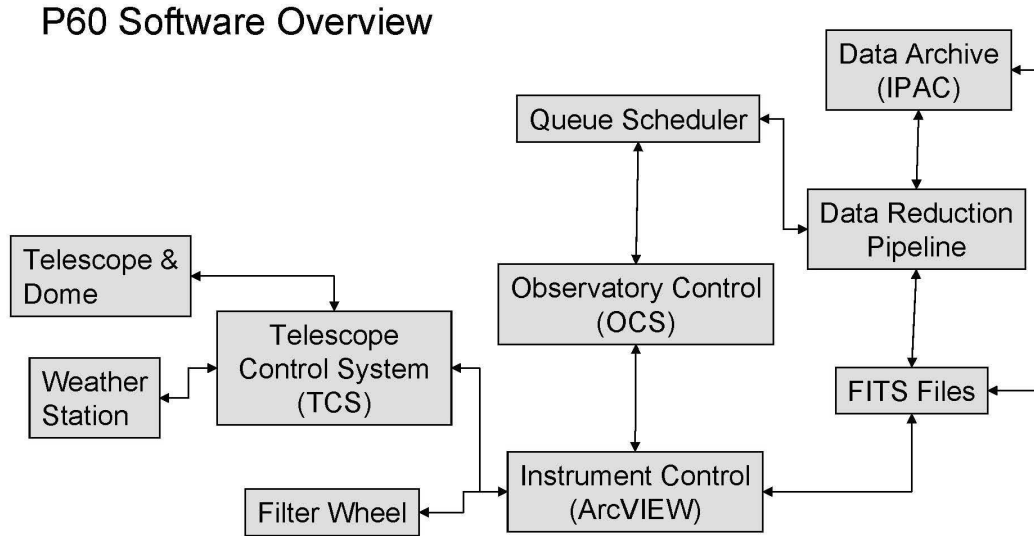
Figure 2.5 — P60 software overview. Arrows indicate direct channels of communication. The modular design was chosen to ensure both stability and ease of upgrade/repair.

robust system, as failure in one component does not necessarily imply complete system failure. Modular designs have long been in use at automated facilities and have proved both reliable and effective (e.g., Steele & Carter, 1997; Granzer et al., 2001; Bloom et al., 2006). On the P60, ArcVIEW acts as a single point of contact between hardware operation (telescope, CCD, and filter wheel) and all other system components (Figure 2.5).

2.3.2 Observatory Control System

The purpose of the observatory control system (OCS) is to provide intelligent oversight of nightly observations and to coordinate information from all system components (Figure 2.5). We identify four primary tasks for which the OCS is responsible, each discussed below.

First, at the beginning of each night, the OCS spawns the queue-scheduling software in a separate process (Section 2.3.3). These two systems communicate throughout the night via a socket, as real-time target selection depends on the success of

previous observations.

After receiving an observation request, the OCS is then responsible for executing it in a safe and efficient manner. Communication with the TCS, via the transparent ArcVIEW intermediary, ensures that external conditions permit the requested observation. All component tasks that can be completed in parallel (e.g., moving the telescope and filter wheel) are done so to improve system efficiency. An observation is considered to have completed successfully when the readout of the final exposure begins.

Third, after the successful completion of the first images on any given night, the OCS spawns the data reduction pipeline in a separate process (Section 2.3.4). These two systems communicate to ensure the integrity of science images, most notably by maintaining telescope focus throughout the night (Section 2.4.3).

Finally, the OCS handles any errors that arise during the normal course of operations. Each error condition is assigned a level in a hierarchy of functionality. Lower levels correspond to more basic, elementary functionality, and vice versa. When an error is discovered, the OCS will begin at the appropriate error level and work downward until the depth of the error condition is determined. The OCS then works to restore the system to functionality. If no solution can be found, the system goes into a safe mode, closing the dome and terminating observations. Email notices and text messages are sent to alert users of this condition.

As an example, we consider an error generated by the focus encoder during routine operation. The OCS first verifies communication with the TCS. If this fails and cannot be restored, the system checks communication with ArcVIEW, as it is responsible for routing most communication. If this too fails and cannot be restarted, the OCS checks for Internet connectivity. This process continues until either a solution is discovered or human intervention is required. Similar systems have been used successfully on other automated facilities (Granzer et al., 2001).

2.3.3 Observation Scheduling System

In the design of the observation schedule system (OSS), we have deliberately pursued a "short-sighted" strategy of selecting targets in real-time. That is, observations are chosen at each point in the night when the OCS reports being in a ready state, rather than attempting to optimize a sequence of observations over the course of a full night (or over multiple nights). This strategy is relatively well suited to ground-based observations, where future observing conditions are unknown and observing overheads are a relatively minor concern. Moreover, the scheduling protocol and target list for P60 observations are modest enough that a full evaluation of the target list can be performed in a matter of seconds. This principle of "just in time" scheduling has also been pursued at several larger scale queue-observing facilities (Chavan et al., 1998; Sasaki et al., 2000; Adamson et al., 2004), as well as more modest robotic observatories (Honeycutt et al., 1990; Fraser & Steele, 2004).

Target scores are determined on the basis of raw target priorities, which are fixed in advance, combined with the application of several parametric weightings. The most important of these for scheduling purposes are the `Airmass` and `Night` weighting variables, which take as input the current airmass of the target and the number of hours left before the target becomes unobservable (due to target-set or morning twilight), respectively.

The nature of the effect of each weighting is the same. Based on the value of the input variable, the weight is calculated and applied as a multiplier to the target score (initially, the target priority). If the weighting is found to be zero, then the target score is necessarily zero; otherwise, the target score will be increased or decreased depending on whether the weight in question is calculated to be greater or less than one.

The full list of possible weighting variables includes:

- `Airmass`, with input variable the current airmass of the target. This weighting prefers sources that are close to transit (minimum airmass).

- `Night`, with input variable the number of hours until the source becomes unob-

servable. This weighting helps ensure efficiency of the scheduler operations since it prefers sources that are setting rather than rising. The estimated duration of the target's full exposure sequence is included in the calculation.

- `Moondeg`, with input variable 180° minus the current angular distance from the target to the moon. This avoids taking images with high sky background due to moonlight.

- `Seeing`, with input variable the current seeing in arcseconds. This allows the segregation of programs according to whether their science is adversely affected by poor seeing.

- `Extinction`, with input variable the current magnitude of extinction, in the R band, due to clouds. This allows segregation of programs according to how strongly they are affected by reduced sensitivity.

The `Seeing` and `Extinction` weightings are not yet in operation, but should be applied dynamically within the OSS by the end of Summer 2008.

In addition to these parametric weightings, target scores are also adjusted based on timing criteria. The default logarithmic timing scheme steadily increases the score of a target from night to night until it has been observed. Alternate timing schemes allow for periodic (ephemeris-based) or regular aperiodic ("best effort") monitoring of targets, or for target activation within a specified window of time only.

Finally, we have found it important to increase the score of targets once they have been observed on a given night, so that they are more likely to be observed to completion (one or more sets of the requested exposure sequence) during that night. This prevents fragmentation of observer programs and reduces overheads that are mostly incurred on a per-target basis.

2.3.4 Image Analysis Pipeline

The constituent routines for our image analysis pipeline are composed within the context of PyRAF[1], a Python wrapper for the IRAF data reduction environment of the NOAO[2]. The pipeline is instantiated in a single Python script which can be run from the Linux command line. The script runs continuously throughout the night, identifying new raw images as they are copied into the target directory, and processing them in real time.

PyRAF allows access to IRAF routines from within Python, a scriptable, object-oriented, high-level language environment. In particular, Python performs active memory management and, with its various included modules, supports mathematical and logical operations on array variables, regular-expression matching against text strings, and easy access to FITS headers and data.

Python scripts that access arbitrary PyRAF routines can be executed from the command line. The speed of these scripts is not as fast as compiled C routines. However, the single most substantial overhead for script execution is incurred at startup as the PyRAF libraries (including IRAF) are loaded into memory. Once cached in memory, the speed of execution of our scripts is competitive with native IRAF and adequate to our purposes.

The routines of the P60 pipeline execute the following reduction steps in sequence: (1) De-mosaicking, which performs overscan subtraction on the separate image extensions produced by the two amplifiers, and combines them into a monolithic image while preserving the values of unique header keywords associated with each extension; (2) Bias subtraction against our nightly bias image; (3) Flat-fielding against the dome-flat images taken during the afternoon or previous morning, sky-subtraction, and addition of the dead-reckoning world-coordinate system (WCS); (4) Masking of bad pixels, using the nightly bad pixel mask; (5) Object detection, using a spawned Sextractor[3] process; (6) WCS refinement via triangle-matching against the USNO

---

[1]See http://www.stsci.edu/resources/software_hardware/pyraf.
[2]See http://iraf.noao.edu.
[3]See http://terapix.iap.fr/soft/sextractor.

B-1.0 catalog[4], using the ASCFIT software (Jørgensen et al., 2002); and (7) Seeing and zero-point estimation using USNO B-1.0 catalog stars identified in the image.

If an insufficient number of stars are identified during the WCS refinement process for an image, then the dead-reckoning WCS is left untouched and the seeing and zero-point estimation steps are skipped. Calibration products are produced from raw calibration bias and dome-flat images at the start of the night as a separate process.

The final analysis task, which is performed by a special single-purpose script, is to determine our best focus value and current seeing from a single focus-run (multiple exposures and a single readout) on a bright star. For the sake of speed, this task omits most of the standard processing steps.

Additional routines have been coded but are not run in an automated fashion, either because of difficulty in robustly defining their operations, or because of excessive processing requirements. These include: fringe image creation and defringing of I- and z'-band images; co-addition of multiple dithered images to achieve greater depth of field; and mosaic co-addition of multiple images, using SWarp[5], to cover areas significantly larger than the CCD field of view.

The P60 pipeline routines are general and can be readily applied to other data reduction tasks; indeed, we have already adapted them to the construction of an interactive pipeline for Wide-Field Infrared Camera (WIRC; Wilson et al., 2003) data reduction at the Hale 200 inch (5.08 m) telescope.

2.3.5 Data Archive

The P60 data archive is designed to securely store data collected at the robotic facility, and to provide efficient and convenient access to users from the P60 partner institutions. In return for a 10% share of telescope time, the Infrared Processing and Analysis Center (IPAC) has assumed responsibility for the procurement, installation, and maintenance of the archive hardware, as well as for database software development, following specifications provided by the P60 science team at Caltech.

---

[4]See http://www.nofs.navy.mil/data/FchPix.
[5]See http://terapix.iap.fr/soft/swarp.

The archive routinely stores the entire set of raw frames, calibration data, and pipeline-processed images collected nightly at the telescope. The data are transmitted down from Palomar Mountain to the Caltech campus over the new HPWREN fast data link. The images are transmitted in a non-lossy compressed form, and MD5 checksums are used to verify their integrity. At IPAC, all files are stored on a cluster of Sun Microsystems computers hosting the archive server and database structure. A RAID5 Nexsan ATAboy disk farm provides approximately 3 TB of disk space. A second copy of the data is kept on Caltech computers at Robinson Laboratory as backup. Each nightly batch of data is ingested into the database software, which has an astronomy-optimized architecture similar to other IRSA archives. User access is provided through a web-based interface. Using the archive web page, users can query the database, locate data they require, and request it from the archive. Data delivery is from a staging area, following e-mail notification to the user. Under normal operating conditions, small data packets can be obtained in this way within minutes.

2.4 Automated System Performance

The P60 has been running in a fully automated mode since 2004 September. This includes all aspects of operation, from the automated queue scheduler through nightly ingest of archival data. Here we present an overview of the current system performance, focusing primarily on information relevant for interested P60 observers.

2.4.1 CCD Camera, Telescope, and Filters

As of 2006 June, the camera is performing reliably and has met all relevant specifications. Since the fall of 2004, the amount of time lost due to detector or electronics problems (or related software) is small ($< 5\%$). A summary of the relevant camera details can be found in Tables 2.1 and 2.2.

The most relevant characteristic for our science goals is the readout time. The full frame readout time of the system is 24 seconds. This can be significantly reduced,
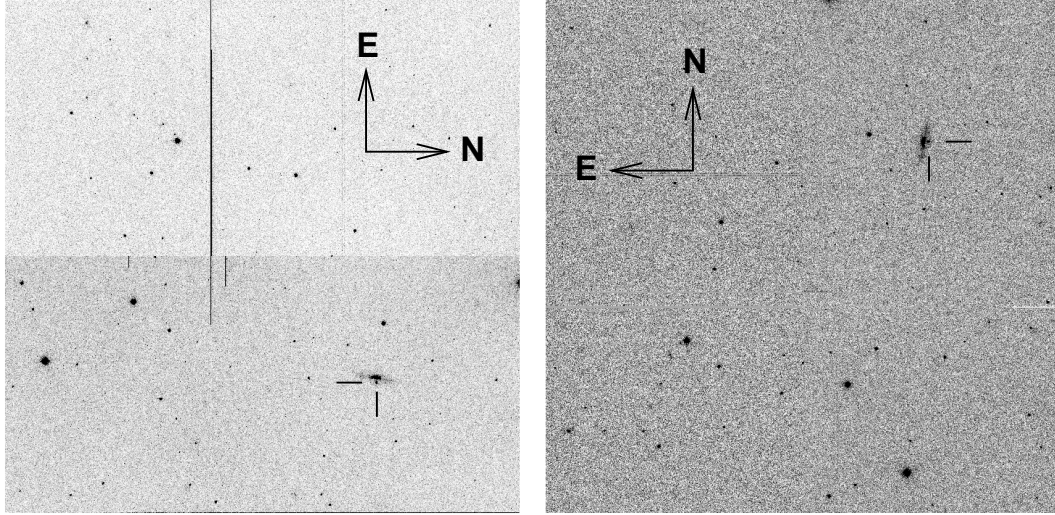
Figure 2.6 — P60 on-sky images. *Left*: Raw P60 image of SN 2006be. The object, located just West of its host galaxy IC 4582, is indicated with the two black tick marks. The row of bad columns is clearly visible on the top amplifier. Because of these cosmetic defects and the higher read noise of the top amplifier, we recommend a small coordinate offset (3′ north, 3′ west) for non-extended sources, as has been applied for this object. *Right*: Processed P60 image of SN 2006be. Here we display the output of the real-time data reduction pipeline, as described in Section 2.3.4. The image has been rotated to the standard orientation of north up and east to the left.

however, by using the region-of-interest mode (Section 2.3.1.1). For instance, a $6′ \times 6′$ field (1/4 of the chip) requires only 10 s to read out.

We have found amplifier 1 (the "bottom" amplifier) has a significantly lower read noise than amplifier 2 (the "top" amplifier; 5.3 vs. 7.8 e^-). The top region of the CCD is also cosmetically less pleasing than the bottom region, as several adjacent bright columns run through the center portion of the CCD (see Figure 2.6). We therefore recommend applying a small offset from the central location ($+3′$ R.A., $-3′$ decl.) for non-extended sources. We have added an optional offset parameter to our target specification protocol to make this change easier for users.

The pointing accuracy of the system is more than sufficient for our needs, with typical rms values of $15″$. However, we have found, somewhat deviant behavior (up to $45″$ offsets) for targets observed at large airmass (> 3). We believe this is caused by different pointing behavior with the eyepiece mounted (used for rapid manual calculation of the pointing model) than with the CCD camera mounted (nightly

observations). We are currently investigating this issue in more depth. However, we note that given our large field of view, even pointing errors as large as $1'$ are unlikely to cause significant problems.

Our typical filter wheel configuration consists of a set of standard broadband filters: Johnson UBV (Bessell, 1990, and references therein), Kron RI (functionally similar to Cousins $R_{\rm C}I_{\rm C}$; Bessell, 1990), Sloan $i'\,z'$ (Fukugita et al., 1996), and Gunn g (Thuan & Gunn, 1976); two variations on Sloan z': $z_{\rm short}$ and $z_{\rm long}$; and two narrow-band Hα filters ($\lambda_c/\Delta\lambda = 6564/100$, and $6584.65/17.5$). We have found significant deviations from the canonical transmission curves for some of our broadband filters. We therefore measured the transmission curves of all of our broadband filters, and the results are shown in Figure 2.7. These measurements are also available in tabular form online[6].

2.4.2 Observatory Conditions

Observing conditions at Palomar are highly seasonally dependent. In the summer months, it is rare to lose an entire night due to weather. The average seeing at the P60 in the summer is $\sim 1\rlap{.}''1$ in R-band. The winter months, however, are much worse. As an extreme example, the P60 was closed for 15 full nights in 2005 January. Average seeing degrades to $\sim 1\rlap{.}''6$, and can at times be significantly worse. The seeing we experience at the P60 is often times slightly worse (by $\sim 0\rlap{.}''2$) than the values reported at the Hale 200 inch telescope. We attribute this primarily to the difficultly we have encountered determining and maintaining an accurate focus value (Section 2.4.3).

Sky background levels are generally good at Palomar, although they have increased somewhat over the last decade as the area has become more populated. In recent images at P60 with the new CCD we have found sky background levels of 19.9, 19.0, 18.8, and 17.7 mag per PSF (here approximated as a circular aperture of $1.5''$ diameter) in B, V, R, and I respectively. The $3\,\sigma$ limiting magnitudes of our current system

---

[6]See http://www.astro.caltech.edu/~ams/P60/filters.html.
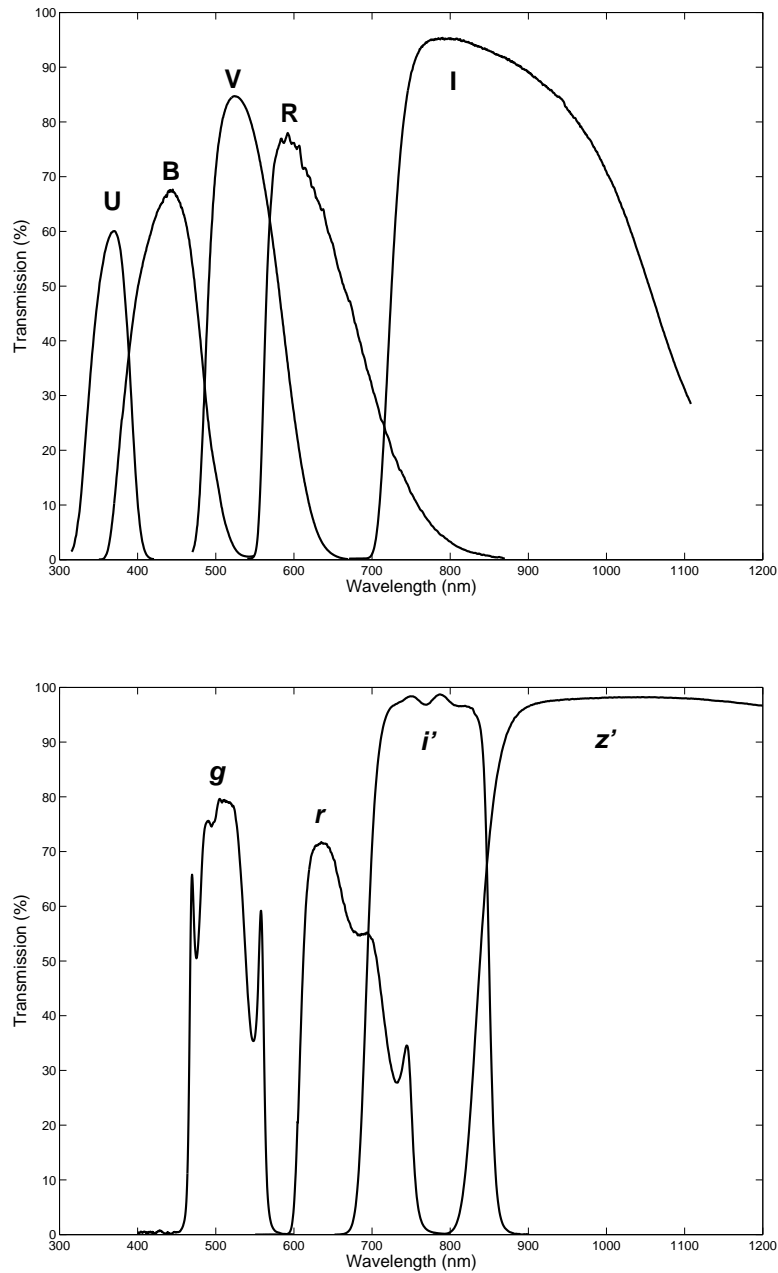
Figure 2.7 — P60 broadband filter transmission curves. The top plot shows the Johnson UBV and Kron RI, while the bottom plot shows Gunn gr and Sloan $i'z'$. These results can be found in tabular form online at http://www.astro.caltech.edu/~ams/P60/filters.html.

Table 2.3.   P60 On-Sky Performance

	B	V	R	I
Sky Brightness	$\cdots$	$\cdots$	$\cdots$	$\cdots$
(mag per arcsec^2)	20.8	19.9	19.6	18.6
(mag per arcmin^2)	11.9	11.0	10.8	9.8
(mag per PSF)[a]	20.1	19.2	19.0	18.0
Limiting Magnitude[b]	20.5	20.5	20.5	19.8

[a]We approximate our PSF here as a circular aperture of diameter $1\rlap{.}''5$.

[b]$3\,\sigma$ limiting magnitude for an isolated point source in a 60 s exposure.

are 20.5 mag in B, V, and R, and 19.8 mag in I-band for an isolated point source in a 1 minute exposure. These results are summarized in Table 2.3.

The shortest recommended exposure time is set by the shutter mechanism. For exposures shorter than 2 s, the shutter speed becomes important, and the true opening time (measured from a flat-field linearity curve) is not strictly repeatable. The longest recommend exposure is limited by the fact that we are not using a guider to assist in telescope tracking. This value is therefore dependent upon external conditions. In standard seeing of $1\rlap{.}''5$, exposure lengths longer than 180 s begin to show image degradation. Under good seeing conditions of $1\rlap{.}''0$, we have noticed degradation in images longer than 90 s. Users requiring deep images of a field will need to split up their observations into exposures of this length and thereby sacrifice readout overhead.

2.4.3   Observatory Efficiency

The P60 currently devotes on average $\approx 50\%$ of the time the dome is open for observations to science exposures. This value is quite variable, however, depending primarily on the number of different fields observed each night. An overview of the typical nightly efficiency is presented in Table 2.4. Please note the values presented are given in terms of the total time the dome is open, not the total available dark time. Additional factors such as weather can affect the overall efficiency significantly.

Table 2.4.   P60 Nightly Efficiency

Property	Time Spent
Science Exposures	53%
Focusing	12%
Readout Time	8%
Photometric Standards	4%
Scheduler Calculations	< 1%
Other[a]	23%
Total	100%

[a]"Other" includes all additional system components, such as telescope motion, changing filters, adjusting focus, and gathering status information. Because most of these operations are done in parallel, it is impossible to disentangle each individual contribution.

Besides required operations such as telescope slews, the primary constraint on our system efficiency comes from focusing. We have found the secondary mirror on the telescope to be unstable, particularly at higher elevations. Large telescope slews unpredictably alter the secondary mirror position, thereby taking the telescope out of focus. While engineering work to reinforce the structural support of the secondary mirror in the Spring of 2006 has improved stability, we still conduct a focus loop every time we slew to a new target to maintain focus (this loop is disabled for rapid-response observations). As each individual focus loop takes ≈ 3 minutes, visiting a large number of fields each night can have a significant impact on our system efficiency.

Additionally, our relative efficiency is lowered by $\lesssim 5\%$ because the P60 is not equipped with a guider. As mentioned in Section 2.4.2, this puts an upper limit on suggested exposure times. In many cases we must use shorter exposures than would otherwise be optimal to minimize the fraction of time spent in CCD readout. We note, however, that real-time scheduling has no noticeable impact on efficiency, as the OSS spends less than 1% of the available time each night calculating which target to observe next.

2.5 Science Highlights and Future Directions

In this chapter, we have presented our efforts to automate and roboticize the Palomar 60 inch telescope. As of 2004 September, all components of the system operate in a fully automated fashion, making P60 one of the few robotic, medium-aperture facilities in the world. The P60 has been routinely responding to *Swift* GRB alerts over the last three years, and will continue to do so over the lifetime of the *Swift* mission.

To give a flavor of some of the science achieved with P60, we briefly summarize a handful of science highlights from the last four years of automated operation.

- **GRB 050904: A Cosmic Explosion from the Epoch of Re-ionization** — Early P60 R- and i'-band limits, coupled with the simultaneous detection of a bright NIR J-band afterglow the 4 m SOAR telescope, immediately suggested a high-redshift ($z \approx 6$) origin for GRB 050904. Subsequent P60 optical limits, together with broadband NIR afterglow photometry, allowed us to measure a photometric redshift of $z = 6.39 \pm 0.12$ (Figure 2.8; Haislip et al., 2006). Shortly thereafter, GRB 050904 was spectroscopically confirmed to lie at $z = 6.295$ (Kawai et al., 2006), still the most distant cosmic explosion detected to date.

- **GRB 070610: A Curious Galactic Transient** — The P60 light curve of GRB 070610 (Figure 2.9) exhibited dramatic flares on extremely short time scales ($\Delta i' \approx 3 \, \mathrm{mag}$ in less than 60 s) as late as days after the burst trigger. The low Galactic latitude ($b = -1.0°$), coupled with the dramatic optical and X-ray variability, suggest GRB 070610 is in fact a new class of black hole binary, the fast X-ray novae, which may in fact more frequent than cosmological (i.e., massive star core-collapse) long-duration GRBs (Kasliwal et al., 2008).

- **Luminous Red Novae: A New Class of Optical Transients** — Originally classified as a SN, our P60 monitoring of M85 OT2006-1 indicated it actually fell intermediate in absolute brightness between a nova and a supernova. In addition, the plateau phase, lasting about 50 days, was too short to be considered
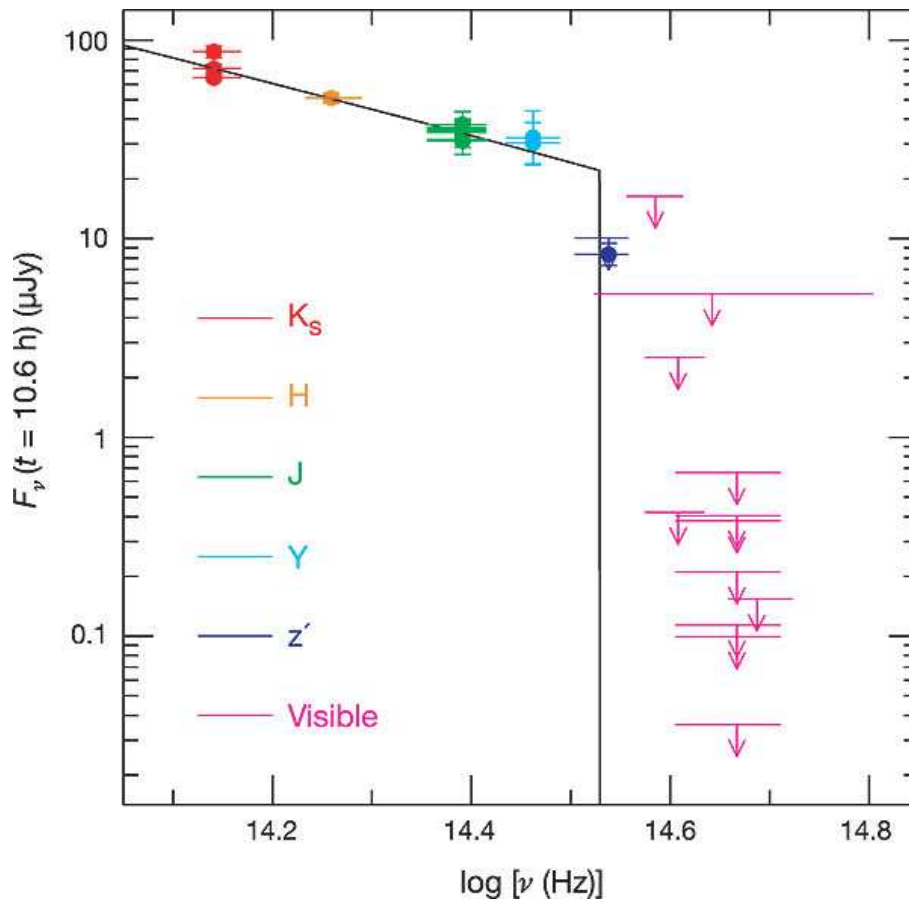
Figure 2.8 — Optical/NIR SED of the $z = 6.3$ GRB 050904. The steep cutoff at $\nu \approx 10^{14.5}$ Hz is due to Ly-α absorption in the IGM. The location of this cutoff frequency allows for a photometric estimate of the GRB redshift: in this case $z \approx 6.3$. From Haislip et al. (2006).

a Luminous Blue Variable outburst (e.g., η Carina). While the origin is still uncertain, eruptive mechanisms such as a binary stellar merger or a planetary capture are plausible candidates to explain this unique event (Kulkarni et al., 2007).

- **SN 2006gy: An Extremely Bright Supernova** — With an extinction-corrected V-band peak absolute magnitude of ≈ -22, SN 2006gy is probably the brightest SN ever observed (Ofek et al., 2007a; Smith et al., 2007). The P60 light curve indicates SN 2006gy emitted more than 10^{51} erg solely in optical radiation. The nature of the progenitor of SN 2006gy, however, is still a mystery. One of the most intriguing possibilities is that SN 2006gy is the first example
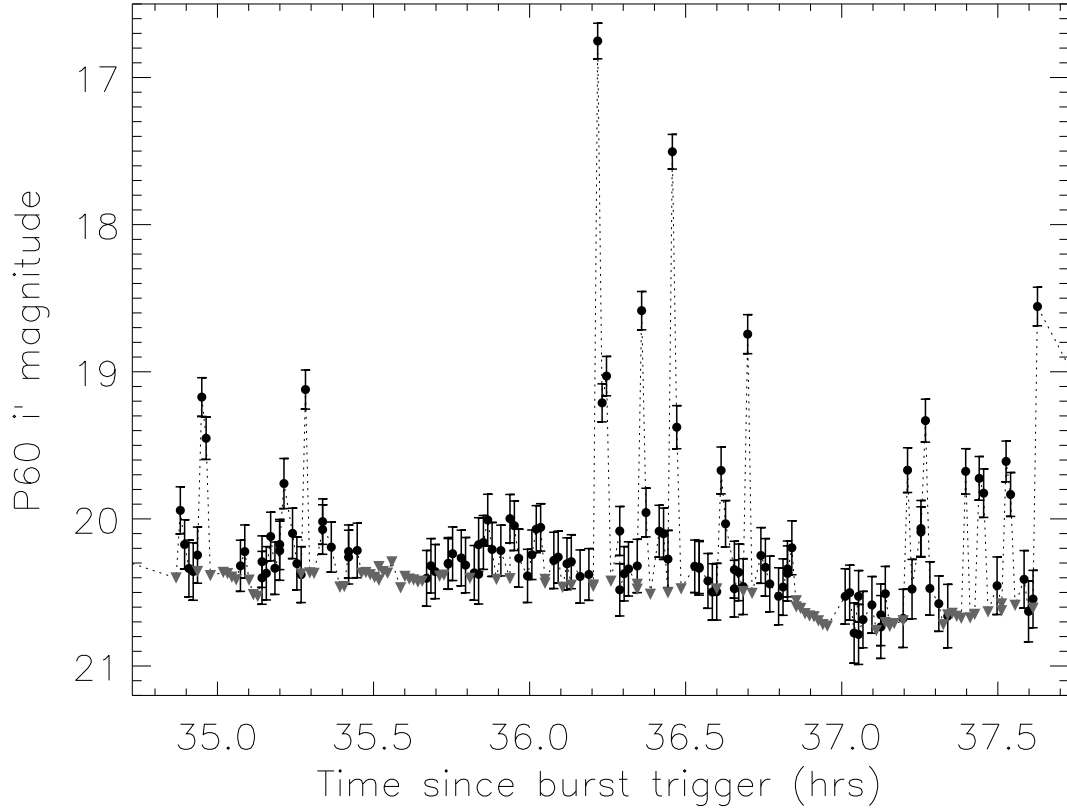
Figure 2.9 — P60 i' light curve of GRB 070610. The dramatic short-time scale variability is unlike any previously observed GRB afterglow. Most likely the progenitor system is a black hole binary in our Galaxy. From Kasliwal et al. (2008).

of a pair-instability supernova from a super-massive star (Ober et al., 1983).

Besides continued follow-up of GRBs, P60 soon will provide multi-color follow-up observations for the Palomar Transient Factory (PTF). PTF is a wide-field (7.8 square degrees, many times the size of the full Moon), high cadence (time scales of hours to days) survey of the optical sky with the Palomar 48 inch (1.2 m) Oschin-Schmidt telescope, optimized to identify variable and/or transient sources. Over the course of its lifetime, PTF should detect thousands of new SNe, hundreds of novae, and identify new types of optical transients in the relatively unexplored phase space between novae and SNe (e.g., luminous red novae).

P60 is currently undergoing upgrades to become fully compliant with the Virtual

Observatory Event Network (VOEventNet[7]) protocol, and, once complete, will be capable of two-way communication with all other VOEvent facilities. P60 will therefore be capable of intelligent (i.e., filter and cadence selection) real-time follow-up of PTF-discovered transients without any human intervention. To complete the loop, P60 will provide feedback so that future transients are classified in a more reliable manner. The facility will therefore continue to contribute to transient astronomy well into the LSST era and beyond.

---

[7]See http://voevent.net.

Part II

γ-Ray Burst Energetics in the *Swift* Era

Preamble

Accurate calorimetry is fundamental to understanding astrophysical phenomena. In the case of long-duration γ-ray bursts (GRBs), the initial report in 2001 of a nearly universal prompt energy release of $\sim 10^{51}$ erg helped to establish the connection between GRBs and massive stars, since core-collapse supernovae (SNe) emit a comparable amount of energy via electromagnetic radiation. This result led to efforts to utilize GRBs as standardizable candles to constrain the cosmology of our universe, much has been done for Type Ia supernovae.

By detailed modeling of some of the best-sampled events in the *Swift* era, I demonstrate in the following two chapters that the true energy distribution of GRBs is actually much broader than previously believed. While the existence of sub-luminous events has been known for many years, I have found for the first time a sub-population of events that are over-luminous by over an order of magnitude. The existence of these events poses a challenge to GRB progenitor models and significantly diminishes the prospects of using GRBs as cosmological probes.

Chapter 3, my multi-wavelength study of GRB 050820A, is taken from an article published in *The Astrophysical Journal* (Cenko et al., 2006b). My study of GRB 050525A and GRB 060418 in Chapter 4 is currently being prepared for submission.

Chapter 3

Multi-Wavelength Observations of GRB 050820A: An Exceptionally Energetic Event Followed from Start to Finish

S. B. Cenko[a], M. M. Kasliwal[b], F. A. Harrison[a], V. Pal'shin[c],

D. A. Frail[d], P. B. Cameron[b], E. Berger[e,f], D. B. Fox[g], A. Gal-Yam[b],

S. R. Kulkarni[b], D.-S. Moon[a], E. Nakar[h], E. O. Ofek[b], B. E. Penprase[i],

P. A. Price[j], R. Sari[h], B. P. Schmidt[k], A. M. Soderberg[b], R. Aptekar[c],

D. Frederiks[c], S. Golenetskii[c], D. N. Burrows[g], R. A. Chevalier[l],

N. Gehrels[m], P. J. McCarthy[e], AND T. Piran[n]

[a]Space Radiation Laboratory, MS 220-47, California Institute of Technology, Pasadena, CA 91125

[b]Department of Astronomy, Mail Stop 105-24, California Institute of Technology, Pasadena, CA 91125

[c]Ioffe Physico-Technical Institute, 26 Polytekhnicheskaya, St. Petersburg 194021, Russia

[d]National Radio Astronomy Observatory, P.O. Box 0, 1003 Lopezville Road, Socorro, NM 87801

[e]Observatories of the Carnegie Institute of Washington, 813 Santa Barbara Street, Pasadena, CA 91101

[f]Princeton University Observatory, Peyton Hall, Ivy Lane, Princeton, NJ 08544

[g]Department of Astronomy & Astrophysics, 525 Davey Laboratory, Pennsylvania State University, University Park, PA 16802

[h]Theoretical Astrophysics, California Institute of Technology, MS 130-33, Pasadena, CA 91125

[i]Department of Physics and Astronomy, Pomona College, 610 North College Avenue, Claremont, CA 91711

[j]Institute for Astronomy, University of Hawai'i, 2680 Woodlawn Drive, Honolulu, HI 96822

[k]Research School of Astronomy and Astrophysics, Australian National University, Mont Stromlo Observatory, Cotter Road, Weston Creek, Canberra ACT 2611, Australia

[l]Deparment of Astronomy, University of Virginia, P.O. Bos 3818, Charlottesville, VA 22903

[m]NASA Goddard Space Flight Center, Greenbelt, MD 20771

[n]Racah Institute of Physics, Hebrew University, Jerusalem 91904, Israel

Abstract

We present observations of the unusually bright and long γ-ray burst GRB 050820A, one of the best-sampled broadband data sets in the *Swift* era. The γ-ray light curve is marked by a soft precursor pulse some 200 s before the main event; the lack of any intervening emission suggests that it is due to a physical mechanism distinct from the GRB itself. The large time lag between the precursor and the main emission enabled simultaneous observations in the γ-ray, X-ray, and optical bandpasses, something only achieved for a handful of events to date. While the contemporaneous X-rays are the low-energy tail of the prompt emission, the optical does not directly track the γ-ray flux. Instead, the early-time optical data appear consistent with the forward shock synchrotron peak frequency passing through the optical, and are therefore likely the beginning of the afterglow. On hour time scales after the burst, the X-ray and optical light curves are inconsistent with an adiabatic expansion of the shock into

the surrounding region, but rather indicate that there is a period of energy injection. Observations at late times allow us to constrain the collimation angle of the relativistic outflow to $6.8° \lesssim \theta \lesssim 9.3°$. Our estimates of both the kinetic energy of the afterglow ($E_{\mathrm{KE}} = 5.2^{+7.9}_{-4.1} \times 10^{51}$ erg) and the prompt γ-ray energy release ($E_\gamma = 7.5^{+6.7}_{-2.4} \times 10^{51}$ erg) make GRB 050820A one of the most energetic events for which such values could be determined.

3.1 Introduction

With the discovery of the cosmological nature of γ-ray bursts (GRBs) in 1997 (Metzger et al., 1997), astronomers were suddenly forced to explain the enormous isotropic energy release of these distant explosions. Some of the most energetic events, such as GRB 990123, seemingly released enough energy in the prompt γ-rays ($E_{\gamma,\mathrm{iso}} = 1.2 \times 10^{54}$ erg; Briggs et al., 1999) to rival the rest mass of a neutron star. Furthermore, broadband modeling of the best-sampled events has shown that a comparable amount of energy remains in the shock, powering the long-lived X-ray, optical, and radio afterglow (e.g., Panaitescu & Kumar, 2001; Yost et al., 2003).

The hypothesis that GRBs are aspherical explosions (Rhoads, 1999), supported by the appearance of achromatic "jet breaks" in a large number of afterglow light curves (Sari et al., 1999), proved to be a turning point. With typical opening angles of a few degrees, the true energy release from most GRBs is $\sim 10^{51}$ erg, on par with that of a supernova (SN). This realization enabled the discovery of a standard energy reservoir for the collimation-corrected prompt energy (Frail et al., 2001) and kinetic energy of the afterglow (Berger et al., 2003a). GRBs are now considered promising standard candle candidates, with the hope of Hubble diagrams out to $z \approx 6$ offering complementary constraints to Type Ia SNe on the cosmology of our universe (Firmani et al., 2006; Dai et al., 2004; c.f. Friedman & Bloom, 2005).

Launched in 2004 November, the *Swift* γ-Ray Burst Explorer (Gehrels et al., 2004) was designed to position GRBs, disseminate accurate coordinates to ground-based observatories in real time, and follow the UV and X-ray afterglows from minutes to

days after the event. In its first year of full operation, *Swift* brought about a number of fundamental advances in the GRB field, including the discovery of the first X-ray (GRB 050509b; Gehrels et al., 2005) and near-infrared (GRB 050724; Berger et al., 2005b) afterglows of a short-hard burst, the detection of the high-redshift ($z = 6.3$) GRB 050904 (Haislip et al., 2006; Cusumano et al., 2006), and the ability to measure broadband light curves starting shortly after, and in a few cases, even during the γ-ray event itself.

Despite these advances, measuring the bolometric fluences of *Swift* events has proved challenging, for a number of reasons. First, the limited energy range (15–150 keV) of the *Swift* Burst Alert Telescope (BAT; Barthelmy et al., 2005a) means that *Swift* can accurately characterize only the softest GRB spectra. Second, few *Swift* events have shown conclusive signs of a jet break, leaving geometric corrections highly uncertain. Finally, the X-ray light curves of *Swift* afterglows have shown both bright flares (Burrows et al., 2005b) and slow decays (Nousek et al., 2006). Both behaviors have been attributed to late-time ($t \gg t_{\mathrm{GRB}}$) energy injection, and at times have rivaled the energy release of the prompt γ-ray emission (e.g., Falcone et al., 2006b).

On 2005 August 20 UT, the BAT detected and localized the unusually bright and long GRB 050820A, a truly rare burst in the *Swift* sample. The γ-ray light curve is marked by a soft pulse of emission preceding the main event by over 200 s. The main emission was bright enough to be detected by the Konus-*Wind* instrument, providing a γ-ray spectrum extending beyond 1 MeV, as well as continuous coverage over the entire ~ 600 s burst duration.

Since *Swift* triggered on the precursor, both space- and ground-based facilities were able to image the transient during the bulk of the prompt emission. Such contemporaneous multi-wavelength observations have only been achieved for a handful of bursts to date. The bright X-ray ($F_\nu \sim 0.7$ mJy) and optical ($R \sim 14.5$ mag) afterglows made it possible to study the evolution of the afterglow for weeks after the burst, providing one of the most detailed broadband light curves in the *Swift* era. Finally, late-time *Hubble Space Telescope* (*HST*) observations allowed us to constrain

the jet break time, and hence the geometry of the outflow. Even after applying the collimation correction, we find GRB 050820A is an exceptionally energetic event.

Our work proceeds as follows: in Section 3.2, we outline our broadband observations of GRB 050820A, beginning with the high-energy prompt emission and followed by the X-ray, optical, and radio afterglow. We find that the afterglow data are incompatible with the standard model of synchrotron radiation from a single, highly-relativistic shock expanding adiabatically into the surrounding medium (Sari et al., 1998). Instead, in Section 3.3 we use power-law fits ($F_\nu \propto t^{-\alpha}\nu^{-\beta}$) to model the afterglow, dividing the burst into segments based on noticeable temporal breaks in the X-ray and optical light curves. This analysis allows us to investigate the early broadband light curve (Sections 3.4.1 and 3.4.2), late-time ($t \gg t_{GRB}$) energy injection in the forward shock (Section 3.4.3), the structure of the circumburst medium (Section 3.4.4), and the geometry and energetics of the event (Section 3.4.5).

Throughout this work we adopt a standard ΛCDM cosmology with $H_0 = 71$ km s^{-1} Mpc^{-1}, $\Omega_M = 0.73$, and $\Omega_\Lambda = 0.27$. We also make use of the notation $Q_X \equiv 10^X \times Q$. Unless otherwise noted, all errors quoted are 90% confidence limits.

3.2   Observations and Data Reduction

In this section, we present our broadband observations of GRB 050820A, which span the spectral range from γ-rays to radio frequencies and extend in time out to 61 days after the burst. We include an independent analysis of the *Swift* BAT data set, as well as the complete light curve and spectrum from the Konus-*Wind* instrument (Aptekar et al., 1995), which, unlike the BAT, was able to observe GRB 050820A over its entire duration (Section 3.2.1). In Section 3.2.2 we provide an analysis of the *Swift* X-Ray Telescope (XRT; Burrows et al., 2005a) data, with afterglow detections out to two weeks after the event. We present contemporaneous optical data from the automated Palomar 60 inch (1.5 m) telescope (P60; Cenko et al., 2006a) and the *Swift* Ultra-Violet Optical Telescope (UVOT; Roming et al., 2005), supplemented by late-time images taken with the 9.2 m Hobby-Eberly Telescope (HET) and *HST*

(Section 3.2.3). Finally, we monitored GRB 050820A in the radio with the Very Large Array[1] beginning only hours after the burst and continuing for approximately two months (Section 3.2.4).

3.2.1 γ-Ray Observations

3.2.1.1 *Swift* Burst Alert Telescope

At 06:34:53 on 2005 August 20 UT[2], the BAT triggered and located GRB 050820A (*Swift* trigger 151207; Page et al., 2005b). The initial location calculated on-board was a $4'$ error circle centered at $\alpha = 22^{\mathrm{h}}29^{\mathrm{m}}35\overset{s}{.}9$, $\delta = +19°11'14\overset{''}{.}2$ (J2000.0). Cummings et al. (2005a) describe a multi-peaked light curve ($t_{90} = 26 \pm 2$ s) with clear spectral evolution (hard to soft) within each peak.

Following the report of additional high-energy emission from the Konus-*Wind* instrument (Pal'shin & Frederiks, 2005; Section 3.2.1.2), the BAT team re-analyzed their full light curve and found evidence of a much stronger, harder episode of emission from GRB 050820A (Cummings et al., 2005b). Unfortunately, the satellite entered the South Atlantic Anomaly (SAA) approximately 240 seconds after the burst trigger; estimates of the properties of this second phase are therefore highly uncertain.

Here we have independently analyzed the BAT data from GRB 050820A. We have extracted the 15–350 keV light curve in 1 s timing bins using software tools from the *Swift* data analysis package[3]. The result is shown in Figure 3.1*a*. In addition, we have extracted spectra for the two periods of high energy emission covered by the BAT data (peaks A and B; Section 3.2.1.2). We then fitted these spectra to a power-law distribution of energies ($\mathrm{d}N/\mathrm{d}E \propto E^{-\Gamma}$). We find evidence for strong spectral evolution between these two intervals, as the second peak is significantly harder than

---

[1] The National Radio Astronomy Observatory is a facility of the National Science Foundation operated under cooperative agreement by Associated Universities, Inc.

[2] It is customary to refer to the burst trigger time as T_0, for it is assumed to coincide with the beginning of the prompt emission. Given the unique nature of the high-energy emission from GRB 050820A, we undertake a more detailed study to determine exactly when the prompt emission began (i.e., T_0) in Section 3.4.1. Times measured with reference to the *Swift* trigger time will be referred to as t_{BAT} throughout the remainder of this work.

[3] Part of NASA's High Energy Astrophysics Software package, see http://heasarc.gsfc.nasa.gov/docs/software/lheasoft.
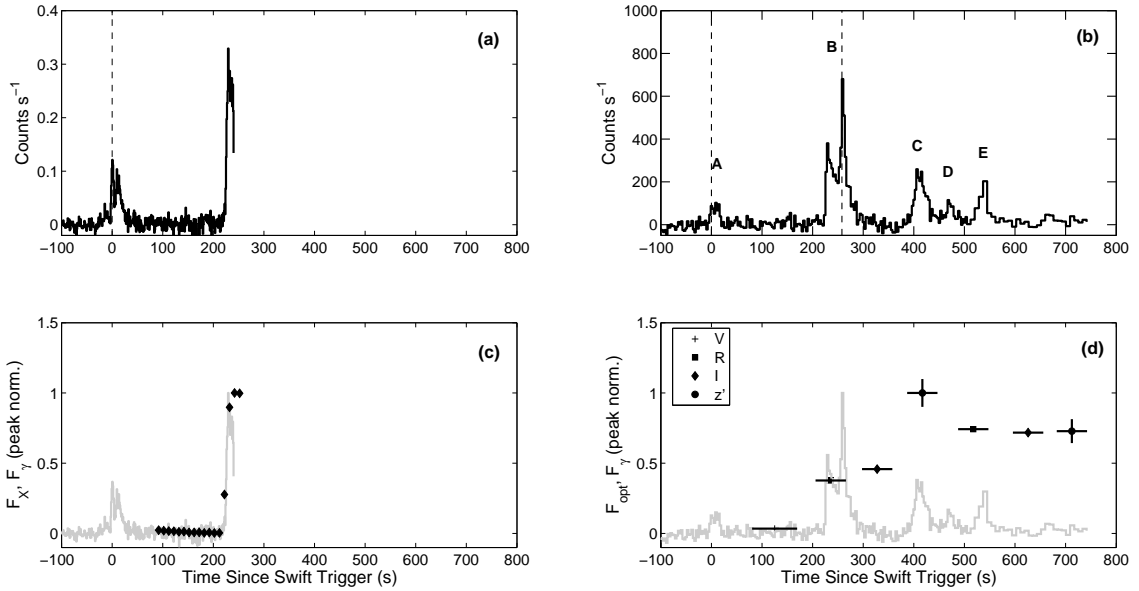
Figure 3.1 — Early broadband emission from GRB 050820A. *(a) Swift* BAT light curve extracted from 15 to 350 keV in 1 s bins. The dashed vertical line is the time of *Swift* trigger, 06:34:53 on 2005 August 20 UT (T_{BAT}). While the second, brighter period of emission is clearly visible, *Swift* entered the SAA approximately 240 s after T_{BAT}, effectively terminating the observations. *(b)* Konus-*Wind* light curve extracted from 18 to 1150 keV. The 5 peaks visible in the Konus-*Wind* light curve are labeled A–E, and defined in Table 3.2. The left dashed vertical line shows the *Swift* trigger time, while the right dashed line shows the Konus-*Wind* trigger time, T_{KW}, 258 s later. The portion of the light curve covered by the BAT comprises only a small fraction of the total γ-ray emission. *(c)* Contemporaneous *Swift* XRT observations (*filled black diamonds*) overlaid on the BAT light curve. The X-ray data nicely track the γ-ray emission. *(d)* Contemporaneous UVOT and P60 optical data overlaid on the Konus-*Wind* light curve. Unlike the X-ray, the optical is not a good trace of γ-ray emission.

Table 3.1.   Spectral Properties of BAT γ-Ray Emission

Time Interval (t_{BAT}, s)	Γ	χ_{r}^2 / d.o.f.
$-17 - 22$	1.74 ± 0.08	1.07 / 75
$217 - 241$	1.07 ± 0.06	0.95 / 76

Note: Spectra were fitted to a power-law model of the form $\mathrm{d}N/\mathrm{d}E \propto E^{-\Gamma}$.

the first. The results of this analysis are shown in Table 3.1.

3.2.1.2   Konus-*Wind*

The main part of GRB 050820A triggered Konus-*Wind* at $T_{\mathrm{KW}} = 06{:}39{:}14.512$ UT, $257.948\,\mathrm{s}$ after the BAT trigger (taking into account the $3.564\,\mathrm{s}$ propagation delay from *Swift* to *Wind*). It was detected by the S2 detector, which observes the north ecliptic hemisphere; the incident angle was $63.2°$. Count rates are continuously recorded by Konus-*Wind* in three energy bands: G1 (18–70 keV), G2 (70–300 keV), and G3 (300–1150 keV). Data collected in this "waiting mode" are acquired in $2.944\,\mathrm{s}$ timing bins. The time history recorded in the three energy ranges can be considered a continuous three-channel spectrum.

Immediately following the Konus-*Wind* trigger, the instrument began simultaneously collecting data in "trigger" mode, as well. From T_{KW} to $T_{\mathrm{KW}} + 491.776\,\mathrm{s}$, 64 spectra were accumulated, each composed of 101 energy channels ranging from 18 keV to 14 MeV. The time resolution of these "trigger mode" spectra varies from 64 ms to $8.192\,\mathrm{s}$ and is determined by an automated on-board algorithm based on count rate. Data were then processed using standard Konus-*Wind* analysis tools and spectra were fit with XSPEC.

At least five pulses are evident in the Konus-*Wind* light curve (labeled A–E; Figure 3.1*b* and Table 3.2). Peak A, which generated the BAT trigger, appears to be a weak precursor. Figure 3.2 shows the three-channel light curve of GRB 050820A,

as well as the hardness ratios. With the exception of the precursor (peak A), the burst shows an overall hard-to-soft evolution over the entire burst duration, as well as within some of the individual peaks (B and C).

The spectra of individual pulses are well fitted by a cutoff power-law model: $dN/dE \propto E^{-\alpha} \exp[-(2-\alpha)E/E_\mathrm{p}]$; here α is the photon index and E_p is the peak energy of the νF_ν spectrum. Fitting the overall Konus-*Wind* "trigger" mode spectrum, accumulated from $0 < t_\mathrm{KW} < 295$ $(258 < t_\mathrm{BAT} < 553)$[4] in the 18–2000 keV range yields $\alpha = 1.41^{+0.25}_{-0.31}$, and a peak energy $E_\mathrm{p} = 271^{+359}_{-91}$ keV ($\chi^2_\mathrm{r} = 0.74$ for 62 d.o.f.).

However, in examining the full Konus-*Wind* light curve (Figure 3.1*b*), it is clear the above time interval does not include a sizable fraction of the γ-ray emission. To derive the spectral parameters of the time-integrated spectrum over the main part of the GRB (peaks B–E), we simultaneously fit the three-channel Konus-*Wind* spectrum accumulated from $-33 < t_\mathrm{KW} < 0$ and the overall multichannel spectrum. We find $\alpha = 1.12^{+0.13}_{-0.15}$ and a peak energy $E_\mathrm{p} = 367^{+95}_{-62}$ keV ($\chi^2_\mathrm{r} = 0.99$ for 64 d.o.f.). Not surprisingly, the peak energy increased significantly, as the beginning of Peak B was the hardest portion of the entire burst. We consider this fit the most accurate estimate of the high-energy spectral properties of GRB 050820A.

The fluence and peak flux for each individual episode are shown in Table 3.2. The total fluence received from GRB 050820A from 20 to 1000 keV (observer frame) was $5.27^{+1.58}_{-0.69} \times 10^{-5}$ erg cm^{-2}.

3.2.2 X-Ray Observations

The *Swift* XRT began observations of GRB 050820A 88 s after the burst trigger. A bright, fading X-ray source was detected by the automated on-board processing routine at $\alpha = 22^\mathrm{h}29^\mathrm{m}37\overset{s}{.}8$, $\delta = +19°33'32\overset{''}{.}7$ (7″ error radius) and reported in real-time (Page et al., 2005b). Data was taken in window timing mode until ~ 1.29 hr after the burst, when, due to the decreased count rate, photon counting mode was automatically initiated.

---

[4]After this time only a weak tail is seen in the G1 band up to $t_\mathrm{BAT} \approx 730$ s; this tail contains less than 5% of the total burst fluence.
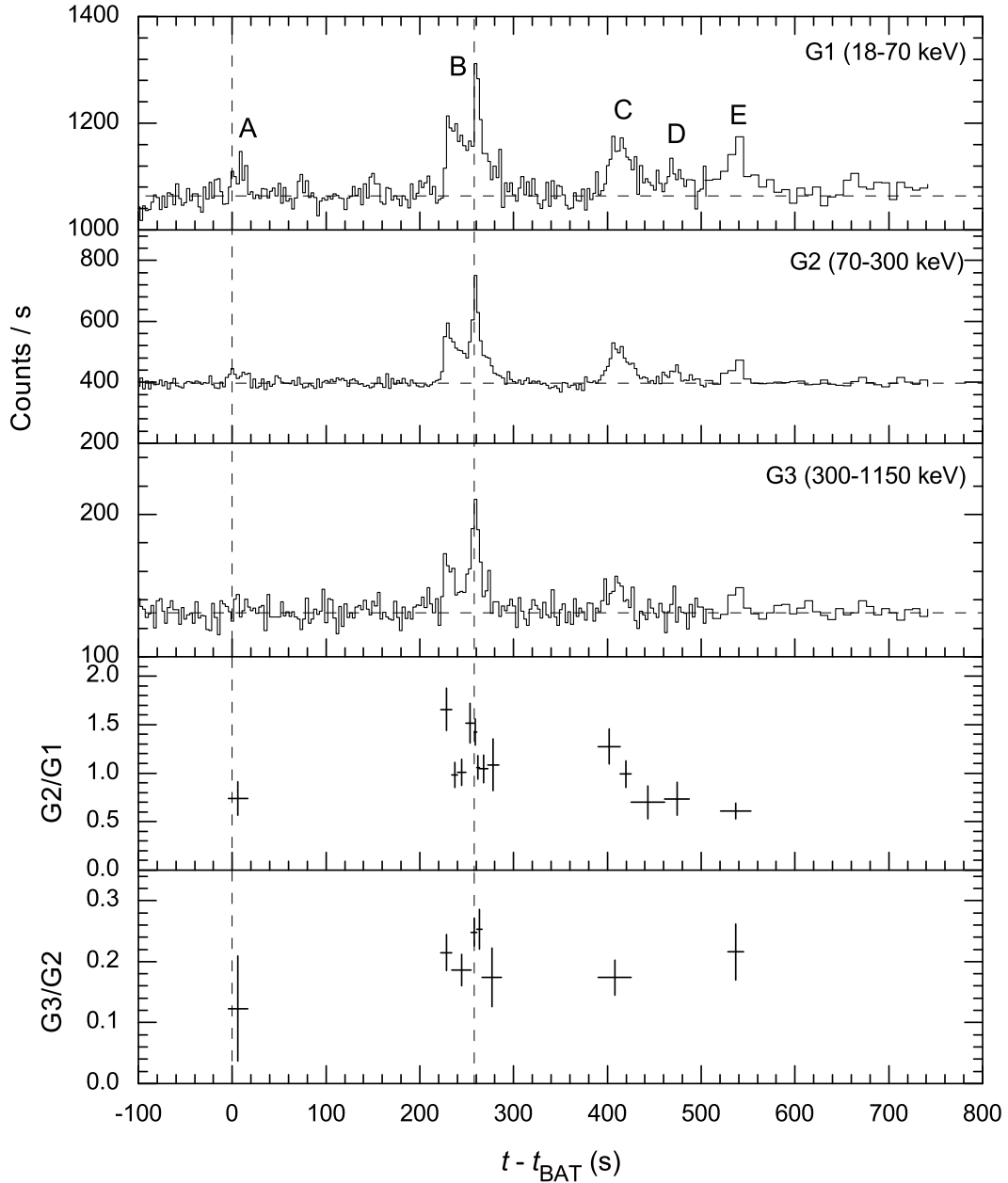
Figure 3.2 — Spectral evolution of GRB 050820A. The top three panels show the Konus-*Wind* light curve divided into three energy bands: G1 $\equiv$ 18 − 70 keV, G2 $\equiv$ 70 − 300 keV, and G3 $\equiv$ 300 − 1150 keV. The bottom two panels show the resulting hardness ratios: G2/G1 and G3/G2. Background levels are indicated with horizontal dashed lines. The vertical dashed lines denote the BAT (T_{BAT}) and Konus-*Wind* (T_{KW}) trigger times. With the notable exception of the precursor, the burst shows an overall hard-to-soft evolution, both over the entire duration and within individual bright peaks (B and C).

Table 3.2. Properties of Konus-*Wind* γ-Ray Light Curve

Peak ID	Time Interval $(t_{\mathrm{BAT}}, \mathrm{s})$	Fluence[a] $(10^{-6}\ \mathrm{erg\ cm^{-2}})$	Peak Flux $(10^{-7}\ \mathrm{erg\ cm^{-2}\ s^{-1}})$
A	$-4.3 - 19.3$	2.77	1.7
B	$222.4 - 282.8$	28.7	13
C	$397.5 - 430.2$	10.2	4.3
D	$454.8 - 479.4$	3.20	1.9
E	$520.4 - 544.9$	4.93	2.6
Total	$-4.3 - 544.9$	$52.7^{+15.8}_{-6.9}$	

[a]The fluence was extracted from the 20 to 1000 keV energy range (observer frame) assuming a cutoff power-law spectrum of the form $\mathrm{d}N/\mathrm{d}E \propto E^{-\alpha} \exp^{-(2-\alpha)E/E_{\mathrm{P}}}$.

Here we have independently processed and reduced the XRT data from GRB 050820A (for a previous analysis of the early-time X-ray data, see O'Brien et al., 2006). To reduce the X-ray data, we used the software tools available from the *Swift* Data Center. We followed standard reduction steps, except for taking measures to mitigate the effects of pulse pileup in our spectral analysis. During the steep rise in the X-ray light curve at $t_{\mathrm{BAT}} \approx 220\,\mathrm{s}$, the XRT count rate exceeds the 200 counts s^{-1} at which pileup can affect the detector response (Romano et al., 2006). For this segment, we removed the central 2 pixels from the point-source image. At the beginning of photon counting mode, we removed the central 4 pixels of the photon counting mode image for our spectral analysis, again in order to mitigate the effect of pulse pileup (Vaughan et al., 2006).

We fitted the X-ray spectrum for phases 1a, 1b, and 2 separately (see Section 3.3 for a full discussion of the division of the X-ray light curve into phases). We used an absorbed power-law model, and fit both with the column fixed to the Galactic value ($n_{\mathrm{H,Gal}} = 5.0 \times 10^{20}\,\mathrm{cm^{-2}}$; Dickey & Lockman, 1990), as well as with the column floating. For phase 1a, the best fit column is consistent with $n_{\mathrm{H,Gal}}$, and there is little difference between fits with the column floating and fixed. For both phases 1b and 2 we find acceptable fits with fixed column; however, the best fit columns are $(1.5 \pm 0.23) \times 10^{21}\ \mathrm{cm^{-2}}$ and $(1.3 \pm 0.09) \times 10^{21}\ \mathrm{cm^{-2}}$, respectively. Therefore we

Table 3.3.   X-Ray Afterglow Spectral and Temporal Fits

Phase	$t_{\mathrm{BAT}}^{\mathrm{start}}$ (s)	$t_{\mathrm{BAT}}^{\mathrm{stop}}$ (s)	α	$\chi_{\mathrm{r}}^2(\alpha)$ / d.o.f.	β	$\chi_{\mathrm{r}}^2(\beta)$ / d.o.f.
1a	0	217	2.2 ± 0.3	1.18 / 11	0.90 ± 0.09	0.63 / 349
1b	217	257	. . .	. . .	-0.10 ± 0.03	1.02 / 749
2	4.8×10^3	8.7×10^4	0.93 ± 0.03	1.14 / 29	1.20 ± 0.04	1.00 / 770
3	8.7×10^4	1.7×10^6	1.25 ± 0.07	. . .	. . .	. . .

Note: We separately fitted the X-ray light curves and spectra to power-law models of the form $F_\nu \propto t^{-\alpha}$ and $F_\nu \propto \nu^{-\beta}$, respectively. The temporal decay in phases 2 and 3 were fit jointly as a broken power-law, with the break time as a free parameter. In phase 3, we could not meaningfully constrain the spectral index due to the low count rate.

find marginal evidence for absorption in excess of the Galactic value (c.f., Page et al., 2005a).

The results of our analysis of the X-ray light curve of GRB 050820A are shown in Table 3.6. For the discussion that follows, we adopt the spectral fits in Table 3.3. These were used to scale the binned count rates to fluxes and flux density at a nominal energy of 5 keV.

3.2.3   Optical Observations

3.2.3.1   Palomar 60 Inch Telescope

The automated P60 responded to GRB 050820A and began a pre-programmed sequence of observations starting 3.43 minutes after the *Swift* trigger. The system is equipped with an optical CCD with a pixel scale of $0\rlap{.}''378\,\mathrm{pixel}^{-1}$. Images were taken in the Kron R and I and Gunn g and z filters. All P60 images are processed with standard IRAF (Tody, 1986) routines by an automated reduction pipeline in real time. Manual inspection of the first images revealed a bright variable source inside the XRT error circle at $\alpha = 22^{\mathrm{h}}29^{\mathrm{m}}38\rlap{.}''11$, $\delta = +19°33'37\rlap{.}''1$ (Figure 3.3). This position was promptly reported as the afterglow of GRB 050820A (Fox & Cenko, 2005), allowing others to obtain high-resolution spectroscopy of the afterglow (Prochaska

et al., 2005). We continued to monitor the afterglow of GRB 050820A with P60 for the following 7 nights, until it was too faint for quantitative photometry.

Optical photometry of the afterglow was complicated by the presence of two nearby objects: one $R \sim 20.2$ mag star located $4.0''$ south-west of the afterglow, and a fainter $R \sim 21.3$ mag object located only $2.9''$ north-east of the afterglow (Figure 3.3, right panel). On some nights of poor seeing, the FWHM of our point-spread function (PSF) was larger than $2''.0$. We have therefore performed PSF-matched image subtraction using the common PSF method (CPM) of Gal-Yam et al. (2004) on our optical data. Errors were estimated by placing 5 artificial stars with flux equivalent to the afterglow in locations with similar background contamination. In addition, we have also used aperture photometry (DAOPHOT) to extract the afterglow flux. On the first night, the afterglow was bright enough to be well detected either in single images or short co-additions (≤ 360 s). For these images, both nearby sources were below our detection limit. Results from aperture photometry and image subtraction were therefore consistent. We quote our aperture photometry results for these data, as image defects from imperfect PSF subtraction seemed to artificially inflate these errors. However, on subsequent nights the afterglow flux was either near or below the level of these nearby objects, and we therefore report results from our image subtraction technique.

Photometric calibration was performed relative to 20 field stars provided in Henden (2005). Kron R is similar to Cousins R ($R_{\rm C}$) and was treated as identical for photometric calibration of these images. Magnitudes from the standard Johnson/Cousins system were transformed to Gunn g using the empirical relation from Kent (1985). We found, however, a better correlation between our i-band filter and the Cousins I ($I_{\rm C}$) filter than from the transformation to Gunn i provided in Thuan & Gunn (1976). We therefore use $I_{\rm C}$ in the remainder of this work. For the Gunn z filter, we used the Two Micron All Sky Survey (2MASS; Skrutskie et al., 2006) catalog and the optical photometry provided by Henden (2005) to interpolate the spectral energy distributions (SEDs) of 10 sources to the Sloan z' bandpass. Typical rms variations in the calibration sources were 0.03 mag in $R_{\rm C}$ and $I_{\rm C}$, 0.04 mag in g, and 0.15 in z'.

The results of our P60 observations are shown in Table 3.7. While the expected

Galactic extinction in this direction is small [$E(B - V) = 0.044$ mag; Schlegel et al., 1998], we have incorporated it into our results because of the large wavelength range spanned by our observations [$E(U - z') = 0.17$ mag]. Errors quoted are 1σ photometric and instrumental errors summed in quadrature. For this and all other optical data in this work, magnitudes are converted to flux densities using the zero points reported in Fukugita et al. (1995).

3.2.3.2   *Swift* Ultra-Violet Optical Telescope

The *Swift* UVOT automatically slewed to the BAT location and began observations only 80 s after the trigger. However, the UVOT also becomes inoperable in the SAA and therefore does not cover the main period of γ-ray emission.

The *Swift* team reduced the early-time UVOT data and reported detections in the V, B, U, and $UVW1$ bands (Chester et al., 2005). Here we have independently reduced the U-, B-, and V-band UVOT data following the recipe outlined in Li et al. (2006). As a check, we re-calculated the B and V zero points with respect to the field stars from Henden (2005). While our zero points are consistent with the ones quoted in Li et al. (2006), we found a much larger scatter (~ 0.10 mag vs. 0.01 mag) that could not be attributable solely to spread in the field stars. We have therefore incorporated the resulting zero point errors for these data points (as well as a similar value for U-band). The results of these observations are shown in Table 3.7.

3.2.3.3   Hobby-Eberly Telescope

We triggered target-of-opportunity observations on the 9.2 m HET beginning on the night of August 26 UT. Observations were taken in both R_C and I_C filters. A second reference epoch was taken on August 29 UT. Image subtraction was performed on the two epochs to remove contamination from nearby sources (as described in Section 3.2.3.1). Photometric calibration was performed relative to 10 reference objects from Henden (2005), and the absolute calibration was of similar quality to the P60 data set. Our results are reported in Table 3.7.
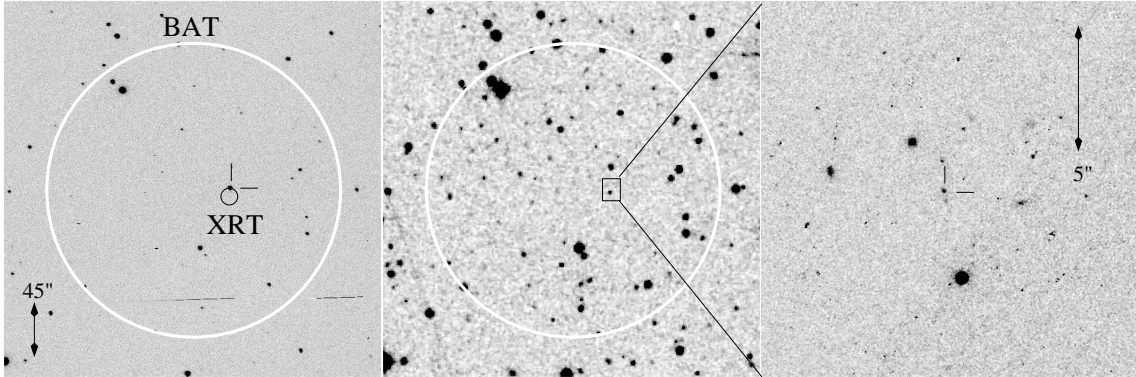
Figure 3.3 — R-band imaging of the field of GRB 050820A. *Left*: P60 $R_{\rm C}$-band discovery image of the afterglow of GRB 050820A. The BAT ($2'$ radius, *white circle*) and XRT ($7''$ radius *black circle*) error circles are labeled. The afterglow is identified with the two black tick marks. *Center*: The Second-Generation Digitized Sky Survey image of the identical field. The afterglow is not visible in this reference image. *Right*: *HST* F625W image of the afterglow (indicated again with the two black tick marks). The two nearby objects complicating the ground-based photometry are visible (see Section 3.2.3.1 for details). All images are oriented with north up and east to the left.

3.2.3.4   *Hubble Space Telescope*

To better constrain the late-time evolution of GRB 050820A, we triggered our Cycle 14 *HST* program (GO-10551; PI: Kulkarni). Using the Wide-Field Camera (WFC) channel of the Advanced Camera for Surveys (ACS), we imaged the field of GRB 050820A on 2005 September 29 UT ($t_{\rm BAT} \approx 37\,{\rm days}$) in the F625W ($r'$), F775W ($i'$), and F850LP ($z'$) filters (Figure 3.3).

The *HST* data were processed using the `multidrizzle` routine (Fruchter & Hook, 2002) in the `stsdas` IRAF package. We used `pixfrac`= 0.8 and `pixscale`= 1.0 for the drizzling procedure, resulting in a pixel scale of $0\rlap{.}''05\,{\rm pixel}^{-1}$. The astrometry on these images was then tied to a P60 co-addition of all the $R_{\rm C}$-band data taken on 2005 August 20 (which is itself tied to the USNO-B1 astrometric grid).

The afterglow is well separated from any nearby objects in the field, and so we have followed the recipe for aperture photometry from Sirianni et al. (2005). As a note of caution, however, flux from an underlying host galaxy could affect the results reported here. F625W and F775W magnitudes were converted to the $R_{\rm C}$ and $I_{\rm C}$ bandpasses using synthetic spectra from Table 22 of Sirianni et al. (2005). The results of our

Table 3.4.   Radio Observations of GRB 050820A

Observation Date (2005 UT)	t_{BAT} (days)	Frequency (GHz)	Flux Density[a] (μJy)
Aug 20.39	0.116	4.86	< 102
Aug 20.39	0.116	8.46	110 ± 40
Aug 20.39	0.116	22.5	< 186
Aug 21.20	0.93	8.46	634 ± 62
Aug 22.42	2.15	4.86	256 ± 78
Aug 22.42	2.15	8.46	419 ± 50
Aug 22.42	2.15	22.5	< 216
Aug 24.38	4.11	4.86	171 ± 47
Aug 24.38	4.11	8.46	74 ± 36
Aug 25.32	5.05	8.46	< 114
Aug 26.40	6.13	8.46	< 120
Aug 28.37	8.10	8.46	166 ± 45
Sep 1.33	12.06	8.46	89 ± 39
Sep 4.18	14.91	8.46	106 ± 33
Sep 15.20	25.93	8.46	76 ± 30
Oct 20.19	60.92	8.46	< 70

[a]Errors quoted for detections are at the 1σ level. Upper limits are reported as 2σ rms noise.

measurements are shown in Table 3.7.

3.2.4   Radio Observations

In Table 3.4 we summarize our radio observations of GRB 050820A, spanning 0.1–61 days after the explosion. All observations were conducted with the VLA in standard continuum mode with a bandwidth of $2 \times 50\,\mathrm{MHz}$ centered at 4.86, 8.46, or 22.5 GHz. The array was in the C configuration, with an angular resolution of $2\rlap{.}''3$. We used 3C48 (J0137+331) for flux calibration, while J2212+239 and J2225+213 were used to monitor phase. Data were reduced using standard packages within the Astronomical Image Processing System (AIPS).

3.3 Analysis

In this section we provide an analysis of the X-ray, optical, and radio light curves and spectra of the afterglow of GRB 050820A. We have divided the X-ray and optical light curves into segments (phases 1–4) based on noticeable temporal breaks. We then investigated each segment independently, fitting the light curve and spectra to power-law indices of the form: $F_\nu \propto t^{-\alpha} \nu^{-\beta}$. The lack of a bright afterglow makes such an analysis impossible in the radio.

The X-ray and optical light curves, with temporal divisions marked as dashed vertical lines, are shown in Figure 3.4. Phase 1 begins with the BAT trigger and ends with the resumption of X-ray observations at $t_{\mathrm{break},1} \equiv 4785\,\mathrm{s}$. The X-ray and optical data behave differently in phase 1, resulting in unique subdivisions for the two bandpasses. However, phase 1 is the only epoch to show such divergent behavior.

With the emergence of *Swift* from the SAA at $t_{\mathrm{break},1}$, both the X-ray and optical light curves exhibit a relatively shallow decline. This characterizes phase 2, which ends when the X-ray decline steepens at $t_{\mathrm{break},2} \equiv 8.7 \times 10^4\,\mathrm{s}$. The decay slope in phase 3 is steeper than in phase 2 in both bandpasses.

Phase 3 extends out to the last X-ray detection at $t_{\mathrm{break},3} \equiv 1.7 \times 10^6\,\mathrm{s}$. Between this time and the *HST* optical observations, the optical decay must have significantly steepened. This last epoch, with only optical data, we define as phase 4.

The results of this power-law analysis are shown in Tables 3.3 and 3.5. Each bandpass is discussed in further detail below.

3.3.1 X-Ray Light Curve and Spectrum

The X-ray light curve of GRB 050820A is shown in the top panel of Figure 3.4. In phase 1, we see two distinct behaviors: initially the X-ray light curve falls rapidly with a decay slope $\alpha_{\mathrm{1a,x}} = 2.2 \pm 0.3$. This continues until $t_{BAT} = 217\,\mathrm{s}$, and we define this as phase $1a_x$. The X-ray emission then rises rapidly ($217 < t_{\mathrm{BAT}} < 257$ s; phase $1b_x$), after which *Swift* enters the SAA. It is clear from the correlation between the γ-ray and X-ray emission in this epoch that the two are related (Figure 3.1c). A full

Table 3.5.   Optical Afterglow Spectral and Temporal Fits

Phase	$t_{\mathrm{BAT}}^{\mathrm{start}}$ (s)	$t_{\mathrm{BAT}}^{\mathrm{stop}}$ (s)	α	β	χ_{r}^2 / d.o.f.
1a	T_{BAT}	626	-0.35 ± 0.02	. . .	3.00 / 13
1b	626	4.8×10^3	0.97 ± 0.01	0.57 ± 0.06	1.53 / 14
2	4.8×10^3	8.7×10^4	0.78 ± 0.01	0.77 ± 0.08	5.7 / 31
3	8.7×10^4	1.7×10^6	0.99 ± 0.06	. . .	1.43 / 18
4	1.7×10^6	3.2×10^6	≥ 2.1	. . .	. . .

Note: We have fit the optical data to a power-law model of the form $F_\nu \propto t^{-\alpha}\nu^{-\beta}$ where possible. In some phases (1a and 3), we have limited spectral coverage and could not meaningfully constrain β. Thus we have only fit for the temporal decay index α. In phase 4, we can only place an upper limit on the decay slope.

study of the properties of phase $1b_{\mathrm{x}}$ is left to Section 3.4.2.

Following *Swift*'s emergence from the SAA, the light curve in phase 2 shows evidence for a shallower epoch of decline. With the large gap in coverage, we cannot constrain when this transition occurs. We therefore define $t_{\mathrm{break,1}}$ to coincide with the resumption of XRT observations at $t_{\mathrm{BAT}} = 4785\,\mathrm{s}$. A similar break in the optical light curve is also seen near this time (Section 3.3.2).

The X-ray data after $t_{\mathrm{break,1}}$ are not well fitted by a single power-law decay ($\chi_{\mathrm{r}}^2 = 3.7$; 31 d.o.f.), due mostly to a steepening of the decay at $t_{\mathrm{BAT}} \approx 10^5\,\mathrm{s}$. Fitting a broken power-law model to this data, we find an acceptable fit with $t_{\mathrm{break,2}} = (8.7 \pm 2.4) \times 10^4\,\mathrm{s}$ ($\chi_{\mathrm{r}}^2 = 1.19$; 25 d.o.f.). The resulting decay index before the break (phase 2) is $\alpha_{2,\mathrm{x}} = 0.93 \pm 0.03$. For phase 3, we find $\alpha_{3,\mathrm{x}} = 1.25 \pm 0.07$.

The X-ray spectral index in phase $1a_{\mathrm{x}}$ is relatively steep: $\beta_{1a,\mathrm{x}} = 0.90 \pm 0.09$. The spectrum hardens significantly in phase $1b_{\mathrm{x}}$ ($\beta_{1b,\mathrm{x}} = -0.10 \pm 0.03$), further justifying our decision to split phase 1 into two separate X-ray segments. In phase 2, the spectrum softens again, to $\beta_{2,\mathrm{x}} = 1.20 \pm 0.04$. There are too few X-ray counts in phase 3 to meaningfully constrain the spectrum.

The results of our analysis of the X-ray data set are summarized in Table 3.3.

3.3.2 Optical Light Curve and Spectrum

The optical light curve from GRB 050820A is shown in the bottom panel of Figure 3.4. Phases 1 ($0 < t_{\mathrm{BAT}} < 4785$), 2 ($4785 < t_{\mathrm{BAT}} < 8.7 \times 10^4$), and 3 ($8.7 \times 10^4 < t_{\mathrm{BAT}} < 1.7 \times 10^6$) of the optical light curve have already been defined in terms of the X-ray decay. However, unlike the X-ray, the earliest optical observations indicate the afterglow was getting brighter with time (Cenko & Fox, 2005; Wren et al., 2005). This rise continues until a peak at $t_{\mathrm{BAT}} \approx 600$ s, marking the end of phase $1a_{\mathrm{opt}}$. After the peak, the optical light curve in all 4 P60 filters decays steadily with $\alpha_{1b,\mathrm{opt}} = 0.97 \pm 0.01$ until $t_{\mathrm{break},1}$. We note that for this and all subsequent phases, we have constrained α to be identical in all optical filters. A more thorough discussion of phase 1 is left to Section 3.4.2.

Much like the X-ray, the optical decay in phases 2 and 3 is poorly fit by a single power-law ($\chi_{\mathrm{r}}^2 = 13.7$; 49 d.o.f.). In phase 2, the optical decay noticeably flattens ($\alpha_{2,\mathrm{opt}} = 0.78 \pm 0.01$). A much higher degree of variability is seen in the different filters, resulting in a poor fit statistic. After $t_{\mathrm{break},2}$ the decay in phase 3 is again steeper and more uniform, with $\alpha_{3,\mathrm{opt}} = 0.99 \pm 0.06$.

It is clear that if we extrapolate the decay from phase 3 out to the *HST* observations, the late-time flux is greatly overestimated. We conclude therefore a break has occurred in the light curve sometime after $t_{\mathrm{break},3}$, and thus we define phase 4 to span $1.7 \times 10^6 < t_{\mathrm{BAT}} < 3.2 \times 10^6$. We constrain the temporal decay in phase 4 to be $\alpha_{4,\mathrm{opt}} \geq 2.1$.

Due to the limited spectral coverage of our observations, we are unable to provide meaningful constraints on the spectral index β in phases $1a_{\mathrm{opt}}$, 3, and 4. For the remaining epochs, we have excluded the *U*- and *B*-band data from our spectral fits, as these are expected to lie below the Ly-α absorption edge at this redshift. We attempted to solve for the host galaxy reddening $[A_V(\mathrm{host})]$ using extinction laws for the Milky Way, and Large and Small Magellanic Clouds from Pei (1992). In all cases, we find a host extinction consistent with zero. While this result is inconsistent with the column density derived from high-resolution spectroscopy (Ledoux et al., 2005),

it is in agreement with the low host extinction values seen in almost all well-sampled pre-*Swift* afterglows (Kann et al., 2006).

Ignoring host reddening, we find $\beta_{1b,opt} = 0.57 \pm 0.06$ and $\beta_{2,opt} = 0.77 \pm 0.08$. While the optical spectrum appears to have steepened in phase 3, the poor fit quality of this phase precludes any firm conclusions from being drawn.

The results of our analysis of the optical data set are shown in Table 3.5.

3.3.3   Radio Light Curve

The radio emission rises to a peak sometime around 1 day after the burst (Figure 3.5 and Table 3.4). The radio spectrum at early times is quite chaotic, transitioning through a peak around 8.5 GHz at $t_{BAT} = 2.15$ days to optically thin 4.11 days after the burst. We note that some of the variation at early times may be due to inter-stellar scintillation (Goodman, 1997) as has been in seen in many other radio afterglows (e.g., Frail et al., 1997).

The late-time ($t > 7$ days) radio data show no sign of any afterglow brighter than 200 μJy. This is in marked contrast to the bright optical and X-ray afterglows, and is one of the most difficult aspects of the afterglow to account for (Section 3.4.4).

3.4   Discussion

In this section, we use the results from our previous analysis to try and explain the broadband emission from GRB 050820A in the context of the standard fireball model (Section 1.3).

3.4.1   Early γ-Ray Emission

The most striking feature of the γ-ray light curve of GRB 050820A is the large gap between the initial pulse that triggered the *Swift* BAT (Peak A in Figure 3.1*b*) and the bulk of the high-energy emission ($t_{BAT} > 200$ s). The natural question arises as to
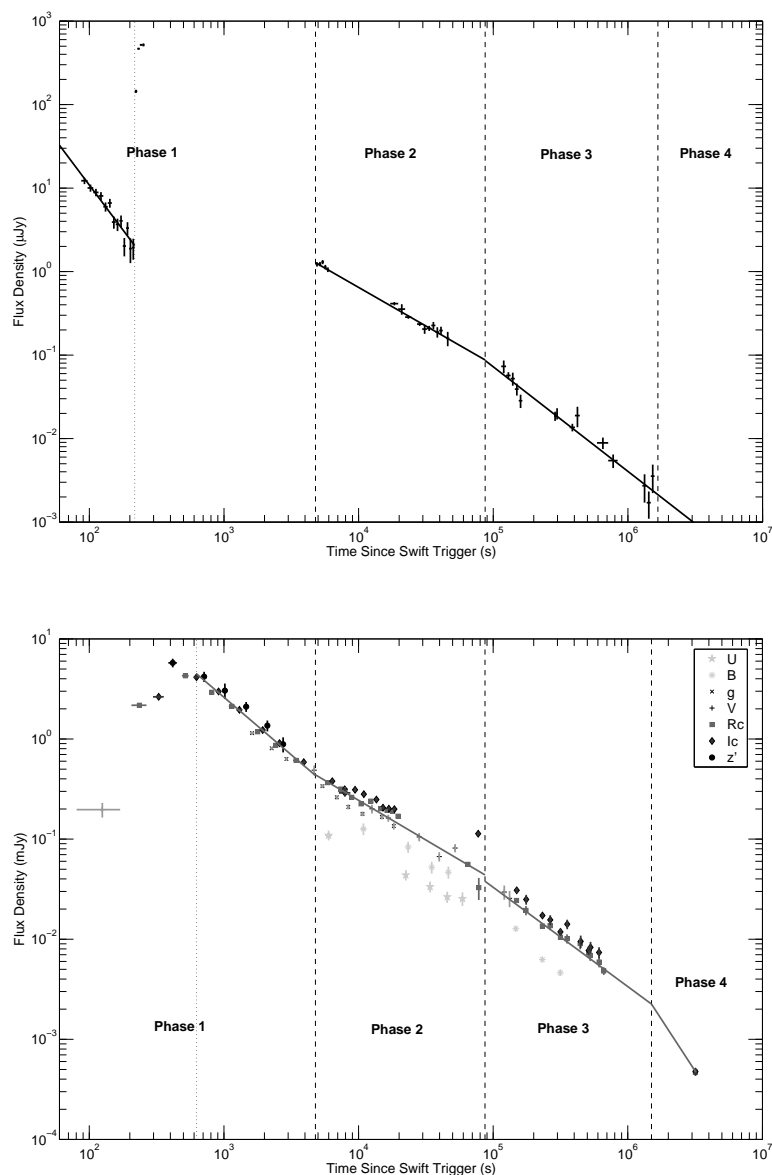
Figure 3.4 — X-ray (*top*) and optical (*bottom*) light curves of GRB 050820A. Both bandpasses have been divided into four segments (phases 1–4), each shown with a vertical dashed line. The unique subdivision of phase 1 is shown as a dotted line in both plots. *Top:* 2–10 keV X-ray fluxes were converted to flux densities at 5 keV using the average spectral slope for each phase. It was assumed the spectrum remained constant from phase 2 to phase 3. The best-fit X-ray temporal decay is shown with a solid line. *Bottom:* Magnitudes were converted to flux densities using zero points from Fukugita et al. (1995). The best-fit R_C-band temporal decay is shown with a solid line.

whether this "precursor"[5] results from the same physical mechanism as the bulk of the high-energy emission. Many models predict a high-energy component distinct from the prompt GRB at early times. Possible mechanisms include the transition from an optically thick to an optically thin environment in the fireball itself (Paczynski, 1986; Lyutikov & Usov, 2000; Mészáros & Rees, 2000; Lyutikov & Blandford, 2003), or the interaction of a jet with a progenitor, presumably a collapsing Wolf-Rayet star (Ramirez-Ruiz et al., 2002; Waxman & Mészáros, 2003).

We can securely rule out both of these models for the precursor of GRB 050820A, as both predict a thermal spectrum. Fitting a thermal model to the BAT precursor spectrum results in a fit statistic of $\chi_r^2 = 3.4$ (75 d.o.f.), while a non-thermal power-law model provides an excellent fit ($\chi_r^2 = 1.07$ for 75 d.o.f.; $\Gamma = 1.74 \pm 0.08$).

While the precursor may be non-thermal, it is noticeably softer than the majority of the remaining prompt emission (Fig. 3.2, bottom two panels). A search for precursors in a sample of long, bright *BATSE* bursts revealed such a soft, non-thermal component in a sizable fraction (20–25%) of these events (Lazzati, 2005). Furthermore, two of the longest, brightest *Swift* bursts observed to date, GRB 041219 (Vestrand et al., 2005; McBreen et al., 2006) and GRB 060124 (Romano et al., 2006) show a faint, soft precursor followed by a large time lag (570 s in the case of GRB 060124).

These soft precursors are inconsistent with the main prompt emission in most GRBs, which exhibits a hard-to-soft evolution in the γ-ray spectrum (Ford et al., 1995; Frontera et al., 2000). The γ-ray light curve of GRB 050820A conforms to this trend only if we ignore the precursor. Furthermore, it is difficult to conceive of a scenario by which internal shocks can generate such long periods of quiescence in a sustained outflow. The large time lag, soft nature, and repeated occurrence of these precursors hint that they are in fact due to a different emission mechanism than the internal dissipation thought to power the bulk of the high-energy emission. However, we cannot state this conclusively, as would be the case if the precursors were thermal.

If we assume a different emission mechanism, the prompt emission did not begin

---

[5]Here we define a precursor as an event that is well separated from and contains only a small fraction of the total high-energy emission. Unlike some other authors, our definition is independent of the mechanism behind the emission. Peak A in GRB 050820A is then clearly a precursor.
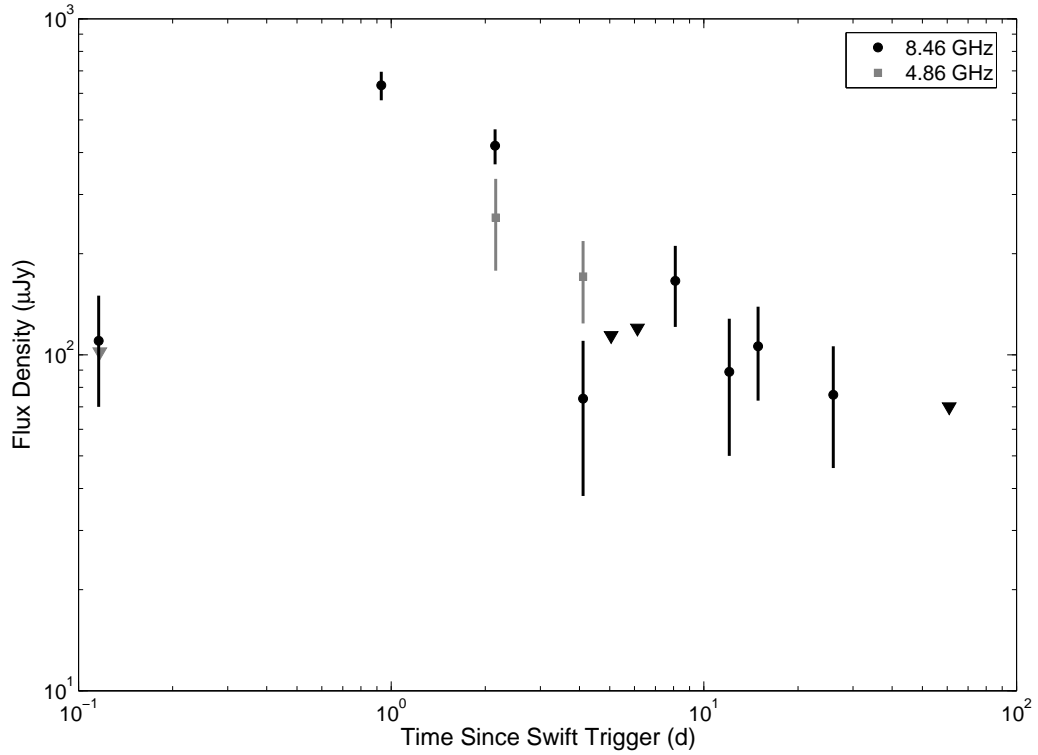
Figure 3.5 — Radio afterglow of GRB 050820a. The early rise in the radio light curve at $t_{\mathrm{BAT}} \approx 1$ day is most easily understood as a reverse shock caused by late-time energy injection, as seen in both the optical and X-ray light curves. The most striking feature of the radio light curve, however, is the lack of a bright radio afterglow at late times (Section 3.4.4).

until 222 s after the *Swift* trigger. This seemingly small discrepancy in defining T_0 affects the calculated temporal decay indices, particularly during the early afterglow (Section 3.4.4). For all temporal decay indices calculated in this work, we consider T_0 to coincide with the beginning of the bulk of the high-energy emission (i.e., 06:38:35 UT on 2005 August 20).

Finally, we consider the early X-ray emission. The temporal decay slope at early times ($\alpha_{1a,X} = 2.2$) is too steep to be attributed to a standard forward shock afterglow. The most popular explanation for the rapid decline of early X-ray emission in *Swift* GRBs is "high-latitude emission": prompt emission from large angles ($\theta > \Gamma^{-1}$) that, due to relativistic beaming effects, reaches the observer at late times [$\Delta t \sim (1 + z)R\theta^2/2c$; Kumar & Panaitescu, 2000]. However, this results in a well-
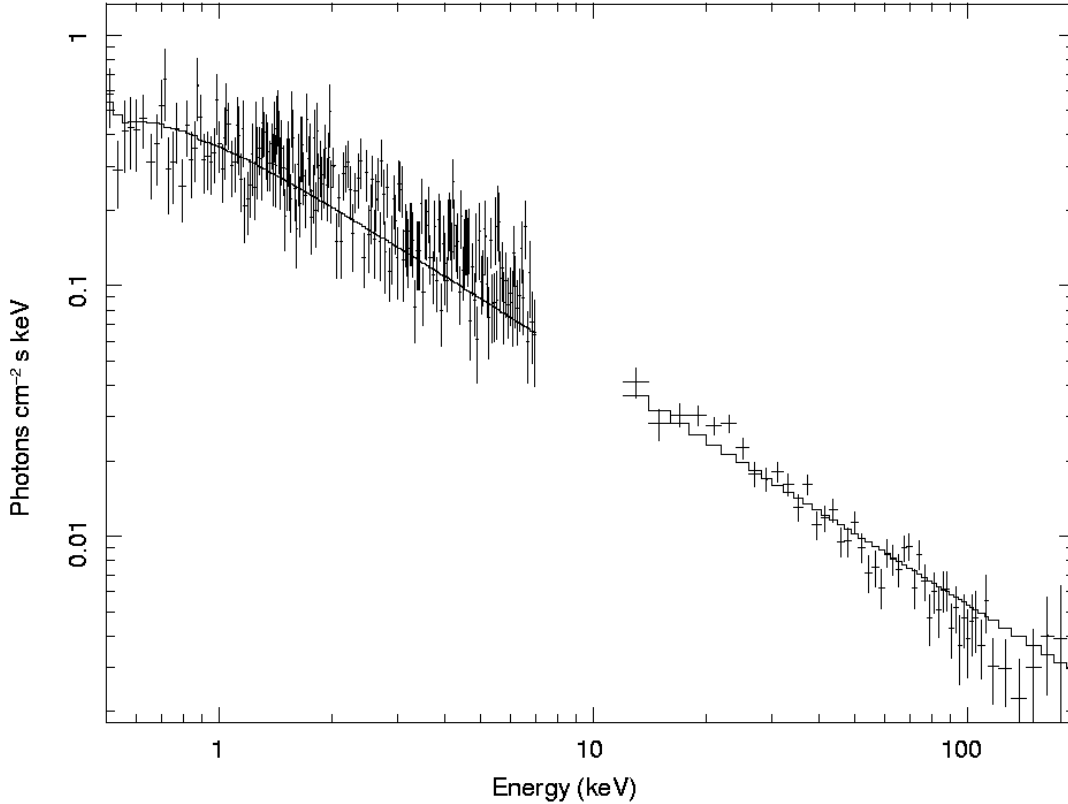
Figure 3.6 — Joint BAT/XRT spectrum of the main pulse of prompt emission ($217 <$ $t_{\mathrm{BAT}} < 257\,\mathrm{s}$). While there is no region of direct overlap, the XRT data is clearly the low-energy tail of the prompt BAT emission, forming one continuous spectrum. The best fit spectrum ($\Gamma = 0.94$) is shown as a solid line. Both the BAT and XRT data have been binned for plotting purposes.

defined relationship between the spectral and temporal indices ($\alpha = \beta + 2$) which is inconsistent with the observed values for GRB 050820A.

Zhang et al. (2006) discuss possible mechanisms that could cause the early-time decay slope to deviate from this behavior. The most realistic possibility is if the X-rays were below the cooling frequency at this very early epoch. Then the closure relation would take the form $\alpha \approx 1 + 3\beta/2 = 2.4$ (Sari & Piran, 1999b), in good agreement with the observed value.

3.4.2 Contemporaneous X-Ray and Optical Emission

Given the long duration and bright fluence, GRB 050820A provides a rare opportunity to study contemporaneous emission in the optical, X-ray, and γ-ray bandpasses. In Figure 3.1, we show the early time ($t_{\mathrm{BAT}} \lesssim 800\,\mathrm{s}$) emission in X-rays (Figure 3.1c) and optical (Figure 3.1d) overlaid onto the high-energy light curve of GRB 050820A.

A look at the X-ray data in Figure 3.1c shows a strong correlation between the X-ray and γ-ray light curves. The X-ray light curve, previously in the midst of a decline, abruptly jumps in sync with the high energy emission at $t_{BAT} \approx 222\,\mathrm{s}$ (phase 1b$_{\mathrm{X}}$). In addition to temporal similarities, the X-ray photon index at this epoch ($\Gamma_{\mathrm{XRT}} = 0.90 \pm 0.03$) is much harder than at any other epoch in the X-ray light curve, and similar to that derived from the BAT ($\Gamma_{\mathrm{BAT}} = 1.07 \pm 0.06$). Thus motivated, we have performed a joint fit of the BAT and XRT spectra at this epoch. Unfortunately Konus-*Wind* had yet to trigger, and so no high-energy multi-channel spectra are available from that instrument. We find that both bandpasses are well fitted by a single power-law with index $\Gamma = 0.94 \pm 0.03$ ($\chi_{\mathrm{r}}^2 = 1.3$; 391 d.o.f.). The resulting unfolded spectrum is shown in Figure 3.6. We conclude the X-rays in phase 1b$_{\mathrm{X}}$ are generated by the same mechanism as the prompt emission.

It is clear from Figure 3.1d that, unlike in the X-ray band, there is no strong correlation between optical and γ-ray flux from GRB 050820A. Radical spectral evolution would be required in the optical to explain both bandpasses as arising from the same emission mechanism. We consider this scenario highly unlikely and conclude that, at the very least, the dominant contribution to the optical emission in phase 1 has a different origin than the prompt emission.

We next consider if our optical observations in phase 1 can be explained solely in terms of the standard afterglow formulation. We have attempted to fit both a simple broken power-law (Sari et al., 1998) and an analytic solution for the flux density near the optical peak (Granot & Sari, 2002) to our R_{C}-, I_{C}-, and z'-band early-time data. The resulting fit quality is quite poor ($\chi_{\mathrm{r}}^2 = 3.0$; 14 d.o.f.) with the dominant contribution coming from the data in phase 1a$_{\mathrm{opt}}$ (i.e., before the peak). In spite of

the poor fit, we have included the results for phase 1a$_{\mathrm{opt}}$ in Table 3.5 for reference.

This result is not unexpected, as Vestrand et al. (2006) have shown that contemporaneous optical imaging of GRB 050820A with the RAPTOR telescope can be well fitted as the sum of two independent components: one representing the forward shock and another proportional to the high-energy prompt emission. We attempted an analogous fit with the P60 and Konus-*Wind* data set. While a better fit statistic ensues, we still do not find an acceptable result ($\chi^2_{\mathrm{r}} = 2.2$; 14 d.o.f.). We conclude that the relatively sparse time sampling of our observations, coupled with the frequent filter changes, make it impossible to verify this result.

Independent of any correlation between the prompt optical and γ-ray emission, we note that the decay after $t_{\mathrm{BAT}} = 600\,\mathrm{s}$ is dominated by the forward shock. Unlike the bright, early-time emission seen from GRB 990123 (Akerlof et al., 1999), we see no evidence for rapidly decaying [$\alpha_{\mathrm{RS}} = (27p + 7)/35 \approx 2$; Kobayashi, 2000] reverse shock emission from an optical flare.

Finally, using the combination of optical and γ-ray data, we consider the broadband SED of GRB 050820A at early times. For each of the contemporaneous optical observations, we have extracted fluxes and (where possible) spectra from the corresponding Konus-*Wind* observations (Figure 3.8 and Table 3.8). Following the method of Vestrand et al. (2005), we have calculated the γ-ray-to-optical color index, $C_{\mathrm{O}\gamma} \equiv -2.5 \log[F(\mathrm{opt})/F(\gamma)]$, or lower limits, for each interval. The ratio varies significantly over the course of our observations. The value of $C_{\mathrm{O}\gamma} = 12.5$ in interval 2 is consistent with that seen from GRB 041219a, while later intervals are even brighter in the optical. In fact, the optical-to-γ-ray flux ratio in interval 5 is over 240 times larger than that observed for GRB 050401 (Rykoff et al., 2005). Evidently a large diversity exists in the broadband SEDs of GRBs at early times.

3.4.3 Late-Time Energy Injection

The majority of XRT light curves observed to date have exhibited a period of shallow decline ($0.2 \lesssim \alpha \lesssim 0.8$) that is inconsistent with the standard afterglow formulation

(Nousek et al., 2006). Two models have been invoked to explain this phase, both of which involve injecting energy into the forward shock at late times ($t \gg t_{\mathrm{GRB}}$; e.g., Zhang et al., 2006). In the first, the central engine is active for long time periods, $t \gg t_{\mathrm{GRB}}$. The late-time emission of highly relativistic material injects additional energy into the forward shock, flattening the decay slope (Katz & Piran, 1997; Rees & Mészáros, 2000). Alternatively, towards the end of the γ-ray emission, the central engine may eject material with a smooth distribution of (decreasing) Lorentz factors. Slower moving material will catch up with the forward shock when it has swept up enough circumburst material, resulting in a smooth injection of energy at late times (Rees & Meszaros, 1998; Sari & Mészáros, 2000). While both models explain the flattening of the XRT light curves, they provide different constraints on the nature of the central engine.

In the first (long-lived central engine) model, the central engine's luminosity, $L(t)$, is characterized as:

$$L(t) = L_0 \left(\frac{t}{t_0} \right)^{-q}.$$
(3.1)

This results in the following spectral and temporal power-law indices for a constant density medium:

$$
\begin{aligned}
\nu < \nu_m \; : \; \alpha \;\; &= \;\; \frac{5q - 8}{6} \\
&= \;\; (q - 1) + \frac{(2 + q)\beta}{2} \\
\nu_m < \nu < \nu_c \; : \; \alpha \;\; &= \;\; \frac{(2p - 6) + (p + 3)q}{4} \\
&= \;\; (q - 1) + \frac{(2 + q)\beta}{2} \\
\nu > \nu_c \; : \; \alpha \;\; &= \;\; \frac{(2p - 4) + (p + 2)q}{4} \\
&= \;\; \frac{q - 2}{2} + \frac{(2 + q)\beta}{2}.
\end{aligned}
$$
(3.2)

(3.3)

(3.4)

For a wind-like medium, the analogous results are

$$\nu < \nu_m \; : \; \alpha \;\; = \;\; \frac{q - 1}{3}$$

$$= \frac{q}{2} + \frac{(2+q)\beta}{2} \tag{3.5}$$

$$\nu_m < \nu < \nu_c \; : \; \alpha \;\; = \;\; \frac{(2p-2) + (p+1)q}{4}$$

$$= \frac{q}{2} + \frac{(2+q)\beta}{2} \tag{3.6}$$

$$\nu > \nu_c \; : \; \alpha \;\; = \;\; \frac{(2p-4) + (p+2)q}{4}$$

$$= \frac{q-2}{2} + \frac{(2+q)\beta}{2}. \tag{3.7}$$

The refreshed shock scenario is parametrized in terms of the amount of mass ejected with Lorentz factor greater than γ:

$$M(> \gamma) \propto \gamma^{-s}. \tag{3.8}$$

For the circumburst profiles considered here, we can define a new variable, $\hat{q}$, such that we reproduce identical afterglow behavior to that of Equations 3.2–3.4 or Equations 3.5–3.7 by simply substituting $\hat{q}$ for q. Parameter $\hat{q}$ is related to the mass ejection parameter s by the following equations (Zhang et al., 2006):

$$\hat{q} = \;\; \frac{10 - 2s}{7 + s} \quad \text{(ISM)} \tag{3.9}$$

$$= \;\; \frac{4}{3 + s} \quad \text{(Wind)}. \tag{3.10}$$

While the X-ray decay in phase 2 is not as flat as that seen in other *Swift* bursts, the temporal and spectral decay indices are nonetheless inconsistent with the standard afterglow model for $\nu(X) > \nu_c$ (Equations 1.17 and 1.25). Furthermore, the optical light curve shows a flattening during phase 2 and is inconsistent with both the closure relations in either medium for $\nu_m < \nu(\text{opt}) < \nu_c$ (Equations 1.16 and 1.24). We conclude that we are therefore seeing a milder version of the energy injection phase present in many *Swift* X-ray afterglows.

For the X-ray data in phase 2, we find an acceptable fit for the energy injection models only if $\nu(X) > \nu_c$. This corresponds to values of $q_X = 0.66 \pm 0.08$ ($s_{X,\text{ISM}} = 2.0 \pm 0.3$, $s_{X,\text{Wind}} = 3.1 \pm 0.7$) and $p_X = 2.4 \pm 0.2$. The optical data in phase 2 are

best fitted with a constant density medium and $\nu_m < \nu(\mathrm{opt}) < \nu_{\mathrm{c}}$: $q_{\mathrm{opt}} = 0.73 \pm 0.09$ ($s_{\mathrm{ISM,opt}} = 1.8 \pm 0.3$) and $p_{\mathrm{opt}} = 2.5 \pm 0.2$. Both the X-ray and the optical fall in the expected spectral regime, providing further confidence in this interpretation.

A prediction of the energy injection hypothesis is a bright reverse shock at early times most easily visible in the radio (Sari & Mészáros, 2000). A reverse shock nicely explains the rapid decline in flux at 8.5 GHz from 1 to 4 days after the burst. Furthermore, the transition from a spectrum peaked around 8.5 GHz at $t_{\mathrm{BAT}} = 2.15$ days to an optically thin radio spectrum at $t_{\mathrm{BAT}} = 4.11$ days can be understood as the reverse shock peak frequency, ν_m^{RS}, passing through the radio. Since $\nu_m^{\mathrm{RS}} \approx \nu_m^{\mathrm{FS}}/\Gamma^2$, this should occur well before the forward shock peak frequency reaches the radio bands.

Distinguishing between the two theories to explain the energy injection is quite difficult, as both models can be identically parametrized. Progress in this area would require a large sample of bursts with detailed contemporaneous X-ray and optical light curves. If the refreshed shocks are due to continued engine activity, they should be correlated with the bright X-ray flares seen in some XRT afterglows. On the other hand, if the flat decay is caused by slow-moving ejecta, this behavior should be more uniform from burst to burst. Such an analysis is beyond the scope of this work.

3.4.4 Burst Environment and Progenitor Models

We now turn our attention to the issue of the circumburst medium. As discussed earlier, the radial profile of the burst environment affects the temporal decay below the cooling frequency (Equations 1.10–1.12, 1.18–1.20). In particular, the closure relations (Equations 1.14–1.16, 1.22–1.24) are sufficiently different that we should be able to distinguish between the competing models for a well-sampled event like GRB 050820A.

First, we examine the X-ray data. As discussed previously (Section 3.4.3), the X-ray observations in phase 2 require invoking mild energy injection to explain the shallower than expected decay for $\nu(\mathrm{X}) > \nu_c$. If we assume the X-ray spectral index does not change from phase 2 to phase 3, then we find $\alpha_{3,\mathrm{X}}$ and $\beta_{3,\mathrm{X}}$ satisfy the

standard afterglow closure relation for $\nu_X > \nu_c$ (Equations 1.17 and 1.25). The corresponding values for the electron index are: $p_{\alpha3,X} = 2.3 \pm 0.1$, $p_{\beta3,X} = 2.40 \pm 0.08$.

Unlike the X-ray observations, the optical bands typically probe frequencies below the cooling frequency, where the closure relations are different for different circumburst media (Equations 1.16 and 1.24). We have shown already in Section 3.4.3 that the optical data in phase 2 are better fit by a constant density medium. We find that a constant density medium is favored in the optical in phase $1b_{opt}$ and phase 3 as well. The only closure relation satisfied in phase $1b_{opt}$ is for an ISM with $\nu_m < \nu(\text{opt}) < \nu_c$ (Equation 1.16). The resulting p-values are $p_{\alpha1b,opt} = 2.29 \pm 0.02$, $p_{\beta1b,opt} = 2.1 \pm 0.1$. We note that had we equated the BAT trigger time, T_{BAT}, with the onset of the burst (T_0), the temporal slope in phase $1b_{opt}$ would have been inconsistent with all closure relations.

In phase 3, we cannot meaningfully constrain the optical spectral slope. However, using the X-ray-to-optical spectral slope in this phase, $\beta_{\text{OX},3} \approx 0.8$, we conclude the optical data in this segment still fall below the cooling frequency. Based solely on the temporal decline then, we can rule out a wind-like medium in this phase. The corresponding electron index ($p \approx 1.7 \pm 0.1$) would result in a divergent total energy. While this possibility has been addressed with more complicated electron energy distributions (e.g., Dai & Cheng, 2001), we consider this possibility unlikely.

Taken together, the X-ray and optical data provide a consistent picture of the forward shock expanding into a constant density medium. The late-time ($t_{\text{BAT}} > 1\,\text{week}$) radio observations, however, are inconsistent with this interpretation. For a constant density medium, the peak flux density, $F_{\nu,\text{max}}$, should remain constant in time. This would predict, if we have correctly interpreted the optical peak as the forward shock (Section 3.4.2), a similar peak ($F_{\nu,\text{max}} \approx 5\,\text{mJy}$) in the radio at $t_{\text{BAT}} \approx 7\,\text{days}$ ($\nu_m \propto t^{-3/2}$). This is well above the VLA detection limit at this epoch, yet we only measure $F_\nu \approx 100\,\mu\text{Jy}$. While the energy injection phase will delay the arrival of ν_m in the radio ($\nu_m^{\text{inject}} \propto t^{-3/2}t^{3(s-1)/2(7+s)}$), our radio limits extend out to two months after the burst. It would be very difficult, if not impossible, to delay the peak this long. Furthermore, during the energy injection phase, the peak

flux increases with time ($F_{\nu,\text{max}}^{\text{inject}} \propto t^{3(s-1)/(7+s)}$). Thus we would expect to see rising emission earlier relative to the peak, counteracting the delay of the peak radio flux.

One explanation for the lack of a bright, late-time radio afterglow is an early jet break ($t \lesssim 1\,\text{day}$), as was invoked for GRB 990123 (Kulkarni et al., 1999b). However, we find no evidence for a jet break in the optical or X-ray light curves out to at least 17 days after the burst (Section 3.4.5).

Another possibility, invoked to explain the relatively low late-time radio flux from GRB 050904, is a high ambient density (Frail et al., 2006). In the case of GRB 050904, it was argued that the large density raised the self-absorption frequency, ν_a, above the radio observing bands. This greatly suppresses the radio flux, for the spectrum in this regime is proportional to ν^2 (Equation 1.6). There is no evidence in the radio data for an optically thick spectrum, although spectral data is sparse at late times. Furthermore, broadband modeling of this event (Section 3.4.5) rules out a high ambient density for typical values of the micro-physical parameters ϵ_e and ϵ_B. We therefore consider this explanation unlikely.

Alternatively, a natural explanation for the low radio flux at late times is a wind-like medium. In a wind-like medium, the forward shock peak flux density declines in time as $F_{\nu,\text{max}} \propto t^{-3/2}$. The decreasing peak flux counteracts the rising synchrotron emission, suppressing any late-time radio data. This is of course inconsistent with our X-ray and optical data, which strongly favor a constant density medium. One can imagine a scenario in which the environment near the burst (the regime sampled predominantly by the X-ray and optical data) is approximately constant in density, while the outer regions (sampled by the radio at later times) have a wind-like profile. However, without a physical justification for such a density profile, this remains little more than speculation. The lack of a bright radio afterglow remains a puzzling aspect of GRB 050820A.
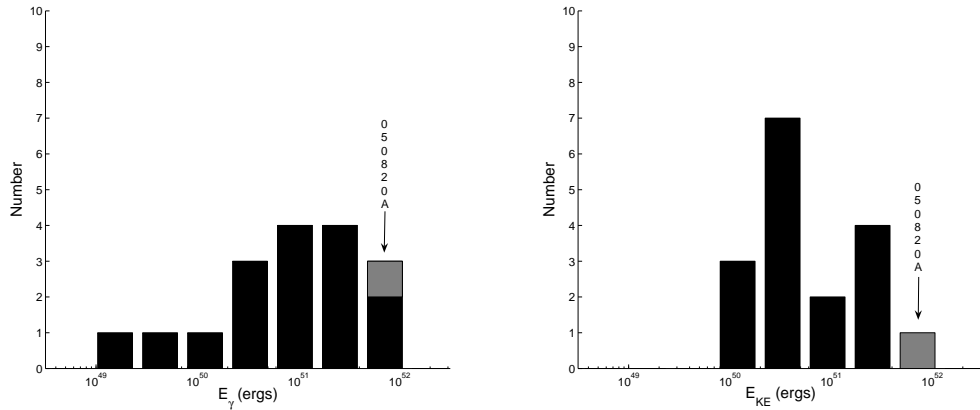
Figure 3.7 — Total energy release of GRB 050820A. *Left:* Collimation-corrected energy release in the prompt emission (E_γ) of a sample of cosmological GRBs, including GRB 050820A. *Right:* Collimation-corrected blast-wave energy (E_{KE}) for the same sample. (References: Berger et al., 2004; Yost et al., 2003; Panaitescu & Kumar, 2002; Berger et al., 2001; Chevalier et al., 2004; Soderberg et al., 2004; Berger et al., 2003b).

3.4.5 Geometry and Energetics

Using the high-energy fluence derived from Konus-*Wind* (Section 3.2.1.2), we calculate the total isotropic energy release in the prompt emission was $E_{\gamma,iso} = 8.3^{+2.5}_{-1.1} \times 10^{53}$ erg (assuming a redshift of $z = 2.615$; Prochaska et al., 2005; Ledoux et al., 2005). This makes GRB 050820A one of the most energetic events (in terms of $E_{\gamma,iso}$) for which a redshift has been measured (Amati, 2006).

However, only a fraction of the explosion energy is converted into prompt emission via internal dissipation. The rest remains in the kinetic energy of the outflow, powering the forward shock and hence the afterglow. We can estimate the kinetic energy of the afterglow ($E_{KE,iso}$) by examining the X-ray emission at $t_{BAT} > 10$ hr (Freedman & Waxman, 2001). At this point, the X-rays should be above the cooling frequency. The flux density is then independent of ambient density and only weakly dependent on ϵ_B. A joint fit of the phase 3 optical and X-ray data (after the energy injection has ceased and the system has returned to adiabatic expansion) constrains the electron energy index: $p = 2.34 \pm 0.06$. If we take typical values for ϵ_e (0.1–0.3) and ϵ_B (0.01–0.1) (Yost et al., 2003), we find that $15 \lesssim E_{KE,iso,52} \lesssim 100$.

For an accurate accounting of the total energy emitted by this event, however, we must determine the degree of collimation of the emission. We therefore examine all the temporal breaks in the optical and X-ray light curves to determine which one (if any) shows an achromatic steepening to the t^{-p} decay expected from a jet (Sari et al., 1999). The only plausible candidate is the transition from phase 3 to 4 in the optical light curve. The steepening here is achromatic (i.e., it is seen in all three *HST* filters) and much too large to be explained solely by the cooling frequency passing through the optical bands (although this may have occurred as well). Any contribution from an underlying host galaxy would only further steepen the decay in phase 4.

With only one observation, it is impossible to constrain the post-break decay index. Instead, we assume the post-break decay has a power-law index $\alpha = p \approx 2.34$. We then find $t_j = 18 \pm 2$ days. This result is consistent with our X-ray observations, which put a lower limit on the jet break time of $t_j \gtrsim 17$ days.

We note that the jet break time we have inferred for GRB 050820A is extremely large. In the host galaxy reference frame, the break occurs at $t_j^{\text{host}} \approx 5$ days, a factor of three larger than any jet break seen in the pre-*Swift* era (Zeh et al., 2006). In this respect, too, GRB 050820A is a strong outlier.

To convert the jet break times to a range of opening angles, we use the relation (Sari et al., 1999):

$$\theta = 0.161 \left(\frac{t_j}{1+z} \right)^{3/8} \left(\frac{n\eta_\gamma}{E_{\gamma,\text{iso},52}} \right)^{1/8}. \tag{3.11}$$

Here η_γ is the fraction of the total energy converted to prompt γ-ray emission. The only remaining unknown in Equation 3.11 is the ambient density, n. Using the ratio of the X-ray and optical data, as well as the canonical values of ϵ_e and ϵ_B, we find the density of the burst must be low: $n \leq 1\,\text{cm}^{-3}$. Afterglow modeling of the late-time optical and X-ray data (phase 3, after any continued energy injection has ceased and the shock expands adiabatically) using the technique of Yost et al. (2003) confirms this result: $n \lesssim 0.1$.

Combining the above results, we find the opening angle is constrained to fall between $6.8° \lesssim \theta \lesssim 9.3°$, corresponding to a beaming factor $f_b \equiv 1 - \cos\theta \approx 10^{-2}$.

While the opening angle is large for a long-soft burst, there are several comparable events in the pre-*Swift* sample (Zeh et al., 2006). The total collimation-corrected energy emitted in γ-rays (E_γ) from GRB 050820A is therefore $7.5^{+6.7}_{-2.4} \times 10^{51}$ ergs. The corresponding value for the blast-wave energy (E_{KE}) is $5.2^{+7.9}_{-4.1} \times 10^{51}$ ergs.

Ghirlanda et al. (2004a) have demonstrated an empirical relation between E_γ and the peak energy of the prompt emission spectrum in the GRB rest frame ($E_\mathrm{p}^\mathrm{rest}$). GRB 050820A is more energetic than any of the 37 bursts considered in their sample (in terms of E_γ), and therefore proves an interesting test case for the so-called Ghirlanda relation. Using our calculated value of E_γ, the Ghirlanda relation predicts $E_\mathrm{p}^\mathrm{rest} = 2.0^{+2.5}_{-1.2}$ MeV. This is marginally consistent with the actual value of $E_\mathrm{p}^\mathrm{rest} = 1.3^{+0.3}_{-0.2}$ MeV derived from the Konus-*Wind* data set.

In Figure 3.7 we plot a histogram of E_γ and E_{KE} for the ~ 15 long-soft cosmological bursts for which both quantities have been derived. We have not included the most nearby events (GRB 980425, GRB 031203, and GRB 060218) in our analysis, as these events released significantly less energy than the typical cosmological GRB (Soderberg et al., 2006c). Soderberg et al. (2004) have shown that, with the exception of the most nearby events, the sum of E_γ and E_{KE} is clustered around 2×10^{51} erg. GRB 050820A is clearly an over-energetic exception, an order of magnitude more energetic than this sample. In fact, it would require the direct conversion of $\approx 10^{-2}$ M$_\odot$ (with 100% efficiency) to release this much energy.

Finally, it is important to consider how robust our estimates of $E_{\mathrm{KE,iso}}$, θ, and n are given that the standard afterglow model fails to explain the broadband behavior of GRB 050820A. We note that the opening angle is relatively insensitive to both variables (Eqn. 3.11); factors of order unity will be greatly reduced by the $\frac{1}{8}$ exponent. It is difficult to conceive of a long-soft GRB environment where the ambient density is less than 10^{-2} cm^{-2}, and high densities would only increase the opening angle and thus the energy release.

3.5   Conclusion

GRB 050820A joins a select sample of events with simultaneous observations in the γ-ray and optical bands, and an even smaller group with contemporaneous X-ray observations as well. Such events have led to fundamental advances in our understanding of GRBs, including the discovery of a reverse-shock optical flash from GRB 990123 (Akerlof et al., 1999) and possibly from GRB 050904 (Boër et al., 2006). The early-time optical emission from GRB 041219A also showed a bright optical flash, but the rise was correlated with an accompanying peak of γ-ray emission, suggesting a common origin for the two components (Vestrand et al., 2005).

The early behavior of GRB 050820A is unlike either of these events. Vestrand et al. (2006) have shown that the contemporaneous optical emission is well described as the sum of two components: one proportional to the prompt γ-ray emission and one smoothly varying forward shock term. While the γ-ray component is important for $t_{\rm BAT} < 300\,{\rm s}$, the optical peak at $t_{\rm BAT} \approx 600\,{\rm s}$ is dominated by emission from the external shock region. Furthermore, the post-peak decay rate is inconsistent with reverse-shock emission. Instead we interpret this as the forward shock peak frequency (ν_m) passing through the optical bands. This is not unlike what was seen in the optical for GRB 060124 (Romano et al., 2006), although the time resolution in the prompt phase was much poorer than for this burst. The contemporaneous optical light curves of GRB 050319 (Quimby et al., 2006; Woźniak et al., 2005) and GRB 050401 (Rykoff et al., 2005) did not show this peak phase, but extrapolations to late-times were consistent with the adiabatic expansion of a forward shock. Another different behavior was seen in the early optical light curve of GRB 050801, which showed an extended plateau phase correlated with the X-ray emission, hinting at continued energy injection from a central engine refreshing the external shocks (Rykoff et al., 2006).

The contemporaneous X-ray emission, on the other hand, is the low-energy tail of the prompt emission. This behavior was also seen for GRB 060124 (Romano et al., 2006) and has been hinted at in the rapid decline in early X-ray light curves attributed

to high-latitude emission (Liang et al., 2006), as well as the bright X-ray flares seen in many XRT light curves (Burrows et al., 2005b). It is clear then, that, in marked contrast to the X-ray emission, contemporaneous optical emission exhibits a large diversity in behavior. Unfortunately the physical mechanism behind this diversity remains to be explained.

The issue of burst geometry is a particularly interesting one in the *Swift* era. The steep post-break decay slope, seen simultaneously in multiple filters, makes GRB 050820A one of the most convincing examples of a beamed event in the *Swift* sample. The X-ray afterglow, however, is too faint at late times to provide broadband confirmation. In fact, very few *Swift* bursts, including those, like GRB 050408 (Foley et al., 2006), that have been followed for months, show signs of a jet break in the XRT light curve (Nousek et al., 2006).

Typical jet breaks in pre-*Swift* bursts occurred on time scales of several days (Zeh et al., 2006). Perna et al. (2003) predicted that *Swift* would detect bursts with wider opening angles than previous missions due to the increased sensitivity of the BAT. However, not a single *Swift* afterglow has shown a convincing jet break transition in multiple bandpasses (candidates include GRB 050525A and GRB 050801; see Panaitescu et al., 2006, and references therein for a more thorough discussion). While it may be that most jet breaks, like GRB 050820A, occur at late times, beyond the sensitivity of the XRT and most ground-based facilities, this is nonetheless troubling. On the one hand, few if any X-ray jet breaks were seen in pre-*Swift* bursts; all collimation angles were determined from optical (and sometimes radio) light curves. Conversely, given the large number of well-sampled XRT light curves, and the fact that such fundamental results for GRB cosmology as the Ghirlanda relation rest on our picture of GRBs as aspherical events, this is clearly a matter that merits further investigation.

One consequence of the large opening angle associated with GRB 050820A is a correspondingly large burst and afterglow energy. In fact, of all the bursts compiled in the Ghirlanda et al. (2004b) sample, GRB 050820A has the largest prompt energy release. And unlike GRB 990123 (Panaitescu & Kumar, 2001), this large γ-ray energy

was accompanied by a correspondingly large kinetic energy imparted to the afterglow. The only comparable event for which such energies could be determined was the high-redshift GRB 050904, which released a total energy of $\sim 10^{52}$ ergs (Tagliaferri et al., 2005; Frail et al., 2006). Given the large γ-ray fluence, similar events should have been easily detected by both *Swift* and previous GRB missions. And given the bright optical afterglow and the late jet-break, such events are strongly favored for ground-based follow-up (i.e., redshift determination). The lack of a large sample of such events means they must be relatively rare in the universe.

Like many other *Swift* GRBs, the X-ray light curve of GRB 050820A exhibits a phase of shallow decay incompatible with the standard forward shock model (Nousek et al., 2006). GRB 050820A is relatively unique, however, in that this epoch is also well sampled in the optical. The seemingly simultaneous breaks in the optical light curve bolster the commonly held belief that this phase is caused by some form of refreshed shocks (Zhang et al., 2006). Coupled with the large gap between the precursor and the bulk of the prompt emission, the late-time energy injection poses fundamental challenges to any central engine model.

Finally, we return to the question of the radio afterglow. Radio observations typically probe low Lorentz factor ejecta ($\Gamma \sim 2$–3) at large distances from the central engine ($r \sim 10^{17}$ cm). The forward shock peak frequency reaches the radio much later than the optical or X-ray bands. Thus, radio emission is usually visible at later times than optical or X-ray emission, and is well suited to study afterglows when the emission is isotropic (i.e., after the jet break) or even in some cases when the ejecta has slowed to Newtonian expansion (Berger et al., 2004). For this reason, late-time radio observations are considered the most accurate method for model-independent calorimetry. For GRB 050820A, this paradigm has broken down. The burst had a bright optical and X-ray afterglow, but weak emission in the radio. It is hoped that further studies of such energetic GRBs in the *Swift* era will help to elucidate some of these puzzles.
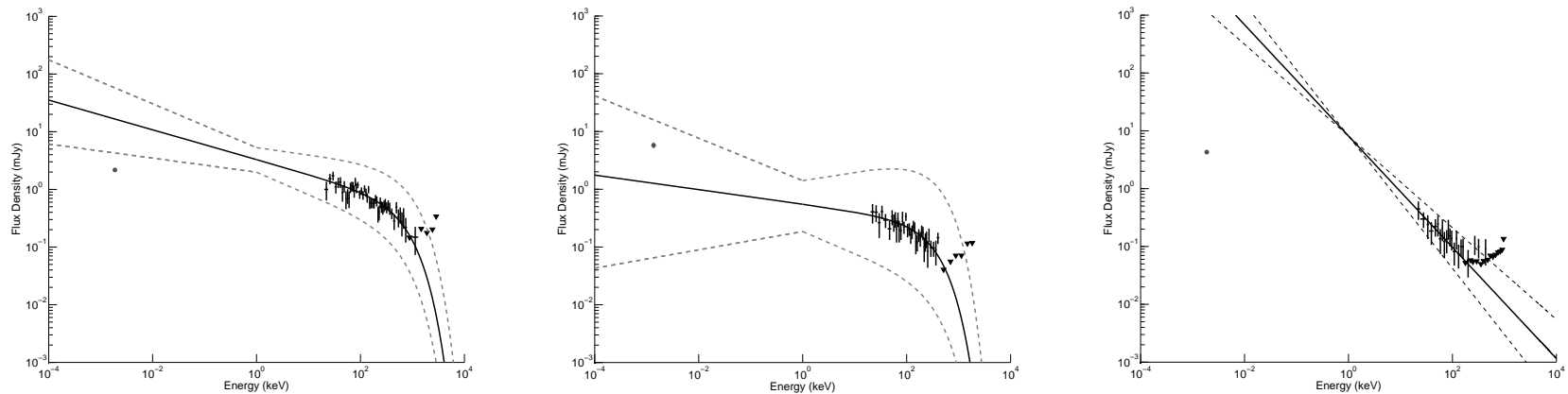
Figure 3.8 — Early-time broadband SED of GRB 050820A. Konus-*Wind* spectral data for the given intervals (see Table 3.8 for definitions of the intervals) are shown (*crosses*) alongside the corresponding optical observations (*circles*). The 2σ upper limits in the high-energy spectra are plotted as triangles. The best-fit model to the Konus-*Wind* spectrum is shown as a solid line, and the dashed lines show the 90% confidence intervals for the spectral fits. The ratio of optical to γ-ray flux varies significantly between the three intervals. *Left*: Interval 2. This interval covers only a small fraction of the time of the corresponding P60 image because Konus-*Wind* only triggered on GRB 050820A (and hence began collecting multi-channel spectra) in the middle of this image. The optical R_C-band data point lies below the extrapolation of the γ-ray spectrum. *Center*: Interval 4. Here the Konus-*Wind* and P60 intervals are nearly simultaneous. Unlike the other intervals, the P60 z'-band point lies above the predicted value and within the 90% confidence interval of the extrapolation of the high-energy spectrum. *Right*: Interval 5. Here the high-energy extrapolation greatly overestimates the optical flux. However, the γ-ray flux in this interval is quite low, and the low number of high-energy photons makes it difficult to constrain a cutoff power-law spectrum. In fact this interval was best fitted with a power-law spectrum.

Table 3.6.   XRT Observations of GRB 050820A

Mean Observation Date (2005 UT)	t_{BAT} (s)	Duration (s)	Spectral Index (β)	2–10 keV Flux (10^{-11} ergs cm^{-2} s^{-1})
Aug 20 06:36:25	92.0	10.0	0.90	14.9 ± 1.3
Aug 20 06:36:35	102.0	10.0	...	12.2 ± 1.2
Aug 20 06:36:45	112.0	10.0	...	10.8 ± 1.1
Aug 20 06:36:55	122.0	10.0	...	9.8 ± 1.1
Aug 20 06:37:05	132.0	10.0	...	7.3 ± 0.9
Aug 20 06:37:15	142.0	10.0	...	8.1 ± 1.0
Aug 20 06:37:25	152.0	10.0	...	4.8 ± 0.8
Aug 20 06:37:35	162.0	10.0	...	4.5 ± 0.8
Aug 20 06:37:45	172.0	10.0	...	4.9 ± 0.8
Aug 20 06:37:55	182.0	10.0	...	2.5 ± 0.6
Aug 20 06:38:05	192.0	10.0	...	4.0 ± 0.7
Aug 20 06:38:15	202.0	10.0	...	2.3 ± 0.8
Aug 20 06:38:25	212.0	10.0	...	2.4 ± 0.7
Aug 20 06:38:35	222.0	10.0	-0.10	175.1 ± 7.9
Aug 20 06:38:45	232.0	10.0	...	567.0 ± 14.2
Aug 20 06:38:55	242.0	10.0	...	631.3 ± 15.0
Aug 20 06:39:05	252.0	10.0	...	629.7 ± 26.5
Aug 20 07:56:43	4.910×10^3	250.0	1.20	3.0 ± 0.2
Aug 20 08:00:53	5.160×10^3	250.0	...	3.1 ± 0.2
Aug 20 08:05:03	5.410×10^3	250.0	...	3.2 ± 0.2
Aug 20 08:09:13	5.660×10^3	250.0	...	2.8 ± 0.2
Aug 20 08:13:23	5.901×10^3	250.0	...	2.6 ± 0.2
Aug 20 11:41:43	1.841×10^4	2.5×10^3	...	1.02 ± 0.05
Aug 20 12:23:23	2.091×10^4	2.5×10^3	...	0.9 ± 0.1
Aug 20 13:05:03	2.341×10^4	2.5×10^3	...	0.71 ± 0.03
Aug 20 14:28:23	2.841×10^4	2.5×10^3	...	0.58 ± 0.03
Aug 20 15:10:03	3.091×10^4	2.5×10^3	...	0.51 ± 0.06
Aug 20 15:51:43	3.341×10^4	2.5×10^3	...	0.52 ± 0.04
Aug 20 16:33:23	3.591×10^4	2.5×10^3	...	0.56 ± 0.06
Aug 20 17:15:03	3.841×10^4	2.5×10^3	...	0.47 ± 0.07
Aug 20 17:56:43	4.091×10^4	2.5×10^3	...	0.49 ± 0.05
Aug 20 19:20:03	4.951×10^4	2.5×10^3	...	0.39 ± 0.08
Aug 21 15:48:01	1.196×10^5	1.0×10^4	...	0.18 ± 0.03
Aug 21 18:34:41	1.296×10^5	1.0×10^4	...	0.14 ± 0.01
Aug 21 21:21:21	1.396×10^5	1.0×10^4	...	0.13 ± 0.02
Aug 22 00:08:01	1.496×10^5	1.0×10^4	...	0.10 ± 0.02

Table 3.6 (cont'd)

Mean Observation Date (2005 UT)	t_{BAT} (s)	Duration (s)	Spectral Index (β)	2–10 keV Flux (10^{-11} ergs cm^{-2} s^{-1})
Aug 22 02:54:41	1.596×10^5	1.0×10^4	...	0.07 ± 0.01
Aug 23 14:30:22	2.877×10^5	1.0×10^4	...	0.046 ± 0.006
Aug 23 17:17:02	2.977×10^5	1.0×10^4	...	0.050 ± 0.008
Aug 24 18:02:47	3.869×10^5	3.5×10^4	...	0.034 ± 0.004
Aug 25 03:46:07	4.219×10^5	3.5×10^4	...	0.05 ± 0.01
Aug 27 19:38:46	6.518×10^5	1.25×10^5	...	0.022 ± 0.003
Aug 29 06:22:06	7.768×10^5	3.5×10^4	...	0.014 ± 0.002
Sep 04 15:45:23	1.329×10^6	1.0×10^5	...	$(6.8 \pm 2.5) \times 10^{-3}$
Sep 05 19:32:03	1.429×10^6	1.0×10^5	...	$(4.2 \pm 1.5) \times 10^{-3}$
Sep 06 23:18:43	1.529×10^6	1.0×10^5	...	$(8.8 \pm 3.3) \times 10^{-3}$

Note: The four phases of the X-ray light curve are delineated by horizontal lines (Section 3.3.1). We assumed the spectral index was constant in each phase to convert count rates to the flux values shown here. We also assumed the spectral index remained constant from phase 2 to phase 3. All errors quoted are at the 1σ level.

Table 3.7.   Optical Observations of GRB 050820A

Mean Observation Date (2005 UT)	t_{BAT} (s)	Telescope	Filter	Exposure Time (s)	Magnitude[a] (Vega)	Reference
Aug 20 08:14:47	5.994×10^3	UVOT	U	693.3	18.12 ± 0.13	*
Aug 20 12:49:02	2.245×10^4	UVOT	U	899.8	19.11 ± 0.14	*
Aug 20 16:01:58	3.404×10^4	UVOT	U	899.8	19.40 ± 0.14	*
Aug 20 19:14:54	4.560×10^4	UVOT	U	899.8	19.66 ± 0.15	*
Aug 20 22:59:51	5.910×10^4	UVOT	U	392.3	19.70 ± 0.18	*
Aug 20 09:36:06	1.087×10^4	UVOT	B	899.8	18.79 ± 0.16	*
Aug 20 13:04:10	2.336×10^4	UVOT	B	899.8	19.24 ± 0.15	*
Aug 20 16:17:05	3.493×10^4	UVOT	B	897.3	19.74 ± 0.16	*
Aug 20 19:30:02	4.651×10^4	UVOT	B	899.8	19.87 ± 0.16	*
Aug 21 23:30:41	1.473×10^5	RTT150	B	1800.0	21.28 ± 0.06	1
Aug 22 22:58:17	2.318×10^5	RTT150	B	7860.0	22.05 ± 0.06	2
Aug 23 22:09:05	3.153×10^5	RTT150	B	5400.0	22.38 ± 0.08	2
Aug 20 07:01:53	1.620×10^3	P60	g	120.0	16.27 ± 0.04	*
Aug 20 07:12:35	2.262×10^3	P60	g	120.0	16.65 ± 0.04	*
Aug 20 07:23:24	2.911×10^3	P60	g	120.0	16.92 ± 0.05	*
Aug 20 08:04:47	5.394×10^3	P60	g	360.0	17.59 ± 0.05	*
Aug 20 08:29:42	6.889×10^3	P60	g	360.0	17.87 ± 0.06	*
Aug 20 08:54:50	8.397×10^3	P60	g	360.0	18.11 ± 0.06	*
Aug 20 09:33:18	1.071×10^4	P60	g	720.0	18.29 ± 0.06	*
Aug 20 10:43:25	1.491×10^4	P60	g	720.0	18.36 ± 0.06	*
Aug 20 11:39:32	1.829×10^4	P60	g	720.0	18.59 ± 0.09	*
Aug 20 06:36:58	125.0	UVOT	V	89.0	18.18 ± 0.20	*
Aug 20 07:52:58	4.685×10^3	UVOT	V	99.8	17.20 ± 0.13	*
Aug 20 10:04:28	1.258×10^4	UVOT	V	337.0	18.16 ± 0.12	*
Aug 20 11:12:34	1.666×10^4	UVOT	V	899.8	18.39 ± 0.09	*
Aug 20 14:25:30	2.824×10^4	UVOT	V	899.8	18.86 ± 0.11	*
Aug 20 17:38:26	3.981×10^4	UVOT	V	899.8	19.35 ± 0.12	*
Aug 20 21:03:50	5.214×10^4	UVOT	V	899.8	19.14 ± 0.11	*
Aug 21 16:09:34	1.209×10^5	UVOT	V	899.8	20.24 ± 0.19	*
Aug 21 19:22:30	1.325×10^5	UVOT	V	899.8	20.40 ± 0.22	*
Aug 20 06:38:49	236.0	P60	R_{C}	60.0	15.39 ± 0.04	*
Aug 20 06:43:31	517.0	P60	R_{C}	60.0	14.65 ± 0.02	*
Aug 20 06:48:25	812.0	P60	R_{C}	60.0	15.06 ± 0.03	*
Aug 20 06:53:59	1.146×10^3	P60	R_{C}	120.0	15.42 ± 0.02	*
Aug 20 07:04:34	1.781×10^3	P60	R_{C}	120.0	16.05 ± 0.03	*
Aug 20 07:15:19	2.426×10^3	P60	R_{C}	120.0	16.39 ± 0.02	*

Table 3.7 (cont'd)

Mean Observation Date (2005 UT)	t_{BAT} (s)	Telescope	Filter	Exposure Time (s)	Magnitude[a] (Vega)	Reference
Aug 20 07:32:13	3.440×10^3	P60	R_{C}	360.0	16.77 ± 0.02	*
Aug 20 08:12:58	5.885×10^3	P60	R_{C}	360.0	17.32 ± 0.04	*
Aug 20 08:38:05	7.392×10^3	P60	R_{C}	360.0	17.48 ± 0.04	*
Aug 20 08:46:53	7.920×10^3	PROMPT-5	R_{C}	660.0	17.52 ± 0.09	3
Aug 20 09:03:19	8.906×10^3	P60	R_{C}	360.0	17.69 ± 0.04	*
Aug 20 09:28:50	1.044×10^4	P60	R_{C}	360.0	17.85 ± 0.04	*
Aug 20 10:00:44	1.235×10^4	P60	R_{C}	360.0	17.78 ± 0.04	*
Aug 20 10:38:59	1.465×10^4	P60	R_{C}	360.0	17.97 ± 0.04	*
Aug 20 11:05:54	1.626×10^4	P60	R_{C}	360.0	18.01 ± 0.04	*
Aug 20 11:33:14	1.790×10^4	P60	R_{C}	360.0	18.03 ± 0.04	*
Aug 20 12:02:31	1.966×10^4	P60	R_{C}	360.0	18.16 ± 0.05	*
Aug 21 00:37:53	6.498×10^4	RTT150	R_{C}	900.0	19.36 ± 0.01	1
Aug 21 04:16:53	7.812×10^4	PROMPT-5	R_{C}	5370.0	19.94 ± 0.31	3
Aug 22 00:00:05	1.491×10^5	RTT150	R_{C}	1800.0	20.26 ± 0.05	1
Aug 22 07:17:03	1.753×10^5	P60	R_{C}	6840.0	20.51 ± 0.11	*
Aug 22 23:00:41	2.319×10^5	RTT150	R_{C}	3900.0	20.90 ± 0.03	2
Aug 23 08:06:11	2.647×10^5	P60	R_{C}	8400.0	20.89 ± 0.10	*
Aug 23 22:18:05	3.158×10^5	RTT150	R_{C}	2700.0	21.18 ± 0.04	2
Aug 24 08:46:32	3.535×10^5	P60	R_{C}	8400.0	21.22 ± 0.11	*
Aug 25 09:33:11	4.427×10^5	P60	R_{C}	2880.0	21.34 ± 0.13	*
Aug 26 05:05:39	5.130×10^5	HET	R_{C}	600.0	21.57 ± 0.08	*
Aug 26 08:28:20	5.252×10^5	P60	R_{C}	3600.0	21.64 ± 0.12	*
Aug 27 08:37:13	6.121×10^5	P60	R_{C}	4800.0	21.80 ± 0.12	*
Aug 27 22:49:53	6.633×10^5	RTT150	R_{C}	1500.0	22.02 ± 0.10	4
Sep 26 01:39:38	3.179×10^6	HST	$F625W$	800.0	24.59 ± 0.08	*
			R_{C}		24.55 ± 0.08	*
Aug 20 06:40:21	328.0	P60	I_{C}	60.0	14.91 ± 0.02	*
Aug 20 06:45:19	626.0	P60	I_{C}	60.0	14.42 ± 0.01	*
Aug 20 06:50:06	913.0	P60	I_{C}	60.0	14.78 ± 0.01	*
Aug 20 06:56:37	1.304×10^3	P60	I_{C}	120.0	15.24 ± 0.02	*
Aug 20 07:07:15	1.942×10^3	P60	I_{C}	120.0	15.74 ± 0.02	*
Aug 20 07:18:03	2.590×10^3	P60	I_{C}	120.0	16.07 ± 0.02	*
Aug 20 07:40:11	3.918×10^3	P60	I_{C}	360.0	16.54 ± 0.03	*
Aug 20 08:21:15	6.382×10^3	P60	I_{C}	360.0	17.02 ± 0.05	*
Aug 20 08:46:26	7.893×10^3	P60	I_{C}	360.0	17.22 ± 0.04	*
Aug 20 08:46:53	7.920×10^3	PROMPT-3	I_{C}	1560.0	17.31 ± 0.08	3

Table 3.7 (cont'd)

Mean Observation Date (2005 UT)	t_{BAT} (s)	Telescope	Filter	Exposure Time (s)	Magnitude[a] (Vega)	Reference
Aug 20 09:11:47	9.414×10^3	P60	I_{C}	360.0	17.23 ± 0.05	*
Aug 20 09:37:27	1.095×10^4	P60	I_{C}	360.0	17.34 ± 0.03	*
Aug 20 10:21:01	1.357×10^4	P60	I_{C}	360.0	17.48 ± 0.04	*
Aug 20 10:47:55	1.518×10^4	P60	I_{C}	360.0	17.68 ± 0.04	*
Aug 20 11:14:54	1.680×10^4	P60	I_{C}	360.0	17.71 ± 0.05	*
Aug 20 11:42:22	1.845×10^4	P60	I_{C}	360.0	17.72 ± 0.04	*
Aug 21 04:04:53	7.740×10^4	PROMPT-3	I_{C}	5440.0	18.33 ± 0.11	3
Aug 22 00:07:53	1.496×10^5	RTT150	I_{C}	1800.0	19.74 ± 0.07	1
Aug 22 07:25:05	1.758×10^5	P60	I_{C}	6840.0	19.97 ± 0.12	*
Aug 22 23:06:41	2.323×10^5	RTT150	I_{C}	3900.0	20.37 ± 0.05	2
Aug 23 08:22:42	2.657×10^5	P60	I_{C}	7560.0	20.48 ± 0.12	*
Aug 23 22:24:05	3.162×10^5	RTT150	I_{C}	2700.0	20.78 ± 0.09	2
Aug 24 09:11:48	3.550×10^5	P60	I_{C}	8400.0	20.59 ± 0.11	*
Aug 25 10:44:39	4.470×10^5	P60	I_{C}	2400.0	21.02 ± 0.15	*
Aug 26 04:49:33	5.121×10^5	HET	I_{C}	1200.0	21.25 ± 0.10	*
Aug 26 09:27:24	5.288×10^5	P60	I_{C}	4800.0	21.17 ± 0.14	*
Aug 27 08:34:02	6.120×10^5	P60	I_{C}	4440.0	21.30 ± 0.13	*
Sep 26 02:01:58	3.180×10^6	HST	$F775W$	800.0	24.32 ± 0.09	*
			I_{C}		24.27 ± 0.09	*
Aug 20 06:41:50	417.0	P60	z'	60.0	13.93 ± 0.11	*
Aug 20 06:46:45	712.0	P60	z'	60.0	14.27 ± 0.14	*
Aug 20 06:51:50	1.017×10^3	P60	z'	60.0	14.62 ± 0.21	*
Aug 20 06:59:16	1.463×10^3	P60	z'	120.0	15.02 ± 0.13	*
Aug 20 07:09:56	2.103×10^3	P60	z'	120.0	15.49 ± 0.14	*
Aug 20 07:20:45	2.752×10^3	P60	z'	120.0	15.96 ± 0.20	*
Sep 26 03:06:14	3.184×10^6	HST	$F850LP$	1600.0	24.09 ± 0.09	*

[a]Errors quoted are 1σ photometric and instrumental errors summed in quadrature. Galactic extinction ($E(B{-}V) =$ 0.044; Schlegel et al., 1998) has been incorporated in the reported magnitudes.

References: * = this work; 1 = Bikmaev et al. (2005); 2 = Khamitov et al. (2005); 3 = MacLeod & Nysewander (2005); 4 = Aslan et al. (2005).

Table 3.8.   Joint γ-Ray/Optical Early-Time Data

Interval ID	$t_{\mathrm{BAT}}^{\mathrm{start}}$ (s)	Duration (s)	γ-Ray Flux[a] $(10^{-8}$ erg cm^{-2} s$^{-1})$	α[b]	E_{p}[b] (keV)	χ_{r}^2 / d.o.f.	Optical Filter	Optical Flux Density[a] (mJy)	$C_{\mathrm{O}\gamma}$[c]
1	80.949	85.376	< 1.3	. . .	. . .	. . .	V	0.20 ± 0.03	< 10.2
2	257.839	8.448	$96.2^{+13.9}_{-0.80}$	1.26 ± 0.14	510^{+211}_{-120}	0.83 / 62	R_{C}	2.17 ± 0.08	12.5
3	297.775	59.904	< 3.2	. . .	. . .	. . .	I_{C}	2.64 ± 0.04	< 8.8
4	389.167	57.344	$19.06^{+0.03}_{-6.61}$	$1.13^{+0.24}_{-0.29}$	269^{+107}_{-59}	0.78 / 62	z'	5.77 ± 0.57	10.0
5	487.471	57.344	$9.35^{+0.53}_{-2.38}$	1.96 ± 0.18	. . .	1.01 / 58	R_{C}	4.28 ± 0.08	9.2
6	602.159	49.152	< 2.3	. . .	. . .	. . .	I_{C}	4.14 ± 0.05	< 7.9
7	684.079	57.344	< 4.1	. . .	. . .	. . .	z'	4.20 ± 0.49	< 8.7

[a]Errors quoted are at the 1σ level.

[b]Spectral fits of the form $\mathrm{d}N/\mathrm{d}E \propto E^{-\alpha} \exp^{-(2-\alpha)E/E_{\mathrm{p}}}$ were performed for the case of intervals 2 and 4. For interval 5, the highest-energy data were not of sufficient quality to estimate E_{p}. Instead a power-law fit $(\mathrm{d}N/\mathrm{d}E \propto E^{-\alpha})$ was used. Errors quoted are 90% confidence limits.

[c]The γ-ray-to-optical color index: $C_{\mathrm{O}\gamma} \equiv -2.5 \log[F(\mathrm{opt})/F(\gamma)]$.

Chapter 4

Broadband Modeling of the Afterglows of GRB 050525A and GRB 060418 and the Emergence of a Class of Hyper-Energetic *Swift* Events

S. B. Cenko[a], J. Kelemen[b], F. A. Harrison[a], D. A. Frail[c], D. B. Fox[d],

S. R. Kulkarni[e], M. M. Kasliwal[e], E. O. Ofek[e], A. Rau[e],

A. M. Soderberg[f,g], A. Gal-Yam[h], A. Cucchiara[d], P. Chandra[i]

[a]Space Radiation Laboratory, MS 220-47, California Institute of Technology, Pasadena, CA 91125

[b]Konkoly Observatory, H-1525, Box 67, Budapest, Hungary

[c]Department of Astronomy & Astrophysics, 525 Davey Laboratory, Pennsylvania State University, University Park, PA 16802

[d]National Radio Astronomy Observatory, P.O. Box 0, 1003 Lopezville Road, Socorro, NM 87801

[e]Department of Astronomy, Mail Stop 105-24, California Institute of Technology, Pasadena, CA 91125

[f]Observatories of the Carnegie Institute of Washington, 813 Santa Barbara Street, Pasadena, CA 91101

[g]Princeton University Observatory, Peyton Hall, Ivy Lane, Princeton, NJ 08544

[h]Astrophysics Group, Faculty of Physics, Weizmann Institute of Science, Rehovot 76100, Israel

[i]Department of Astronomy, University of Virginia, P.O. Box 3818, Charlottesville, VA 22903

Abstract

We present broadband (radio–X-ray) observations of the long-duration γ-ray bursts GRB 050525A and GRB060418. Using our multi-parameter fitting software, we model the afterglows to extract constraints on the energetics, geometry, and environments of both events. Like many *Swift* bursts, we find no evidence for any achromatic jet break from GRB 050525A and GRB 060418 if we assume a constant density circumburst medium. The energetic implications of such isotropic explosions are profound, with total energy release in excess of 10^{53} erg. On the other hand, a wind-like circumburst environment can accommodate a collimated outflow for both events, with opening angles of $13.4^{+2.3}_{-1.5}{}^{\circ}$ (GRB 050525A) and $37.9^{+1.6}_{-6.3}{}^{\circ}$ (GRB 060418). Though this greatly relaxes the total energy requirements for each event, GRB 060418 remains an order of magnitude more energetic than the typical pre-*Swift* GRB. We discuss the implications of this emerging class of hyper-energetic *Swift* GRBs.

4.1 Introduction

Accurate calorimetry is fundamental to understanding any astrophysical phenomenon. In the case of long-duration γ-ray bursts (GRBs), the initial report in 2001 of a nearly universal prompt energy release of $\sim 10^{51}$ erg (Frail et al., 2001) helped to establish the connection between GRBs and massive stars, as core-collapse supernovae (SNe) emit a comparable amount of energy via electromagnetic radiation. Efforts are now underway to utilize GRBs as standardizable candles to constrain the cosmology of our universe (Firmani et al., 2006; Dai et al., 2004), much as has been done for Type Ia SNe (Riess et al., 1998; Perlmutter et al., 1999).

Most current attempts at cosmology with GRBs neglect to include the most nearby ($z \lesssim 0.3$) long-duration events, as these have proven to be several orders of magnitude less energetic than cosmological events (e.g., Soderberg et al., 2006c). It is still not clear whether these nearby events form a distinct sub-population of long-duration GRBs, or if they represent the low energy tail of a single, continuous population.

Unveiling the true energy distribution of long-duration GRBs is one of the important outstanding problems in the field.

Measuring bolometric fluences has nonetheless proven to be a challenging task. The energy carried by the prompt γ-rays (E_γ) is only a fraction of the total energy release. The kinetic energy remaining in the relativistic outflow (E_{KE}) powers the long-lived, broadband afterglow as accelerated electrons swept up by the outgoing shock front emit synchrotron radiation. Inferring physical properties of the outflow from the observed emission requires a detailed understanding of the underlying physics as well as broadband afterglow observations over the duration of its evolution.

Even in the *Swift* era (Gehrels et al., 2004), where detailed early-time follow-up observations are routinely achieved, significant obstacles to accurate calorimetry still exist. First, the limited bandpass (15–150 keV) of the *Swift* Burst Alert Telescope (BAT; Barthelmy et al., 2005a) captures only a fraction of the photons in the traditional γ-ray bandpass. Extrapolating the observed spectrum up to energies as high as 10 MeV introduces significant uncertainties into the prompt fluence measurement (Butler et al., 2007).

Second, GRBs are now widely believed to be highly aspherical explosions (opening angles of a few to tens of degrees; Rhoads, 1999; Sari et al., 1999). Constraining the true energy release therefore requires a knowledge of the degree of collimation. Typically the opening angle is inferred by observing an achromatic steepening in the afterglow light curve attributed to relativistic beaming effects (Figure 1.7). However, very few *Swift* events have shown evidence for such a truly achromatic (i.e., X-ray, optical, and radio) jet break in the *Swift* era (Burrows & Racusin, 2007; Panaitescu, 2007; Liang et al., 2008). Without these collimation corrections, the true energy release from *Swift* events has remained highly uncertain (e.g., Kocevski & Butler, 2007).

Finally, *Swift* data have shown that the central engine generating the ultra-relativistic outflow is capable of injecting energy into the forward shock at late times ($t \gg \Delta t_{\mathrm{GRB}}$). Observations with the *Swift* X-Ray Telescope (XRT; Burrows et al., 2005a) have revealed bright, short-lived X-ray flares superposed on the afterglow de-

cay at late times that can contain a comparable amount of energy to E_γ (Burrows et al., 2005b). Many X-ray light curves also exhibit extended periods of shallow decay (so-called "plateau" phases) inconsistent with standard afterglow models (Nousek et al., 2006; Zhang et al., 2006). Both discoveries suggest that our simplistic adiabatic picture of afterglow evolution may need to be revised.

In this chapter, we present broadband (radio–X-ray) observations of two *Swift* events: GRB 050525A and GRB 060418. Both GRBs are unique in that they were also detected by the Konus-*Wind* instrument, providing continuous γ-ray coverage beyond 10 MeV and therefore a well determined measurement of the prompt γ-ray fluences. In addition, both events have well-sampled afterglows in the X-ray, optical, and radio bandpasses. This is crucial at late times ($t \gtrsim 1$ week), primarily for two reasons. First, such observations enable us to study the afterglow after energy injection from the central engine has ceased, during the adiabatic decay where our models are significantly better understood. Second, late measurements provide the strongest constraints on the opening angle of the outflow, and are therefore vital for accurate collimation-corrected calorimetry.

With the broadband observations in hand, we attempt to model the afterglows of both events using the multi-parameter fitting program developed by Yost et al. (2003). For both events we find reasonable agreement with the afterglow models, assuming we only consider observations taken at $t \gtrsim 0.1$ d. We also find evidence for an additional component of late time emission from GRB 050525A that we attribute to an associated SN. Surprisingly, we find the total energy release from GRB 060418 to be well in excess of 10^{52} erg, an order of magnitude above the canonical value for pre-*Swift* GRBs. GRB 060418 is therefore the fourth member of an emerging class of "hyper-energetic" GRBs. We conclude by discussing the implications of such events on our understanding of GRB progenitor models and the future of using GRBs as cosmological probes.

Throughout this work, we adopt a standard ΛCDM cosmology with $h_0 = 0.71$ km s^{-1} Mpc^{-1}, $\Omega_{\rm m} = 0.27$, and $\Omega_\Lambda = 1 - \Omega_{\rm m} = 0.73$ (Spergel et al., 2007). We define the flux density power-law temporal and spectral decay indices α and β as $f_\nu \propto t^{-\alpha} \nu^{-\beta}$

(e.g., Sari et al., 1998). All errors quoted are 1 σ (68%) confidence intervals unless otherwise noted.

4.2 Observations and Data Reduction

4.2.1 Optical Observations

We began observing both GRB 050525A and GRB 060418 several hours after the bursts with the automated Palomar 60 inch (1.5 m) telescope (Cenko et al., 2006a). All P60 data were reduced in the IRAF[1] environment using our custom real-time reduction pipeline (Cenko et al., 2006a). Where necessary, co-addition was performed using Swarp[2]. Afterglow magnitudes were calculated with aperture photometry using an inclusion radius roughly matched to the stellar PSF FWHM.

Additional optical imaging was obtained with two large ground-based facilities to supplement the P60 light curves at late times: the Large Format Camera (LFC) mounted on the Palomar 200" Hale Telescope, and the Low Resolution Imaging Spectrometer (LRIS; Oke et al., 1995) mounted on the 10 m Keck I telescope. All data were reduced in a similar manner to the P60 images using standard IRAF routines.

Photometric calibration for our ground-based optical imaging was performed relative to the calibration files provided by A. Henden[3] for both events, resulting in rms variations of $\lesssim 0.05$ mag in all filters. Photometric and instrumental errors have been added in quadrature to obtain the results presented in Table 4.3. We note that the magnitudes reported in Table 4.3 have not been corrected for Galactic extinction along the line-of-sight. When necessary for analysis, this correction has been applied using the dust extinction maps of Schlegel et al. (1998) and the Milky Way extinction curve of Cardelli et al. (1989).

Finally, late-time observations of GRB 050525A (GO-10135; PI: Kulkarni) and

---

[1] IRAF is distributed by the National Optical Astronomy Observatory, which is operated by the Association for Research in Astronomy, Inc., under cooperative agreement with the National Science Foundation.

[2] See http://terapix.iap.fr/soft/swarp.

[3] Available via ftp at ftp.aavso.org.

GRB 060418 (GO-10551; PI: Kulkarni) were obtained with the Wide-Field Camera (WFC) channel of the Advanced Camera for Surveys (ACS) on *HST*. We processed the data using the `multidrizzle` routine (Fruchter & Hook, 2002) in the `stsdas` IRAF package. We used `pixfrac` $= 0.8$ and `pixscale` $= 1.0$ for the drizzling procedure, resulting in a pixel scale of $0.05''$ pixel^{-1}. The astrometry on these images was then tied to deep P60 imaging of each field (which is itself tied to the USNO-B1 astrometric grid). Photometry for both events was performed following the recipes in Sirianni et al. (2005). The results of these observations are shown in Table 4.3.

4.2.2   X-Ray Observations

We utilize the *Swift* XRT light curves for both GRB 050525A and GRB 060418 from the on-line *Swift*-XRT light curve repository[4] (Evans et al., 2007). We converted the provided 0.3–10 keV fluxes to flux densities at a nominal energy of 2 keV assuming a power-law X-ray spectrum with photon index $\Gamma = 1.9$ (GRB 050525A; Blustin et al., 2006) or $\Gamma = 2.04$ (GRB 060418; Falcone et al., 2006c).

4.2.3   Radio Observations

We began observations of the fading optical counterpart of GRB 050525A with the Very Large Array (VLA[5]) 10 hours after the burst, and detected the afterglow at 22.5 GHz (Cameron & Frail, 2005). The results of this and subsequent observations at 1.4, 4.9, 8.5, and 22.5 GHz for 39 day days post-burst are summarized in Table 4.4. During this time the VLA antennas were initially in the B configuration, and switched to the BnC configuration in mid-June. The data were reduced with the Astronomical Image Processing Software (AIPS) in the standard manner.

GRB 060418 was observed at 8.5 GHz with the VLA beginning 1 day after the burst and continuing for the next two months. For all observations the antennae were in the A configuration. All images were reduced in the same manner as for

---

[4]See http://www.swift.ac.uk/xrt_curves.

[5]The VLA is operated by the National Radio Astronomy Observatory, a facility of the National Science Foundation operated under cooperative agreement by Associated Universities, Inc.

GRB 050525A, and the results are shown in Table 4.4.

4.3 Broadband Modeling Efforts

In the standard "fireball" formulation (see Chapter 1 for more details), the afterglow is powered by relativistic electrons in the circumburst medium accelerated by an outgoing blast wave emitting synchrotron radiation (the so-called "forward shock"). The resulting spectrum is well described as a series of broken power-laws with three characteristic frequencies: ν_a, the frequency below which the radiation is self-absorbed; ν_m, the characteristic frequency of the emitting electrons; and ν_c, the frequency above which electrons are able to cool efficiently through radiation (Sari et al., 1998; Figure 1.5).

The temporal evolution of the afterglow depends on the density profile of the circumburst medium. We consider here two possibilities: a constant density circumburst medium $[\rho(r) \propto r^0]$, as would be expected in an ISM-like environment (Sari et al., 1998), and a wind-like environment $[\rho(r) \propto r^{-2}]$, as would be the case for a massive star progenitor shedding its outer envelope at a constant mass loss rate before core-collapse (Chevalier & Li, 2000).

GRBs are believed to be highly collimated explosions (Rhoads, 1999; Sari et al., 1999). At early times, observers only notice emission from a narrow cone (opening angle $\theta \sim \Gamma^{-1}$, where Γ is the Lorentz factor of the expanding shock) due to relativistic beaming. The resulting evolution therefore mimics an isotropic explosion. As the shock slows, however, lateral spreading of the jet becomes important, and the observer eventually notices "missing" emission from wider angles. This hydrodynamic transition manifests itself as an achromatic steepening in the afterglow light curve. Measuring the time of this jet break ($t_{\rm j}$) allows us to infer the opening angle of the outflow (θ).

Our objective here is to translate the observed three critical frequencies, together with the peak flux density, $F_{\nu,\rm max}$, and the jet break time, $t_{\rm j}$, into a physical description of the outflow. In particular, we shall attempt to estimate five parameters: $E_{\rm KE}$, the

kinetic energy of the blast wave, n, the density of the circumburst medium, ϵ_e, the fraction of the total energy apportioned to electrons, ϵ_B, the fraction of the total energy apportioned to the magnetic field, and θ, the jet opening angle. We make use of the software described in Yost et al. (2003), a multi-parameter fitting program incorporating the standard afterglow formulation, as well as corrections for radiative losses and Inverse Compton emission (Sari & Esin, 2001).

In addition to the forward shock emission, we consider two other sources of radiation that can affect the afterglow evolution: reverse shock and supernovae emission. While the forward shock propagates into the circumburst medium, electrons in the shock-heated ejecta behind the contact discontinuity can also emit synchrotron radiation (Sari & Piran, 1999a). The resulting reverse shock emission can manifest itself as a bright but rapidly decaying optical or radio flare (Sari & Piran, 1999a). The hydrodynamics of reverse shock emission are described in detail in Kobayashi (2000). Likewise, at late times ($t \gtrsim 1\,\text{week}$), rising optical emission from a supernova has been seen in several nearby GRB afterglows (e.g., Woosley & Bloom, 2006). We shall consider these emissions mechanisms to supplement our forward shock models where appropriate.

4.3.1 GRB 050525A

GRB 050525A was discovered by *Swift* at 00:02:53.26 UT on 2005 May 25 (Blustin et al., 2006). The prompt emission was extremely bright; with a 15–350 keV fluence of $F_\gamma = (18.6 \pm 0.3) \times 10^{-6}\,\text{erg cm}^{-2}$, GRB 050525A falls in the top 5% of *Swift* events in the sample of Butler et al. (2007). At a redshift of $z = 0.606$ (Valle et al., 2006b), the isotropic prompt energy release from GRB 050525A was $E_{\gamma,\text{iso}} = 2.04^{+0.11}_{-0.09} \times 10^{52}\,\text{erg}$ (1 keV–10 MeV rest frame; Butler et al., 2007).

Observations of the bright X-ray and optical afterglow of GRB 050525A have been reported by a number of other authors (Blustin et al., 2006; Klotz et al., 2005; Valle et al., 2006b). We show our broadband observations of GRB 050525A, together with the late-time optical observations of Valle et al. (2006b), in Figures 4.1–4.3.
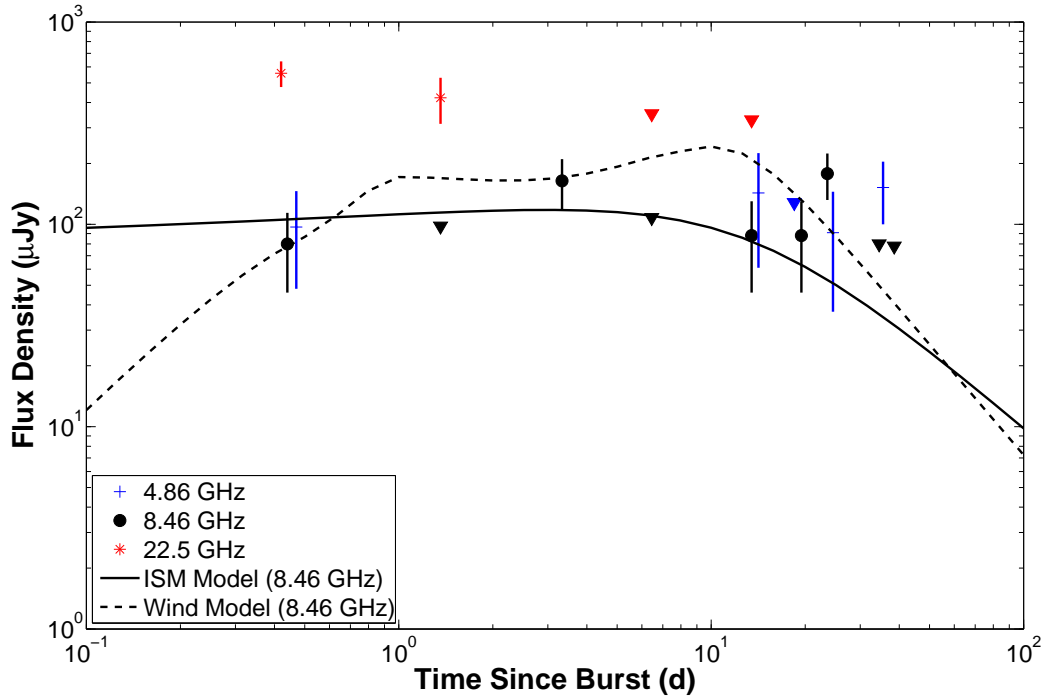
Figure 4.1 — Forward shock models of the afterglow of GRB 050525A — Radio. Both the constant density and wind-like media provide similar quality fits to the data in the radio band.

4.3.1.1 Early Excess Emission

The early optical light curve of GRB 050525A demonstrated several deviations from power-law behavior that are difficult to reconcile with standard forward shock models. Klotz et al. (2005) observed a sharp ($\Delta R \sim 0.65\,\mathrm{mag}$) re-brightening at $t \approx 33\,\mathrm{min}$ after the trigger, while Blustin et al. (2006) report a relatively flat optical decay in the first four hours after the burst. Several authors have attributed this to a fast-fading reverse shock component that dominates the afterglow at early times (Blustin et al., 2006; Shao & Dai, 2005).

Our early radio data offer some additional evidence in support of an extra emission component at early times. The observed radio flux at $22.5\,\mathrm{GHz}$ in our first two epochs ($t \lesssim 3\,\mathrm{d}$) is significantly in excess of our forward shock models (see Figure 4.1). If we assume the reverse shock peak frequency, ν_m^r, passes through the radio bands sometime between our initial radio observation and $t \sim 6\,\mathrm{d}$, we find the reverse shock
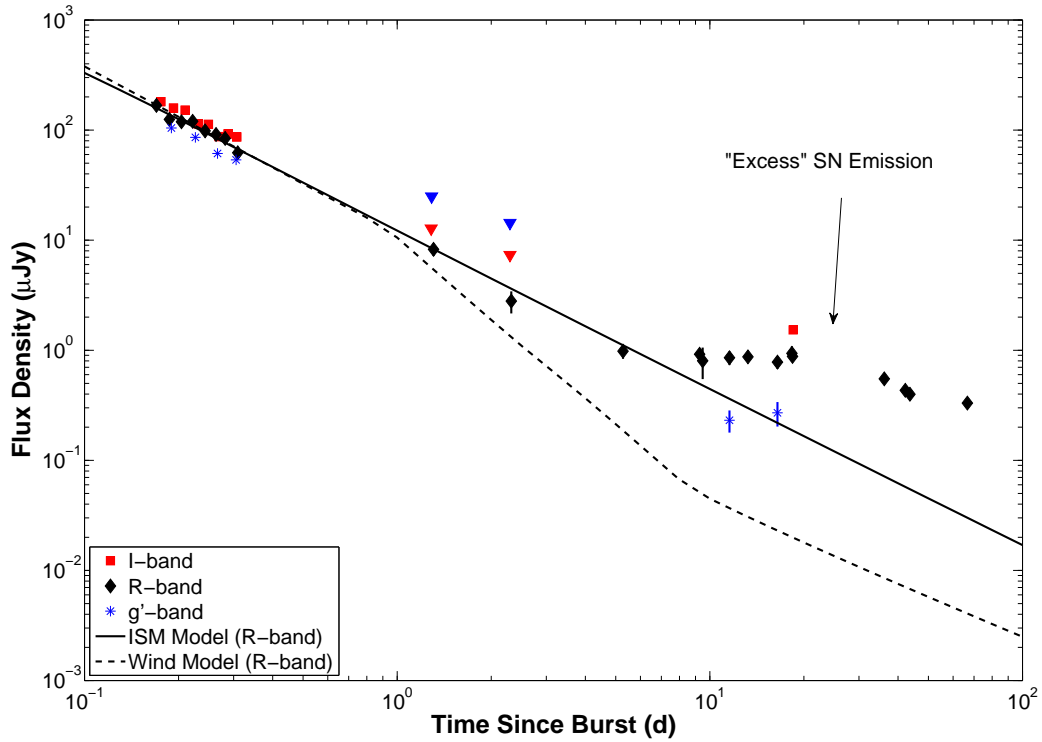
Figure 4.2 — Forward shock models of the afterglow of GRB 050525A — Optical. The ISM provides a better fit in the optical bands due to the early jet break ($t \sim 1\,\mathrm{d}$) required in the wind-like model. The late-time bump in optical light curve is due to an associated SN.

emission should peak in the optical sometime between 0.6–10 min after the trigger (this result is valid both for the thin- and thick-shell cases, as both predict the peak flux frequency to scale in time roughly as $\nu_m^r \propto t^{-3/2}$; Kobayashi, 2000). However no bright optical flare is seen in V-band images beginning only 66 s after the burst trigger (Blustin et al., 2006).

This does not entirely rule out a reverse shock origin, however. The radio spectrum at early times is optically thick with a steep power-law index of $\beta = 1.8 \pm 0.4$. This result implies synchrotron self-absorption may play some role in suppressing the radio flux at early times. Without additional data no firm conclusions can be reached on the origin of the excess emission at early times.
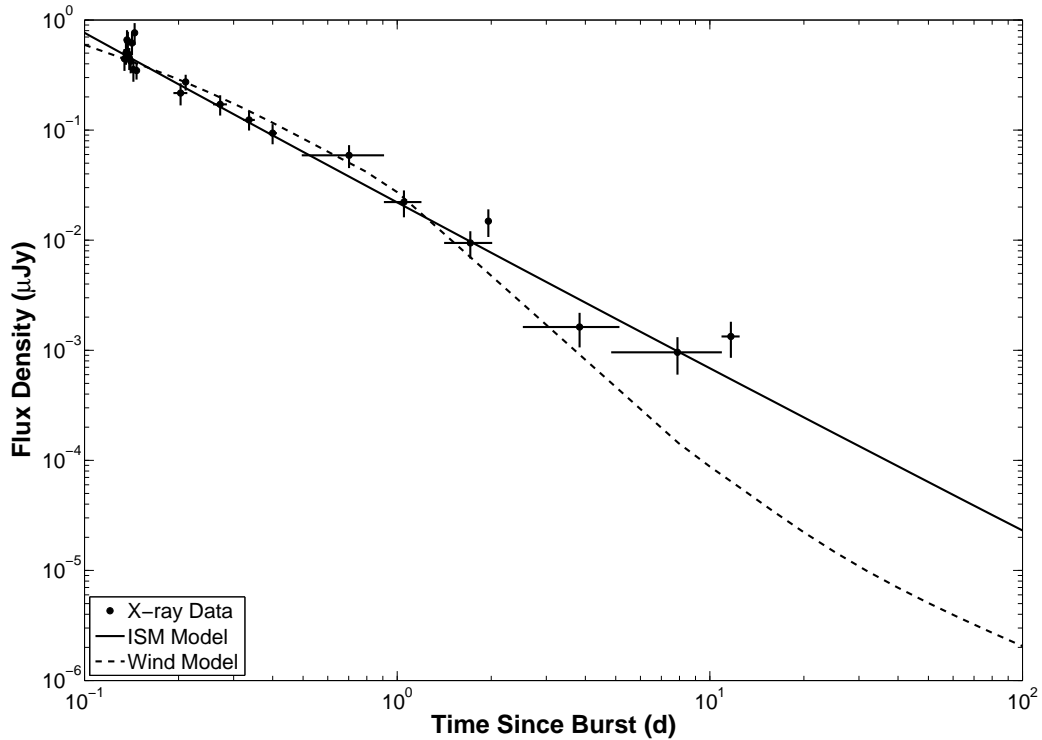
Figure 4.3 — Forward shock models of the afterglow of GRB 050525A — X-ray. Much like the optical, the early jet break required in the wind-like model provides a poorer fit in the X-ray bandpass.

4.3.1.2 Forward Shock Models

Given the possibility of reverse shock emission at early times (Section 4.3.1.1), coupled with the late-rising supernova component (Section 4.3.1.3), the forward shock emission is only expected to dominate the afterglow over a finite range of time. To remove the reverse shock contribution, we have excluded all early X-ray ($t < 0.1\,\mathrm{d}$), optical ($t < 0.1\,\mathrm{d}$), and radio ($t < 3\,\mathrm{d}$) observations from our forward shock model fits. We note that the different exclusion regions are necessary due to the frequency dependent evolution of the reverse shock. Likewise, emission from the supernova should dominate in the optical bandpass at late times ($t \gtrsim 5\,\mathrm{d}$), but the X-ray and radio emission at these times are still expected to derive from the forward shock.

Given these constraints, our resulting broadband fits are displayed in Figures 4.1–4.3 and Table 4.1. Like Blustin et al. (2006), we find the ISM model is favored over

Table 4.1. GRB 050525A Forward Shock Best Fit Parameters

Model	$E_{\rm KE,iso}$ $(10^{52}\,{\rm erg})$	$n^{\rm a}$ $({\rm cm}^{-3})$	ϵ_e	ϵ_B %	θ $(°)$	p	A_V(host) (mag)	$\chi^2_{\rm r}$ (d.o.f.)
ISM-like[b]	$3.9^{+1.0}_{-0.3}$	$0.036^{+0.013}_{-0.008}$	$0.71^{+0.06}_{-0.08}$	$19.3^{+1.8}_{-6.1}$	$180^{\rm d}$	2.04 ± 0.01	$0.19^{+0.06}_{-0.04}$	0.97 (63)
Wind-like[c]	$2.1^{+1.0}_{-0.4}$	$5.0^{+2.2}_{2.0}$	$0.52^{0.13}_{-0.12}$	$0.044^{+0.004}_{-0.024}$	$13.4^{+2.3}_{-1.5}$	$2.05^{+0.04}_{-0.01}$	$< 10^{-4{\rm e}}$	1.67 (63)

[a]For a wind-like medium, the density parameter is better known as A_*, where $\rho \equiv 5 \times 10^{11} A_* r^{-2}$.

[b]For an ISM-like medium, $\rho \propto r^0$.

[c]For a wind-like medium, $\rho \propto r^{-2}$.

[d]Including a collimation-correction did not improve the the model fits. We therefore assume isotropy.

[e]We could only calculate an upper limit for the host extinction.

the wind-like environment ($\chi^2_{\rm r} = 0.97$ for the ISM model, compared to $\chi^2_{\rm r} = 1.67$ for the wind model), a result difficult to reconcile with the massive star progenitor implied by the supernova detection. In both models, the electron partition factor, ϵ_e, falls well above its equipartition value of 1/3. With the exception of the opening angle for the ISM case, the remaining derived parameters are in reasonable agreement with previous broadband studies of GRB afterglows (Panaitescu & Kumar, 2002; Yost et al., 2003).

Blustin et al. (2006) attribute a steepening of the optical and X-ray decay at $t \sim 0.15\,{\rm d}$ to a jet break, and use this to derive an opening angle of $\theta = 3.2°$. We find this result is inconsistent with our data, particularly in the radio bandpass. For instance, in the constant density model, such a narrowly collimated outflow would imply a rapid decline in the radio light curve after $t_{\rm j}$. The observed radio flux, however, remains relatively constant over the first month (Figure 4.1).

Surprisingly, we find no need for a collimated outflow in the ISM case. Without any collimation correction, the energy release in both the prompt γ-rays and the afterglow would be well in excess of $10^{52}\,{\rm erg}$, an order of magnitude larger than typical pre-*Swift* events (Frail et al., 2001; Berger et al., 2003a). Including the contribution of the associated SN emission (Section 4.3.1.3) results in a staggering electromagnetic energy release approaching $10^{53}\,{\rm erg}$, a value difficult to reconcile with the collapse of even the most massive star progenitor.

Alternatively, the best-fit model for the wind-like medium results in a relatively early jet break ($t_j \approx 1\,\mathrm{d}$), with a correspondingly modest opening angle: $\theta = 13.4^{+2.3}_{-1.5}°$. The early jet break is required in the wind case to suppress the radio emission at $t \sim 40\,\mathrm{d}$. The corresponding collimation-corrected energy release in both γ-rays ($E_\gamma = 5.6^{+2.4}_{-1.4} \times 10^{50}\,\mathrm{erg}$) and the afterglow ($E_{\mathrm{KE}} = 5.7^{+5.9}_{-2.0} \times 10^{50}\,\mathrm{erg}$) are much more in line with previously observed GRBs. However, the resulting fit to the post-jet break optical and X-ray light curves is much worse than the constant density medium, as neither shows evidence for a steepening at $t \sim 1\,\mathrm{d}$ (Figures 4.2–4.3).

Finally, we note that both the ISM and wind-like environments require a relatively large efficiency in converting blast wave kinetic energy into prompt emission: $\eta_\gamma \equiv E_\gamma/(E_\gamma + E_{\mathrm{KE}}) \approx 0.5$. While the internal shock model widely believed to account for the prompt emission predicts significantly lower efficiencies ($\eta_\gamma \lesssim 0.1$; Kobayashi et al., 1997; Daigne & Mochkovitch, 1998), a similar result has been obtained for many GRBs to date (e.g., Chandra et al., 2008).

4.3.1.3   Supernova Emission

In Figure 4.4 we plot the late-time ($t > 2\,\mathrm{d}$) R-band light curve of GRB 050525A. It is clear that the forward shock power-law decay significantly underestimates the late-time flux (solid black line), even accounting for the constant host galaxy contribution (dashed black line). Such a late-time red bump has been seen in many relatively nearby ($z \lesssim 0.7$) GRB afterglow light curves (Zeh et al., 2004), and is believed to be caused by an associated underlying SN. In the case of GRB 050525A, the associated supernova has been named SN 2005nc (Valle et al., 2006b).

We compare the late-time emission from GRB 050525A with the prototypical GRB-associated SN, GRB 980425/SN 1998bw (Galama et al., 1998), in Figure 4.4 (dashed blue line). Even after correcting for Galactic extinction and applying a k-correction to transform SN 1998bw to $z = 0.606$, we find SN 2005nc is significantly fainter than SN 1998bw. Including both the forward shock afterglow and constant host galaxy flux components, we find a reasonable fit to the observed light curve if SN 2005nc is $\approx 0.6\,\mathrm{mag}$ fainter than SN 1998bw (Figure 4.4, solid red line). From our
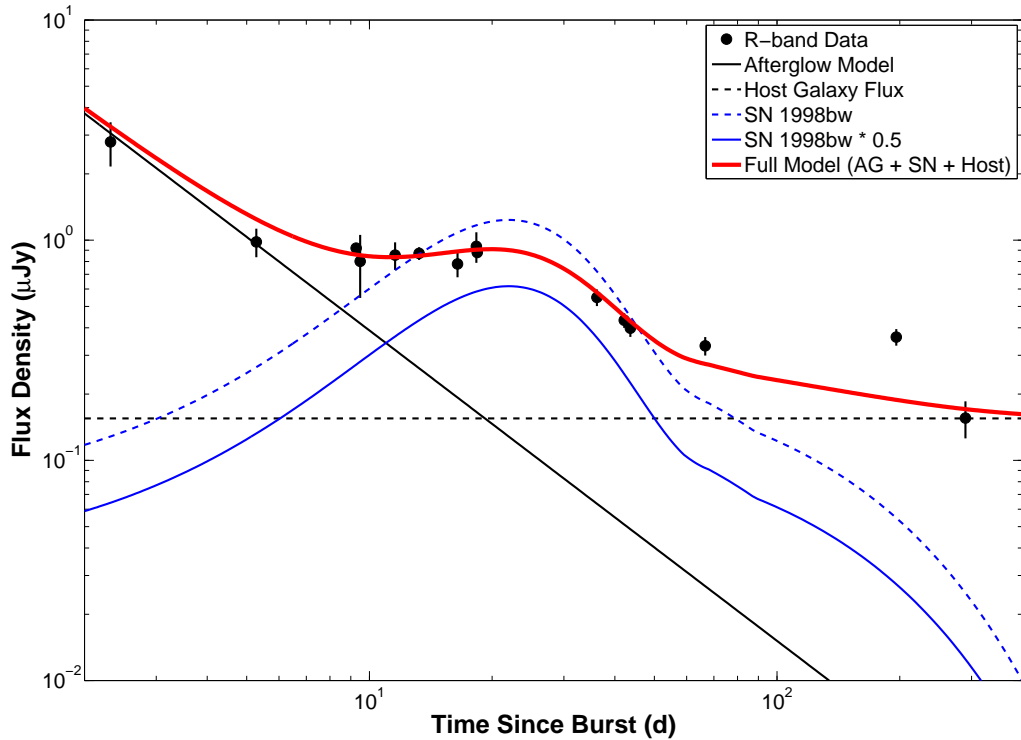
Figure 4.4 — SN 2005nc associated with GRB 050525A. The late-time light curve of GRB 050525A shows a significant excess over the power-law afterglow decay (*black solid line*). This bump can be well fitted by including a contribution from an underlying SN (SN 2005nc; Valle et al., 2006b). The light curve of SN 1998bw (Galama et al., 1998), redshifted to $z = 0.606$, is clearly too bright to fit the observed data (*dashed blue line*). Dimming SN 1998bw by ≈ 0.6 mag (*solid blue line*), together with the afterglow and host galaxy (*dashed black line*) contribution, provide a a reasonable fit to the observed data (*solid red line*).

afterglow modeling it appears as though the host galaxy extinction is relatively small $[A_V(\text{host}) \lesssim 0.2\,\text{mag}]$, and so the faintness is an intrinsic property of SN 2005nc.

4.3.2   GRB 060418

GRB 060418 was discovered by *Swift* at 03:06:48 UT on 2005 April 18 (Falcone et al., 2006a). At a redshift of $z = 1.490$ (Vreeswijk et al., 2007), the total isotropic energy release in the rest-frame 1 keV–10 MeV bandpass was $1.0^{+0.7}_{-0.2} \times 10^{53}$ erg (Butler et al., 2007). We began observing the bright optical afterglow of GRB 060418 with P60 as
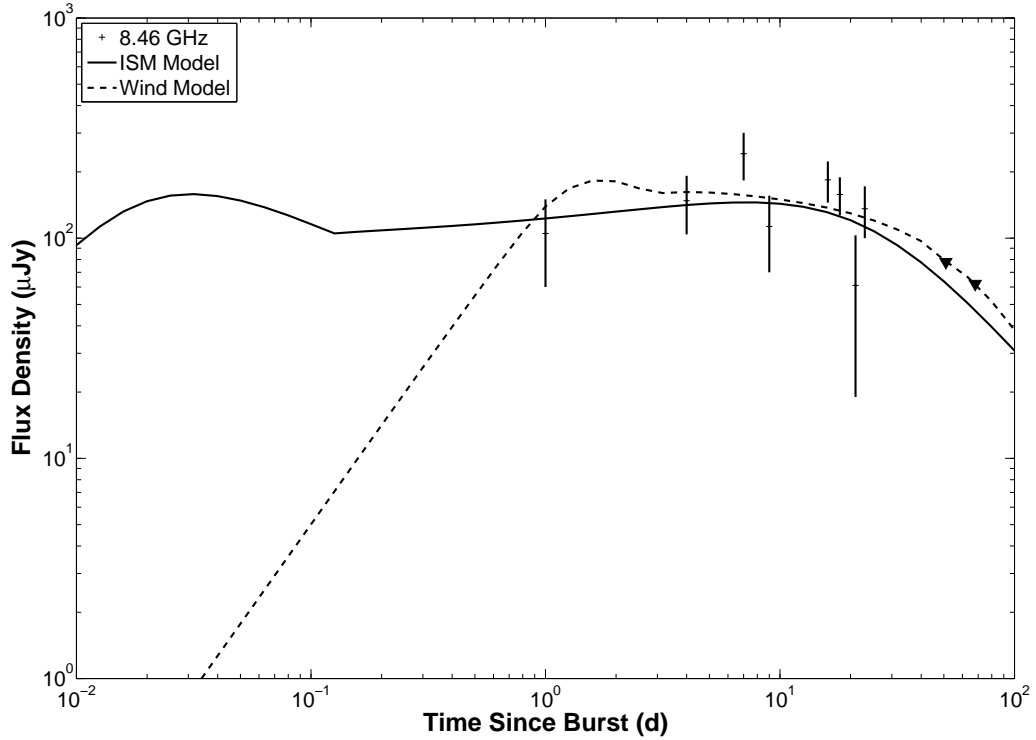
Figure 4.5 — Forward shock models of the afterglow of GRB 060418 — Radio. While the ISM and wind-like environment predict different radio fluxes at early times, our data are not sufficient to distinguish between the two competing models.

soon as it was visible at Palomar Observatory (several hours after the trigger). Our broadband observations of GRB 060418 are shown in Figures 4.5–4.7.

The most striking feature in the light curve is the bright X-ray flare at $t \approx 300\,\mathrm{s}$. Such flares have been reported in a large fraction of *Swift* XRT light curves (Falcone et al., 2007), and are widely believed to be caused by late-time energy injection from the central engine (Zhang et al., 2006). These X-ray flares can in some cases contribute a significant fraction of the prompt energy release to the total energy budget, and therefore have a large effect on the post-flare decay (Falcone et al., 2007). Rapid variability in the X-ray light curve of GRB 060418, inconsistent with standard afterglow models, is seen as late as several hours after the burst. Like GRB 050525A, we therefore only include observations at $t \gtrsim 0.1\,\mathrm{d}$ in our broadband modeling analysis.
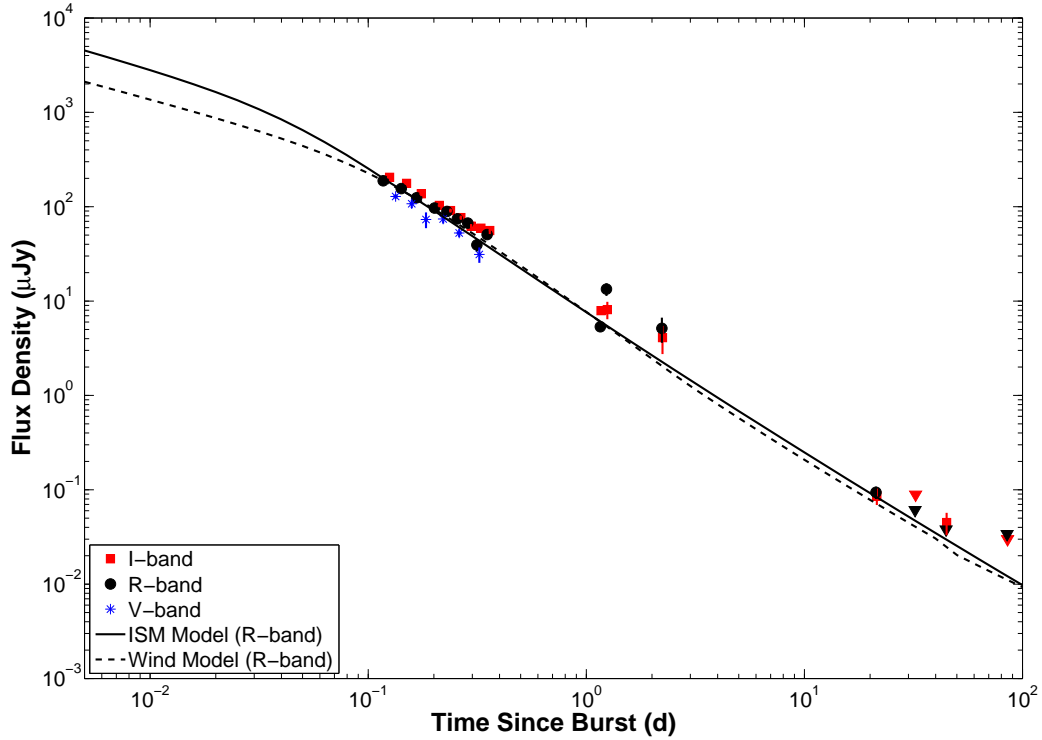
Figure 4.6 — Forward shock models of the afterglow of GRB 060418 — Optical. Because the cooling frequency falls below the optical bandpass, the model fits for the constant density and wind-like media are nearly identical.

The resulting fits and best-fit parameters are shown in Figures 4.5–4.7 and Table 4.2. The overall fit quality for both the ISM- and wind-like medium is reasonable, with the wind-like medium marginally favored ($\chi_r^2 = 1.24$ for the wind-like medium compared with $\chi_r^2 = 1.48$ for the constant density medium).

Unlike most previously modeled afterglows (c.f., GRB 050904; Frail et al., 2006), our results indicate the electron cooling frequency, ν_c, fell below the optical bands over the duration of our observations. The forward shock emission above ν_c is independent of the circumburst medium profile, leading to indistinguishable fits in the X-ray and optical bandpasses. While the radio behavior is divergent at early times, our observations are not sufficient to conclusively distinguish between the two models.

We note that projecting the model flux back to the time immediately following X-ray flare ($t \sim 10^{-2}$ d) significantly over-predicts the X-ray flux. This is not entirely
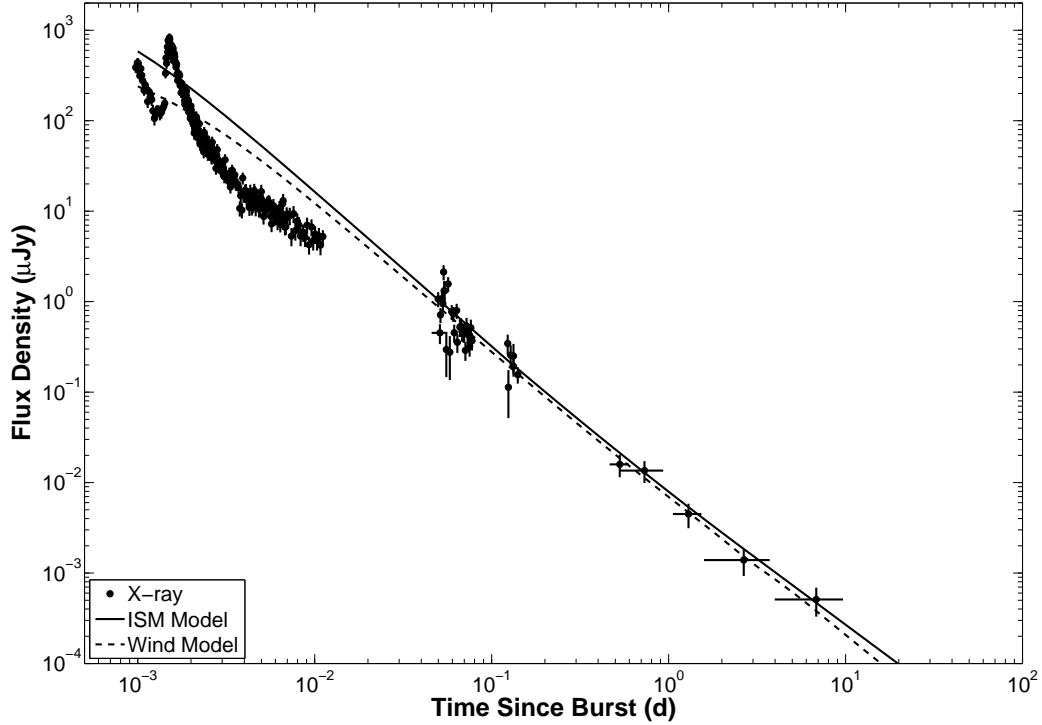
Figure 4.7 — Forward shock models of the afterglow of GRB 060418 — X-ray. Much like the optical, the models fits are nearly identical in the X-ray bandpass.

unexpected, as the X-ray flare is impulsively injecting a significant amount of energy into the outgoing shock. While the power-law decay underlying this flare is quite difficult to ascertain, it does appear the decay has undergone some steepening in the time between $10^{-2}\,\mathrm{d} \lesssim t \lesssim 5 \times 10^{-1}\,\mathrm{d}$. If so, it would be difficult for our forward shock model to account for this.

Again we find an isotropic outflow is favored in the constant density case for GRB 060418. The energy requirements here are even more severe than for GRB 050525A, with the total electromagnetic energy release well in excess of $10^{53}\,\mathrm{erg}$.

Alternatively, in the wind-like environment, the energy requirement is significantly relaxed. Given the opening angle of $\theta = 37.9^{+1.6}_{-6.3}\,^{\circ}$, the prompt emission energy release from GRB 060418 was $E_\gamma = 2.1^{+1.8}_{-0.9} \times 10^{52}\,\mathrm{erg}$, while the kinetic energy powering the afterglow was $E_{\mathrm{KE}} = 3.2^{+1.4}_{-1.6} \times 10^{50}\,\mathrm{erg}$. The primary drawback of the wind-like scenario, however, is the extremely high γ-ray efficiency. Somehow the physical

Table 4.2.   GRB 060418 Forward Shock Best Fit Parameters

Model	$E_{\rm KE, iso}$ $(10^{52}\,{\rm erg})$	$n^{\rm a}$ $({\rm cm}^{-3})$	ϵ_e	ϵ_B (%)	θ (°)	p	A_V(host) (mag)	$\chi_{\rm r}^2$ (d.o.f.)
ISM-like[b]	$34.7^{+9.0}_{-6.8}$	$2.2^{+1.0}_{-0.4}$	$0.75^{+0.05}_{-0.04}$	$0.023^{+0.005}_{0.012}$	$180^{\rm d}$	$2.13^{+0.04}_{-0.01}$	$0.22^{+0.04}_{-0.08}$	1.48 (56)
Wind-like[c]	$0.15^{+0.05}_{-0.04}$	$0.34^{+0.06}_{-0.12}$	$0.54^{+0.04}_{-0.05}$	$7.0^{+8.9}_{-2.2}$	$37.9^{+1.6}_{-6.3}$	$2.19^{+0.03}_{-0.05}$	$< 10^{-4{\rm e}}$	1.24 (56)

[a]For a wind-like medium, the density parameter is better known as A_*, where $\rho \equiv 5 \times 10^{11} A_* r^{-2}$.

[b]For an ISM-like medium, $\rho \propto r^0$.

[c]For a wind-like medium, $\rho \propto r^{-2}$.

[d]Including a collimation correction did not improve the the model fits. We therefore assume isotropy.

[e]We could only calculate an upper limit for the host extinction.

process generating the prompt emission must have been capable of converting $\approx 98\%$ of the outgoing blast wave energy to γ-rays, while most internal shock models predict a maximum γ-ray efficiency of $\sim 10\%$ (Kobayashi et al., 1997; Daigne & Mochkovitch, 1998).

4.4   Discussion

In Section 4.3, we showed that both GRB 050525A and GRB 060418 can be fit reasonably well in the context of the standard afterglow model, with best-fit physical parameters mostly consistent with results found for pre-*Swift* GRBs (Panaitescu & Kumar, 2002; Yost et al., 2003). While the afterglow of GRB 060418 favors a wind-like environment, GRB 050525A fit much better to a constant density medium. Given the emergence of late-time SN emission (Section 4.3.1.3) from this relatively nearby event, we would on the contrary expect evidence of progenitor mass loss to manifest itself in the afterglow light curves.

One possibility to explain this behavior may be the distance scale probed by afterglow observations. The relativistic outflow powering GRB afterglow emission quickly sweeps up the material immediately surrounding the progenitor star, and most of the emitting electrons at the forward shock front are located at a distance $r \gtrsim 0.1\,{\rm pc}$ from the explosion (e.g., Piran, 2005). The sub-relativistic outflow probed

by radio emission from non-GRB SNe shows clear evidence of pre-explosion progenitor mass loss (e.g., Soderberg et al., 2006b). Because of the lower Lorentz factor of the outflow, such observations are sensitive to emission from regions significantly closer to the explosion site, where signatures of progenitor mass loss should be stronger.

Even more troubling for these two events, however, are the energetic implications of a constant density environment. The lack of achromatic jet breaks in the *Swift* era has been well documented (e.g., Burrows & Racusin, 2007; Panaitescu, 2007; Liang et al., 2008). Neither GRB 050525A nor GRB 060418 shows any sign of a jet break out to late times in any bandpass. In fact our modeling does not even lead to any useful constraints on the opening angle for either event in the ISM case; both best-fit models suggest a fully isotropic explosion. The energetics implied by a lack of collimation (Kocevski & Butler, 2007) are difficult to reconcile with the "collapsar" model (Woosley, 1993).

In Figure 4.8 we plot the energy release in the prompt emission (E_γ) against the kinetic energy powering the afterglow (E_{KE}) for all previous GRBs with broadband modeling fits. With the exception of the most nearby, under-luminous events, the total energy release from most pre-*Swift* events is clustered around 2×10^{51} erg (Soderberg et al., 2004). In the *Swift* era, we have seen evidence for an emerging class of "hyper-energetic" GRBs; i.e., $E_{\mathrm{tot}} \equiv E_\gamma + E_{\mathrm{KE}} > 10^{52}$ erg. Both GRB 050525A and GRB 060418 would qualify as hyper-energetic events in the constant density environment models. In fact GRB 060418 would be the most energetic GRB ever reported.

Alternatively, in both cases the wind model greatly eases the total energy requirements (Figure 4.8). Even though in some cases the ISM seems to provide a better fit, our model uncertainties are still a relatively large unknown in our analysis. We may therefore in fact be over-estimating the total energy release of some events by assuming a constant density environment. But while this would bring the total energy release from GRB 050525A in line with previous pre-*Swift* events, GRB 060418 remains solidly above the hyper-energetic threshold.

With GRB 060418, we now have found 4 *Swift* events with total energy release in excess of 10^{52} erg: GRB 070125 (Chandra et al., 2008), GRB 050904 (Frail et al., 2006),
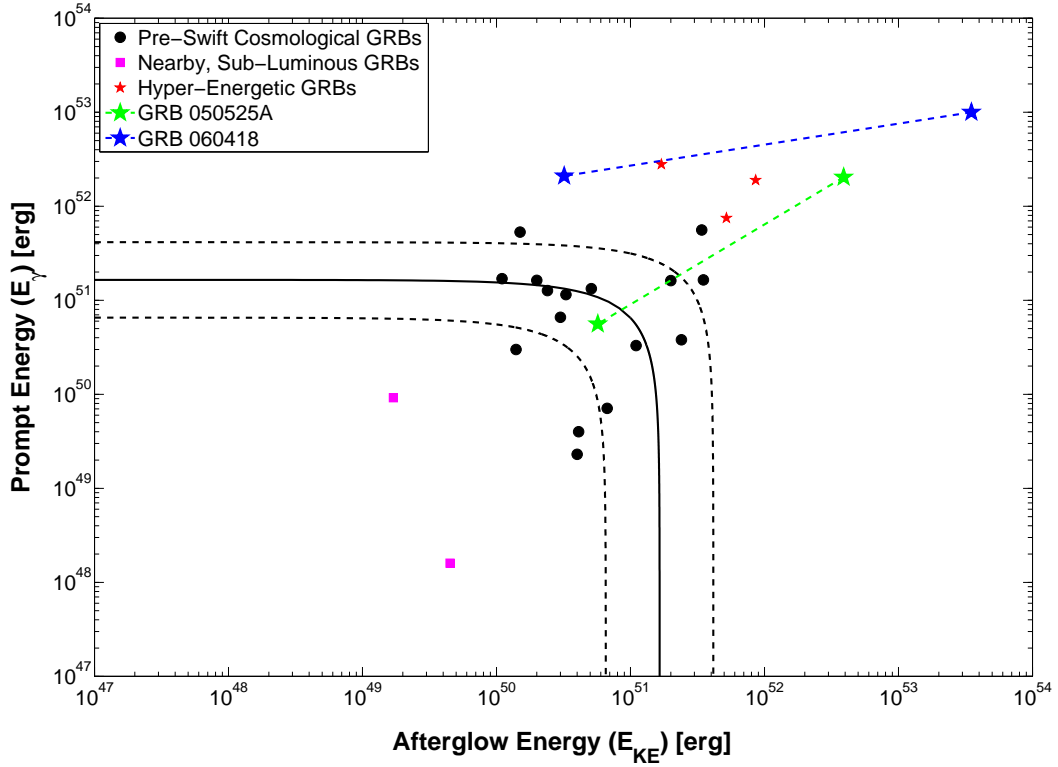
Figure 4.8 — GRB energetics in the *Swift* era. Pre-*Swift* cosmological ($z \lesssim 0.3$) GRBs showed a total relativistic energy release ($E_\gamma + E_{\mathrm{KE}}$) clustered around 2×10^{51} erg (Soderberg et al., 2004; *solid line*). The most nearby events appear to be several orders of magnitude less energetic. Our results for the ISM and wind-like media for GRB 050525A (*green stars*) and GRB 060418 (*blue stars*) are also shown. For a wind-like environment, the total energy release of GRB 050525A is on par with pre-*Swift* events. GRB 060418, on the other hand, appears to be "hyper-energetic" ($E > 10^{52}$ erg) regardless of the circumburst environment. This makes it the fourth such over-luminous event discovered by *Swift*.

and GRB 050820A (Cenko et al., 2006b). While both GRB 050904 and GRB 070125 appear to have exploded in an extremely dense circumburst environment, the inferred densities for GRB 050820A and GRB 060418 are more typical of pre-*Swift* events. Moreover, with the exception of the total energy release, other parameters derived from broadband modeling are in line with previous studies of less energetic GRBs (Panaitescu & Kumar, 2002; Yost et al., 2003). It seems likely, therefore, that some factor intrinsic to the progenitor system is responsible for the large energy release.

At first blush, it seems surprising that *Swift* has detected 4 of the most energetic

GRBs ever. With its increased high-energy sensitivity, *Swift* should preferentially select GRBs at the low end of the luminosity distribution. We note, however, that a strong selection bias exists. As first noted by Kocevski & Butler (2007), in many *Swift* X-ray light curves, the last XRT measurement is not sufficient to rule out a collimation-corrected prompt energy release of $\sim 10^{51}$ erg. Similarly, in the optical bandpass, Dai et al. (2007) have shown that at least some jet breaks occur at late times beyond the sensitivity of medium aperture facilities.

While a detailed discussion of the relative rates of hyper-energetic events is still premature, it is clear at this point that, at the very least, the prompt γ-ray energy distribution is significantly broader than previously believed (Kocevski & Butler, 2007). Coupled with the recent controversy surrounding the validity of the many high-energy correlations underpinning current efforts (Butler et al., 2007), we believe the future utility of GRBs as cosmological probes is significantly diminished.

Even more importantly, however, hyper-energetic GRBs have important consequences for progenitor models. Sustained engine activity has been seen now in many GRBs. This poses a problem for the collapsar model, as the duration of the central engine should not significantly exceed the accretion time scale onto the remnant black hole (Woosley, 1993). Late-time engine activity is naturally accommodated by models in which the central object is a magnetar (Usov, 1992). The existence of hyper-energetic GRBs, however, is a direct and severe challenge to the magnetar model.

With the current rate of hyper-energetic events ($\sim 1\,\mathrm{yr}^{-1}$), coupled with the difficulty in measuring late jet breaks for more typical *Swift* events, future prospects look grim. However, the impending launch of *GLAST* offers a new hope in the study of GRB energetics. Much like blazars, those GRBs capable of producing GeV photons detectable by the Large Area Telescope should be the most energetic and narrowly beamed events. Together, synergistic *GLAST* and *Swift* observations in the coming years should be able to shed light on the opening angles and energy release of a large sample of GRBs.

Table 4.3.   Optical Observations of GRB 050525A and GRB 060418

GRB Name	UT Date[a]	Telescope / Instrument	Time Since Burst[b] (s)	Filter	Exposure Time (s)	Magnitude
GRB 050525A	2005 May 25.1698	P60	1.467×10^4	R_C	360.0	18.38 ± 0.04
$\cdots$	2005 May 25.1754	P60	1.516×10^4	i	360.0	17.96 ± 0.06
$\cdots$	2005 May 25.1868	P60	1.615×10^4	R_C	360.0	18.70 ± 0.06
$\cdots$	2005 May 25.1875	P60	1.638×10^4	g	720.0	19.19 ± 0.11
$\cdots$	2005 May 25.1925	P60	1.664×10^4	i	360.0	18.11 ± 0.06
$\cdots$	2005 May 25.2041	P60	1.764×10^4	R_C	360.0	18.75 ± 0.05
$\cdots$	2005 May 25.2098	P60	1.814×10^4	i	360.0	18.16 ± 0.05
$\cdots$	2005 May 25.2217	P60	1.916×10^4	R_C	360.0	18.74 ± 0.05
$\cdots$	2005 May 25.2242	P60	1.956×10^4	g	720.0	19.41 ± 0.11
$\cdots$	2005 May 25.2311	P60	1.997×10^4	i	360.0	18.47 ± 0.06
$\cdots$	2005 May 25.2431	P60	2.101×10^4	R_C	360.0	18.96 ± 0.05
$\cdots$	2005 May 25.2490	P60	2.152×10^4	i	360.0	18.48 ± 0.06
$\cdots$	2005 May 25.2634	P60	2.276×10^4	R_C	360.0	19.04 ± 0.06
$\cdots$	2005 May 25.2642	P60	2.301×10^4	g	720.0	19.77 ± 0.11
$\cdots$	2005 May 25.2694	P60	2.328×10^4	i	360.0	18.76 ± 0.08
$\cdots$	2005 May 25.2817	P60	2.435×10^4	R_C	360.0	19.13 ± 0.05
$\cdots$	2005 May 25.2879	P60	2.488×10^4	i	360.0	18.70 ± 0.06
$\cdots$	2005 May 25.3032	P60	2.638×10^4	g	720.0	19.92 ± 0.11
$\cdots$	2005 May 25.3077	P60	2.672×10^4	R_C	600.0	19.46 ± 0.05
$\cdots$	2005 May 25.3067	P60	2.651×10^4	i	360.0	18.77 ± 0.07
$\cdots$	2005 May 26.2863	P60	1.126×10^5	i	3240.0	> 21.6
$\cdots$	2005 May 26.2883	P60	1.129×10^5	R_C	3600.0	21.65 ± 0.13
$\cdots$	2005 May 26.2912	P60	1.130×10^5	g	3240.0	> 21.5

Table 4.3 (cont'd)

GRB Name	UT Date[a]	Telescope / Instrument	Time Since Burst[b] (s)	Filter	Exposure Time (s)	Magnitude
$\cdots$	2005 May 27.2917	P60	2.002×10^5	R_C	4680.0	22.82 ± 0.22
$\cdots$	2005 May 27.2972	P60	2.005×10^5	g	4320.0	> 22.1
$\cdots$	2005 May 27.2979	P60	2.007×10^5	i	4680.0	> 22.2
$\cdots$	2005 Jun 3.4886	Keck / LRIS	8.198×10^5	B_C	300.0	> 24.9
$\cdots$	2005 Jun 3.4908	Keck / LRIS	8.200×10^5	R_C	600.0	24.18 ± 0.30
$\cdots$	2005 Jun 5.5586	Keck / LRIS	9.986×10^5	R_C	600.0	24.11 ± 0.15
$\cdots$	2005 Jun 5.5586	Keck / LRIS	9.986×10^5	g'	600.0	25.83 ± 0.31
$\cdots$	2005 Jun 10.4518	Keck / LRIS	1.421×10^6	R_C	600.0	24.21 ± 0.13
$\cdots$	2005 Jun 10.4518	Keck / LRIS	1.421×10^6	g'	600.0	25.66 ± 0.29
$\cdots$	2005 Jun 12.3909	HST / ACS	1.589×10^6	R_C	3332.0	24.08 ± 0.05
$\cdots$	2005 Jun 12.4743	HST / ACS	1.596×10^6	I_C	3414.0	23.15 ± 0.05
$\cdots$	2005 Jul 7.6579	HST / ACS	3.772×10^6	R_C	4268.0	24.94 ± 0.09
$\cdots$	2005 Jul 30.6460	HST / ACS	5.758×10^6	R_C	4268.0	25.14 ± 0.10
$\cdots$	2006 Mar 10.8256	HST / ACS	2.503×10^7	I_C	4268.0	25.01 ± 0.12
$\cdots$	2006 Mar 10.8256	HST / ACS	2.504×10^7	R_C	4268.0	25.96 ± 0.19
GRB 060418	2006 Apr 18.2429	P60	1.011×10^4	R_C	600.0	18.61 ± 0.07
$\cdots$	2006 Apr 18.2511	P60	1.083×10^4	i'	600.0	18.59 ± 0.18
$\cdots$	2006 Apr 18.2593	P60	1.153×10^4	V_C	600.0	19.36 ± 0.09
$\cdots$	2006 Apr 18.2675	P60	1.224×10^4	R_C	600.0	18.82 ± 0.08
$\cdots$	2006 Apr 18.2757	P60	1.295×10^4	i'	600.0	18.75 ± 0.20
$\cdots$	2006 Apr 18.2841	P60	1.368×10^4	V_C	600.0	19.55 ± 0.12
$\cdots$	2006 Apr 18.2924	P60	1.440×10^4	R_C	600.0	19.06 ± 0.14
$\cdots$	2006 Apr 18.3009	P60	1.513×10^4	i'	600.0	19.03 ± 0.20

Table 4.3 (cont'd)

GRB Name	UT Date[a]	Telescope / Instrument	Time Since Burst[b] (s)	Filter	Exposure Time (s)	Magnitude
$\cdots$	2006 Apr 18.3098	P60	1.590×10^4	$V_{\rm C}$	600.0	19.97 ± 0.21
$\cdots$	2006 Apr 18.3271	P60	1.740×10^4	$R_{\rm C}$	600.0	19.34 ± 0.09
$\cdots$	2006 Apr 18.3376	P60	1.830×10^4	i'	600.0	19.34 ± 0.19
$\cdots$	2006 Apr 18.3465	P60	1.907×10^4	$V_{\rm C}$	600.0	19.95 ± 0.12
$\cdots$	2006 Apr 18.3553	P60	1.983×10^4	$R_{\rm C}$	600.0	19.43 ± 0.10
$\cdots$	2006 Apr 18.3642	P60	2.059×10^4	i'	600.0	19.47 ± 0.19
$\cdots$	2006 Apr 18.3821	P60	2.215×10^4	$R_{\rm C}$	600.0	19.62 ± 0.11
$\cdots$	2006 Apr 18.3837	P60	2.258×10^4	$V_{\rm C}$	1200.0	20.32 ± 0.12
$\cdots$	2006 Apr 18.3917	P60	2.297×10^4	i'	600.0	19.66 ± 0.19
$\cdots$	2006 Apr 18.4118	P60	2.471×10^4	$R_{\rm C}$	600.0	19.73 ± 0.12
$\cdots$	2006 Apr 18.4222	P60	2.561×10^4	i'	600.0	19.89 ± 0.19
$\cdots$	2006 Apr 18.4408	P60	2.722×10^4	$R_{\rm C}$	600.0	20.31 ± 0.16
$\cdots$	2006 Apr 18.4456	P60	2.793×10^4	$V_{\rm C}$	1200.0	20.89 ± 0.20
$\cdots$	2006 Apr 18.4544	P60	2.839×10^4	i'	600.0	19.94 ± 0.19
$\cdots$	2006 Apr 18.4767	P60	3.031×10^4	$R_{\rm C}$	600.0	20.04 ± 0.12
$\cdots$	2006 Apr 18.4864	P60	3.116×10^4	i'	600.0	20.00 ± 0.20
$\cdots$	2006 Apr 19.3560	P60	1.069×10^5	$R_{\rm C}$	1800.0	21.48 ± 0.17
$\cdots$	2006 Apr 19.3669	P60	1.078×10^5	i'	1800.0	22.10 ± 0.27
$\cdots$	2006 Apr 19.3782	P60	1.088×10^5	$V_{\rm C}$	1800.0	> 21.4
$\cdots$	2006 Apr 20.3405	P60	1.919×10^5	$R_{\rm C}$	1800.0	22.52 ± 0.29
$\cdots$	2006 Apr 20.3535	P60	1.931×10^5	i'	1800.0	22.84 ± 0.36
$\cdots$	2006 Apr 19.2870	P200 / LFC	1.002×10^5	r'	300.0	22.08 ± 0.07
$\cdots$	2006 Apr 19.2954	P200 / LFC	1.009×10^5	i'	300.0	21.65 ± 0.13

Table 4.3 (cont'd)

GRB Name	UT Date[a]	Telescope / Instrument	Time Since Burst[b] (s)	Filter	Exposure Time (s)	Magnitude
$\cdots$	2006 Apr 19.3033	P200 / LFC	1.016×10^5	z'	300.0	21.47 ± 0.09
$\cdots$	2006 Apr 19.3122	P200 / LFC	1.024×10^5	g'	300.0	22.73 ± 0.07
$\cdots$	2006 May 9.4161	*HST* / ACS	1.839×10^6	$R_{\rm C}$	4220.0	26.89 ± 0.15
$\cdots$	2006 May 9.6130	*HST* / ACS	1.856×10^6	$I_{\rm C}$	4220.0	26.54 ± 0.19
$\cdots$	2006 May 20.2953	*HST* / ACS	2.779×10^6	$R_{\rm C}$	5500.0	> 27.3
$\cdots$	2006 May 20.4926	*HST* / ACS	2.796×10^6	$I_{\rm C}$	3700.0	> 26.5
$\cdots$	2006 Jun 1.7528	*HST* / ACS	3.855×10^6	$R_{\rm C}$	8772.0	> 27.8
$\cdots$	2006 Jun 2.0193	*HST* / ACS	3.879×10^6	$I_{\rm C}$	8772.0	27.25 ± 0.26
$\cdots$	2006 Jul 11.1211	*HST* / ACS	7.343×10^6	$R_{\rm C}$	8772.0	> 27.9
$\cdots$	2006 Jul 12.5207	*HST* / ACS	7.378×10^6	$I_{\rm C}$	8772.0	> 27.7

[a]UT at beginning of exposure.

[b]Time from mid-point of exposure to *Swift*-BAT trigger.

Table 4.4.   Radio Observations of GRB 050820A and GRB 060418

GRB Name	UT Date[a]	Time Since Burst[b] (d)	Frequency (GHz)	Flux Density[c] (μJy)
GRB 050525A	2005 May 25.44	0.44	4.86	97 ± 49
$\cdots$	2005 May 25.44	0.44	8.46	80 ± 34
$\cdots$	2005 May 25.44	0.44	22.5	558 ± 81
$\cdots$	2005 May 26.36	1.36	8.46	< 49
$\cdots$	2005 May 26.36	1.36	22.5	422 ± 108
$\cdots$	2005 May 28.33	3.33	8.46	164 ± 46
$\cdots$	2005 May 31.45	6.45	8.46	< 54
$\cdots$	2005 May 31.45	6.45	22.5	< 176
$\cdots$	2005 Jun 7.47	13.47	4.86	143 ± 82
$\cdots$	2005 Jun 7.47	13.47	8.46	88 ± 42
$\cdots$	2005 Jun 7.47	13.47	22.5	< 164
$\cdots$	2005 Jun 13.44	19.44	1.43	< 206
$\cdots$	2005 Jun 13.44	19.44	4.86	< 64
$\cdots$	2005 Jun 13.44	19.44	8.46	88 ± 42
$\cdots$	2005 Jun 17.54	23.54	4.86	91 ± 54
$\cdots$	2005 Jun 17.54	23.54	8.46	178 ± 46
$\cdots$	2005 Jun 28.48	34.48	4.86	152 ± 52
$\cdots$	2005 Jun 28.48	34.48	8.46	< 40
$\cdots$	2005 Jul 2.52	38.52	8.46	< 39
GRB 060418	2006 Apr 19.1	1.0	8.46	105 ± 45
$\cdots$	2006 Apr 22.1	4.0	8.46	148 ± 44
$\cdots$	2006 Apr 25.1	7.0	8.46	242 ± 59
$\cdots$	2006 Apr 27.1	9.0	8.46	113 ± 43
$\cdots$	2006 May 4.1	16.0	8.46	184 ± 39
$\cdots$	2006 May 6.1	18.0	8.46	158 ± 31
$\cdots$	2006 May 9.1	21.0	8.46	61 ± 42
$\cdots$	2006 May 11.1	23.0	8.46	136 ± 36
$\cdots$	2006 Jun 8.1	51.0	8.46	< 39
$\cdots$	2006 Jun 25.1	68.0	8.46	< 31

[a]UT at mid-point of exposure.

[b]Time from mid-point of exposure to *Swift*-BAT trigger.

[c]Upper limits are reported as 1 σ rms per beam area.

Part III

The Environments of *Swift* γ-Ray Bursts

Preamble

The association between massive stars and long-duration γ-ray bursts (GRBs) should be reflected in the environments of these powerful explosions. On the pc scale, the resulting wind from outer envelope mass loss should be discernible in the temporal evolution of the broadband afterglow. On larger (kpc) scales, the dense galactic disks where massive stars form should be revealed as strong absorption features in the rest-frame UV spectra, as well as dust extinction in broadband afterglow spectral energy distributions.

The following two chapters are dedicated primarily to the study of GRB environments. In Chapter 5, I find the global (i.e., kpc scale) environment of GRB 070125 is unlike any previous long-duration GRB, and is instead indicative of a halo origin. I speculate that GRB 070125 may have occurred far away from the disk of its host in a compact star-forming cluster. Such distant stellar clusters, typically formed by dynamical galaxy interactions, have been observed in the nearby universe, and should be more prevalent at $z > 1$, where galaxy mergers occur more frequently.

In Chapter 6, I construct a complete sample of all 29 *Swift* events observed by the automated Palomar 60 inch telescope (P60) within an hour after the burst trigger. I find nearly half of these events show a suppression of the optical flux with regards to the X-ray emission at early times ($t = 10^3$ s). Multi-color P60 photometry demonstrates this is in large part due to extinction in the GRB host galaxy. Such highly obscured GRBs have largely been missed by previous statistical studies of GRB optical afterglows, which focused predominantly on the brightest, best-sampled events.

Chapter 5 is taken from an article published in *The Astrophysical Journal* (Cenko et al., 2008), while the P60-*Swift* Early Optical Afterglow Catalog presented in Chapter 6 is currently being prepared for submission.

Chapter 5

GRB 070125: The First Long-Duration γ-Ray Burst in a Galaxy Halo

S. B. Cenko[a], D. B. Fox[b], B. E. Penprase[c], A. Cucchiara[b], P. A. Price[d], E. Berger[e,f], S. R. Kulkarni[g], F. A. Harrison[a], A. Gal-Yam[h], E. O. Ofek[g], A. Rau[g], P. Chandra[i], D. A. Frail[j], M. M. Kasliwal[g], B. P. Schmidt[k], A. M. Soderberg[g], P. B. Cameron[g], and K. C. Roth[l]

[a]Space Radiation Laboratory, MS 220-47, California Institute of Technology, Pasadena, CA 91125

[b]Department of Astronomy & Astrophysics, 525 Davey Laboratory, Pennsylvania State University, University Park, PA 16802

[c]Department of Physics and Astronomy, Pomona College, 610 North College Avenue, Claremont, CA 91711

[d]Institute for Astronomy, University of Hawai'i, 2680 Woodlawn Drive, Honolulu, HI 96822

[e]Observatories of the Carnegie Institute of Washington, 813 Santa Barbara Street, Pasadena, CA 91101

[f]Princeton University Observatory, Peyton Hall, Ivy Lane, Princeton, NJ 08544

[g]Department of Astronomy, Mail Stop 105-24, California Institute of Technology, Pasadena, CA 91125

[h]Astrophysics Group, Faculty of Physics, Weizmann Institute of Science, Rehovot 76100, Israel

[i]Department of Astronomy, University of Virginia, P.O. Box 3818, Charlottesville, VA 22903

[j]National Radio Astronomy Observatory, P.O. Box 0, 1003 Lopezville Road, Socorro, NM 87801

[k]Research School of Astronomy and Astrophysics, Australian National University, Mont Stromlo Observatory, Cotter Road, Weston Creek, Canberra ACT 2611, Australia

[l]Gemini Observatory, 670 North A'ohoku Place, Hilo, HI 96720

Abstract

We present the discovery and high signal-to-noise spectroscopic observations of the optical afterglow of the long-duration γ-ray burst GRB 070125. Unlike all previously observed long-duration afterglows in the redshift range $0.5 \lesssim z \lesssim 2.0$, we find no strong (rest-frame equivalent width $W_r \gtrsim 1.0\,\text{Å}$) absorption features in the wavelength range 4000–10000 Å. The sole significant feature is a weak doublet that we identify as Mg II $\lambda\lambda$ 2796 ($W_r = 0.18 \pm 0.02\,\text{Å}$), 2803 ($W_r = 0.08 \pm 0.01\,\text{Å}$) at $z = 1.5477 \pm 0.0001$. The low observed Mg II and inferred H I column densities are typically observed in galactic halos, far away from the bulk of massive star formation. Deep ground-based imaging reveals no host directly underneath the afterglow to a limit of $R > 25.4\,\text{mag}$. Either of the two nearest blue galaxies could host GRB 070125; the large offset ($d \geq 27\,\text{kpc}$) would naturally explain the low column densities. To remain consistent with the large local (i.e., parsec scale) circumburst density inferred from broadband afterglow observations, we speculate GRB 070125 may have occurred far away from the disk of its host in a compact star-forming cluster. Such distant stellar clusters, typically formed by dynamical galaxy interactions, have been observed in the nearby universe, and should be more prevalent at $z > 1$, where galaxy mergers occur more frequently.

5.1 Introduction

The connection between long-duration ($t_{90} \gtrsim 2$ s) γ-ray bursts (GRBs) and hydrogen-stripped, core-collapse supernovae (i.e., Type Ib/c SNe) is now well established in the nearby universe (e.g., Woosley & Bloom, 2006). At $z \gtrsim 0.3$, where the overwhelming majority of GRBs are detected (Berger et al., 2005a; Jakobsson et al., 2006b), Type Ib/c SNe are too faint, absorbed, and redshifted to be observed routinely with current facilities. Observations of the environments of distant GRBs, however, are consistent with a massive star origin. GRB hosts are typically faint, blue, irregular galaxies with large specific star-formation rates (star formation rate per unit stellar mass; Floc'h et al., 2003; Christensen et al., 2004). And within their hosts, GRB afterglows are found to be concentrated in the innermost regions, tracing the blue light from hot young stars even more strongly than Type Ib/c SNe (Bloom et al., 2002; Fruchter et al., 2006).

Bright GRB afterglows are therefore ideally suited to probe the dense gas in the very regions where stars are being formed. This stands in marked contrast to quasar (QSO) sight lines, which sample galaxies according to gas cross section and are therefore much more likely to probe the outer regions of galaxy halos (e.g., Prochaska et al., 2007b).

While the sample of afterglow absorption spectra suitable for elemental abundance studies is still quite small compared with QSOs, a general picture has nonetheless begun to take hold. GRB systems are characterized by 1) large metal equivalent widths and correspondingly large metal column densities (e.g., Metzger et al., 1997); 2) extremely high neutral hydrogen column densities (e.g., Hjorth et al., 2003a), typically falling at $\log N(\text{H \textsc{i}}) > 20.3$ (the so-called damped Ly-α systems, or DLAs; Wolfe et al., 2005); and 3) sub-solar metallicities, typically $Z \sim 0.1\,Z_{\odot}$ (e.g., Berger et al., 2006). All three findings are consistent with a massive star origin for long-duration GRBs.

Here we present observations of a long-duration event, GRB 070125, that does not fit neatly into this paradigm. Despite deep spectroscopy of a bright ($R \approx 19\,\text{mag}$)

afterglow, we detect only weak Mg II absorption at $z = 1.55$, a firm upper limit on the Mg II column density of the host galaxy. Coupled with the large offset between the afterglow and the nearest detected host galaxy candidate, our observations indicate the large-scale (i.e., ISM) burst environment is dramatically different from all previously observed GRB hosts.

5.2   Observations and Data Reduction

GRB 070125 was discovered by the Inter-Planetary Network at 07:20:45 UT on 2007 January 25 (Hurley et al., 2007). The burst was notable both for its brightness ($F_\gamma = 1.75^{+0.18}_{-0.15} \times 10^{-4}\,\mathrm{erg\,cm^{-2}}$; Golenetskii et al., 2007) and its long duration ($t_{90} \gtrsim$ 200 s; Hurley et al., 2007; Golenetskii et al., 2007). The well-characterized prompt emission allowed measurements of the peak energy of the spectrum ($E_p = 367^{+65}_{-51}\,\mathrm{keV}$; Golenetskii et al., 2007), as well as a "pseudo-redshift" (Pélangeon, 2006) of $z_\mathrm{p} = 1.3 \pm 0.3$ (Pelangeon & Atteia, 2007).

We began observing the field of GRB 070125 with the automated Palomar 60 inch (1.5 m) telescope (P60; Cenko et al., 2006a) at 02:18:59 UT on 2007 January 26 ($\Delta t = 19.0\,\mathrm{hr}$). Inside the burst error circle, we found a bright, stationary source ($R = 18.59 \pm 0.03\,\mathrm{mag}$) not present in the Sloan Digital Sky Survey images of this field (Adelman-McCarthy et al., 2006) that we identified as the optical afterglow of GRB 070125 (Cenko & Fox, 2007; Figure 5.1). Our subsequent broadband monitoring of the afterglow of GRB 070125 is presented in a separate work (Chandra et al., 2008).

We also undertook spectroscopic observations of GRB 070125 with the Gemini Multi-Object Spectrograph (GMOS; Hook et al., 2004) mounted on the 8 m Gemini North Telescope beginning on the night of 2007 January 26. For all spectra, we employed a 2×2 binning to increase the CCD signal-to-noise ratio, and we used the R400 grating and $1''$ slit. Our configuration resulted in a spectral resolution of $\sim 8\,\text{Å}$ and a dispersion of $1.34\,\text{Å}\,\mathrm{pix^{-1}}$. The details of our observations are shown in Table 5.1.

Table 5.1. Log of Spectroscopic Observations of GRB 070125

Identification	UT Date[a]	Age[b] (days)	Primary Target	Wavelength Coverage (Å)	Airmass[c]	Exposure Time (s)
1a	2007 Jan 26.228	0.922	Afterglow	5900–10000	1.98	1800
1b	2007 Jan 26.250	0.944	Afterglow	5900–10000	1.67	1800
1c	2007 Jan 26.272	0.966	Afterglow	4000–8100	1.45	1800
1d	2007 Jan 26.294	0.989	Afterglow	4000–8100	1.30	1800
2a	2007 Jan 29.247	3.941	Afterglow	5900–10000	1.60	1800
2b	2007 Jan 29.269	3.963	Afterglow	5900–10000	1.41	1800
2c	2007 Jan 29.290	3.984	Afterglow	5900–10000	1.27	1800
2d	2007 Jan 29.312	4.006	Afterglow	5900–10000	1.18	1800
3a	2007 Feb 4.340	9.992	R1	5900–10000	1.06	2400
3b	2007 Feb 4.369	10.063	R1	5900–10000	1.03	2400

[a]UT at midpoint of exposure.

[b]Age in days from detection of the burst at 7:20:45 UT on 2007 January 25 (Hurley et al., 2007).

[c]Average airmass of exposure.

All spectra were reduced in the IRAF[1] environment using standard routines. Pairs of dithered spectra were subtracted to remove residual sky lines. Cosmic rays were removed using the LA Cosmic routine (van Dokkum, 2001). Spectra were extracted optimally (Horne, 1986), and wavelength calibration was performed first relative to CuAr lamps and then tweaked based on night sky lines in each individual image. In all cases, the resulting rms wavelength uncertainty was $\lesssim 0.3$ Å. Both air-to-vacuum and heliocentric corrections were then applied to all spectra. Extracted spectra were divided through by a smoothed flux standard to remove narrow band (< 50 Å) instrumental effects (Bessell, 1999). Finally, telluric atmospheric absorption features were removed using the continuum from spectrophotometric standards (Wade & Horne, 1988; Matheson et al., 2000).

Deep, late-time imaging to search for the host galaxy of GRB 070125 was taken with the Low-Resolution Imaging Spectrometer (LRIS: Oke et al., 1995) mounted on the 10 m Keck I telescope. LRIS employs a dichroic beam splitter, allowing simultaneous imaging in both g'- and R-band filters. We obtained 4×300 s images at a mean epoch of 7:12:06.6 UT on 2007 February 16. Individual images were bias-

[1]IRAF is distributed by the National Optical Astronomy Observatory, which is operated by the Association for Research in Astronomy, Inc., under cooperative agreement with the National Science Foundation.
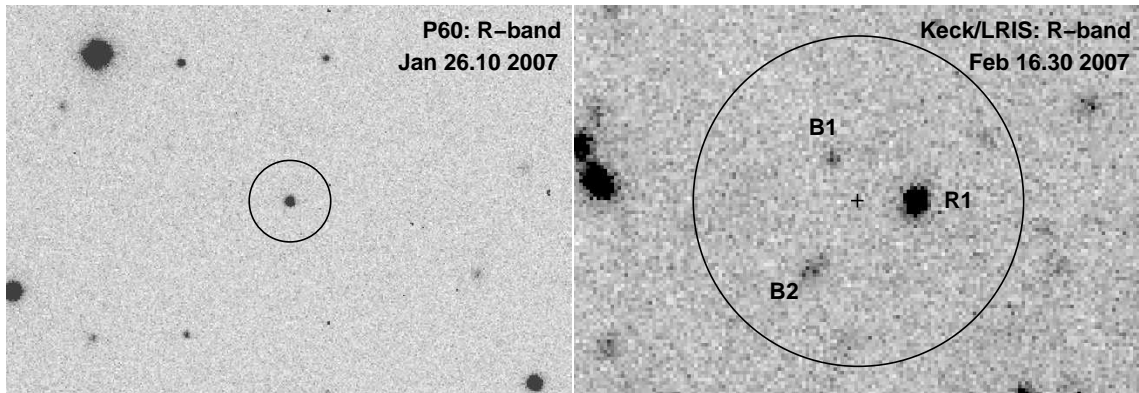
Figure 5.1 — Optical imaging of the field of GRB 070125. *Left*: P60 *R*-band discovery image of the optical afterglow of GRB 070125. The afterglow is centered inside a circle of radius 10″. *Right*: Late-time Keck/LRIS *R*-band image of the field. The location of the afterglow is marked with a cross. The black circle again has a radius of 10″. We find no evidence for an underlying host, to limits of $R > 25.4$ mag, $g' > 26.1$ mag. The three galaxies nearest to the afterglow location are marked (B1, B2, and R1). R1, initially suggested as a possible host for GRB 070125 (Bloom et al., 2007), is a red, foreground galaxy ($z = 0.897$) with little current star formation. B1 and B2 are both quite blue ($g' - R \approx 0$), typical of long-duration GRB hosts. Both images are oriented with north up and east to the left.

subtracted and flat-fielded using standard IRAF routines. Co-addition was performed using SWarp[2]. The resulting *R*-band image is shown in Figure 5.1 (*right panel*).

5.3   Results

In Figure 5.2 we show a sum of all four GMOS spectra obtained on the night of 2007 January 26 ($1a$–$1d$; Table 5.1), normalized by the continuum. The strongest absorption feature present is a doublet at $\lambda\lambda$ 7124,7142 Å, with observed equivalent widths of 0.47 ± 0.05 Å ($\lambda_1 = 7124.23 \pm 0.35$ Å) and 0.21 ± 0.04 Å ($\lambda_2 = 7142.45 \pm 0.42$ Å). Despite the weakness of the feature, the doublet is detected in separate co-additions of spectra from the two different instrumental configurations ($\lambda_{\text{central}} = 6000$ Å vs. $\lambda_{\text{central}} = 8000$ Å), providing strong confirmation of its reality (Figure 5.2, *right inset*). Inspection of the two-dimensional spectra reveals the only other significant absorption feature, at $\lambda = 6283$ Å, is offset slightly from the center of the trace. Furthermore, it

---

[2]See http://terapix.iap.fr.

is only detected in one instrumental configuration. We therefore believe this feature is most likely an artifact of the data reduction process.

We find marginal ($\lesssim 2\sigma$) evidence for strengthening of both features in the doublet over the duration of our observations. Variability has been reported before in GRB afterglow spectra, both within the GRB host itself (time-dependent excitation caused by UV photons from the GRB afterglow; Vreeswijk et al., 2007) and in intervening absorbers (caused by variability in the GRB beam size relative to intervening clouds; Hao et al., 2007). However, because of the uncertainty of this result, we proceed using average values measured from the sum of all our spectra obtained on the night of 2007 January 26.

Based on the lack of Ly-α absorption, we place an upper limit on the afterglow redshift of $z \leq 2.3$. Prochaska et al. (2007c) report a contemporaneous LRIS spectrum of the afterglow with coverage extending down to the atmospheric cutoff at $\lambda \approx 3000\,\text{Å}$. Based on the absence of damped Ly-α absorption or Ly-α forest emission, they report a redshift upper limit of $z < 1.4$. Given the weakness of the observed doublet, the expected weakness of the associated Ly-α absorption (see below), and the decrease in sensitivity at the bluest LRIS wavelengths, we believe this limit is too strict. Instead, we adopt a more conservative value of $z < 1.8$ (corresponding to $\lambda_{\text{Ly}-\alpha} \leq 3500\,\text{Å}$) throughout this work.

Consistent with the above redshift constraint, we identify the observed doublet as Mg II $\lambda\lambda$ 2796, 2803 at $z = 1.5477 \pm 0.0001$. Besides the observed wavelength ratio, we offer two additional pieces of evidence in support of this association. First, the observed equivalent width ratio (Mg II λ 2796 / Mg II λ 2803) is consistent with the value of 2:1 predicted for weak, unsaturated absorption from this transition. Second, the Mg II $\lambda\lambda$ 2796, 2803 doublet is the strongest absorption feature observed in *all* GRB hosts identified in the redshift range $0.5 \lesssim z \lesssim 2.0$ (see below). Even if the system does not arise from the GRB host, this doublet is commonly found in intervening systems of both QSOs (Steidel & Sargent, 1992) and GRBs (Prochter et al., 2006). At this redshift, we place an upper limit on the rest-frame equivalent width of absorption from Mg I λ 2852 of $W_r < 0.06\,\text{Å}$ (Figure 5.2, *left inset*).

Based on the observed Mg II equivalent widths, we can calculate corresponding column densities in the optically thin (i.e., unsaturated) limit:

$$N = \frac{m_e c^2}{\pi e^2} \frac{W_r}{f \lambda^2} = 1.13 \times 10^{20} \mathrm{cm}^{-2} \frac{(W_r/\text{Å})}{(\lambda/\text{Å})^2 f}, \tag{5.1}$$

where f is the oscillator strength (from Morton, 1991), W_r is the rest-frame equivalent width, and λ is the rest wavelength. The results are shown in Table 5.2. For the observed system we measure a column density of log $N(\text{Mg II}) = 12.61 \pm 0.05$. The corresponding upper limit on the Mg I column density is log $N(\text{Mg I}) < 11.7$.

To compare our observed Mg II system with previous samples, we would like to know whether it arises from the GRB host or some intervening galaxy. To this end, we undertook a second epoch of GMOS spectroscopy on the night of 2007 January 29 ($2a$–$2d$; Table 5.1) to search for nebular emission lines at the location of the afterglow. While still bright enough to provide a reliable trace ($R \sim 21.5$ mag) at this epoch, the decreased afterglow flux improved our sensitivity to faint emission lines. At $z = 1.5477$, the only common line indicative of active star formation to fall in our bandpass is [O II λ 3727] ($\lambda_{\mathrm{obs}} \approx 9497$). The presence of several bright night sky lines nearby significantly affected our sensitivity. Nonetheless, we put an upper limit on the observed flux[3] from [O II λ 3727] at $z = 1.5477$ of $< 5 \times 10^{-18}$ erg cm^{-2} s^{-1}. Using the relation from Kennicutt (1998), this corresponds to an upper limit on the star-formation rate of < 1 M$_\odot$ yr^{-1}. This lies on the low end of star-formation rates observed in previous GRB hosts (Christensen et al., 2004).

Without a secure emission-line redshift, we cannot determine the nature of the Mg II system (i.e., host or intervening). Nonetheless, because of our redshift constraints, $1.55 \leq z \leq 1.8$, the Mg II $\lambda\lambda$ 2796, 2803 transition from the host is guaranteed to fall within our observed bandpass (n.b., this is the case even if we apply our weaker $z \leq 2.3$ constraint). Therefore, even if the observed Mg I system is from an intervening galaxy, the measured equivalent widths are a firm upper limit on the presence of Mg II in the host system. In what follows we shall assume that $z = 1.55$

---

[3]Throughout this work, we adopt a ΛCDM cosmology with the latest parameters from *WMAP* ($H_0 = 70.9$ km s^{-1} Mpc^{-1}; $\Omega_{\mathrm{m}} = 0.266$; $\Omega_\Lambda = 1 - \Omega_{\mathrm{m}}$; Spergel et al., 2007).
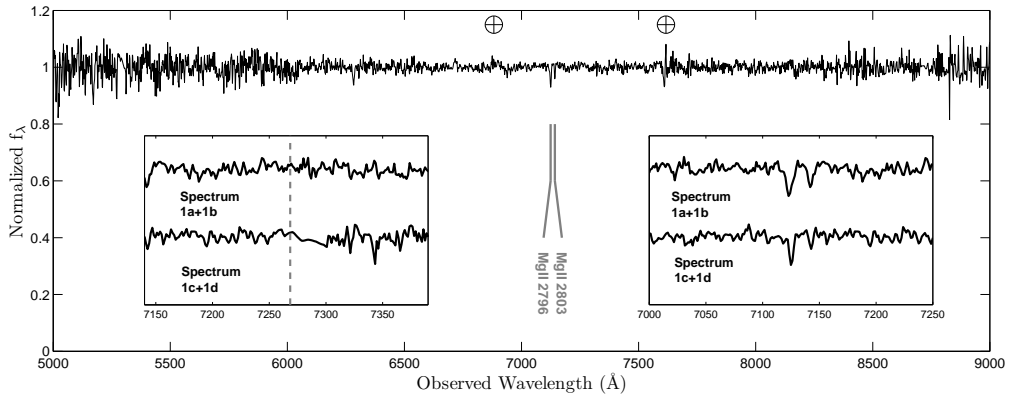
Figure 5.2 — Gemini/GMOS spectrum of the afterglow of GRB 070125. In the primary plot we show the sum of all four spectra obtained the night of 2007 January 26 after normalizing by the continuum (1*a*–1*d*; Table 5.1). The region from 6000–8000 Å shows the highest signal-to-noise ratio, as it was covered in all four spectra. Telluric atmospheric absorption features are indicated by circled plus signs. No strong absorption features are present in the spectrum. The strongest feature is a doublet at 7124/7142 Å, which we identify as Mg II $\lambda\lambda$ 2796, 2803 at $z = 1.55$. Despite its weakness, the doublet is visible in spectra from both configurations taken on 2007 January 26 (*right inset*). In the left inset, we zoom in on the Mg I λ 2852 transition at $z = 1.55$. No absorption is detected in either configuration to $W_r < 0.06$ Å.

is the redshift of the GRB host; all our conclusions below are only strengthened for $z > 1.55$.

In Figure 5.3 we plot the observed Mg II λ 2796 rest-frame equivalent width for GRB 070125 compared to all previously observed GRB hosts. On the ordinate axis we plot the ratio between the 2796 Å and 2803 Å components of the doublet. We find GRB 070125 is an outlier on both axes. Clearly the inferred column density is significantly lower than any other GRB host galaxy. Furthermore, the Mg II λ 2796/Mg II λ 2803 ratio in all previous GRBs was ≈ 1, indicating significant saturation. For saturated lines, the optically thin approximation (Equation 5.1) breaks down and can significantly underestimate the true column density. The difference in Mg II column density between the host galaxy of GRB 070125 and all previous GRB hosts is therefore even larger than the factor of ≈ 10–15 derived above.

To verify that the sample of GRB hosts used above is not biased toward strong

Mg II absorbers, we searched through the GRB Circulars Network (GCN)[4] archive to review all reported long-duration afterglow absorption spectra. Neglecting the most nearby events, $z \lesssim 0.3$, for which the strongest absorbers still lie in the UV, we find only a single report of a high signal-to-noise spectrum absent any absorption features in the optical bandpass (GRB 061021; Thoene et al., 2006). Alternatively, of the 17 long-duration events with a reported redshift and spectral coverage of the host Mg II $\lambda\lambda$ 2796, 2803 transition, but without reported equivalent widths (i.e., not included in Figure 5.3), 16 report a detection of this doublet. The sole exception, a spectrum of GRB 050802, contains several absorption features, but their identification was uncertain (Fynbo et al., 2005). We can therefore rule out a significant population of weak Mg II absorbers from GRB hosts at a high degree of confidence.

The detection of Mg I from GRB hosts is thought to indicate that these observations probe distances far away (≥ 100 pc) from the GRB itself (Prochaska et al., 2007b; Vreeswijk et al., 2007). The first ionization energy of Mg is 7.6 eV, and therefore UV photons from the GRB afterglow are able to ionize any Mg I in the circumburst medium to Mg II (subsequent ionizations beyond Mg II are likely shielded by neutral hydrogen, as their ionization energies lie above 1 ryd). It is therefore important to determine if we would expect to see Mg I absorption from GRB 070125, or whether the feature would be too weak to detect in our spectra.

Comparing the equivalent width ratio of Mg II λ 2803 (the weaker of the Mg II doublet, and therefore less saturated) to that of Mg I λ 2853 in previously observed GRB hosts, we find ratios ranging from 1.7 (GRB 970508; Metzger et al., 1997) to 2.8 (GRB 060418; Prochaska et al., 2007a; Vreeswijk et al., 2007). Again we note these values are really a lower limit, as saturation will be more significant for the stronger Mg II λ 2803 feature. Nonetheless, we predict an Mg I λ 2853 rest frame equivalent width of $W_r \lesssim 0.03$–0.05 Å. This is below our sensitivity limit, and we therefore believe we would not be sensitive to Mg I absorption even if it were present at expected levels.

To convert our measured Mg column density (assumed to be dominated by Mg II)

---

[4]See http://gcn.gsfc.nasa.gov/gcn3_archive.html.
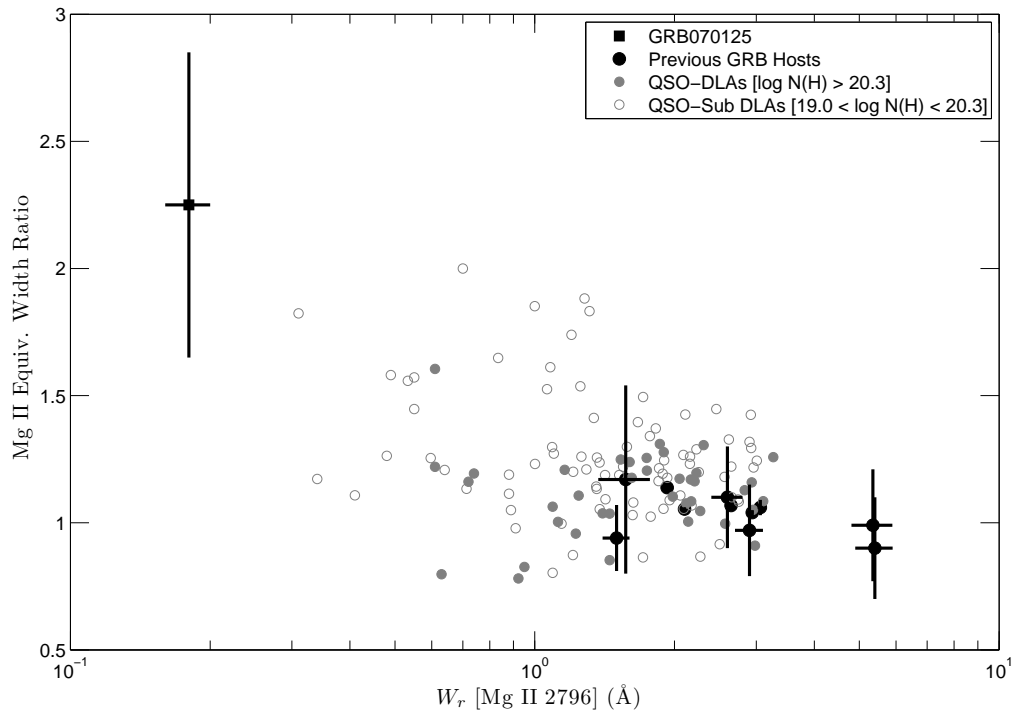
Figure 5.3 — Mg II absorption in GRB host galaxies. Here we plot a compilation of all the equivalent width measurements of the Mg II λ 2796 absorption feature in GRB host galaxies. On the y-axis, we plot the observed ratio between the Mg II λ 2796 and Mg II λ 2803 absorption lines. Ratios deviating from 2 indicate the lines have become saturated and the corresponding optically thin column densities should be treated as lower limits. Thus the factor of $\approx$ 10–15 discrepancy between GRB 070125 and all previous GRB hosts actually underestimates the true difference in column densities. Shown in gray are analogous measurements for QSO-DLAs [log N(H I) > 20.3; *filled circles*] and QSO-Sub DLAs [19.0 < log N(H I) < 20.3; *empty circles*]. References: GRB 970508: Metzger et al., 1997; GRB 990123: Kulkarni et al., 1999a; GRB 000926: Castro et al., 2003; GRB 010222: Mirabal et al., 2002; GRB 020813: Barth et al., 2003; GRB 030226: Shin et al., 2006; Klose et al., 2004; GRB 030328: Maiorano et al., 2006; GRB 041006: Soderberg et al., 2006d; GRB 051111: Penprase et al., 2006; Prochaska et al., 2007a; GRB 060418: Vreeswijk et al., 2007; Prochaska et al., 2007a; GRB 070208: Cucchiara et al., 2007 (in preparation); QSOs: Rao et al., 2006.

to neutral hydrogen, we must estimate the ratio of Mg:H in the host. Previous GRB hosts range in metallicity from $-2.0 \lesssim [M/H] \lesssim -0.5$ (Berger et al., 2005b; Prochaska et al., 2007b), much like QSO-DLAs (Prochaska et al., 2003). At $z < 2$, no QSO-DLA has ever been observed with $[M/H] < -2$ (Wolfe et al., 2005), and a near-solar metallicity is difficult to reconcile with a star-forming galaxy at $z = 1.55$. If we neglect the cold, dense, disk depletion model, ruled out for all GRB hosts observed to date (Savaglio et al., 2003; Berger et al., 2005b; Penprase et al., 2006), all other environments predict an Mg depletion of $[Mg/M] \approx -0.5$ (Savage & Sembach, 1996). With the above limits, we estimate the neutral hydrogen column density to fall within $18.0 \lesssim \log N(\text{H\,I}) \lesssim 19.5$ (using solar abundances from Asplund et al., 2005).

The implied Mg:H ratio is in good agreement with previously observed GRBs, as well as the broader sample of QSOs. While $N(\text{Mg\,II})$ and $N(\text{H\,I})$ have never been accurately measured simultaneously in a single GRB host, two events provide upper limits: $[\text{Mg\,II}/\text{H\,I}] > -2.7$ for GRB 000926 (Fynbo et al., 2002; Castro et al., 2003), and $[\text{Mg\,II}/\text{H\,I}] > -1.6$ for GRB 030226 (Klose et al., 2004; Shin et al., 2006). For QSO-DLAs at $z < 1.65$, the mean equivalent width for the Mg II λ 2796 transition is 1.8 Å, while for sub-DLAs ($19.0 \leq \log N(\text{H\,I}) \leq 20.3$) the corresponding value is $\langle W_r \rangle = 1.6$ Å (Rao et al., 2006). For comparison, we also plot these QSO-Mg II systems in Figure 5.3. In a sample of eight weak ($W_r < 0.3$ Å) Mg II absorbers, Churchill et al. (1999) found all had $\log N(\text{H\,I}) < 19.0$. In fact, six of the eight systems exhibited no sign of a Lyman limit break, indicating not only $\log N(\text{H\,I}) < 17$, but also that neutral hydrogen was optically thin in those clouds (Tytler, 1982).

An alternative way to determine the neutral hydrogen column density is by modeling the afterglow spectral energy distribution (SED). Our models of the X-ray spectrum and optical SED do not require any dust extinction in addition to the Galactic component (Chandra et al., 2008; see also Racusin & Vetere, 2007). However, because of the relatively large Galactic column $[N(\text{H}) \approx 5 \times 10^{20} \, \text{cm}^{-2}$; Dickey & Lockman, 1990] and the large effect of redshift on dust obscuration, these limits are not nearly as constraining as those derived from the optical spectrum.

All told, we have strong evidence that the neutral hydrogen column density in the host of GRB 070125 is quite low: $\log N(\text{H I}) < 19.5$, if not significantly smaller. Such densities are usually associated with galaxy halos, and stand in contrast with the sample of previously observed GRB hosts, which are commonly attributed to a disk population. The sample of previously observed GRB hosts has a median $\log N(\text{H I}) \approx 21.3$, with an observed standard deviation of 0.9 dex (Jakobsson et al., 2006a). In other words, to fall within 1 σ of the known distribution, a GRB host must be a DLA. Only three previous events, GRBs 021004 (Möller et al., 2002), 050908 (Foley et al., 2005), and 060607 (Jakobsson et al., 2006a) had measured $\log N(\text{H I}) < 19.5$, and none report significantly lower values. All three exhibited strong absorption from other metals in addition to Ly-α, again distinguishing them from the mostly featureless spectrum of GRB 070125.

In our late-time imaging of the field of GRB 070125 (Figure 5.1, *right panel*), we find no host directly underneath the afterglow location to limits of $R > 25.4$ mag (Vega), $g' > 26.1$ mag (AB). Using a synthetic spectrum of a star-forming galaxy from Kinney et al. (1996), we estimate a limit on the absolute magnitude of $M_V > -19.2$ mag for any underlying host. Many GRB host galaxies are fainter than $M_V > -19.2$ (Fruchter et al., 2006), so it is entirely possible our limits are too shallow to detect the underlying emission. Nonetheless, because of the low density environment, we also consider the possibility that the afterglow lies significantly further away from its host than the typical GRB (≤ 10 kpc; Bloom et al., 2002; Fruchter et al., 2006).

We identify three candidate host galaxies within $10''$ of the afterglow location: R1, B1, and B2 (Figure 5.1, *right panel*). R1, $3.''6$ to the west of the afterglow, is a red ($g' - R \approx 2.4$ mag) galaxy identified by Bloom et al. (2007) as a possible host for GRB 070125. Based on a Gemini-GMOS spectrum obtained on the night of 2007 February 4 (3a–3b; Table 5.1), we identify a strong continuum break at ~ 7500 Å as the rest frame 4000 Å break. Ca H+K and G-band absorption confirm the galaxy lies in the foreground at $z = 0.897$.[5] The other two objects, B1 at $3.''2$ distance, and

---

[5]At a distance of $3.6''$, $R1$ would need to be extremely massive ($\sim 10^{13}$ M$_\odot$) for gravitational lensing to significantly affect the afterglow.

B2 at a distance of $5\rlap{.}''5$, are both blue ($g' - R \approx 0$ mag) and compact, more typical of long-duration GRB hosts (Floc'h et al., 2003). Unfortunately neither galaxy fell on the slit in any of our spectra.

5.4   Discussion

Finally, we speculate on the origin of GRB 070125. At first glance, a compact binary progenitor system, as has been argued to explain most short-duration bursts (Eichler et al., 1989) seems appealing for GRB 070125: the large host offset and low density environment could naturally be explained by the asymmetric "kick" imparted to such systems as the members become SNe (Fryer et al., 1999; Bloom et al., 1999). The accretion disk formed in such a merger is expected to last only a fraction of a second (Narayan et al., 2001), a serious discrepancy with the observed duration. However, the recent discovery of two nearby, long-duration GRBs lacking associated SN emission (Gal-Yam et al., 2006; Fynbo et al., 2006; Valle et al., 2006a; Ofek et al., 2007b) leads us to at least consider an origin not associated with massive stars.

In a separate work, Chandra et al. (2008) study the broadband afterglow emission from GRB 070125. Two findings from this study cast doubt on a compact binary merger origin for this event. First, the total energy release from GRB 070125, including the collimation correction, is extreme even for long bursts ($E \gtrsim 10^{52}$ erg). Short-duration bursts typically are less energetic ($E \lesssim 10^{50}$ erg; Fox et al., 2005), although the higher redshift examples discussed in Berger et al. (2007) appear to be more luminous, and may call this into question.

More importantly, however, based on the broadband SED (particularly the self-absorbed radio spectrum), we conclude the *local* (parsec scale) circumburst density is quite high, even for typical long-duration afterglows ($n \sim 20$ cm^{-3} for a constant density environment). While this may seem inconsistent with the low Mg II column density derived from absorption spectroscopy, we instead consider the two observations the strongest evidence to date that afterglow studies and absorption spectroscopy probe distinct regions: the parsec-scale circumburst medium for the afterglow vs. the

more distant ($\geq 100\,\mathrm{pc}$) ISM for absorption spectroscopy (Prochaska et al., 2007b; Vreeswijk et al., 2007). In the compact binary merger scenario, a large host offset should imply a low circumburst density ($n \lesssim 10^{-3}\,\mathrm{cm}^{-3}$), as has been seen for many short-duration bursts already (Fox et al., 2005; Soderberg et al., 2006a; Panaitescu, 2006).

Because of the long duration, large local density, and large energy release, we return again to consider a massive star progenitor. Instead, we now must explain how a massive star could end up so far away from the dense disk of its host. For the closest putative host from our LRIS imaging, the observed offset of $3\farcs2$ corresponds to a projected distance of $\approx 27\,\mathrm{kpc}$ at $z = 1.5477$. To travel this distance in its short lifetime, a massive star would need an extremely large peculiar velocity: $\sim 10^4$ km s^{-1} for a 20 Myr lifetime. The fastest known object in the Milky Way is the Guitar pulsar, with a peculiar velocity of 1600 km s^{-1} (Cordes et al., 1993), while Galactic stars have been identified with peculiar velocities as large as $500\,\mathrm{km\,s}^{-1}$ (presumably accelerated by interacting with a black hole; Brown et al., 2006). It is much more probable that the progenitor was formed in situ.

Such a scenario has precedent in the local universe, where young, massive, compact star clusters have been found at large distances (i.e., several times the optical radius) either in extended UV disks (e.g., M83: Thilker et al., 2005; NGC4625: de Paz et al., 2005) or in tidal tails of interacting galaxies (e.g., "Antenna" system: Hibbard et al., 2005; Zhang et al., 2001; "Tadpole" galaxy: Jarrett et al., 2006). In some of the most strongly interacting systems, $\geq 10\%$ of the current star formation is occurring in such clusters (Jarrett et al., 2006). Broadband surveys of nearby galaxies indicate a significant fraction ($\lesssim 1\%$) of the current star formation in the local universe takes place in these extreme environments (D. Calzetti, private communication). With our current understanding of hierarchical galaxy formation, such interactions should only increase in frequency as a function of look-back time.

In retrospect, it is not entirely surprising that, of the ~ 50 long-duration GRBs with absorption spectra, we should discover such an event. While a thorough discussion of the relative frequency of such events is premature, the rarity of events

like GRB 070125 implies star formation in the outer regions of galaxies in the distant universe is likely not dramatically different from what we observe today.

Table 5.2.   GRB 070125 Absorption Line Identifications

Observed Wavelength (Å)	Identification	Rest Wavelength (Å)	Redshift	Rest Frame Equivalent Width (Å)	Oscillator Strength[a]	Column Density log (cm^{-2})
7124.23 ± 0.35	Mg II	2796.352	1.54769 ± 0.00012	0.18 ± 0.02	0.612	12.63 ± 0.05
7142.45 ± 0.42	Mg II	2803.531	1.54766 ± 0.00015	0.08 ± 0.01	0.305	12.58 ± 0.06
7268.49^b	Mg I	2852.964	1.5477	< 0.06	1.810	< 11.7

[a]Reference: Morton, 1991.

[b]The Mg I upper limits assume a redshift of $z = 1.5477$ and a line width of 20 km s^{-1}.

Chapter 6

Dark Bursts in the *Swift* Era: The Palomar 60 Inch-*Swift* Early Optical Afterglow Catalog

S. B. Cenko[a], J. Kelemen[b], F. A. Harrison[a], D. B. Fox[c],

S. R. Kulkarni[d], M. M. Kasliwal[d], E. O. Ofek[d], A. Rau[d], D. A. Frail[e],

A. M. Soderberg[f,g], A. Gal-Yam[h], A. Cucchiara[c], P. Chandra[i]

[a]Space Radiation Laboratory, MS 220-47, California Institute of Technology, Pasadena, CA 91125

[b]Konkoly Observatory, H-1525, Box 67, Budapest, Hungary

[c]Department of Astronomy & Astrophysics, 525 Davey Laboratory, Pennsylvania State University, University Park, PA 16802

[d]Department of Astronomy, Mail Stop 105-24, California Institute of Technology, Pasadena, CA 91125

[e]National Radio Astronomy Observatory, P.O. Box 0, 1003 Lopezville Road, Socorro, NM 87801

[f]Observatories of the Carnegie Institute of Washington, 813 Santa Barbara Street, Pasadena, CA 91101

[g]Princeton University Observatory, Peyton Hall, Ivy Lane, Princeton, NJ 08544

[h]Astrophysics Group, Faculty of Physics, Weizmann Institute of Science, Rehovot 76100, Israel

[i]Department of Astronomy, University of Virginia, P.O. Box 3818, Charlottesville, VA 22903

Abstract

We present multi-color ($g'R_\mathrm{C}i'z'$) optical observations of long-duration γ-ray bursts (GRBs) made with the robotic Palomar 60 inch telescope (P60). Our sample includes all 29 events discovered by *Swift* over a three year time period in which P60 began observations less than an hour after the burst trigger. We are able to recover 80% of the optical afterglows from this prompt sample, and we attribute this high efficiency to our red coverage. Like Melandri et al. (2008), we find a significant fraction ($\approx 50\%$) of *Swift* events show a suppression of the optical flux with regards to the X-ray emission (so-called "dark" bursts). Our multi-color photometry demonstrates this is due in large part to extinction in the host galaxy. We argue that previous studies, by selecting only the brightest and best-sampled optical afterglows, have significantly underestimated the amount of dust present in typical GRB environments.

6.1   Introduction

The launch of the *Swift* γ-Ray Burst (GRB) Explorer (Gehrels et al., 2004) in 2004 November has ushered in a new era in the study of GRB afterglows. *Swift* offers a unique combination of event rate ($\sim 100\,\mathrm{yr}^{-1}$; almost an order of magnitude increase over previous missions) and precise localization ($\sim 3'$ radius error circles are distributed seconds after the burst, and refined to $\sim 3''$ minutes later). The on-board X-ray Telescope (XRT; Burrows et al., 2005a) and UV-Optical Telescope (UVOT; Roming et al., 2005), together with the rapid relay of these precise localizations to ground-based observers, has enabled an unprecedented glimpse into the time period immediately following the prompt emission over a broad frequency range.

Observations of X-ray afterglows with the XRT have generated particular interest in recent years. In the pre-*Swift* era, X-ray observations were limited to hours or days after the prompt emission, and were often poorly sampled compared with the optical and radio bandpasses. Routine XRT observations of *Swift* GRBs beginning at early times have revealed a central engine capable of injecting energy into the forward

shock at times well beyond the duration of the prompt emission (e.g., Burrows et al., 2005b; Zhang et al., 2006). This discovery has not surprisingly had a profound effect on our understanding of progenitor models (e.g., Metzger et al., 2007).

While the X-ray afterglow is currently a well-explored phase space, comparatively few analogous studies have been performed in the optical bandpass. Berger et al. (2005a) first suggested that *Swift* optical afterglows were 1.5 mag fainter in the *R*-band than pre-*Swift* events (at a common epoch of 12 hours after the burst). Likewise, Roming et al. (2006) found that only 6 of the first 19 *Swift* bursts with prompt ($\Delta t \lesssim$ 100 s) UVOT coverage yielded optical afterglow detections. Since then, explaining the relative faintness of *Swift* optical afterglows has remained one of the outstanding questions in the field.

Kann et al. (2007) have conducted the most comprehensive literature-based analysis of *Swift* optical afterglows to date. By compiling multi-color observations of the best-studied events, these authors have inferred the amount of line-of-sight extinction native to the GRB host for a relatively large sample of *Swift* GRBs (15 events in their "golden" sample). Interestingly, these authors find only a modest amount of dust ($\langle A_V \rangle = 0.20$ mag) present in nearly all GRB host galaxies, much as was found for pre-*Swift* GRBs (Kann et al., 2006). Instead, they attribute much of the faintness of the *Swift* sample to redshift: the median redshift of *Swift* events is significantly higher than the pre-*Swift* sample ($\langle z_{Swift} \rangle = 2.8$ vs. $\langle z_{\mathrm{pre}-Swift} \rangle = 1.1$; Berger et al., 2005a; Jakobsson et al., 2006b). The primary drawback of this study, however, is the large and uncertain role of selection effects: by only including the brightest, best-sampled optical afterglows, Kann et al. (2007) are preferentially selecting those events in low-extinction environments.

On the other hand, Melandri et al. (2008) have recently presented a sample of 63 GRBs observed in the optical with the robotic 2 m Liverpool Telescope and Faulkes Telescopes (North and South). The selection criteria for including a burst in their sample is never explicitly stated, and several non-*Swift* bursts are included, making a direct comparison with the results of Kann et al. (2007) difficult. However, Melandri et al. (2008) do not exclude the significant fraction of events without optical detec-

tions from their analysis, providing a relatively unbiased look at optical afterglow properties. Interestingly, by measuring the ratio of optical to X-ray flux at a common time, these authors find that roughly half of the GRBs in their sample exhibit a relative suppression of the optical flux inconsistent with our standard picture of afterglow emission (e.g., Sari et al., 1998). This finding suggests that a high-redshift origin alone cannot explain the faintness of *Swift* optical afterglows. The mechanism behind this suppression, however, is largely left a mystery by these authors.

The Palomar 60 inch telescope (P60) is a robotic, queue-scheduled facility dedicated to rapid-response observations of GRBs and other transient events (Cenko et al., 2006a). With a response time of $\Delta t \lesssim 3$ min and a limiting magnitude of $R \gtrsim 20.5$ (60 s exposure), the P60 aperture is well suited to detect most *Swift* optical afterglows (Akerlof & Swan, 2007). In addition, with a broadband filter wheel providing coverage from the near-UV to the near-IR, P60 can also provide multi-color data on the afterglow evolution.

In this work, we present the P60-*Swift* Early Optical Afterglow sample: 29 unambiguously long-duration GRBs detected by the *Swift* Burst Alert Telescope (BAT; Barthelmy et al., 2005a) with P60 observations beginning at most one hour after the burst trigger time. This sample offers two distinct advantages over previous efforts to understand the optical afterglow emission from GRBs. First and foremost, our study enforces a strict selection criterion independent of the optical afterglow properties, and therefore will allow us to study the properties of the *Swift* population in a relatively unbiased manner. Secondly, nearly all events contain multi-color ($g'\,R_{\rm C}\,i'\,z'$) observations that allow us to evaluate the importance of host galaxy extinction for a significant fraction of our sample.

Throughout this work, we adopt a standard ΛCDM cosmology with $h_0 = 0.71$ km s^{-1} Mpc^{-1}, $\Omega_{\rm m} = 0.27$, and $\Omega_{\Lambda} = 1 - \Omega_{\rm m} = 0.73$ (Spergel et al., 2007). We define the flux density power-law temporal and spectral decay indices α and β as $f_{\nu} \propto t^{-\alpha} \nu^{-\beta}$ (e.g., Sari et al., 1998). All errors quoted are 1 σ (i.e., 68%) confidence intervals unless otherwise noted.

6.2   Observations and Data Reduction

The P60-*Swift* Early Optical Afterglow Catalog is shown in Table A.1. We have included here all optical afterglows of events localized by *Swift* in the three year period from 2005 April 1–2008 March 31 (roughly coinciding with the beginning of real-time GRB alerts and narrow-field instrument follow-up) for which we began P60 observations within one hour after the BAT trigger.

All P60 data were reduced in the IRAF[1] environment using our custom real-time reduction pipeline (Cenko et al., 2006a). Where necessary, co-addition was performed using SWarp[2]. For the vast majority of events, magnitudes were calculated using aperture photometry with the inclusion radius roughly matched to the stellar PSF FWHM. For the few events with either extremely crowded fields or variable, elevated backgrounds (due to nearby bright stars or the moon), image subtraction was performed using the ISIS package (Alard & Lupton, 1998).

Photometric calibration was performed relative to the SDSS data release 6 (Adelman-McCarthy et al., 2008) where possible, typically resulting in rms variations of $\lesssim$ 0.05 mag in all filters. For those fields without Sloan coverage, we made use of the calibration files provided by A. Henden[3] when available, resulting in similar quality calibrations to the SDSS. The remaining events were calibrated relative to the USNO-B1 catalog[4], resulting in significantly poorer zero point fits. Particularly in the g, z, and z' filters, the rms errors for these events could be quite large (~ 0.6 mag). Photometric and instrumental errors have been added in quadrature to obtain the results presented in Table A.1.

Filter transformations (either from the Johnson-Kron-Cousins Vega system to the SDSS AB system, or vice versa) were made using the results from Jordi et al. (2006). Throughout this work, the Gunn g and z filters have been calibrated relative to the

---

[1] IRAF is distributed by the National Optical Astronomy Observatory, which is operated by the Association for Research in Astronomy, Inc., under cooperative agreement with the National Science Foundation.

[2] See http://terapix.iap.fr/soft/swarp.

[3] Available via ftp at ftp.aavso.org.

[4] See http://www.nofs.navy.mil/data/fchpix.

Table 6.1.   P60 Filter Reference

P60 Filter	Central Wavelength[a] (Å)	Reference Filter	Photometric System	Zeropoint[a] (Jy)
g	4927	g'	AB	3631
V_C	5505	V_C	Vega	3590
R_C	6588	R_C	Vega	3020
i'	7706	i'	AB	3631
i	7973	I_C	Vega	2380
I_C	8060	I_C	Vega	2380
z	9133	z'	AB	3631
z'	9222	z'	AB	3631

[a]Reference: Fukugita et al., 1995.

SDSS g' and z' filters, and their corresponding magnitudes are reported in the AB system. The Gunn i filter, used for some early observations in 2005, was found to best match the Cousins I_C filter, and hence is reported on the Vega system. The remaining filters have magnitudes reported in their native photometric system (i.e., Vega for V_C, R_C, and I_C, and AB for i' and z'). A summary of the relevant photometric calibration and appropriate zero-point for flux conversion can be found in Table 6.1. Full throughput curves for all P60 filters can be found in Cenko et al. (2006a).

Finally, we note that the magnitudes reported in Table A.1 have not been corrected for Galactic extinction along the line-of-sight. When necessary for analysis, this correction has been applied using the dust extinction maps of Schlegel et al. (1998) and the Milky Way extinction curve from Cardelli et al. (1989).

6.3   Analysis

The standard theoretical paradigm to explain GRBs is the relativistic fireball model (see Section 1.2 for a more thorough review). In the case of long-duration GRBs, accretion onto the black hole remnant of massive star core-collapse powers an ultra-relativistic outflow of matter and/or radiation (Woosley, 1993). Shocks and/or instabilities within the outflow generate the prompt γ-rays (i.e., internal shocks). The

afterglow emission, on the other hand, is powered by electrons in the circumburst medium accelerated by the outgoing blast wave (i.e., external shocks). The resulting synchrotron spectrum and light curve are well described by a series of broken power-laws (Equations 1.6–1.25), with the break frequencies determined not only by properties of the outflow (E, θ, etc.), but also by the nature of the circumburst medium. In what follows we attempt to understand the early optical afterglow phase in the context of this model.

The R-band optical light curves (and upper limits) for all 29 events in the P60-*Swift* Early Optical Afterglow Sample are shown in Figure 6.1. For all events with P60 optical detections, we have simultaneously fit both the spectral and temporal evolution of the light curve, assuming a power-law spectrum and either a single or broken power-law temporal evolution. The results of this analysis are shown in Table 6.2.

Because afterglow emission is a broadband phenomenon, multi-wavelength observations can often provide important constraints that would be overlooked by considering only a single bandpass. We have therefore obtained XRT light curves from the on-line *Swift*-XRT light curve repository[5] (Evans et al., 2007). We converted the 0.3–10 keV fluxes to flux densities at a nominal energy of 2 keV assuming a power-law X-ray spectrum with indices provided in the Gamma-Ray Burst Coordinate Network (GCN)[6] circulars. We then fit the temporal decay of each X-ray light curve, assuming either a single or broken-power law model.

With these results in hand, we now move on to explore the large P60 detection efficiency (Section 6.3.1); the relationship between X-ray and optical flares (Section 6.3.2); the brightness and luminosity distribution of *Swift* optical afterglows (Section 6.3.3); and dark bursts in the *Swift* era (Section 6.3.4).

6.3.1 Detection Efficiency

The most striking feature in Table 6.2 is the large fraction of P60-detected afterglows: of the 29 events in the sample, P60 detected 22 (76%). This stands in stark contrast

---

[5]See http://www.swift.ac.uk/xrt_curves.

[6]See http://gcn.gsfc.nasa.gov/gcn3_archive.html.
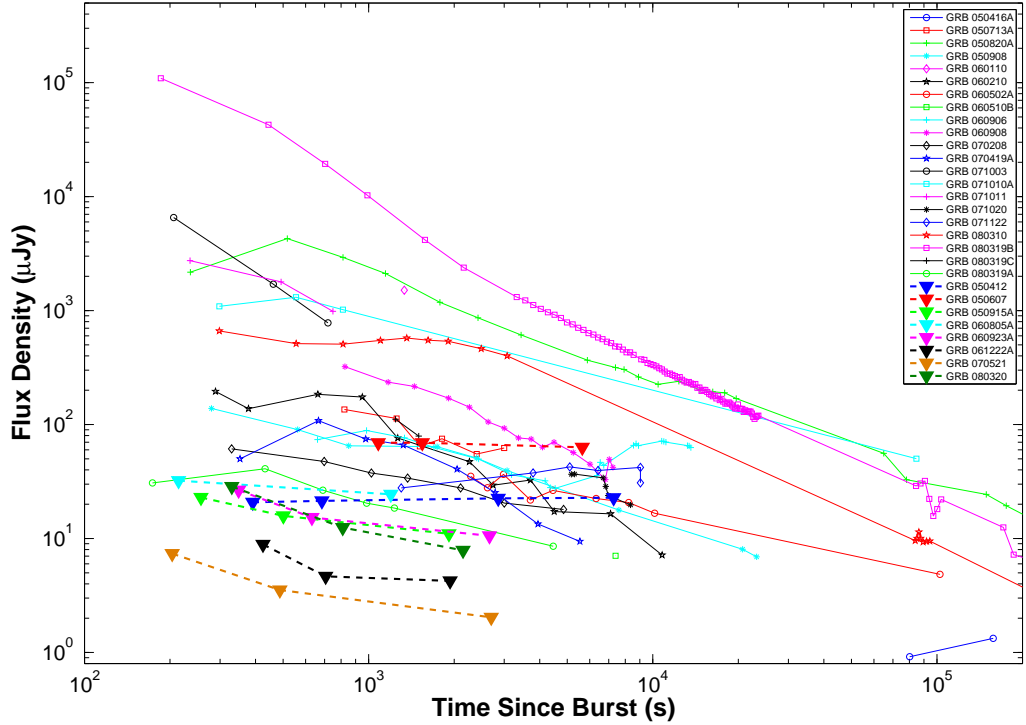
Figure 6.1 — The P60-*Swift* early optical afterglow sample. We plot here $R_{\rm C}$-band light curves or upper limits for all 29 events in the P60-*Swift* Early Afterglow Sample. With the exception of GRB 050607, the upper limits fall securely at the very faint end of the distribution (see also Figure 6.4).

with the 32% afterglow detection efficiency of the UVOT (Roming et al., 2006) and even exceeds the 50% value reported by the larger Liverpool and Faulkes telescopes (Melandri et al., 2008). For those events without P60 detections, one (GRB 050607: Rhoads, 2005) was detected in the optical below our sensitivity limits, while three were detected in the NIR (GRB 050915: Bloom & Alatalo, 2005; GRB 060923A: Tanvir et al., 2006; GRB 061222A: Cenko & Fox, 2006). Only three events (10%) in the entire sample registered no detections in the optical or NIR bandpass: GRBs 050412, 060805, and 070521.

17 of the 29 events (59%) in the sample have redshifts from optical spectroscopy, roughly a factor of two larger than the *Swift* population as a whole. These range from $z = 0.6535$ (GRB 050416A; Soderberg et al., 2007) to $z = 4.9$ (GRB 060510B; Price

et al., 2007). Together with our measured median redshift of $\langle z \rangle \approx 2$, the events in our sample are relatively representative of *Swift* afterglows ($\langle z \rangle \approx 2.7$; Berger et al., 2005a; Jakobsson et al., 2006b). While small number statistics may account for some of our observed deviations from previous studies, we leave a more thorough discussion of our detection efficiency to Section 6.4.1.

6.3.2   X-Ray and Optical Flares

A large fraction ($\approx 33\%$) of *Swift* X-ray light curves exhibit dramatic, short-lived flares superposed on their power-law decay (Falcone et al., 2007). The temporal and spectral structure of these flares indicate they cannot come from the external shock powering the afterglow emission; instead they are widely attributed to late-time activity of the central engine (Zhang et al., 2006). Likewise, a re-brightening at late times in the optical bandpass has now been seen in several *Swift* afterglows (Woźniak et al., 2006; Stanek et al., 2007). Investigating the relationship between these two bandpasses should help shed light on the emission mechanisms responsible for these deviations from standard afterglow theory.

Our early afterglow sample includes four events with contemporaneous optical observations of X-ray flares: GRBs 050820A, 050908, 060210, and 080310 (Figures 6.2 and 6.3). The relationship between the X-ray and optical emission from GRB 050820A is discussed extensively in Cenko et al. (2006b) and Vestrand et al. (2006). While the optical emission clearly jumps in concert with the bright X-ray flare at $t \approx 230\,\mathrm{s}$, the dominant contribution to the optical emission at later times appears to come from the forward shock. In the other three events, the optical emission is completely de-coupled from any flaring in the X-rays.

GRB 060906 is unique in our sample, as we observe a re-brightening by a factor of ≈ 3 at $t \approx 10^4\,\mathrm{s}$ in the optical. The X-ray decay, on the other hand, appears relatively flat during this stage. One possibility to explain the optical flare is an increase in the circumburst density; such a change in the surrounding medium should have no effect on any emission above the synchrotron cooling frequency, ν_c, where the
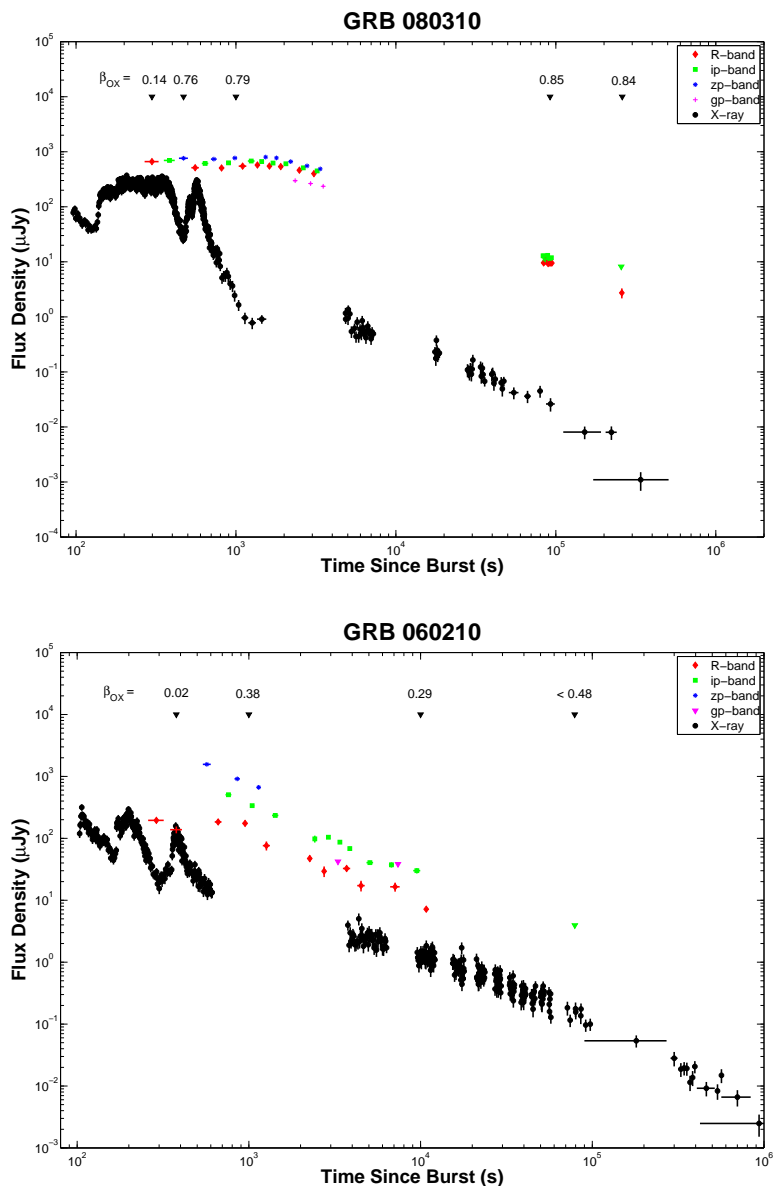
Figure 6.2 — Variation of β_{OX} as a function of time. X-ray and optical light curves of GRB 080310 (top) and GRB 060210 (bottom). With dramatic X-ray variability seen at early times ($t \lesssim 10^3$ s), measurement of the optical to X-ray spectral index (β_{OX}) is a strong function of time. Measuring β_{OX} at early times during an X-ray flare may lead to erroneous classification of some bursts as "dark". Both events, however, show relatively constant β_{OX} values for $t \gtrsim 10^3$ s. GRB 060210, for example, is clearly a dark burst, even at late times.

X-ray bandpass is likely to fall. However, a recent study by Nakar & Granot (2007) has shown that even sharp density changes do not lead to dramatic variability in afterglow light curves; instead any changes in the afterglow evolution occurs smoothly over several orders of magnitude in time. We leave a more thorough discussion of the afterglow of GRB 060906 to Rana et al. (2008, in preparation).

6.3.3   Brightness and Luminosity Distribution

We have interpolated (where possible) or extrapolated the $R_{\rm C}$-band flux to a common time of $t = 10^3$ s in the observer frame for all 22 P60-detected afterglows in our sample. A plot of the resulting cumulative distribution is shown in Figure 6.4. For those events without detections, we take the deepest upper limit obtained before this fiducial time, and plot this as a vertical dashed line in Figure 6.4. For comparison, we also show the analogous result obtained by Akerlof & Swan (2007) in a literature-based study of 43 *Swift* optical afterglows from 2005–2006.

It is clear from the large degree of overlap in the two distributions in Figure 6.4 that our sample, though slightly smaller in size, is representative of the entire *Swift* optical afterglow population. We find a slight degree of variation at the faint end ($R_{\rm C} \gtrsim 21.5$ mag), which likely indicates we are missing a small fraction ($< 10\%$) of the faintest afterglows. However, given that $\sim 70\%$ of *Swift* events seem to have $R_{\rm C} < 22$ mag at this fiducial time (Akerlof & Swan, 2007), the P60 sensitivity is well matched to detect the majority of events.

For those events for which we do not detect an optical afterglow with P60, it is clear from Figures 6.1 and 6.4 that only one event can be attributed to a lack of sensitivity (GRB 050607, which was located only $3''$ from a $R \approx 16$ mag star). The remaining 6 events would all have been easily detected if as bright as a typical afterglow in our sample.

For the 17 GRBs with redshifts, it is also possible to compare optical light curves in the GRB rest frame. We therefore compute the afterglow luminosity at a fiducial time of 10^3 s in the rest frame of the GRB, applying a k-correction to convert our
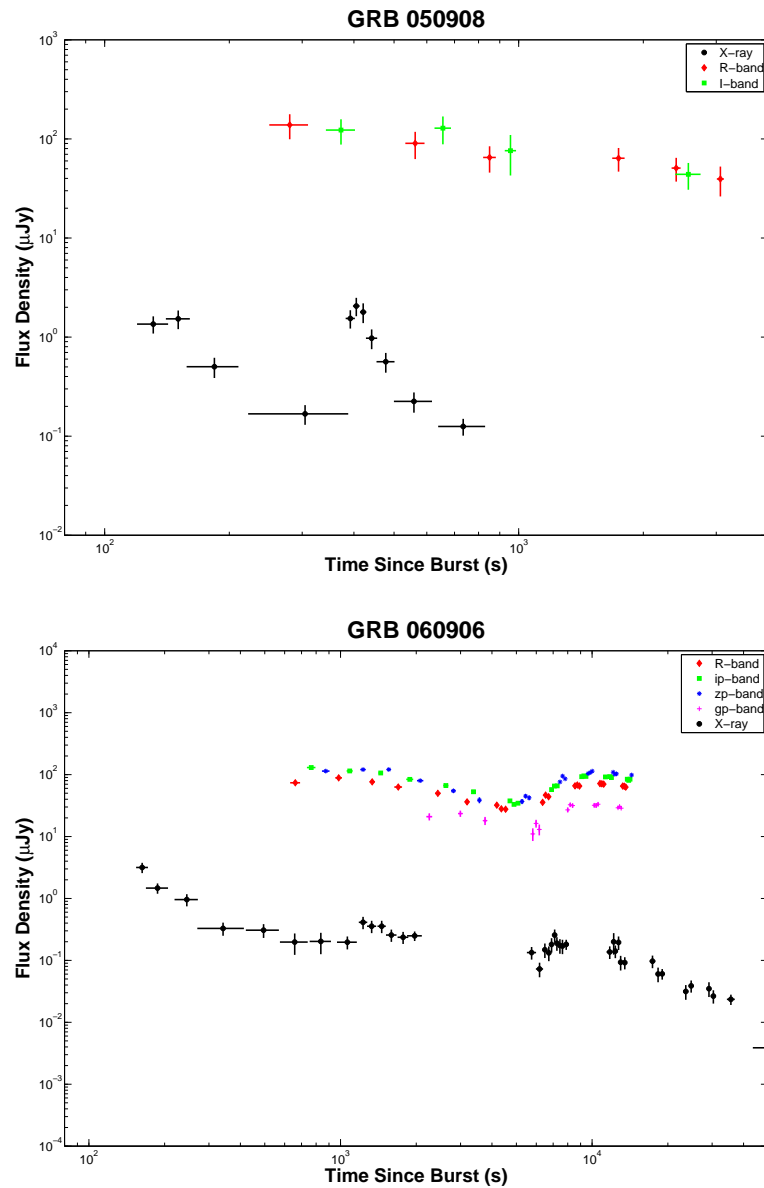
Figure 6.3 – X-ray and optical flares in *Swift* afterglows. *Top:* X-ray and optical light curves of GRB 050908. The X-ray shows a dramatic flare ($\Delta f/f \approx 50$ at $t \approx 400\,\mathrm{s}$) at early times. No corresponding variability is seen in the optical. *Bottom:* X-ray and optical light curves of GRB 060906. In this case, the re-brightening occurs in the optical while the X-ray decay is relatively flat. Both events require additional emission mechanisms beyond the forward shock synchrotron model.
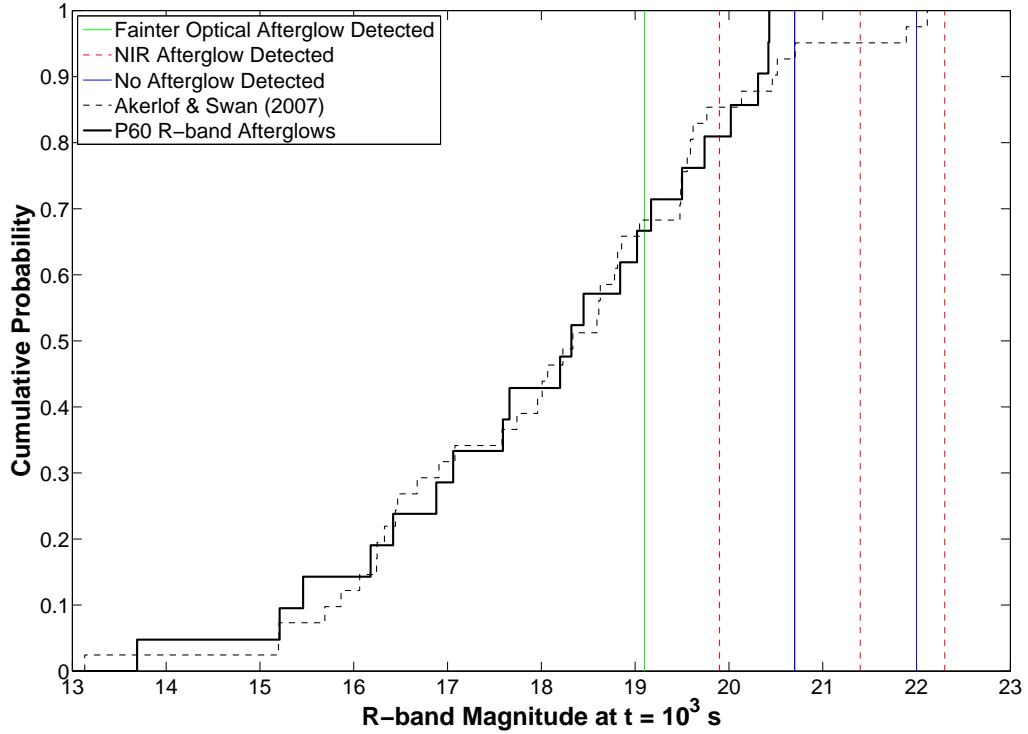
Figure 6.4 — P60-*Swift* optical afterglow brightness distribution. We plot here the observed optical brightness distribution of all events in our early afterglow sample at a common reference time of $t = 10^3$ s (solid line). The dashed line indicates a similar archival analysis performed by Akerlof & Swan (2007). The excellent agreement indicates our sample is representative of the *Swift* afterglow population. Minor deviations can be seen at the very faint end ($R_C \gtrsim 21$ mag), likely indicative of the P60 sensitivity limit. Vertical lines are upper limits for GRBs with optical afterglows from other facilities (green), GRBs with only NIR afterglows (red dashed), and GRBs with no detected optical or NIR afterglows (blue).

observed bandpass to the rest frame R_C-band, as described in Hogg et al. (2002). The resulting histogram is shown in Figure 6.5. At this time, we find a median value for the afterglow luminosity to be $\langle \log(L) \rangle = 46.39 \, \mathrm{erg\,s^{-1}}$ with a standard deviation of 1.4 dex. Also shown in Figure 6.5 is the best-fit single Gaussian distribution.

Several authors (Liang & Zhang, 2006; Nardini et al., 2006; Kann et al., 2006) have argued in favor of a bimodal distribution of intrinsic afterglow luminosity, with a class of nearby, sub-luminous events. Much like Melandri et al. (2008), we find no need for a bimodal distribution. While a single event (GRB 060210) is a significant outlier
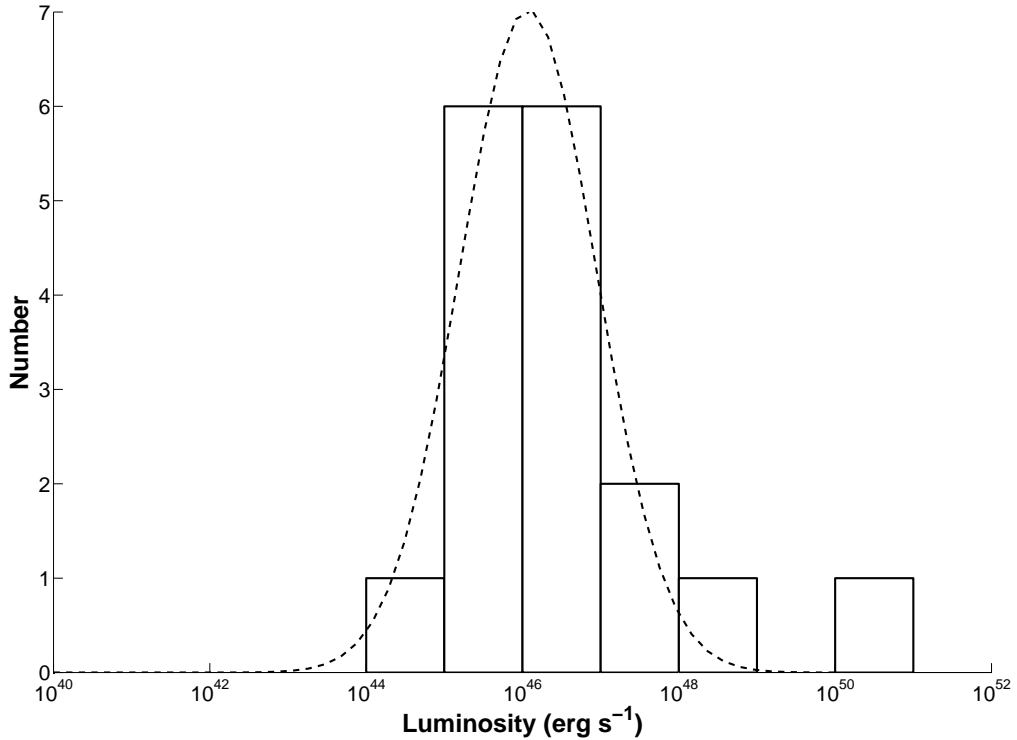
Figure 6.5 — P60-*Swift* optical afterglow luminosity distribution. We have measured the rest frame optical $R_{\rm C}$-band luminosity at a common (rest frame) time of $t = 10^3\,{\rm s}$ for all events in our early sample with a spectroscopic redshift. We find a good fit to a single log-normal distribution with mean $\log L = 46.68\,{\rm erg\,s^{-1}}$ and standard deviation $\sigma = 1.04$. The sole outlier (GRB 060210) falls on the over-luminous end because of its extreme k-correction (see text for details).

on the over-luminous end, we note this event is at relatively high redshift ($z = 3.91$; Cucchiara et al., 2006a) and has an extremely steep spectral index ($\beta = 7.2 \pm 0.7$). The resulting k-correction is therefore extremely large (and relatively uncertain). This seems a more likely explanation than such an extremely luminous burst.

6.3.4   Dark Bursts

We adopt here the definition of a "dark" GRB as one where the optical ($R_{\rm C}$-band) to X-ray spectral index satisfies $\beta_{OX} < 0.5$ (Jakobsson et al., 2004). Unlike definitions based solely on optical brightness, the β_{OX} method is physically motivated: an afterglow qualifies as dark when the ratio of optical to X-ray flux is incompatible

with standard synchrotron afterglow theory. By utilizing both the optical and X-ray afterglows, we can easily distinguish between intrinsically sub-luminous afterglows (i.e., those events that are faint in all bandpasses) and those afterglows that indicate an additional process is selectively suppressing the optical flux (or, alternatively, increasing the X-ray emission).

In Figure 6.6 we compare the X-ray and R_C-band flux densities extrapolated to a common time of $t = 10^3$ s for all 29 afterglows in our sample. The allowed region in the standard afterglow model, $0.50 \lesssim \beta_{OX} \lesssim 1.25$, is marked with solid lines. Like Melandri et al. (2008), we find that 50% of events qualify as dark under this definition. It is clear therefore that the faintness of the *Swift* optical afterglows cannot be attributed solely to distance, as this would not directly affect the measured flux ratio. Furthermore, this result stands in stark contrast with the study of pre-*Swift* events by Jakobsson et al. (2004), who found a dark burst incidence of only 10%.

The most important difference between our study and that of Jakobsson et al. (2004) is the time at which we evaluate β_{OX} ($t = 11$ hr for Jakobsson et al., 2004). In Figure 6.2 we demonstrate the importance of the reference time when calculating β_{OX}. Many *Swift* afterglows exhibit bright X-ray flares at early times (Burrows et al., 2005b), as well as a plateau decay phase indicative of continued energy injection into the forward shock (Nousek et al., 2006; Zhang et al., 2006). This late-time activity could artificially inflate the X-ray flux at early times, leading to spuriously low β_{OX} measurements (see GRB 080310, Figure 6.2).

While our optical coverage at $t = 11$ hr is relatively sparse, we find little evidence for evolution of β_{OX} between these two epochs. For the most part, afterglows evolve along constant curves of β_{OX} from $t = 10^3$ s to the end of our observations. This echoes the result found by Melandri et al. (2008).

Another possibility to explain dark optical afterglows is a high-redshift ($z \gtrsim 5$) origin. In this case, the observed R_C bandpass falls below the Ly-α cut-off in the GRB rest frame, leading to a significant suppression of optical flux due to absorption in the intergalactic medium. This is the case, for example, for GRB 060510B ($\beta_{OX} = 0.04$), which lies at $z = 4.9$ (Figure 6.6; Price et al., 2007).
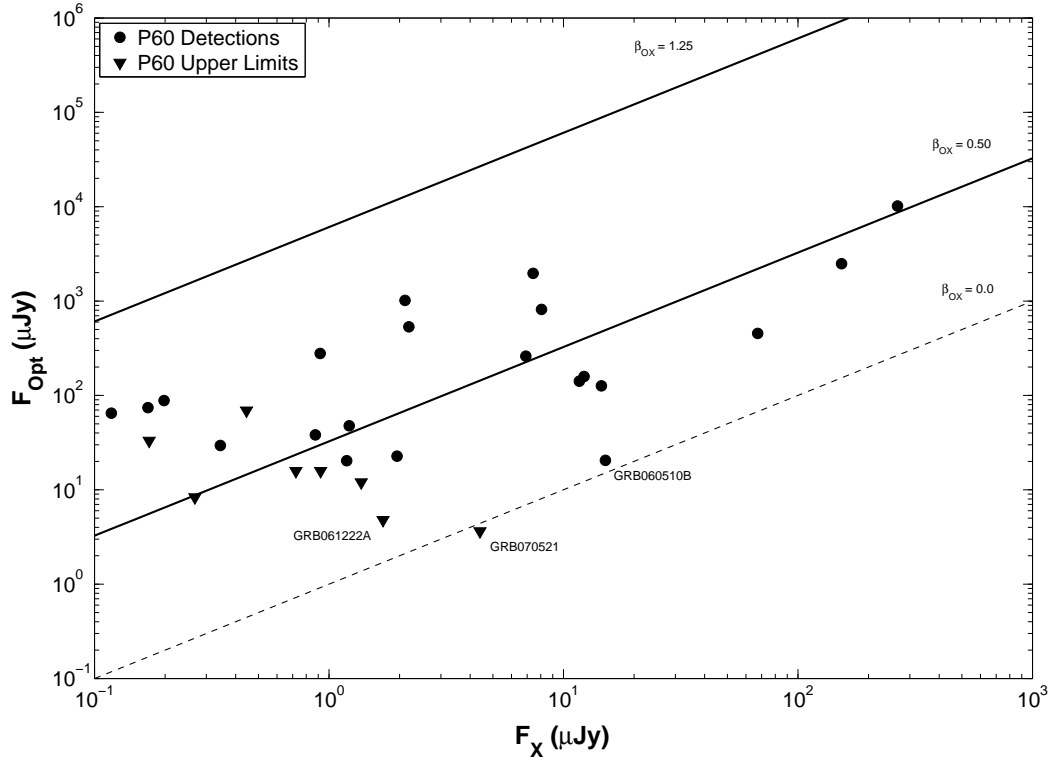
Figure 6.6 — Optical/X-ray spectral energy distribution of *Swift* GRBs. We plot the X-ray and optical flux (or upper limits) at a common reference time of $t = 10^3$ for all events in our P60-*Swift* sample. In standard afterglow theory, the optical to X-ray spectral index, β_{OX} should fall between $0.5 < \beta_{OX} < 1.25$ (solid black lines). In our sample, nearly 50% of afterglows quality as "dark" bursts ($\beta_{OX} < 0.5$). This stands in stark contrast to pre-*Swift* events, for which only $\approx 10\%$ of GRBs were found to be optically dark (Jakobsson et al., 2004).

While a high-redshift origin may account for a fraction of the observed dark bursts, other explanations are necessary for the majority of events. Theoretical models, assuming GRBs trace the cosmic star formation rate, predict a high-redshift ($z \gtrsim 7$) fraction of $\approx 10\%$ (Bromm & Loeb, 2006). Several events with $\beta_{OX} < 0.5$ have measured spectroscopic redshifts, firmly establishing the Ly-α cut-off below the observed R_C filter (e.g., GRB 060210: $\beta_{OX} = 0.37$, $z = 3.91$; Cucchiara et al., 2006a). And we can place upper limits on some events that do not have optical afterglows based on the presence of absorption in excess of the Galactic value in the X-ray afterglow spectrum (e.g., GRB 070521A: $z < 2.4$; Grupe et al., 2007).

Finally, we consider the possibility of extinction native to GRB host galaxies. Because long-duration GRBs have massive star progenitors, it is natural to expect them to explode in dusty, highly extinguished environments. However, broadband studies of some of the best sampled afterglows in the both pre-*Swift* and *Swift* eras indicate only a modest amount of host reddening ($\langle A_V \rangle \approx 0.2$ mag; Kann et al., 2006, 2007).

In contrast, we find evidence for significant host absorption in several of the afterglows in our sample. Using our multi-color P60 observations, we provide best-fit optical power-law spectral indices for all events with sufficient filter coverage in Table 6.2. Of the 7 dark bursts with measured values of β_O, 6 spectral indices are too steep to be explained by the standard afterglow formulation (i.e., $\beta_O > 1.5$).

To further quantify this effect, we have refitted our optical data, but in this case fixing the optical spectral index to $\beta_O = 0.6$ (the average value for bright *Swift* events; Kann et al., 2007). We then incorporated the effects of dust by adding the host galaxy reddening $[A_V(\text{host})]$ as a free parameter to the fit. In general, our data were not sufficient to distinguish between competing extinction laws (i.e., Milky Way, LMC, and SMC; Pei, 1992). We therefore assumed an SMC-like extinction curve, as this model has proved successful for most GRB afterglows. The results are shown in Table 6.2.

It is clear that the afterglows in our sample are significantly more reddened than the brightest afterglows in both the *Swift* and pre-*Swift* eras. Furthermore, even our host absorption measurements are quite biased; we could not measure $A_V(\text{host})$ for those events without P60 afterglows, which are likely to be the most extinguished events in our sample. Even some afterglows that do not qualify as dark, such as GRB 070208 and GRB 070419A, exhibit strong evidence for significant amounts of host galaxy dust $[A_V(\text{host}) \approx 1]$.

6.4   Discussion and Conclusions

6.4.1   Anomalous P60 Detection Efficiency

We have demonstrated in Section 6.3.1 that P60 was able to detect optical afterglow emission from a large fraction ($\sim 80\%$) of events for which observations began within an hour of the burst trigger. While the $1.5\,\mathrm{m}$ aperture is relatively large for a robotic facility, it would be nonetheless informative to understand systematic effects that affect our afterglow recovery rate. The ultimate goal, of course, is to better inform future GRB follow-up campaigns.

The first lesson from this campaign is the importance in observing in redder filters. We have shown in Section 6.3.4 that typical *Swift* events suffer from a non-negligible amount of host galaxy extinction (Table 6.2). Coupled with the additional effect of Ly-α absorption in the IGM from a median redshift of $\langle z \rangle \approx 3$, it is clear that a large fraction of the low UVOT detection efficiency is caused by its blue observing bandpass. The P60 automated follow-up sequence, consisting of alternating exposures in the R_{C}, i', and z' filters, while initially designed for identification of candidate high-z events, is actually well suited to maximize afterglow detection rates.

The large fraction of P60-detected bursts with spectroscopic redshifts, on the other hand, is almost certainly an artifact of the unequal longitudinal distribution of large optical telescopes. With the exception of the South African Large Telescope (SALT), all optical telescopes with apertures larger than $8\,\mathrm{m}$ fall within six time zones (UT-4 to UT-10). It not entirely surprising then, that so many promptly discovered P60 optical afterglows have spectroscopic redshifts from immediate follow-up with the largest optical facilities.

While building the largest optical facilities is often prohibitively expensive for all but the largest collaborations, $1\,\mathrm{m}$ class facilities are much more feasible, both in terms of cost and construction time scale. We wish here to echo the thoughts of many previous GRB observers (e.g., Akerlof & Swan, 2007) that future automated facilities be built at longitudes (and latitudes) not covered by current facilities. NIR coverage is particularly crucial to detect the most extinguished events and provide

tighter constraints on the afterglow SED and hence host galaxy extinction.

A longitudinally spaced ring of 1 m class facilities, as for example envisioned by the Las Cumbres Observatory Global Telescope[7] is well positioned in the future to recover the vast majority of GRB optical afterglows, assuming the follow-up is done in the reddest filters possible. Such coverage will be particularly important as we transition into the GLAST era, with its significantly decreased rate of precise GRB localizations.

6.4.2 Re-Visiting Dark Bursts

We now turn our attention to the issue of dark bursts in the *Swift* era. In Section 6.3.4, we demonstrated that a large fraction ($\approx 50\%$) of *Swift* afterglows showed suppressed emission in the optical bandpass (relative to the X-ray), that was due in large part to extinction in the host galaxy. Given the natural expectation that GRBs, since they are associated with massive stars, should form in relatively dusty environments, we wish to understand why our study of *Swift* events yields such a dramatically different dark burst fraction than previous work on pre-*Swift* GRBs (Jakobsson et al., 2004).

Certainly the higher redshift of *Swift* GRBs plays an important role in this respect. This is due only in part to IGM absorption blueward of Ly-α. For example, consider a host frame extinction of $A_V = 0.1$ mag. At $z = 1$, typical for pre-*Swift* events, the observed R_C filter corresponds roughly to rest frame U-band, and so an extinction of 0.17 mag (assuming a Milky Way-like extinction curve). On the other hand, at $z = 3$, the observed R_C-band corresponds to a rest frame wavelength of $\lambda = 1647$ Å. So at high redshift, the same amount of dust will produce nearly twice as much extinction in the observed bandpass. Solely because of redshifts effects, similar environments will produce different observed spectral slopes. This effect is exacerbated by the nature of dust grains in most GRB host galaxies, as the SMC extinction curve does not show the pronounced 2175 Å bump seen from the Milky Way (Pei, 1992).

On the other hand, selection effects have likely played a large role in our view

---

[7]See http://lcogt.net.

of extinction in GRB host galaxies to date. By selecting only the brightest optical afterglows, previous studies were strongly biased towards unextinguished events.

If GRBs do trace the cosmic star formation rate, our results suggest a significant fraction of star formation occurs in highly obscured environments. Kann et al. (2006) found a weak correlation between host reddening and sub-mm flux, and we believe a sensitive mid-infrared or sub-mm survey of GRB host galaxies would be an important confirmation of our results. However, instead of focusing on the brightest, best studied afterglows, as has often been done in the past (e.g., Tanvir et al., 2004; Michałowski et al., 2008), we instead suggest a survey of the optically darkest GRB afterglows to see if these events really do exhibit signs of obscured star formation.

Table 6.2.   P60-*Swift* Early Optical Afterglow Sample

GRB Name	P60 OT?	Other OT/IRT?[a]	Redshift[b]	α_1[c]	α_2[c]	t_b[c] (10^3 s)	β_O[c]	χ^2_r (d.o.f.)[c]	β_{OX}[d]	A_V (host)[e] (mag)
050412	No	No	···	···	···	···	···	···	< 0.49	···
050416A	Yes	···	0.6535	0.23 ± 0.08	$0.9^{+2.0}_{-0.3}$	$11.6^{+66.6}_{-8.9}$	2.6 ± 1.8	1.33 (7)	0.35	···
050607	No	OT	···	···	···	···	···	···	< 0.72	···
050713A	Yes	···	···	$0.62^{+0.12}_{-0.11}$	···	···	···	0.72 (7)	0.31	···
050820A[f]	Yes	···	2.615	···	···	···	···	···	0.40	< 0.10
050908	Yes	···	3.35	0.69 ± 0.05	···	···	-0.4 ± 1.1	0.75 (12)	0.91	···
050915A	No	IRT	···	···	···	···	···	···	< 0.44	···
060110	Yes	···	···	$0.92^{+0.30}_{-0.25}$	···	···	···	0.23 (8)	0.80	···
060210	Yes	···	3.91	0.93 ± 0.06	···	···	7.2 ± 0.7	1.43 (21)	0.37	$1.21^{+0.16}_{-0.12}$
060502A	Yes	···	1.51	0.49 ± 0.05	···	···	2.1 ± 0.3	0.42 (24)	0.53	0.53 ± 0.13
060510B	Yes	···	4.9	0.3 ± 0.5	···	···	$4.2^{+1.8}_{-2.2}$	0.15 (4)	0.04	···
060805A	No	No	···	···	···	···	···	···	< 0.76	···
060906[g]	Yes	···	3.685	···	···	···	2.2 ± 0.2	0.22 (20)	0.88	$0.20^{+0.01}_{-0.12}$
060908	Yes	···	2.43	1.04 ± 0.02	···	···	0.59 ± 0.07	2.27 (52)	0.82	···
060923A	No	IRT	···	···	···	···	···	···	< 0.41	···
061222A	No	IRT	···	···	···	···	···	···	< 0.15	···
070208	Yes	···	1.165	0.51 ± 0.02	···	···	2.21 ± 0.12	1.65 (23)	0.54	1.03 ± 0.09
070419A	Yes	···	0.97	-1.6 ± 0.3	1.08 ± 0.04	0.59 ± 0.02	1.8 ± 0.2	2.48 (16)	0.87	1.03 ± 0.17
070521	No	No	···	···	···	···	···	···	< −0.03	···
071003	Yes	···	1.60435	1.77 ± 0.05	···	···	0.86 ± 0.19	0.48 (8)	0.27	< 0.26
071010A	Yes	···	···	0.29 ± 0.19	···	···	-1.1 ± 0.7	0.69 (6)	0.89	···
071011	Yes	···	···	0.90 ± 0.20	···	···	1.9 ± 0.7	0.26 (6)	0.66	···
071020	Yes	···	2.145	0.89 ± 0.12	···	···	0.58 ± 0.27	2.16 (14)	0.52	···
071122	Yes	···	1.14	-0.08 ± 0.09	···	···	1.3 ± 0.6	0.36 (11)	0.64	0.58 ± 0.05
080310	Yes	···	2.43	0.02 ± 0.03	$0.68^{+0.11}_{-0.08}$	1.83 ± 0.02	0.91 ± 0.10	0.57 (21)	0.79	< 0.14
080319A	Yes	···	···	-0.9 ± 0.4	0.80 ± 0.07	$0.160^{+0.136}_{-0.070}$	2.0 ± 0.3	1.50 (11)	0.41	···
080319B	Yes	···	0.937	$1.93^{+0.04}_{-0.06}$	1.238 ± 0.004	10.10 ± 0.17	0.50 ± 0.02	0.57 (280)	0.52	···
080319C	Yes	···	1.95	1.4 ± 0.2	···	···	2.4 ± 0.2	2.32 (3)	0.36	0.67 ± 0.06
080320	Yes	···	···	···	···	···	···	···	< 0.31	···

[a]Optical (OT) and Infrared (IRT) transient references — GRB 050607: Rhoads, 2005; GRB 050915A: Bloom & Alatalo, 2005; GRB 060923A: Tanvir et al., 2006; GRB 061222A: Cenko & Fox, 2006.

[b]Redshift references — GRB 050416A: Soderberg et al., 2007; GRB 050908: Fugazza et al., 2005; GRB 060210: Cucchiara et al., 2006a; GRB 060502A: Cucchiara et al., 2006b; GRB 060510B: Price et al., 2007; GRB 060906: Jakobsson et al., 2006a; GRB 060908: Rol et al., 2006; GRB 070208: Cucchiara et al., 2007b; GRB 070419A: Cenko et al., 2007; GRB 071003: Perley et al., 2008; GRB 071020: Jakobsson et al., 2007; GRB 071122: Cucchiara et al., 2007a; GRB 080310: Prochaska et al., 2008; GRB 080319B: Vreeswijk et al., 2008; GRB 080319C: Wiersema et al., 2008.

[c]We fitted the flux density to a single or broken power-law model of the form $F_\nu = t^{-\alpha} \nu^{-\beta}$.

[d]The optical-to-X-ray spectral index, measured at $t = 10^3$ s.

[e]We fitted for the host galaxy reddening by fixing the spectral index to $\beta = 0.6$ and assuming an SMC-like extinction law (Pei, 1992).

[f]The optical light curve of GRB 050820A consists of many power-law segments. See Cenko et al. (2006b) for details.

[g]The optical light curve of GRB 060906 is not well described by either a single or broken power-law. The spectral index was calculated over only a small period of relatively flat evolution ($t > 10^4$ s).

Chapter 7

Summary and Future Directions

The prompt and accurate positions provided by the *Swift* γ-ray Burst (GRB) Explorer (Gehrels et al., 2004) have successfully unveiled a new window in GRB studies: the mysterious early afterglow phase. Robotic optical telescopes like the Palomar 60 inch (P60; Chapter 2) now routinely provide observations immediately following, and in some cases during the prompt emission, something achieved for only handful of events before *Swift*. Together with prompt observations from the on-board X-ray Telescope (XRT; Burrows et al., 2005a), our picture of the central engine powering these explosions has evolved dramatically over the course of the last four years. For instance, the contemporaneous γ-ray, X-ray, and optical observations of the prompt emission from GRB 050820A (Chapter 3) demonstrated that the bright, late-time ($t \gg \Delta t_{\mathrm{GRB}}$) flares seen in many *Swift* X-ray afterglows (Burrows et al., 2005b) arise from delayed engine activity. The simultaneous optical emission, however, appears to be dominated by a different physical mechanism, most likely the onset of the afterglow as the outgoing blast wave is decelerated while sweeping up the circumburst medium.

Despite this great progress, constraining the collimation-corrected energies from *Swift* GRBs has proven significantly more challenging than originally envisioned. Because of its enhanced sensitivity, the Burst Alert Telescope (BAT; Barthelmy et al., 2005a) on-board *Swift* is capable of detecting events with wider opening angles than previous GRB missions. The typical *Swift* afterglow is simply too faint to measure a jet break at these late times, even with a medium aperture facility like P60. In-

stead I required the largest ground-based optical facilities (e.g., GRB 070125; Chandra et al., 2008) or even space-based facilities like *HST* (e.g., GRB 050820A; Chapter 2) to measure the opening angles of even the brightest *Swift* afterglows. Because these resources are significantly more precious than a telescope like P60, I was limited to focusing on only a handful of events.

Nonetheless, the study of energetics in the *Swift* era has yielded some interesting surprises. Given the increased sensitivity of the BAT, one might naively expect to find a preference for under-luminous events too faint for previous missions. I have discovered, however, a new class of *Swift* events that appear to be an order of magnitude more energetic than any well-studied pre-*Swift* event, the so-called "hyper-energetic" GRBs ($E_{\rm tot} > 10^{52}$ erg; Chapters 3–4). Together with the discovery of late-time engine activity, these results pose significant challenges to current GRB progenitor models. One the one hand, a magnetar remnant (Usov, 1992) could more naturally accommodate late-time engine activity, as the surface the neutron star could act to extend the life of the accretion disk powering the ultra-relativistic outflow. It is difficult to conceive, however, how the large energies required by hyper-energetic events could be explained with the less massive progenitors of the magnetar model; even the extremely massive stars resulting in black hole remnants (i.e., "collapsars"; Woosley, 1993) struggle to accommodate an energy release in excess of 10^{52} erg.

In the future, the launch of NASA's *GLAST* satellite will open a new window on GRB energetics. In particular, the on-board Large Area Telescope (LAT) will provide energy coverage extending from ~ 10 MeV–100 GeV. By covering $\sim 20\%$ of the sky at any given time, the LAT should detect dozens of GRBs over its lifetime in an almost entirely unexplored phase space. Much like blazars, those GRBs capable of producing GeV photons should be the most energetic and narrowly beamed events. Together, synergistic *GLAST* and *Swift* observations in the coming years should be able to shed light on the opening angles and energy release of a larger sample of GRBs.

In terms of the study of the environments of GRBs, the path to future progress is not straightforward. It remains puzzling how individual events such as GRB 050525A (Chapter 4), with overwhelming evidence of a massive star origin, appear to favor a

constant density circumburst environment. While the relatively simplistic models for afterglow emission (Section 1.3) may account for some of the discrepancy, progenitor mass loss has been consistently observed in radio light curves from ordinary (i.e., non-relativistic) core-collapse supernovae (SNe). The extreme relativistic events detected by *GLAST* may actually disfavor such studies, as the radial distances probed by *GLAST* afterglows will be even further from the central engine than *Swift* GRBs.

Because of the large event rate, *Swift* will continue to detect occasional bright optical afterglows suitable for absorption spectroscopy in the upcoming years, providing ample opportunity to study the ISM environments where massive stars form. I have shown in Chapter 5 that at least some long-duration GRBs explode far away from the dense disks of their host, and suggest that GRB 070125 be located in a tidal tail enriched by galaxy interaction. Since publication, another event in a halo environment has been discovered (GRB 071003; Perley et al., 2008), and it is possible that others may have been missed by merely associating the strongest absorption system with the GRB host galaxy. It seems likely that more such events will continued to be discovered by *Swift*, suggesting that perhaps they may be able to constrain the fraction of star formation that occurs in such environments at high redshift. Though certainly far off in the future, such a result would have important implications for theories of galaxy formation and large scale structure in the universe.

My study of the early optical afterglows of a sample of 29 events observed with P60 in Chapter 6 led me to conclude that a large fraction ($\sim 50\%$) suffer from significant dust absorption in their host galaxies [$A_V(\text{host}) \gtrsim 0.2$]. While this result would be naively expected from their massive star origin, previous studies of GRB optical afterglows largely missed this obscured population of events. I argue this is due in large part to selection effects. Looking forward, sensitive mid-infrared and sub-mm searches of optically "dark" GRB afterglows might yield important insight into the process of obscured star formation in the universe. Though *Spitzer* will soon run out of coolant, significantly degrading its mid- and far-infrared capabilities, observations with the Combined Array for Research in Millimeter-wave Astronomy (CARMA) and ultimately the Atacama Large Millimeter Array (ALMA) offer the promise of solving

the dark burst mystery once and for all.

Finally, the robotic P60 will continue to perform rapid-response GRB follow-up for the life of *Swift* and beyond. Undoubtedly the system will continue to provide many new and exciting discoveries in the future, much as it has done for the past four years. However, the burgeoning field of transient optical astronomy offers an additional venue well suited to the unique capabilities of the facility. Planned wide-angle, high-cadence optical surveys such as Pan-STARRS (Panoramic Survey Telescope and Rapid Response System; Kaiser et al., 2002) and the Palomar Transient Factory (PTF) will soon be providing dozens of new transient events each night. Multi-color follow-up with P60 will be invaluable to classify and follow up these discoveries. Both will serve as important pathfinders for the Large Synoptic Survey Telescope (LSST; Tyson, 2005), which, with its overwhelming discovery capabilities, should once and for all usher in the era of fully robotic astronomy.

Appendix A

The P60-*Swift* Early Optical Afterglow Catalog

Table A.1: P60-*Swift* Early Optical Afterglow Catalog

GRB Name	UT Date[a]	Time Since Burst[b] (s)	Filter	Exposure Time (s)	Magnitude
GRB 050412	2005 Apr 12.2431	391.0	R_{C}	60.0	> 20.8
$\cdots$	2005 Apr 12.2468	684.7	R_{C}	180.0	> 21.4
$\cdots$	2005 Apr 12.2512	1063.7	i	180.0	> 21.0
$\cdots$	2005 Apr 12.2580	1646.0	z	180.0	> 20.2
$\cdots$	2005 Apr 12.2720	2858.8	R_{C}	960.0	> 22.5
$\cdots$	2005 Apr 12.2831	2817.0	i	960.0	> 22.0
GRB 050416A[c]	2005 Apr 16.4641	216.0	I_{C}	120.0	18.82 ± 0.11
$\cdots$	2005 Apr 16.4659	371.5	I_{C}	120.0	18.86 ± 0.11
$\cdots$	2005 Apr 16.4677	527.0	I_{C}	120.0	19.16 ± 0.13
$\cdots$	2005 Apr 16.4696	691.2	I_{C}	120.0	19.35 ± 0.23
$\cdots$	2005 Apr 16.4714	846.7	I_{C}	120.0	19.01 ± 0.12
$\cdots$	2005 Apr 16.4731	1002.2	I_{C}	120.0	19.53 ± 0.18
$\cdots$	2005 Apr 16.4772	1347.8	z	360.0	19.16 ± 0.27
$\cdots$	2005 Apr 16.4833	1874.9	I_{C}	60.0	19.09 ± 0.20
$\cdots$	2005 Apr 16.4880	2281.0	I_{C}	60.0	19.34 ± 0.23
$\cdots$	2005 Apr 17.3895	8.017×10^4	R_{C}	4320.0	22.62 ± 0.30
$\cdots$	2005 Apr 17.4006	8.113×10^4	z	2880.0	> 20.4
$\cdots$	2005 Apr 17.4087	8.179×10^4	i	4200.0	22.05 ± 0.30
$\cdots$	2005 Apr 18.2884	1.578×10^5	R_{C}	8280.0	> 23.6
$\cdots$	2005 Apr 18.4031	1.677×10^5	i	8280.0	> 22.8
GRB 050607	2005 Jun 7.3951	1081.0	R_{C}	60.0	> 19.1
$\cdots$	2005 Jun 7.3997	1545.0	R_{C}	180.0	> 19.1
$\cdots$	2005 Jun 7.4017	1713.2	i	180.0	> 18.7
$\cdots$	2005 Jun 7.4029	1816.4	z	180.0	> 18.6
$\cdots$	2005 Jun 7.4194	3334.9	z	360.0	> 18.6

Table A.1 — Continued

GRB Name	UT Date[a]	Time Since Burst[b] (s)	Filter	Exposure Time (s)	Magnitude
$\cdots$	2005 Jun 7.4302	5649.1	$R_{\rm C}$	1560.0	> 19.2
$\cdots$	2005 Jun 7.4340	5851.5	i	1440.0	> 18.7
GRB 050713A	2005 Jul 13.1960	821.7	$R_{\rm C}$	60.0	19.62 ± 0.22
$\cdots$	2005 Jul 13.2010	1254.1	$R_{\rm C}$	60.0	19.92 ± 0.26
$\cdots$	2005 Jul 13.2013	1341.0	i	180.0	19.38 ± 0.33
$\cdots$	2005 Jul 13.2040	1514.6	$R_{\rm C}$	60.0	19.92 ± 0.26
$\cdots$	2005 Jul 13.2071	1812.3	$R_{\rm C}$	120.0	19.84 ± 0.22
$\cdots$	2005 Jul 13.2139	2401.1	$R_{\rm C}$	120.0	20.19 ± 0.28
$\cdots$	2005 Jul 13.2143	2552.1	i	360.0	19.48 ± 0.33
$\cdots$	2005 Jul 13.2209	2999.8	$R_{\rm C}$	120.0	19.97 ± 0.24
$\cdots$	2005 Jul 13.2336	4224.4	i	360.0	20.22 ± 0.40
$\cdots$	2005 Jul 13.3431	1.386×10^4	i	720.0	> 20.1
$\cdots$	2005 Jul 13.3433	1.400×10^4	$R_{\rm C}$	960.0	> 19.6
GRB 050820A[d]	2005 Aug 20.2766	236.0	$R_{\rm C}$	60.0	15.39 ± 0.04
$\cdots$	2005 Aug 20.2777	328.0	i	60.0	14.91 ± 0.02
$\cdots$	2005 Aug 20.2787	417.0	z	60.0	13.93 ± 0.11
$\cdots$	2005 Aug 20.2802	518.0	$R_{\rm C}$	60.0	14.65 ± 0.02
$\cdots$	2005 Aug 20.2811	626.0	i	60.0	14.42 ± 0.01
$\cdots$	2005 Aug 20.2821	712.0	z	60.0	14.27 ± 0.14
$\cdots$	2005 Aug 20.2833	812.0	$R_{\rm C}$	60.0	15.06 ± 0.03
$\cdots$	2005 Aug 20.2844	913.0	i	60.0	14.78 ± 0.01
$\cdots$	2005 Aug 20.2856	1017.0	z	60.0	14.62 ± 0.21
$\cdots$	2005 Aug 20.2868	1146.0	$R_{\rm C}$	120.0	15.42 ± 0.02
$\cdots$	2005 Aug 20.2886	1304.0	i	120.0	15.24 ± 0.02
$\cdots$	2005 Aug 20.2905	1463.0	z	120.0	15.02 ± 0.13
$\cdots$	2005 Aug 20.2923	1620.0	g	120.0	16.27 ± 0.04
$\cdots$	2005 Aug 20.2941	1781.0	$R_{\rm C}$	120.0	16.05 ± 0.03
$\cdots$	2005 Aug 20.2960	1942.0	i	120.0	15.74 ± 0.02
$\cdots$	2005 Aug 20.2979	2103.0	z	120.0	15.49 ± 0.14
$\cdots$	2005 Aug 20.2997	2262.0	g	120.0	16.62 ± 0.04
$\cdots$	2005 Aug 20.3016	2426.0	$R_{\rm C}$	120.0	16.39 ± 0.02
$\cdots$	2005 Aug 20.3035	2590.0	i	120.0	16.07 ± 0.02
$\cdots$	2005 Aug 20.3054	2752.0	z	120.0	15.96 ± 0.20
$\cdots$	2005 Aug 20.3072	2911.0	g	120.0	16.92 ± 0.05
$\cdots$	2005 Aug 20.3130	3440.0	$R_{\rm C}$	360.0	16.77 ± 0.02
$\cdots$	2005 Aug 20.3175	3918.0	i	360.0	16.54 ± 0.03
$\cdots$	2005 Aug 20.3346	5394.0	g	360.0	17.59 ± 0.05
$\cdots$	2005 Aug 20.3413	5885.0	$R_{\rm C}$	360.0	17.32 ± 0.04
$\cdots$	2005 Aug 20.3460	6382.0	i	360.0	17.02 ± 0.05
$\cdots$	2005 Aug 20.3519	6889.0	g	360.0	17.87 ± 0.06
$\cdots$	2005 Aug 20.3587	7392.0	$R_{\rm C}$	360.0	17.48 ± 0.04
$\cdots$	2005 Aug 20.3635	7893.0	i	360.0	17.22 ± 0.04
$\cdots$	2005 Aug 20.3693	8397.0	g	360.0	18.11 ± 0.06

Table A.1 — Continued

GRB Name	UT Date[a]	Time Since Burst[b] (s)	Filter	Exposure Time (s)	Magnitude
$\cdots$	2005 Aug 20.3763	8906.0	$R_{\rm C}$	360.0	17.69 ± 0.04
$\cdots$	2005 Aug 20.3811	9414.0	i	360.0	17.23 ± 0.05
$\cdots$	2005 Aug 20.3940	1.044×10^4	$R_{\rm C}$	360.0	17.85 ± 0.04
$\cdots$	2005 Aug 20.3940	1.070×10^4	g	720.0	18.29 ± 0.06
$\cdots$	2005 Aug 20.3989	1.095×10^4	i	360.0	17.34 ± 0.03
$\cdots$	2005 Aug 20.4161	1.235×10^4	$R_{\rm C}$	360.0	17.78 ± 0.04
$\cdots$	2005 Aug 20.4292	1.357×10^4	i	360.0	17.48 ± 0.04
$\cdots$	2005 Aug 20.4427	1.465×10^4	$R_{\rm C}$	360.0	17.97 ± 0.04
$\cdots$	2005 Aug 20.4357	1.491×10^4	g	720.0	18.36 ± 0.06
$\cdots$	2005 Aug 20.4479	1.518×10^4	i	360.0	17.68 ± 0.04
$\cdots$	2005 Aug 20.4614	1.626×10^4	$R_{\rm C}$	360.0	18.01 ± 0.04
$\cdots$	2005 Aug 20.4666	1.680×10^4	i	360.0	17.71 ± 0.05
$\cdots$	2005 Aug 20.4804	1.790×10^4	$R_{\rm C}$	360.0	18.03 ± 0.04
$\cdots$	2005 Aug 20.4816	1.828×10^4	g	720.0	18.59 ± 0.09
$\cdots$	2005 Aug 20.4857	1.845×10^4	i	360.0	17.72 ± 0.04
$\cdots$	2005 Aug 20.5007	1.966×10^4	$R_{\rm C}$	360.0	18.16 ± 0.05
$\cdots$	2005 Aug 22.2243	1.753×10^5	$R_{\rm C}$	6840.0	20.51 ± 0.11
$\cdots$	2005 Aug 22.2299	1.758×10^5	i	6840.0	19.97 ± 0.12
$\cdots$	2005 Aug 23.2404	2.647×10^5	$R_{\rm C}$	8400.0	20.89 ± 0.10
$\cdots$	2005 Aug 23.2616	2.657×10^5	i	7560.0	20.48 ± 0.12
$\cdots$	2005 Aug 24.2684	3.535×10^5	$R_{\rm C}$	8400.0	21.22 ± 0.11
$\cdots$	2005 Aug 24.2860	3.550×10^5	i	8400.0	20.59 ± 0.11
$\cdots$	2005 Aug 25.3647	4.427×10^5	$R_{\rm C}$	2880.0	21.34 ± 0.13
$\cdots$	2005 Aug 25.4199	4.470×10^5	i	2400.0	21.02 ± 0.15
$\cdots$	2005 Aug 26.3113	5.252×10^5	$R_{\rm C}$	3600.0	21.64 ± 0.12
$\cdots$	2005 Aug 26.3385	5.288×10^5	i	4800.0	21.17 ± 0.14
$\cdots$	2005 Aug 27.3056	6.120×10^5	i	4440.0	21.30 ± 0.13
$\cdots$	2005 Aug 27.3036	6.121×10^5	$R_{\rm C}$	4800.0	21.80 ± 0.12
GRB 050908	2005 Sep 8.2408	279.9	$R_{\rm C}$	60.0	18.46 ± 0.13
$\cdots$	2005 Sep 8.2418	372.3	i	60.0	18.10 ± 0.16
$\cdots$	2005 Sep 8.2440	562.4	$R_{\rm C}$	60.0	18.99 ± 0.19
$\cdots$	2005 Sep 8.2451	656.2	i	60.0	18.02 ± 0.14
$\cdots$	2005 Sep 8.2474	850.7	$R_{\rm C}$	60.0	19.28 ± 0.22
$\cdots$	2005 Sep 8.2477	941.6	z	180.0	> 18.2
$\cdots$	2005 Sep 8.2486	955.4	i	60.0	18.66 ± 0.21
$\cdots$	2005 Sep 8.2573	1742.4	$R_{\rm C}$	120.0	19.37 ± 0.15
$\cdots$	2005 Sep 8.2650	2400.9	$R_{\rm C}$	120.0	19.54 ± 0.16
$\cdots$	2005 Sep 8.2655	2569.5	i	360.0	19.20 ± 0.14
$\cdots$	2005 Sep 8.2674	2735.3	z	360.0	> 19.3
$\cdots$	2005 Sep 8.2727	3069.9	$R_{\rm C}$	120.0	19.80 ± 0.19
$\cdots$	2005 Sep 8.3206	7598.4	$R_{\rm C}$	900.0	20.68 ± 0.14
$\cdots$	2005 Sep 8.2655	2569.5	i	360.0	19.20 ± 0.14
$\cdots$	2005 Sep 8.4723	2.071×10^4	$R_{\rm C}$	900.0	21.62 ± 0.24

Table A.1 — Continued

GRB Name	UT Date[a]	Time Since Burst[b] (s)	Filter	Exposure Time (s)	Magnitude
$\cdots$	2005 Sep 8.4905	2.237×10^4	i	1080.0	20.70 ± 0.16
$\cdots$	2005 Sep 8.5011	2.319×10^4	R_{C}	900.0	21.66 ± 0.28
$\cdots$	2005 Sep 9.2955	9.273×10^4	i	2700.0	> 21.3
$\cdots$	2005 Sep 9.2968	9.320×10^4	R_{C}	3420.0	> 22.3
GRB 050915A	2005 Sep 15.4767	257.0	R_{C}	60.0	> 20.3
$\cdots$	2005 Sep 15.4780	365.5	i	60.0	> 19.6
$\cdots$	2005 Sep 15.4792	472.5	z	60.0	> 19.1
$\cdots$	2005 Sep 15.4799	501.1	R_{C}	180.0	> 20.7
$\cdots$	2005 Sep 15.4812	611.5	i	180.0	> 20.5
$\cdots$	2005 Sep 15.4824	721.5	z	180.0	> 19.6
$\cdots$	2005 Sep 15.4963	1916.6	R_{C}	360.0	> 21.1
$\cdots$	2005 Sep 15.4986	2117.9	i	360.0	> 21.0
$\cdots$	2005 Sep 15.5009	2319.4	z	360.0	> 20.0
GRB 060110	2006 Jan 10.3493	1334.5	R_{C}	60.0	17.45 ± 0.22
$\cdots$	2006 Jan 10.3590	2170.0	i'	60.0	17.45 ± 0.20
$\cdots$	2006 Jan 10.3608	2312.8	i'	30.0	17.46 ± 0.21
$\cdots$	2006 Jan 10.3621	2424.5	i'	30.0	17.77 ± 0.23
$\cdots$	2006 Jan 10.3634	2538.9	i'	30.0	17.83 ± 0.26
$\cdots$	2006 Jan 10.3647	2648.0	i'	30.0	17.85 ± 0.25
$\cdots$	2006 Jan 10.3660	2758.8	i'	30.0	17.55 ± 0.22
$\cdots$	2006 Jan 10.3674	2883.9	i'	30.0	17.80 ± 0.23
$\cdots$	2006 Jan 10.3687	2992.6	i'	30.0	17.87 ± 0.24
$\cdots$	2006 Jan 10.3700	3104.7	i'	30.0	17.95 ± 0.28
$\cdots$	2006 Jan 10.4083	6476.3	i'	150.0	18.60 ± 0.24
$\cdots$	2006 Jan 10.4322	8536.1	i'	150.0	> 18.8
GRB 060210	2006 Feb 10.2105	289.2	R_{C}	60.0	18.22 ± 0.26
$\cdots$	2006 Feb 10.2115	377.9	R_{C}	60.0	18.60 ± 0.29
$\cdots$	2006 Feb 10.2138	569.4	z'	60.0	16.05 ± 0.41
$\cdots$	2006 Feb 10.2148	662.6	R_{C}	60.0	18.29 ± 0.29
$\cdots$	2006 Feb 10.2160	760.8	i'	60.0	17.34 ± 0.22
$\cdots$	2006 Feb 10.2171	855.5	z'	60.0	16.64 ± 0.36
$\cdots$	2006 Feb 10.2182	950.3	R_{C}	60.0	18.35 ± 0.27
$\cdots$	2006 Feb 10.2193	1044.9	i'	60.0	17.78 ± 0.21
$\cdots$	2006 Feb 10.2204	1140.6	z'	60.0	16.98 ± 0.38
$\cdots$	2006 Feb 10.2215	1265.7	R_{C}	120.0	19.25 ± 0.30
$\cdots$	2006 Feb 10.2233	1425.1	i'	120.0	18.18 ± 0.21
$\cdots$	2006 Feb 10.2330	2262.9	R_{C}	120.0	19.77 ± 0.26
$\cdots$	2006 Feb 10.2349	2422.1	i'	120.0	19.12 ± 0.23
$\cdots$	2006 Feb 10.2386	2743.7	R_{C}	120.0	20.28 ± 0.31
$\cdots$	2006 Feb 10.2404	2904.8	i'	120.0	19.06 ± 0.20
$\cdots$	2006 Feb 10.2430	3304.4	g	480.0	> 20.2
$\cdots$	2006 Feb 10.2460	3387.9	i'	120.0	19.25 ± 0.20
$\cdots$	2006 Feb 10.2484	3710.8	R_{C}	360.0	20.17 ± 0.26

Table A.1 — Continued

GRB Name	UT Date[a]	Time Since Burst[b] (s)	Filter	Exposure Time (s)	Magnitude
$\cdots$	2006 Feb 10.2516	3870.3	i'	120.0	19.51 ± 0.21
$\cdots$	2006 Feb 10.2570	4501.8	R_C	450.0	20.86 ± 0.32
$\cdots$	2006 Feb 10.2636	5068.1	i'	450.0	20.08 ± 0.21
$\cdots$	2006 Feb 10.2833	6768.5	i'	450.0	20.17 ± 0.23
$\cdots$	2006 Feb 10.2845	7105.1	R_C	900.0	20.91 ± 0.30
$\cdots$	2006 Feb 10.2853	7391.3	g	1350.0	> 20.3
$\cdots$	2006 Feb 10.3124	9511.9	i'	900.0	20.41 ± 0.23
$\cdots$	2006 Feb 10.3271	1.078×10^4	R_C	900.0	> 20.8
$\cdots$	2006 Feb 11.1063	7.915×10^4	i'	3000.0	> 22.5
GRB 060502A	2006 May 2.1536	2287.2	R_C	60.0	19.93 ± 0.19
$\cdots$	2006 May 2.1549	2397.3	i'	60.0	19.67 ± 0.27
$\cdots$	2006 May 2.1561	2508.5	z'	60.0	20.43 ± 0.71
$\cdots$	2006 May 2.1574	2619.4	R_C	60.0	20.18 ± 0.21
$\cdots$	2006 May 2.1586	2725.1	i'	60.0	19.93 ± 0.29
$\cdots$	2006 May 2.1600	2838.6	z'	60.0	19.20 ± 0.71
$\cdots$	2006 May 2.1613	2982.9	R_C	120.0	19.88 ± 0.15
$\cdots$	2006 May 2.1634	3168.1	i'	120.0	20.03 ± 0.29
$\cdots$	2006 May 2.1677	3537.1	g	120.0	21.18 ± 0.35
$\cdots$	2006 May 2.1697	3708.2	R_C	120.0	20.45 ± 0.18
$\cdots$	2006 May 2.1718	3892.4	i'	120.0	20.23 ± 0.30
$\cdots$	2006 May 2.1727	4088.6	z'	360.0	19.68 ± 0.49
$\cdots$	2006 May 2.1762	4267.4	g	120.0	21.35 ± 0.37
$\cdots$	2006 May 2.1783	4454.1	R_C	120.0	20.23 ± 0.17
$\cdots$	2006 May 2.1805	4642.6	i'	120.0	20.07 ± 0.28
$\cdots$	2006 May 2.1848	5016.4	g	120.0	21.48 ± 0.38
$\cdots$	2006 May 2.1980	6318.2	R_C	450.0	20.41 ± 0.14
$\cdots$	2006 May 2.2054	6956.9	g	450.0	21.62 ± 0.33
$\cdots$	2006 May 2.2127	7591.7	i'	450.0	20.51 ± 0.29
$\cdots$	2006 May 2.2201	8228.6	R_C	450.0	20.50 ± 0.14
$\cdots$	2006 May 2.2275	8870.9	g	450.0	21.81 ± 0.34
$\cdots$	2006 May 2.2349	9509.8	i'	450.0	20.44 ± 0.28
$\cdots$	2006 May 2.2423	1.015×10^4	R_C	450.0	20.74 ± 0.15
$\cdots$	2006 May 2.2498	1.079×10^4	g	450.0	21.84 ± 0.34
$\cdots$	2006 May 2.2700	1.254×10^4	i'	450.0	20.81 ± 0.29
$\cdots$	2006 May 3.2888	1.019×10^5	i'	3150.0	22.01 ± 0.33
$\cdots$	2006 May 3.2951	1.025×10^5	R_C	3150.0	22.08 ± 0.22
$\cdots$	2006 May 3.3023	1.047×10^5	g	3150.0	> 22.9
$\cdots$	2006 May 4.1513	1.756×10^5	i'	1500.0	> 21.4
$\cdots$	2006 May 4.1709	1.773×10^5	R_C	1500.0	> 21.4
GRB 060510B	2006 May 10.3671	1610.7	R_C	60.0	> 19.5
$\cdots$	2006 May 10.3681	1698.0	i'	60.0	> 20.3
$\cdots$	2006 May 10.3692	1793.5	z'	60.0	19.51 ± 0.71
$\cdots$	2006 May 10.3696	1892.3	R_C	180.0	> 20.2

Table A.1 — Continued

GRB Name	UT Date[a]	Time Since Burst[b] (s)	Filter	Exposure Time (s)	Magnitude
$\cdots$	2006 May 10.3707	1983.5	i'	180.0	> 20.3
$\cdots$	2006 May 10.3718	2079.7	z'	180.0	19.68 ± 0.71
$\cdots$	2006 May 10.3828	3117.1	$R_{\rm C}$	360.0	> 20.7
$\cdots$	2006 May 10.3846	3272.3	i'	360.0	21.19 ± 0.45
$\cdots$	2006 May 10.3864	3430.1	z'	360.0	19.77 ± 0.68
$\cdots$	2006 May 10.3882	3585.8	g	360.0	> 21.4
$\cdots$	2006 May 10.4240	7397.9	$R_{\rm C}$	1800.0	21.68 ± 0.25
$\cdots$	2006 May 10.4393	8628.7	i'	1620.0	21.31 ± 0.39
$\cdots$	2006 May 10.4494	9597.6	z'	1800.0	20.48 ± 0.67
GRB 060805A	2006 Aug 5.2020	214.4	$R_{\rm C}$	60.0	> 20.0
$\cdots$	2006 Aug 5.2030	304.7	i'	60.0	> 20.4
$\cdots$	2006 Aug 5.2042	402.6	z'	60.0	> 19.7
$\cdots$	2006 Aug 5.2044	447.2	i'	180.0	> 20.7
$\cdots$	2006 Aug 5.2055	543.7	z'	120.0	> 20.0
$\cdots$	2006 Aug 5.2127	1196.7	$R_{\rm C}$	180.0	> 20.3
GRB 060906	2006 Sep 6.3634	661.0	$R_{\rm C}$	60.0	19.18 ± 0.16
$\cdots$	2006 Sep 6.3646	765.2	i'	60.0	18.73 ± 0.23
$\cdots$	2006 Sep 6.3659	874.0	z'	60.0	18.85 ± 0.37
$\cdots$	2006 Sep 6.3671	983.4	$R_{\rm C}$	60.0	18.98 ± 0.14
$\cdots$	2006 Sep 6.3683	1087.8	i'	60.0	18.87 ± 0.25
$\cdots$	2006 Sep 6.3700	1229.3	z'	60.0	18.79 ± 0.35
$\cdots$	2006 Sep 6.3712	1336.5	$R_{\rm C}$	60.0	19.14 ± 0.15
$\cdots$	2006 Sep 6.3725	1445.3	i'	60.0	18.95 ± 0.19
$\cdots$	2006 Sep 6.3737	1555.5	z'	60.0	18.78 ± 0.50
$\cdots$	2006 Sep 6.3750	1696.3	$R_{\rm C}$	120.0	19.35 ± 0.14
$\cdots$	2006 Sep 6.3772	1885.3	i'	120.0	19.21 ± 0.18
$\cdots$	2006 Sep 6.3794	2073.7	z'	120.0	19.23 ± 0.37
$\cdots$	2006 Sep 6.3815	2254.0	g	120.0	20.82 ± 0.22
$\cdots$	2006 Sep 6.3836	2437.7	$R_{\rm C}$	120.0	19.61 ± 0.17
$\cdots$	2006 Sep 6.3857	2622.5	i'	120.0	19.46 ± 0.23
$\cdots$	2006 Sep 6.3879	2810.6	z'	120.0	19.65 ± 0.38
$\cdots$	2006 Sep 6.3901	2995.9	g	120.0	20.69 ± 0.26
$\cdots$	2006 Sep 6.3922	3183.7	$R_{\rm C}$	120.0	19.95 ± 0.16
$\cdots$	2006 Sep 6.3945	3378.2	i'	120.0	19.71 ± 0.32
$\cdots$	2006 Sep 6.3967	3565.0	z'	120.0	20.02 ± 0.39
$\cdots$	2006 Sep 6.3989	3755.2	g	120.0	20.98 ± 0.22
$\cdots$	2006 Sep 6.4038	4180.1	$R_{\rm C}$	120.0	20.08 ± 0.16
$\cdots$	2006 Sep 6.4058	4356.9	$R_{\rm C}$	120.0	20.23 ± 0.17
$\cdots$	2006 Sep 6.4079	4532.3	$R_{\rm C}$	120.0	20.25 ± 0.17
$\cdots$	2006 Sep 6.4100	4715.6	i'	120.0	20.08 ± 0.19
$\cdots$	2006 Sep 6.4120	4892.5	i'	120.0	20.22 ± 0.20
$\cdots$	2006 Sep 6.4141	5075.6	i'	120.0	20.17 ± 0.20
$\cdots$	2006 Sep 6.4163	5264.5	z'	120.0	20.07 ± 0.38

Table A.1 — Continued

GRB Name	UT Date[a]	Time Since Burst[b] (s)	Filter	Exposure Time (s)	Magnitude
$\cdots$	2006 Sep 6.4183	5438.2	z'	120.0	19.86 ± 0.35
$\cdots$	2006 Sep 6.4204	5618.4	z'	120.0	19.93 ± 0.36
$\cdots$	2006 Sep 6.4227	5811.0	g	120.0	21.52 ± 0.28
$\cdots$	2006 Sep 6.4247	5987.7	g	120.0	21.09 ± 0.22
$\cdots$	2006 Sep 6.4268	6168.8	g	120.0	21.33 ± 0.26
$\cdots$	2006 Sep 6.4290	6357.6	R_C	120.0	19.97 ± 0.16
$\cdots$	2006 Sep 6.4310	6533.3	R_C	120.0	19.68 ± 0.17
$\cdots$	2006 Sep 6.4331	6718.0	R_C	120.0	19.75 ± 0.16
$\cdots$	2006 Sep 6.4353	6901.6	i'	120.0	19.63 ± 0.18
$\cdots$	2006 Sep 6.4374	7082.7	i'	120.0	19.48 ± 0.18
$\cdots$	2006 Sep 6.4395	7264.9	i'	120.0	19.48 ± 0.18
$\cdots$	2006 Sep 6.4417	7453.1	z'	120.0	19.29 ± 0.37
$\cdots$	2006 Sep 6.4437	7632.2	z'	120.0	19.05 ± 0.35
$\cdots$	2006 Sep 6.4459	7816.4	z'	120.0	19.16 ± 0.36
$\cdots$	2006 Sep 6.4480	8001.3	g	120.0	20.54 ± 0.18
$\cdots$	2006 Sep 6.4501	8184.1	g	120.0	20.34 ± 0.18
$\cdots$	2006 Sep 6.4522	8365.9	g	120.0	20.37 ± 0.18
$\cdots$	2006 Sep 6.4544	8553.6	R_C	120.0	19.31 ± 0.15
$\cdots$	2006 Sep 6.4565	8731.5	R_C	120.0	19.27 ± 0.16
$\cdots$	2006 Sep 6.4585	8909.2	R_C	120.0	19.31 ± 0.16
$\cdots$	2006 Sep 6.4606	9091.7	i'	120.0	19.10 ± 0.19
$\cdots$	2006 Sep 6.4628	9276.9	i'	120.0	19.07 ± 0.18
$\cdots$	2006 Sep 6.4649	9457.7	i'	120.0	19.09 ± 0.18
$\cdots$	2006 Sep 6.4670	9644.3	z'	120.0	18.95 ± 0.36
$\cdots$	2006 Sep 6.4692	9829.0	z'	120.0	18.91 ± 0.35
$\cdots$	2006 Sep 6.4713	1.001×10^4	z'	120.0	18.85 ± 0.35
$\cdots$	2006 Sep 6.4734	1.020×10^4	g	120.0	20.36 ± 0.19
$\cdots$	2006 Sep 6.4755	1.038×10^4	g	120.0	20.36 ± 0.19
$\cdots$	2006 Sep 6.4776	1.056×10^4	g	120.0	20.32 ± 0.18
$\cdots$	2006 Sep 6.4798	1.075×10^4	R_C	120.0	19.21 ± 0.17
$\cdots$	2006 Sep 6.4819	1.093×10^4	R_C	120.0	19.22 ± 0.17
$\cdots$	2006 Sep 6.4841	1.112×10^4	R_C	120.0	19.24 ± 0.17
$\cdots$	2006 Sep 6.4862	1.130×10^4	i'	120.0	19.11 ± 0.18
$\cdots$	2006 Sep 6.4915	1.176×10^4	i'	120.0	19.10 ± 0.17
$\cdots$	2006 Sep 6.4935	1.194×10^4	i'	120.0	19.14 ± 0.17
$\cdots$	2006 Sep 6.4957	1.213×10^4	z'	120.0	18.89 ± 0.34
$\cdots$	2006 Sep 6.4979	1.231×10^4	z'	120.0	18.98 ± 0.35
$\cdots$	2006 Sep 6.5000	1.249×10^4	z'	120.0	18.96 ± 0.35
$\cdots$	2006 Sep 6.5022	1.268×10^4	g	120.0	20.46 ± 0.17
$\cdots$	2006 Sep 6.5043	1.286×10^4	g	120.0	20.41 ± 0.17
$\cdots$	2006 Sep 6.5065	1.305×10^4	g	120.0	20.48 ± 0.16
$\cdots$	2006 Sep 6.5087	1.324×10^4	R_C	120.0	19.31 ± 0.14
$\cdots$	2006 Sep 6.5107	1.342×10^4	R_C	120.0	19.32 ± 0.14

Table A.1 — Continued

GRB Name	UT Date[a]	Time Since Burst[b] (s)	Filter	Exposure Time (s)	Magnitude
⋯	2006 Sep 6.5129	1.361×10^4	$R_{\rm C}$	120.0	19.36 ± 0.14
⋯	2006 Sep 6.5151	1.379×10^4	i'	120.0	19.21 ± 0.17
⋯	2006 Sep 6.5172	1.398×10^4	i'	120.0	19.25 ± 0.17
⋯	2006 Sep 6.5192	1.415×10^4	i'	120.0	19.20 ± 0.17
⋯	2006 Sep 6.5215	1.435×10^4	z'	120.0	19.01 ± 0.35
⋯	2006 Sep 7.4582	9.618×10^4	$R_{\rm C}$	1920.0	> 21.9
⋯	2006 Sep 7.4570	9.620×10^4	i'	2160.0	> 22.0
⋯	2006 Sep 7.4589	9.625×10^4	g	1920.0	> 22.3
GRB 060923A	2006 Sep 23.2205	348.6	$R_{\rm C}$	60.0	> 20.3
⋯	2006 Sep 23.2216	442.9	i'	60.0	> 20.4
⋯	2006 Sep 23.2227	536.4	z'	60.0	> 19.5
⋯	2006 Sep 23.2231	631.5	$R_{\rm C}$	180.0	> 20.9
⋯	2006 Sep 23.2242	725.1	i'	180.0	> 20.9
⋯	2006 Sep 23.2253	823.5	z'	180.0	> 19.4
⋯	2006 Sep 23.2431	2448.7	i'	360.0	> 20.9
⋯	2006 Sep 23.2450	2611.9	z'	360.0	> 19.7
⋯	2006 Sep 23.2449	2662.6	$R_{\rm C}$	480.0	> 21.3
GRB 061222A	2006 Dec 22.1496	424.8	$R_{\rm C}$	60.0	> 21.6
⋯	2006 Dec 22.1506	512.9	i'	60.0	> 21.3
⋯	2006 Dec 22.1517	607.7	z'	60.0	> 20.8
⋯	2006 Dec 22.1522	705.7	$R_{\rm C}$	180.0	> 22.3
⋯	2006 Dec 22.1532	797.5	i'	180.0	> 22.2
⋯	2006 Dec 22.1543	893.7	z'	180.0	> 21.3
⋯	2006 Dec 22.1649	1774.4	g	120.0	> 21.8
⋯	2006 Dec 22.1654	1934.3	$R_{\rm C}$	360.0	> 22.4
⋯	2006 Dec 22.1672	2090.3	i'	360.0	> 22.2
⋯	2006 Dec 22.1690	2248.0	z'	360.0	> 21.5
⋯	2006 Dec 22.1708	2404.0	g	360.0	> 22.1
GRB 070208	2007 Feb 8.3858	329.6	$R_{\rm C}$	60.0	19.27 ± 0.06
⋯	2007 Feb 8.3875	475.5	i'	60.0	19.17 ± 0.04
⋯	2007 Feb 8.3887	583.2	z'	60.0	18.76 ± 0.10
⋯	2007 Feb 8.3901	697.7	$R_{\rm C}$	60.0	19.55 ± 0.11
⋯	2007 Feb 8.3913	805.5	i'	60.0	19.55 ± 0.06
⋯	2007 Feb 8.3926	917.2	z'	60.0	19.15 ± 0.12
⋯	2007 Feb 8.3938	1022.6	$R_{\rm C}$	60.0	19.80 ± 0.08
⋯	2007 Feb 8.3950	1127.5	i'	60.0	19.65 ± 0.06
⋯	2007 Feb 8.3963	1234.2	z'	60.0	19.40 ± 0.12
⋯	2007 Feb 8.3975	1371.5	$R_{\rm C}$	120.0	19.92 ± 0.08
⋯	2007 Feb 8.3996	1554.0	i'	120.0	19.82 ± 0.09
⋯	2007 Feb 8.4038	1918.2	g	120.0	21.26 ± 0.19
⋯	2007 Feb 8.4053	2104.3	z'	240.0	19.61 ± 0.10
⋯	2007 Feb 8.4060	2106.1	$R_{\rm C}$	120.0	20.13 ± 0.17
⋯	2007 Feb 8.4081	2286.7	i'	120.0	20.02 ± 0.08

Table A.1 — Continued

GRB Name	UT Date[a]	Time Since Burst[b] (s)	Filter	Exposure Time (s)	Magnitude
$\cdots$	2007 Feb 8.4126	2673.1	g	120.0	21.67 ± 0.22
$\cdots$	2007 Feb 8.4161	2946.7	i'	60.0	20.14 ± 0.08
$\cdots$	2007 Feb 8.4164	3001.4	$R_{\rm C}$	120.0	20.46 ± 0.09
$\cdots$	2007 Feb 8.4189	3218.0	z'	120.0	19.54 ± 0.11
$\cdots$	2007 Feb 8.4198	3269.7	i'	60.0	20.48 ± 0.17
$\cdots$	2007 Feb 8.4245	3700.7	i'	120.0	20.26 ± 0.09
$\cdots$	2007 Feb 8.4329	4429.7	i'	120.0	20.35 ± 0.10
$\cdots$	2007 Feb 8.4338	4625.5	z'	360.0	20.53 ± 0.15
$\cdots$	2007 Feb 8.4359	4808.5	g	360.0	21.44 ± 0.16
$\cdots$	2007 Feb 8.4364	4853.9	$R_{\rm C}$	360.0	20.60 ± 0.08
$\cdots$	2007 Feb 8.4416	5177.7	i'	120.0	20.57 ± 0.12
GRB 070419A	2007 Apr 19.4200	352.7	$R_{\rm C}$	60.0	19.52 ± 0.13
$\cdots$	2007 Apr 19.4212	454.7	i'	60.0	18.71 ± 0.05
$\cdots$	2007 Apr 19.4224	560.8	z'	60.0	18.12 ± 0.09
$\cdots$	2007 Apr 19.4236	665.9	$R_{\rm C}$	60.0	18.68 ± 0.07
$\cdots$	2007 Apr 19.4248	766.9	i'	60.0	18.66 ± 0.05
$\cdots$	2007 Apr 19.4260	872.0	z'	60.0	18.43 ± 0.11
$\cdots$	2007 Apr 19.4272	976.0	$R_{\rm C}$	60.0	19.09 ± 0.12
$\cdots$	2007 Apr 19.4284	1081.4	i'	60.0	18.98 ± 0.07
$\cdots$	2007 Apr 19.4297	1189.0	z'	60.0	18.58 ± 0.10
$\cdots$	2007 Apr 19.4309	1324.9	$R_{\rm C}$	120.0	19.22 ± 0.08
$\cdots$	2007 Apr 19.4330	1501.3	i'	120.0	19.17 ± 0.06
$\cdots$	2007 Apr 19.4352	1691.3	z'	120.0	19.56 ± 0.18
$\cdots$	2007 Apr 19.4393	2047.7	$R_{\rm C}$	120.0	19.75 ± 0.12
$\cdots$	2007 Apr 19.4413	2225.1	i'	120.0	20.03 ± 0.11
$\cdots$	2007 Apr 19.4435	2408.2	z'	120.0	19.52 ± 0.20
$\cdots$	2007 Apr 19.4443	2603.5	g	360.0	20.82 ± 0.18
$\cdots$	2007 Apr 19.4478	2787.5	$R_{\rm C}$	120.0	20.26 ± 0.19
$\cdots$	2007 Apr 19.4499	2966.1	i'	120.0	20.36 ± 0.16
$\cdots$	2007 Apr 19.4521	3152.6	z'	120.0	19.91 ± 0.26
$\cdots$	2007 Apr 19.4598	3944.6	$R_{\rm C}$	360.0	20.95 ± 0.24
$\cdots$	2007 Apr 19.4731	5271.5	i'	720.0	21.01 ± 0.15
$\cdots$	2007 Apr 19.4783	5541.4	$R_{\rm C}$	360.0	21.33 ± 0.38
$\cdots$	2007 Apr 19.4793	5807.1	g	720.0	> 21.6
$\cdots$	2007 Apr 20.2267	7.116×10^4	$R_{\rm C}$	2280.0	> 22.7
$\cdots$	2007 Apr 20.2274	7.116×10^4	i'	2160.0	> 22.7
GRB 070521	2007 May 21.2875	203.6	$R_{\rm C}$	60.0	> 21.6
$\cdots$	2007 May 21.2886	296.4	i'	60.0	> 21.5
$\cdots$	2007 May 21.2897	390.0	z'	60.0	> 20.5
$\cdots$	2007 May 21.2901	487.2	$R_{\rm C}$	180.0	> 22.4
$\cdots$	2007 May 21.2912	581.1	i'	180.0	> 22.3
$\cdots$	2007 May 21.2966	1106.3	z'	300.0	> 21.3
$\cdots$	2007 May 21.3142	2536.9	g	120.0	> 22.8

Table A.1 — Continued

GRB Name	UT Date[a]	Time Since Burst[b] (s)	Filter	Exposure Time (s)	Magnitude
$\cdots$	2007 May 21.3153	2695.0	z'	240.0	> 21.3
$\cdots$	2007 May 21.3147	2700.3	R_C	360.0	> 23.0
$\cdots$	2007 May 21.3166	2860.0	i'	360.0	> 22.8
$\cdots$	2007 May 21.3173	2865.2	g	240.0	> 23.3
$\cdots$	2007 May 21.3400	9202.4	i'	9000.0	> 23.6
GRB 071003[f]	2007 Oct 3.3221	206.0	R_C	60.0	14.57 ± 0.06
$\cdots$	2007 Oct 3.3231	291.0	i'	60.0	15.08 ± 0.05
$\cdots$	2007 Oct 3.3241	377.0	z'	60.0	15.37 ± 0.07
$\cdots$	2007 Oct 3.3251	462.0	R_C	60.0	16.03 ± 0.07
$\cdots$	2007 Oct 3.3261	548.0	i'	60.0	16.41 ± 0.07
$\cdots$	2007 Oct 3.3271	633.0	z'	60.0	16.43 ± 0.08
$\cdots$	2007 Oct 3.3281	719.0	R_C	60.0	16.88 ± 0.09
$\cdots$	2007 Oct 3.3291	805.0	i'	60.0	17.12 ± 0.10
$\cdots$	2007 Oct 3.3300	890.0	z'	60.0	17.02 ± 0.11
$\cdots$	2007 Oct 3.3352	1369.0	z'	120.0	17.92 ± 0.20
$\cdots$	2007 Oct 3.3369	1514.0	g	120.0	18.71 ± 0.10
$\cdots$	2007 Oct 3.3420	1951.0	z'	120.0	18.67 ± 0.28
$\cdots$	2007 Oct 3.3437	2097.0	g	120.0	19.33 ± 0.15
$\cdots$	2007 Oct 3.3504	2678.0	g	120.0	19.44 ± 0.20
GRB 071010A	2007 Oct 10.1567	298.3	R_C	60.0	16.37 ± 0.21
$\cdots$	2007 Oct 10.1577	383.8	i'	60.0	16.42 ± 0.17
$\cdots$	2007 Oct 10.1587	469.4	z'	60.0	16.50 ± 0.37
$\cdots$	2007 Oct 10.1597	554.9	R_C	60.0	16.17 ± 0.20
$\cdots$	2007 Oct 10.1607	640.5	i'	60.0	16.56 ± 0.18
$\cdots$	2007 Oct 10.1617	726.0	z'	60.0	16.67 ± 0.36
$\cdots$	2007 Oct 10.1627	811.6	R_C	60.0	16.44 ± 0.19
$\cdots$	2007 Oct 10.1637	897.4	i'	60.0	16.86 ± 0.18
$\cdots$	2007 Oct 10.1646	982.9	z'	60.0	17.29 ± 0.29
$\cdots$	2007 Oct 11.1234	8.469×10^4	R_C	1800.0	19.71 ± 0.21
GRB 071011	2007 Oct 11.5303	235.3	R_C	60.0	17.70 ± 0.22
$\cdots$	2007 Oct 11.5313	320.9	i'	60.0	17.10 ± 0.21
$\cdots$	2007 Oct 11.5323	406.4	z'	60.0	16.47 ± 0.38
$\cdots$	2007 Oct 11.5333	492.0	R_C	60.0	18.17 ± 0.27
$\cdots$	2007 Oct 11.5343	577.7	i'	60.0	17.67 ± 0.24
$\cdots$	2007 Oct 11.5353	663.2	z'	60.0	17.09 ± 0.31
$\cdots$	2007 Oct 11.5362	748.8	R_C	60.0	18.82 ± 0.24
$\cdots$	2007 Oct 11.5372	834.4	i'	60.0	18.00 ± 0.27
$\cdots$	2007 Oct 11.5382	919.9	z'	60.0	17.45 ± 0.33
$\cdots$	2007 Oct 12.2699	4.992×10^4	R_C	1800.0	> 22.8
GRB 071020	2007 Oct 20.3461	4615.8	i'	120.0	19.93 ± 0.09
$\cdots$	2007 Oct 20.3477	4753.8	i'	120.0	19.88 ± 0.08
$\cdots$	2007 Oct 20.3493	4892.7	i'	120.0	20.00 ± 0.08
$\cdots$	2007 Oct 20.3525	5169.1	R_C	120.0	19.96 ± 0.09

Table A.1 — Continued

GRB Name	UT Date[a]	Time Since Burst[b] (s)	Filter	Exposure Time (s)	Magnitude
$\cdots$	2007 Oct 20.3541	5307.3	R_C	120.0	19.96 ± 0.10
$\cdots$	2007 Oct 20.3653	6276.9	i'	120.0	20.00 ± 0.08
$\cdots$	2007 Oct 20.3669	6414.9	i'	120.0	20.44 ± 0.12
$\cdots$	2007 Oct 20.3685	6553.0	i'	120.0	20.20 ± 0.10
$\cdots$	2007 Oct 20.3541	5307.3	R_C	120.0	19.96 ± 0.10
$\cdots$	2007 Oct 20.3559	5586.9	z'	360.0	20.49 ± 0.25
$\cdots$	2007 Oct 20.3701	6691.3	R_C	120.0	20.04 ± 0.10
$\cdots$	2007 Oct 20.3717	6829.3	R_C	120.0	20.23 ± 0.12
$\cdots$	2007 Oct 20.3733	6967.5	R_C	120.0	20.43 ± 0.12
$\cdots$	2007 Oct 20.3751	7246.9	z'	360.0	19.96 ± 0.14
$\cdots$	2007 Oct 20.3845	7937.4	i'	120.0	20.66 ± 0.14
$\cdots$	2007 Oct 20.3861	8075.4	i'	120.0	20.32 ± 0.10
$\cdots$	2007 Oct 20.3877	8213.5	i'	120.0	20.31 ± 0.10
$\cdots$	2007 Oct 20.3893	8351.6	R_C	120.0	20.63 ± 0.15
GRB 071122	2007 Nov 22.0709	1302.5	R_C	360.0	20.22 ± 0.22
$\cdots$	2007 Nov 22.0760	1739.0	i'	360.0	19.89 ± 0.17
$\cdots$	2007 Nov 22.0810	2175.5	z'	360.0	19.71 ± 0.39
$\cdots$	2007 Nov 22.0997	3790.9	R_C	360.0	19.89 ± 0.20
$\cdots$	2007 Nov 22.1048	4227.6	i'	360.0	19.87 ± 0.18
$\cdots$	2007 Nov 22.1149	5101.3	R_C	360.0	19.76 ± 0.19
$\cdots$	2007 Nov 22.1153	5319.5	z'	720.0	19.69 ± 0.38
$\cdots$	2007 Nov 22.1199	5537.9	i'	360.0	19.73 ± 0.18
$\cdots$	2007 Nov 22.1301	6416.3	R_C	360.0	19.84 ± 0.21
$\cdots$	2007 Nov 22.1353	6863.0	i'	360.0	19.82 ± 0.18
$\cdots$	2007 Nov 22.1454	7736.4	R_C	360.0	19.77 ± 0.21
$\cdots$	2007 Nov 22.1458	7954.9	z'	720.0	19.87 ± 0.38
$\cdots$	2007 Nov 22.1504	8173.4	i'	360.0	19.87 ± 0.19
$\cdots$	2007 Nov 22.1606	9046.8	R_C	360.0	20.11 ± 0.22
$\cdots$	2007 Nov 22.1656	9483.5	i'	360.0	19.74 ± 0.18
$\cdots$	2007 Nov 23.0744	8.827×10^4	R_C	900.0	> 20.8
$\cdots$	2007 Nov 23.0783	8.843×10^4	i'	540.0	21.00 ± 0.25
GRB 080310	2008 Mar 10.3628	298.3	R_C	60.0	16.76 ± 0.07
$\cdots$	2008 Mar 10.3638	384.0	i'	60.0	16.87 ± 0.11
$\cdots$	2008 Mar 10.3648	470.2	z'	60.0	16.76 ± 0.08
$\cdots$	2008 Mar 10.3658	555.9	R_C	60.0	17.04 ± 0.09
$\cdots$	2008 Mar 10.3668	641.5	i'	60.0	17.01 ± 0.11
$\cdots$	2008 Mar 10.3678	727.3	z'	60.0	16.80 ± 0.14
$\cdots$	2008 Mar 10.3688	813.0	R_C	60.0	17.05 ± 0.20
$\cdots$	2008 Mar 10.3698	898.7	i'	60.0	16.98 ± 0.06
$\cdots$	2008 Mar 10.3707	984.4	z'	60.0	16.74 ± 0.12
$\cdots$	2008 Mar 10.3717	1100.3	R_C	120.0	16.96 ± 0.05
$\cdots$	2008 Mar 10.3734	1246.0	i'	120.0	16.90 ± 0.06
$\cdots$	2008 Mar 10.3751	1361.8	R_C	60.0	16.91 ± 0.07

Table A.1 — Continued

GRB Name	UT Date[a]	Time Since Burst[b] (s)	Filter	Exposure Time (s)	Magnitude
$\cdots$	2008 Mar 10.3761	1447.5	i'	60.0	16.92 ± 0.04
$\cdots$	2008 Mar 10.3771	1533.4	z'	60.0	16.70 ± 0.05
$\cdots$	2008 Mar 10.3781	1619.3	$R_{\rm C}$	60.0	16.96 ± 0.08
$\cdots$	2008 Mar 10.3791	1705.0	i'	60.0	16.99 ± 0.05
$\cdots$	2008 Mar 10.3801	1790.7	z'	60.0	16.74 ± 0.08
$\cdots$	2008 Mar 10.3811	1906.4	$R_{\rm C}$	120.0	16.98 ± 0.04
$\cdots$	2008 Mar 10.3828	2052.3	i'	120.0	17.02 ± 0.05
$\cdots$	2008 Mar 10.3844	2198.1	z'	120.0	16.91 ± 0.07
$\cdots$	2008 Mar 10.3861	2343.8	g	120.0	17.86 ± 0.13
$\cdots$	2008 Mar 10.3878	2489.8	$R_{\rm C}$	120.0	17.15 ± 0.07
$\cdots$	2008 Mar 10.3895	2635.6	i'	120.0	17.21 ± 0.05
$\cdots$	2008 Mar 10.3912	2781.4	z'	120.0	17.10 ± 0.07
$\cdots$	2008 Mar 10.3929	2927.1	g	120.0	18.00 ± 0.12
$\cdots$	2008 Mar 10.3946	3072.8	$R_{\rm C}$	120.0	17.30 ± 0.06
$\cdots$	2008 Mar 10.3963	3218.6	i'	120.0	17.35 ± 0.05
$\cdots$	2008 Mar 10.3979	3364.3	z'	120.0	17.24 ± 0.05
$\cdots$	2008 Mar 10.3996	3510.1	g	120.0	18.12 ± 0.12
$\cdots$	2008 Mar 11.3202	8.325×10^4	i'	540.0	21.20 ± 0.09
$\cdots$	2008 Mar 11.3273	8.387×10^4	$R_{\rm C}$	540.0	21.36 ± 0.10
$\cdots$	2008 Mar 11.3344	8.449×10^4	i'	540.0	21.22 ± 0.09
$\cdots$	2008 Mar 11.3416	8.511×10^4	$R_{\rm C}$	540.0	21.31 ± 0.11
$\cdots$	2008 Mar 11.3487	8.572×10^4	i'	540.0	21.40 ± 0.24
$\cdots$	2008 Mar 11.3559	8.634×10^4	$R_{\rm C}$	540.0	21.17 ± 0.09
$\cdots$	2008 Mar 11.3630	8.696×10^4	i'	540.0	21.32 ± 0.10
$\cdots$	2008 Mar 11.3702	8.758×10^4	$R_{\rm C}$	540.0	21.31 ± 0.09
$\cdots$	2008 Mar 11.3814	8.882×10^4	i'	1080.0	21.19 ± 0.07
$\cdots$	2008 Mar 11.3886	8.944×10^4	$R_{\rm C}$	1080.0	21.39 ± 0.06
$\cdots$	2008 Mar 11.4100	9.129×10^4	i'	1080.0	21.32 ± 0.07
$\cdots$	2008 Mar 11.4172	9.190×10^4	$R_{\rm C}$	1080.0	21.37 ± 0.08
$\cdots$	2008 Mar 11.4386	9.376×10^4	i'	1080.0	21.29 ± 0.08
$\cdots$	2008 Mar 11.4457	9.437×10^4	$R_{\rm C}$	1080.0	21.37 ± 0.08
$\cdots$	2008 Mar 13.3165	2.564×10^5	i'	1800.0	> 21.7
$\cdots$	2008 Mar 13.3403	2.584×10^5	$R_{\rm C}$	1800.0	22.72 ± 0.21
GRB 080319A	2008 Mar 19.2417	173.5	$R_{\rm C}$	60.0	20.02 ± 0.14
$\cdots$	2008 Mar 19.2427	259.7	i'	60.0	19.45 ± 0.08
$\cdots$	2008 Mar 19.2437	346.0	z'	60.0	19.03 ± 0.09
$\cdots$	2008 Mar 19.2447	432.0	$R_{\rm C}$	60.0	19.71 ± 0.11
$\cdots$	2008 Mar 19.2457	518.0	i'	60.0	19.67 ± 0.08
$\cdots$	2008 Mar 19.2467	604.3	z'	60.0	19.70 ± 0.15
$\cdots$	2008 Mar 19.2477	690.3	$R_{\rm C}$	60.0	20.18 ± 0.17
$\cdots$	2008 Mar 19.2487	776.4	i'	60.0	20.20 ± 0.12
$\cdots$	2008 Mar 19.2497	862.5	z'	60.0	19.40 ± 0.13
$\cdots$	2008 Mar 19.2508	983.6	$R_{\rm C}$	120.0	20.46 ± 0.16

Table A.1 — Continued

GRB Name	UT Date[a]	Time Since Burst[b] (s)	Filter	Exposure Time (s)	Magnitude
$\cdots$	2008 Mar 19.2533	1231.8	$R_{\rm C}$	180.0	20.57 ± 0.14
$\cdots$	2008 Mar 19.2568	1507.0	$R_{\rm C}$	120.0	21.30 ± 0.25
$\cdots$	2008 Mar 19.2577	1550.1	z'	60.0	20.39 ± 0.27
$\cdots$	2008 Mar 19.2578	1593.0	i'	120.0	20.81 ± 0.12
$\cdots$	2008 Mar 19.2910	4462.1	$R_{\rm C}$	120.0	21.41 ± 0.30
$\cdots$	2008 Mar 19.2927	4607.8	i'	120.0	21.38 ± 0.21
$\cdots$	2008 Mar 19.2944	4753.5	z'	120.0	> 20.5
$\cdots$	2008 Mar 20.2489	8.806×10^4	$R_{\rm C}$	1800.0	> 22.0
$\cdots$	2008 Mar 20.2891	9.154×10^4	i'	1800.0	> 22.3
GRB 080319B	2008 Mar 19.2607	185.6	$R_{\rm C}$	60.0	< 11.13
$\cdots$	2008 Mar 19.2617	271.9	i'	60.0	11.55 ± 0.03
$\cdots$	2008 Mar 19.2627	358.1	z'	60.0	11.51 ± 0.10
$\cdots$	2008 Mar 19.2637	444.2	$R_{\rm C}$	60.0	< 12.15
$\cdots$	2008 Mar 19.2647	530.3	i'	60.0	12.59 ± 0.04
$\cdots$	2008 Mar 19.2657	616.6	z'	60.0	12.65 ± 0.26
$\cdots$	2008 Mar 19.2667	702.8	$R_{\rm C}$	60.0	13.01 ± 0.07
$\cdots$	2008 Mar 19.2677	788.7	i'	60.0	13.33 ± 0.04
$\cdots$	2008 Mar 19.2687	874.6	z'	60.0	13.40 ± 0.05
$\cdots$	2008 Mar 19.2697	990.4	$R_{\rm C}$	120.0	13.70 ± 0.04
$\cdots$	2008 Mar 19.2714	1136.1	i'	120.0	14.04 ± 0.13
$\cdots$	2008 Mar 19.2731	1287.0	z'	120.0	14.22 ± 0.07
$\cdots$	2008 Mar 19.2748	1432.7	g	120.0	15.13 ± 0.20
$\cdots$	2008 Mar 19.2765	1578.7	$R_{\rm C}$	120.0	14.68 ± 0.09
$\cdots$	2008 Mar 19.2782	1724.5	i'	120.0	14.99 ± 0.03
$\cdots$	2008 Mar 19.2799	1870.3	z'	120.0	15.01 ± 0.06
$\cdots$	2008 Mar 19.2815	2016.1	g	120.0	15.77 ± 0.21
$\cdots$	2008 Mar 19.2832	2161.8	$R_{\rm C}$	120.0	15.29 ± 0.06
$\cdots$	2008 Mar 19.2849	2307.6	i'	120.0	15.51 ± 0.04
$\cdots$	2008 Mar 19.2866	2453.3	z'	120.0	15.47 ± 0.05
$\cdots$	2008 Mar 19.2883	2599.1	g	120.0	16.14 ± 0.17
$\cdots$	2008 Mar 19.2970	3319.4	$R_{\rm C}$	60.0	15.93 ± 0.05
$\cdots$	2008 Mar 19.2979	3397.6	i'	60.0	16.09 ± 0.03
$\cdots$	2008 Mar 19.2988	3476.3	z'	60.0	16.02 ± 0.06
$\cdots$	2008 Mar 19.2997	3558.2	$R_{\rm C}$	60.0	16.01 ± 0.05
$\cdots$	2008 Mar 19.3006	3636.5	i'	60.0	16.18 ± 0.04
$\cdots$	2008 Mar 19.3015	3714.7	z'	60.0	16.12 ± 0.05
$\cdots$	2008 Mar 19.3025	3796.1	$R_{\rm C}$	60.0	16.11 ± 0.05
$\cdots$	2008 Mar 19.3034	3874.3	i'	60.0	16.27 ± 0.04
$\cdots$	2008 Mar 19.3043	3952.8	z'	60.0	16.23 ± 0.06
$\cdots$	2008 Mar 19.3052	4034.6	$R_{\rm C}$	60.0	16.19 ± 0.06
$\cdots$	2008 Mar 19.3062	4112.8	i'	60.0	16.34 ± 0.03
$\cdots$	2008 Mar 19.3071	4191.1	z'	60.0	16.27 ± 0.04
$\cdots$	2008 Mar 19.3080	4272.6	$R_{\rm C}$	60.0	16.27 ± 0.06

Table A.1 — Continued

GRB Name	UT Date[a]	Time Since Burst[b] (s)	Filter	Exposure Time (s)	Magnitude
$\cdots$	2008 Mar 19.3089	4351.1	i'	60.0	16.41 ± 0.02
$\cdots$	2008 Mar 19.3098	4429.3	z'	60.0	16.33 ± 0.04
$\cdots$	2008 Mar 19.3108	4511.1	$R_{\rm C}$	60.0	16.32 ± 0.05
$\cdots$	2008 Mar 19.3117	4589.4	i'	60.0	16.49 ± 0.03
$\cdots$	2008 Mar 19.3126	4667.7	z'	60.0	16.42 ± 0.03
$\cdots$	2008 Mar 19.3135	4749.3	$R_{\rm C}$	60.0	16.39 ± 0.06
$\cdots$	2008 Mar 19.3144	4827.6	i'	60.0	16.55 ± 0.03
$\cdots$	2008 Mar 19.3153	4905.8	z'	60.0	16.48 ± 0.05
$\cdots$	2008 Mar 19.3163	4987.2	$R_{\rm C}$	60.0	16.49 ± 0.06
$\cdots$	2008 Mar 19.3172	5065.6	i'	60.0	16.61 ± 0.04
$\cdots$	2008 Mar 19.3181	5143.8	z'	60.0	16.53 ± 0.05
$\cdots$	2008 Mar 19.3190	5225.4	$R_{\rm C}$	60.0	16.53 ± 0.05
$\cdots$	2008 Mar 19.3199	5303.6	i'	60.0	16.69 ± 0.03
$\cdots$	2008 Mar 19.3208	5381.9	z'	60.0	16.60 ± 0.03
$\cdots$	2008 Mar 19.3218	5463.4	$R_{\rm C}$	60.0	16.61 ± 0.05
$\cdots$	2008 Mar 19.3227	5541.7	i'	60.0	16.74 ± 0.03
$\cdots$	2008 Mar 19.3236	5619.9	z'	60.0	16.68 ± 0.04
$\cdots$	2008 Mar 19.3245	5701.8	$R_{\rm C}$	60.0	16.65 ± 0.05
$\cdots$	2008 Mar 19.3255	5780.2	i'	60.0	16.81 ± 0.03
$\cdots$	2008 Mar 19.3264	5858.5	z'	60.0	16.71 ± 0.05
$\cdots$	2008 Mar 19.3273	5940.0	$R_{\rm C}$	60.0	16.72 ± 0.06
$\cdots$	2008 Mar 19.3282	6018.3	i'	60.0	16.84 ± 0.03
$\cdots$	2008 Mar 19.3291	6096.5	z'	60.0	16.77 ± 0.04
$\cdots$	2008 Mar 19.3301	6178.3	$R_{\rm C}$	60.0	16.76 ± 0.05
$\cdots$	2008 Mar 19.3310	6256.7	i'	60.0	16.90 ± 0.03
$\cdots$	2008 Mar 19.3319	6335.1	z'	60.0	16.85 ± 0.04
$\cdots$	2008 Mar 19.3328	6416.6	$R_{\rm C}$	60.0	16.82 ± 0.06
$\cdots$	2008 Mar 19.3337	6494.8	i'	60.0	16.95 ± 0.03
$\cdots$	2008 Mar 19.3346	6573.0	z'	60.0	16.91 ± 0.03
$\cdots$	2008 Mar 19.3356	6654.9	$R_{\rm C}$	60.0	16.86 ± 0.05
$\cdots$	2008 Mar 19.3365	6733.1	i'	60.0	16.98 ± 0.04
$\cdots$	2008 Mar 19.3374	6811.5	z'	60.0	16.88 ± 0.03
$\cdots$	2008 Mar 19.3383	6892.9	$R_{\rm C}$	60.0	16.91 ± 0.06
$\cdots$	2008 Mar 19.3392	6971.2	i'	60.0	17.05 ± 0.03
$\cdots$	2008 Mar 19.3401	7049.4	z'	60.0	16.96 ± 0.06
$\cdots$	2008 Mar 19.3411	7131.0	$R_{\rm C}$	60.0	16.94 ± 0.06
$\cdots$	2008 Mar 19.3420	7209.3	i'	60.0	17.09 ± 0.03
$\cdots$	2008 Mar 19.3429	7287.6	z'	60.0	17.00 ± 0.05
$\cdots$	2008 Mar 19.3438	7368.9	$R_{\rm C}$	60.0	17.02 ± 0.06
$\cdots$	2008 Mar 19.3447	7447.2	i'	60.0	17.13 ± 0.06
$\cdots$	2008 Mar 19.3457	7525.5	z'	60.0	17.04 ± 0.06
$\cdots$	2008 Mar 19.3466	7607.1	$R_{\rm C}$	60.0	17.02 ± 0.03
$\cdots$	2008 Mar 19.3475	7685.5	i'	60.0	17.18 ± 0.04

Table A.1 — Continued

GRB Name	UT Date[a]	Time Since Burst[b] (s)	Filter	Exposure Time (s)	Magnitude
$\cdots$	2008 Mar 19.3484	7763.8	z'	60.0	17.12 ± 0.04
$\cdots$	2008 Mar 19.3494	7845.3	$R_{\rm C}$	60.0	17.09 ± 0.06
$\cdots$	2008 Mar 19.3503	7923.7	i'	60.0	17.21 ± 0.03
$\cdots$	2008 Mar 19.3512	8002.4	z'	60.0	17.12 ± 0.06
$\cdots$	2008 Mar 19.3521	8084.1	$R_{\rm C}$	60.0	17.14 ± 0.06
$\cdots$	2008 Mar 19.3530	8162.5	i'	60.0	17.25 ± 0.03
$\cdots$	2008 Mar 19.3539	8241.1	z'	60.0	17.21 ± 0.03
$\cdots$	2008 Mar 19.3549	8322.8	$R_{\rm C}$	60.0	17.15 ± 0.06
$\cdots$	2008 Mar 19.3558	8401.1	i'	60.0	17.30 ± 0.03
$\cdots$	2008 Mar 19.3567	8479.4	z'	60.0	17.21 ± 0.05
$\cdots$	2008 Mar 19.3576	8560.9	$R_{\rm C}$	60.0	17.20 ± 0.06
$\cdots$	2008 Mar 19.3585	8639.2	i'	60.0	17.34 ± 0.03
$\cdots$	2008 Mar 19.3595	8717.5	z'	60.0	17.28 ± 0.03
$\cdots$	2008 Mar 19.3639	9105.0	$R_{\rm C}$	60.0	17.30 ± 0.05
$\cdots$	2008 Mar 19.3648	9183.3	i'	60.0	17.41 ± 0.04
$\cdots$	2008 Mar 19.3657	9261.6	z'	60.0	17.34 ± 0.05
$\cdots$	2008 Mar 19.3667	9342.8	$R_{\rm C}$	60.0	17.31 ± 0.06
$\cdots$	2008 Mar 19.3676	9422.1	i'	60.0	17.45 ± 0.04
$\cdots$	2008 Mar 19.3685	9500.4	z'	60.0	17.33 ± 0.04
$\cdots$	2008 Mar 19.3695	9581.9	$R_{\rm C}$	60.0	17.38 ± 0.05
$\cdots$	2008 Mar 19.3704	9660.1	i'	60.0	17.47 ± 0.04
$\cdots$	2008 Mar 19.3713	9738.6	z'	60.0	17.36 ± 0.04
$\cdots$	2008 Mar 19.3722	9820.1	$R_{\rm C}$	60.0	17.41 ± 0.06
$\cdots$	2008 Mar 19.3731	9898.3	i'	60.0	17.48 ± 0.04
$\cdots$	2008 Mar 19.3740	9976.6	z'	60.0	17.45 ± 0.03
$\cdots$	2008 Mar 19.3750	1.006×10^4	$R_{\rm C}$	60.0	17.43 ± 0.06
$\cdots$	2008 Mar 19.3759	1.014×10^4	i'	60.0	17.52 ± 0.04
$\cdots$	2008 Mar 19.3768	1.021×10^4	z'	60.0	17.49 ± 0.04
$\cdots$	2008 Mar 19.3777	1.030×10^4	$R_{\rm C}$	60.0	17.45 ± 0.06
$\cdots$	2008 Mar 19.3786	1.037×10^4	i'	60.0	17.60 ± 0.03
$\cdots$	2008 Mar 19.3795	1.045×10^4	z'	60.0	17.52 ± 0.06
$\cdots$	2008 Mar 19.3805	1.053×10^4	$R_{\rm C}$	60.0	17.49 ± 0.08
$\cdots$	2008 Mar 19.3814	1.061×10^4	i'	60.0	17.64 ± 0.04
$\cdots$	2008 Mar 19.3823	1.069×10^4	z'	60.0	17.53 ± 0.08
$\cdots$	2008 Mar 19.3832	1.077×10^4	$R_{\rm C}$	60.0	17.52 ± 0.09
$\cdots$	2008 Mar 19.3841	1.085×10^4	i'	60.0	17.63 ± 0.03
$\cdots$	2008 Mar 19.3850	1.093×10^4	z'	60.0	17.54 ± 0.06
$\cdots$	2008 Mar 19.3860	1.101×10^4	$R_{\rm C}$	60.0	17.57 ± 0.06
$\cdots$	2008 Mar 19.3869	1.109×10^4	i'	60.0	17.66 ± 0.02
$\cdots$	2008 Mar 19.3878	1.117×10^4	z'	60.0	17.57 ± 0.08
$\cdots$	2008 Mar 19.3887	1.125×10^4	$R_{\rm C}$	60.0	17.61 ± 0.05
$\cdots$	2008 Mar 19.3897	1.133×10^4	i'	60.0	17.70 ± 0.03
$\cdots$	2008 Mar 19.3906	1.141×10^4	z'	60.0	17.66 ± 0.07

Table A.1 — Continued

GRB Name	UT Date[a]	Time Since Burst[b] (s)	Filter	Exposure Time (s)	Magnitude
$\cdots$	2008 Mar 19.3915	1.149×10^4	$R_{\rm C}$	60.0	17.61 ± 0.05
$\cdots$	2008 Mar 19.3924	1.156×10^4	i'	60.0	17.72 ± 0.03
$\cdots$	2008 Mar 19.3933	1.164×10^4	z'	60.0	17.62 ± 0.04
$\cdots$	2008 Mar 19.3943	1.172×10^4	$R_{\rm C}$	60.0	17.64 ± 0.05
$\cdots$	2008 Mar 19.3952	1.180×10^4	i'	60.0	17.76 ± 0.04
$\cdots$	2008 Mar 19.3961	1.188×10^4	z'	60.0	17.67 ± 0.04
$\cdots$	2008 Mar 19.3971	1.197×10^4	$R_{\rm C}$	60.0	17.67 ± 0.06
$\cdots$	2008 Mar 19.3980	1.205×10^4	i'	60.0	17.78 ± 0.05
$\cdots$	2008 Mar 19.3989	1.212×10^4	z'	60.0	17.71 ± 0.04
$\cdots$	2008 Mar 19.3998	1.221×10^4	$R_{\rm C}$	60.0	17.70 ± 0.06
$\cdots$	2008 Mar 19.4007	1.228×10^4	i'	60.0	17.81 ± 0.04
$\cdots$	2008 Mar 19.4016	1.236×10^4	z'	60.0	17.68 ± 0.04
$\cdots$	2008 Mar 19.4026	1.244×10^4	$R_{\rm C}$	60.0	17.69 ± 0.06
$\cdots$	2008 Mar 19.4035	1.252×10^4	i'	60.0	17.82 ± 0.04
$\cdots$	2008 Mar 19.4044	1.260×10^4	z'	60.0	17.72 ± 0.06
$\cdots$	2008 Mar 19.4053	1.268×10^4	$R_{\rm C}$	60.0	17.75 ± 0.06
$\cdots$	2008 Mar 19.4062	1.276×10^4	i'	60.0	17.85 ± 0.04
$\cdots$	2008 Mar 19.4071	1.284×10^4	z'	60.0	17.71 ± 0.05
$\cdots$	2008 Mar 19.4081	1.292×10^4	$R_{\rm C}$	60.0	17.78 ± 0.06
$\cdots$	2008 Mar 19.4090	1.300×10^4	i'	60.0	17.86 ± 0.06
$\cdots$	2008 Mar 19.4099	1.308×10^4	z'	60.0	17.74 ± 0.08
$\cdots$	2008 Mar 19.4108	1.316×10^4	$R_{\rm C}$	60.0	17.81 ± 0.06
$\cdots$	2008 Mar 19.4118	1.324×10^4	i'	60.0	17.91 ± 0.05
$\cdots$	2008 Mar 19.4127	1.331×10^4	z'	60.0	17.79 ± 0.05
$\cdots$	2008 Mar 19.4136	1.340×10^4	$R_{\rm C}$	60.0	17.80 ± 0.06
$\cdots$	2008 Mar 19.4145	1.347×10^4	i'	60.0	17.90 ± 0.04
$\cdots$	2008 Mar 19.4154	1.355×10^4	z'	60.0	17.88 ± 0.06
$\cdots$	2008 Mar 19.4164	1.363×10^4	$R_{\rm C}$	60.0	17.83 ± 0.07
$\cdots$	2008 Mar 19.4173	1.371×10^4	i'	60.0	17.94 ± 0.04
$\cdots$	2008 Mar 19.4182	1.379×10^4	z'	60.0	17.83 ± 0.04
$\cdots$	2008 Mar 19.4191	1.387×10^4	$R_{\rm C}$	60.0	17.85 ± 0.06
$\cdots$	2008 Mar 19.4200	1.395×10^4	i'	60.0	17.95 ± 0.05
$\cdots$	2008 Mar 19.4209	1.403×10^4	z'	60.0	17.89 ± 0.08
$\cdots$	2008 Mar 19.4219	1.411×10^4	$R_{\rm C}$	60.0	17.84 ± 0.06
$\cdots$	2008 Mar 19.4228	1.419×10^4	i'	60.0	18.01 ± 0.04
$\cdots$	2008 Mar 19.4237	1.427×10^4	z'	60.0	17.93 ± 0.06
$\cdots$	2008 Mar 19.4246	1.435×10^4	$R_{\rm C}$	60.0	17.92 ± 0.07
$\cdots$	2008 Mar 19.4256	1.443×10^4	i'	60.0	18.02 ± 0.04
$\cdots$	2008 Mar 19.4265	1.451×10^4	z'	60.0	17.87 ± 0.08
$\cdots$	2008 Mar 19.4274	1.459×10^4	$R_{\rm C}$	60.0	17.92 ± 0.06
$\cdots$	2008 Mar 19.4283	1.467×10^4	i'	60.0	18.04 ± 0.04
$\cdots$	2008 Mar 19.4293	1.475×10^4	z'	60.0	17.92 ± 0.07
$\cdots$	2008 Mar 19.4302	1.483×10^4	$R_{\rm C}$	60.0	17.99 ± 0.06

Table A.1 — Continued

GRB Name	UT Date[a]	Time Since Burst[b] (s)	Filter	Exposure Time (s)	Magnitude
$\cdots$	2008 Mar 19.4311	1.491×10^4	i'	60.0	18.07 ± 0.04
$\cdots$	2008 Mar 19.4320	1.499×10^4	z'	60.0	17.96 ± 0.04
$\cdots$	2008 Mar 19.4330	1.507×10^4	$R_{\rm C}$	60.0	17.97 ± 0.05
$\cdots$	2008 Mar 19.4339	1.515×10^4	i'	60.0	18.05 ± 0.04
$\cdots$	2008 Mar 19.4348	1.523×10^4	z'	60.0	18.02 ± 0.05
$\cdots$	2008 Mar 19.4357	1.531×10^4	$R_{\rm C}$	60.0	17.97 ± 0.05
$\cdots$	2008 Mar 19.4366	1.538×10^4	i'	60.0	18.10 ± 0.03
$\cdots$	2008 Mar 19.4375	1.546×10^4	z'	60.0	18.17 ± 0.07
$\cdots$	2008 Mar 19.4385	1.554×10^4	$R_{\rm C}$	60.0	18.02 ± 0.06
$\cdots$	2008 Mar 19.4394	1.562×10^4	i'	60.0	18.07 ± 0.03
$\cdots$	2008 Mar 19.4403	1.570×10^4	z'	60.0	18.12 ± 0.07
$\cdots$	2008 Mar 19.4412	1.578×10^4	$R_{\rm C}$	60.0	18.05 ± 0.10
$\cdots$	2008 Mar 19.4421	1.586×10^4	i'	60.0	18.16 ± 0.03
$\cdots$	2008 Mar 19.4430	1.594×10^4	z'	60.0	18.02 ± 0.05
$\cdots$	2008 Mar 19.4440	1.602×10^4	$R_{\rm C}$	60.0	18.07 ± 0.06
$\cdots$	2008 Mar 19.4449	1.610×10^4	i'	60.0	18.19 ± 0.04
$\cdots$	2008 Mar 19.4458	1.618×10^4	z'	60.0	18.12 ± 0.06
$\cdots$	2008 Mar 19.4467	1.626×10^4	$R_{\rm C}$	60.0	18.11 ± 0.07
$\cdots$	2008 Mar 19.4476	1.634×10^4	i'	60.0	18.18 ± 0.03
$\cdots$	2008 Mar 19.4485	1.642×10^4	z'	60.0	18.09 ± 0.05
$\cdots$	2008 Mar 19.4495	1.650×10^4	$R_{\rm C}$	60.0	18.09 ± 0.06
$\cdots$	2008 Mar 19.4504	1.658×10^4	i'	60.0	18.23 ± 0.03
$\cdots$	2008 Mar 19.4513	1.665×10^4	z'	60.0	18.13 ± 0.07
$\cdots$	2008 Mar 19.4522	1.673×10^4	$R_{\rm C}$	60.0	18.16 ± 0.06
$\cdots$	2008 Mar 19.4532	1.681×10^4	i'	60.0	18.20 ± 0.03
$\cdots$	2008 Mar 19.4541	1.689×10^4	z'	60.0	18.02 ± 0.05
$\cdots$	2008 Mar 19.4550	1.697×10^4	$R_{\rm C}$	60.0	18.11 ± 0.07
$\cdots$	2008 Mar 19.4559	1.705×10^4	i'	60.0	18.24 ± 0.03
$\cdots$	2008 Mar 19.4578	1.721×10^4	$R_{\rm C}$	60.0	18.19 ± 0.07
$\cdots$	2008 Mar 19.4587	1.729×10^4	i'	60.0	18.32 ± 0.03
$\cdots$	2008 Mar 19.4596	1.737×10^4	z'	60.0	18.26 ± 0.05
$\cdots$	2008 Mar 19.4606	1.745×10^4	$R_{\rm C}$	60.0	18.17 ± 0.06
$\cdots$	2008 Mar 19.4615	1.753×10^4	i'	60.0	18.28 ± 0.03
$\cdots$	2008 Mar 19.4624	1.761×10^4	z'	60.0	18.18 ± 0.11
$\cdots$	2008 Mar 19.4633	1.769×10^4	$R_{\rm C}$	60.0	18.23 ± 0.07
$\cdots$	2008 Mar 19.4651	1.785×10^4	i'	60.0	18.30 ± 0.03
$\cdots$	2008 Mar 19.4660	1.793×10^4	z'	60.0	18.15 ± 0.06
$\cdots$	2008 Mar 19.4670	1.801×10^4	$R_{\rm C}$	60.0	18.27 ± 0.04
$\cdots$	2008 Mar 19.4680	1.810×10^4	i'	60.0	18.36 ± 0.03
$\cdots$	2008 Mar 19.4690	1.819×10^4	z'	60.0	18.16 ± 0.07
$\cdots$	2008 Mar 19.4700	1.827×10^4	$R_{\rm C}$	60.0	18.27 ± 0.08
$\cdots$	2008 Mar 19.4709	1.835×10^4	i'	60.0	18.36 ± 0.04
$\cdots$	2008 Mar 19.4719	1.843×10^4	z'	60.0	18.11 ± 0.07

Table A.1 — Continued

GRB Name	UT Date[a]	Time Since Burst[b] (s)	Filter	Exposure Time (s)	Magnitude
$\cdots$	2008 Mar 19.4728	1.851×10^4	R_C	60.0	18.24 ± 0.07
$\cdots$	2008 Mar 19.4737	1.859×10^4	i'	60.0	18.40 ± 0.03
$\cdots$	2008 Mar 19.4746	1.867×10^4	z'	60.0	18.30 ± 0.06
$\cdots$	2008 Mar 19.4756	1.875×10^4	R_C	60.0	18.27 ± 0.06
$\cdots$	2008 Mar 19.4765	1.883×10^4	i'	60.0	18.39 ± 0.03
$\cdots$	2008 Mar 19.4774	1.891×10^4	z'	60.0	18.31 ± 0.07
$\cdots$	2008 Mar 19.4783	1.899×10^4	R_C	60.0	18.31 ± 0.06
$\cdots$	2008 Mar 19.4792	1.907×10^4	i'	60.0	18.44 ± 0.03
$\cdots$	2008 Mar 19.4801	1.914×10^4	z'	60.0	18.28 ± 0.07
$\cdots$	2008 Mar 19.4811	1.923×10^4	R_C	60.0	18.34 ± 0.06
$\cdots$	2008 Mar 19.4820	1.930×10^4	i'	60.0	18.39 ± 0.03
$\cdots$	2008 Mar 19.4829	1.938×10^4	z'	60.0	18.23 ± 0.06
$\cdots$	2008 Mar 19.4838	1.946×10^4	R_C	60.0	18.38 ± 0.06
$\cdots$	2008 Mar 19.4847	1.954×10^4	i'	60.0	18.46 ± 0.03
$\cdots$	2008 Mar 19.4856	1.962×10^4	z'	60.0	18.33 ± 0.05
$\cdots$	2008 Mar 19.4866	1.970×10^4	R_C	60.0	18.38 ± 0.05
$\cdots$	2008 Mar 19.4875	1.978×10^4	i'	60.0	18.45 ± 0.04
$\cdots$	2008 Mar 19.4884	1.986×10^4	z'	60.0	18.33 ± 0.08
$\cdots$	2008 Mar 19.4893	1.994×10^4	R_C	60.0	18.29 ± 0.07
$\cdots$	2008 Mar 19.4902	2.002×10^4	i'	60.0	18.46 ± 0.03
$\cdots$	2008 Mar 19.4912	2.010×10^4	z'	60.0	18.38 ± 0.06
$\cdots$	2008 Mar 19.4921	2.018×10^4	R_C	60.0	18.38 ± 0.06
$\cdots$	2008 Mar 19.4930	2.026×10^4	i'	60.0	18.49 ± 0.05
$\cdots$	2008 Mar 19.4939	2.033×10^4	z'	60.0	18.41 ± 0.06
$\cdots$	2008 Mar 19.4949	2.042×10^4	R_C	60.0	18.39 ± 0.04
$\cdots$	2008 Mar 19.4958	2.049×10^4	i'	60.0	18.52 ± 0.04
$\cdots$	2008 Mar 19.4967	2.057×10^4	z'	60.0	18.34 ± 0.10
$\cdots$	2008 Mar 19.4976	2.065×10^4	R_C	60.0	18.39 ± 0.06
$\cdots$	2008 Mar 19.4985	2.073×10^4	i'	60.0	18.54 ± 0.04
$\cdots$	2008 Mar 19.4994	2.081×10^4	z'	60.0	18.32 ± 0.07
$\cdots$	2008 Mar 19.5004	2.089×10^4	R_C	60.0	18.45 ± 0.06
$\cdots$	2008 Mar 19.5013	2.097×10^4	i'	60.0	18.50 ± 0.05
$\cdots$	2008 Mar 19.5022	2.105×10^4	z'	60.0	18.45 ± 0.06
$\cdots$	2008 Mar 19.5031	2.113×10^4	R_C	60.0	18.42 ± 0.06
$\cdots$	2008 Mar 19.5040	2.121×10^4	i'	60.0	18.53 ± 0.04
$\cdots$	2008 Mar 19.5049	2.129×10^4	z'	60.0	18.31 ± 0.05
$\cdots$	2008 Mar 19.5059	2.137×10^4	R_C	60.0	18.44 ± 0.06
$\cdots$	2008 Mar 19.5068	2.145×10^4	i'	60.0	18.54 ± 0.04
$\cdots$	2008 Mar 19.5077	2.153×10^4	z'	60.0	18.38 ± 0.09
$\cdots$	2008 Mar 19.5086	2.161×10^4	R_C	60.0	18.45 ± 0.06
$\cdots$	2008 Mar 19.5095	2.169×10^4	i'	60.0	18.61 ± 0.04
$\cdots$	2008 Mar 19.5105	2.176×10^4	z'	60.0	18.50 ± 0.08
$\cdots$	2008 Mar 19.5114	2.185×10^4	R_C	60.0	18.44 ± 0.05

Table A.1 — Continued

GRB Name	UT Date[a]	Time Since Burst[b] (s)	Filter	Exposure Time (s)	Magnitude
$\cdots$	2008 Mar 19.5123	2.192×10^4	i'	60.0	18.51 ± 0.04
$\cdots$	2008 Mar 19.5132	2.200×10^4	z'	60.0	18.46 ± 0.07
$\cdots$	2008 Mar 19.5142	2.208×10^4	R_C	60.0	18.45 ± 0.06
$\cdots$	2008 Mar 19.5151	2.216×10^4	i'	60.0	18.59 ± 0.05
$\cdots$	2008 Mar 19.5160	2.224×10^4	z'	60.0	18.45 ± 0.10
$\cdots$	2008 Mar 19.5169	2.232×10^4	R_C	60.0	18.49 ± 0.07
$\cdots$	2008 Mar 19.5179	2.241×10^4	i'	60.0	18.60 ± 0.08
$\cdots$	2008 Mar 19.5188	2.248×10^4	z'	60.0	18.49 ± 0.08
$\cdots$	2008 Mar 19.5197	2.257×10^4	R_C	60.0	18.57 ± 0.06
$\cdots$	2008 Mar 19.5206	2.264×10^4	i'	60.0	18.66 ± 0.04
$\cdots$	2008 Mar 19.5215	2.272×10^4	z'	60.0	18.52 ± 0.08
$\cdots$	2008 Mar 19.5225	2.280×10^4	R_C	60.0	18.60 ± 0.07
$\cdots$	2008 Mar 19.5234	2.288×10^4	i'	60.0	18.67 ± 0.05
$\cdots$	2008 Mar 19.5243	2.296×10^4	z'	60.0	18.57 ± 0.10
$\cdots$	2008 Mar 19.5252	2.304×10^4	R_C	60.0	18.57 ± 0.06
$\cdots$	2008 Mar 19.5261	2.312×10^4	i'	60.0	18.65 ± 0.05
$\cdots$	2008 Mar 19.5270	2.320×10^4	z'	60.0	18.62 ± 0.10
$\cdots$	2008 Mar 19.5280	2.328×10^4	R_C	60.0	18.54 ± 0.06
$\cdots$	2008 Mar 19.5289	2.336×10^4	i'	60.0	18.69 ± 0.05
$\cdots$	2008 Mar 19.5298	2.344×10^4	z'	60.0	18.47 ± 0.07
$\cdots$	2008 Mar 19.5307	2.352×10^4	R_C	60.0	18.53 ± 0.07
$\cdots$	2008 Mar 20.2329	8.442×10^4	R_C	540.0	20.08 ± 0.16
$\cdots$	2008 Mar 20.2397	8.501×10^4	i'	540.0	20.17 ± 0.08
$\cdots$	2008 Mar 20.2692	8.756×10^4	R_C	540.0	20.02 ± 0.10
$\cdots$	2008 Mar 20.2761	8.816×10^4	i'	540.0	20.24 ± 0.07
$\cdots$	2008 Mar 20.3056	9.070×10^4	R_C	540.0	19.97 ± 0.17
$\cdots$	2008 Mar 20.3125	9.130×10^4	i'	540.0	20.46 ± 0.08
$\cdots$	2008 Mar 20.3432	9.396×10^4	R_C	540.0	20.36 ± 0.09
$\cdots$	2008 Mar 20.3501	9.455×10^4	i'	540.0	20.62 ± 0.10
$\cdots$	2008 Mar 20.3795	9.709×10^4	R_C	540.0	20.73 ± 0.12
$\cdots$	2008 Mar 20.3864	9.769×10^4	i'	540.0	20.73 ± 0.13
$\cdots$	2008 Mar 20.4164	1.003×10^5	R_C	540.0	20.59 ± 0.10
$\cdots$	2008 Mar 20.4233	1.009×10^5	i'	540.0	20.58 ± 0.06
$\cdots$	2008 Mar 20.4533	1.035×10^5	R_C	540.0	20.37 ± 0.09
$\cdots$	2008 Mar 20.4602	1.041×10^5	i'	540.0	20.55 ± 0.08
$\cdots$	2008 Mar 21.2315	1.712×10^5	R_C	1620.0	20.99 ± 0.10
$\cdots$	2008 Mar 21.2534	1.731×10^5	i'	1620.0	21.32 ± 0.11
$\cdots$	2008 Mar 21.4043	1.863×10^5	R_C	1800.0	21.58 ± 0.12
$\cdots$	2008 Mar 21.4273	1.882×10^5	i'	1800.0	21.66 ± 0.12
$\cdots$	2008 Mar 22.4094	2.749×10^5	R_C	5400.0	21.90 ± 0.11
$\cdots$	2008 Mar 22.4324	2.769×10^5	i'	5400.0	22.21 ± 0.10
$\cdots$	2008 Mar 24.2450	4.335×10^5	R_C	5400.0	22.84 ± 0.27
$\cdots$	2008 Mar 24.2679	4.355×10^5	i'	5400.0	22.48 ± 0.14

Table A.1 — Continued

GRB Name	UT Date[a]	Time Since Burst[b] (s)	Filter	Exposure Time (s)	Magnitude
⋯	2008 Mar 25.2842	5.233×10^5	R_C	5400.0	22.73 ± 0.19
⋯	2008 Mar 25.3072	5.253×10^5	i'	5400.0	22.92 ± 0.17
⋯	2008 Mar 26.2822	6.095×10^5	R_C	5400.0	22.89 ± 0.18
⋯	2008 Mar 26.3051	6.115×10^5	i'	5400.0	22.72 ± 0.12
GRB 080319C	2008 Mar 19.5321	1243.3	R_C	60.0	18.66 ± 0.05
⋯	2008 Mar 19.5330	1329.0	i'	60.0	18.51 ± 0.04
⋯	2008 Mar 19.5340	1414.9	z'	60.0	18.19 ± 0.05
⋯	2008 Mar 19.5350	1500.7	R_C	60.0	19.02 ± 0.05
⋯	2008 Mar 19.5360	1586.6	i'	60.0	18.74 ± 0.04
⋯	2008 Mar 19.5370	1672.4	z'	60.0	18.41 ± 0.05
⋯	2008 Mar 20.3959	7.675×10^4	R_C	1800.0	> 22.0
⋯	2008 Mar 20.4367	8.027×10^4	i'	1800.0	22.24 ± 0.18
⋯	2008 Mar 21.4372	1.667×10^5	i'	1800.0	22.54 ± 0.18
GRB 080320	2008 Mar 20.1963	329.9	R_C	60.0	> 20.1
⋯	2008 Mar 20.1973	415.6	i'	60.0	> 20.2
⋯	2008 Mar 20.1983	501.4	z'	60.0	> 19.1
⋯	2008 Mar 20.2008	810.4	R_C	300.0	> 21.0
⋯	2008 Mar 20.2014	896.2	i'	300.0	> 20.9
⋯	2008 Mar 20.2027	974.6	z'	240.0	20.06 ± 0.21
⋯	2008 Mar 20.2153	2003.4	g	120.0	> 20.9
⋯	2008 Mar 20.2156	2149.0	R_C	360.0	> 21.5
⋯	2008 Mar 20.2173	2294.8	i'	360.0	21.62 ± 0.25
⋯	2008 Mar 20.2190	2440.6	z'	360.0	> 20.5

[a]UT at beginning of exposure.

[b]Time from mid-point of exposure to *Swift*-BAT trigger.

[c]Reference: Soderberg et al., 2007.

[d]Reference: Cenko et al., 2006b.

[d]Reference: Perley et al., 2008.

Bibliography

Adamson, A. J., Tilanus, R. P., Buckle, J., Davis, G. R., Economou, F., Jenness, T., and Delorey, K. 2004, in Proceedings of the Society of Photo-Optical Instrumentation Engineers (SPIE), Vol. 5493, Optimizing Scientific Return for Astronomy through Information Technologies, ed. P. J. Quinn & A. Bridger, 24–32

Adelman-McCarthy, J. K., et al. 2006, The Astrophysical Journal Supplement Series, 162, 38

—. 2008, The Astrophysical Journal Supplement Series, 175, 297

Akerlof, C., et al. 1999, Nature, 398, 400

Akerlof, C. W., and Swan, H. F. 2007, The Astrophysical Journal, 671, 1868

Alard, C., and Lupton, R. H. 1998, The Astrophysical Journal, 503, 325

Amati, L. 2006, Monthly Notices of the Royal Astronomical Society, 372, 233

Aptekar, R. L., et al. 1995, Space Science Reviews, 71, 265

Aslan, Z., et al. 2005, GRB Coordinates Network, 3896, 1

Asplund, M., Grevesse, N., and Sauval, A. J. 2005, in Astronomical Society of the Pacific Conference Series, Vol. 336, Cosmic Abundances as Records of Stellar Evolution and Nucleosynthesis, ed. T. G. Barnes, III & F. N. Bash, 25–+

Band, D., et al. 1993, The Astrophysical Journal, 413, 281

Barth, A. J., et al. 2003, The Astrophysical Journal, 584, L47

Barthelmy, S. D., et al. 2005a, Space Science Reviews, 120, 143

—. 2005b, Nature, 438, 994

Berger, E., et al. 2001, The Astrophysical Journal, 556, 556

—. 2007, The Astrophysical Journal, 664, 1000

—. 2005a, The Astrophysical Journal, 634, 501

Berger, E., Kulkarni, S. R., and Frail, D. A. 2003a, The Astrophysical Journal, 590, 379

—. 2004, The Astrophysical Journal, 612, 966

Berger, E., et al. 2003b, Nature, 426, 154

Berger, E., Penprase, B. E., Cenko, S. B., Kulkarni, S. R., Fox, D. B., Steidel, C. C., and Reddy, N. A. 2006, The Astrophysical Journal, 642, 979

Berger, E., et al. 2005b, Nature, 438, 988

Bessell, M. S. 1990, The Publications of the Astronomical Society of the Pacific, 102, 1181

—. 1999, The Publications of the Astronomical Society of the Pacific, 111, 1426

Bikmaev, I., et al. 2005, GRB Coordinates Network, 3853, 1

Blandford, R. D., and McKee, C. F. 1976, Physics of Fluids, 19, 1130

Bloom, J. S., and Alatalo, K. 2005, GRB Coordinates Network, 3984, 1

Bloom, J. S., Kulkarni, S. R., and Djorgovski, S. G. 2002, The Astronomical Journal, 123, 1111

Bloom, J. S., et al. 2006, The Astrophysical Journal, 638, 354

Bloom, J. S., Sigurdsson, S., and Pols, O. R. 1999, Monthly Notices of the Royal Astronomical Society, 305, 763

Bloom, J. S., Starr, D., and Blake, C. H. 2007, GRB Coordinates Network, 6054, 1

Bloom, J. S., Starr, D. L., Blake, C. H., Skrutskie, M. F., and Falco, E. E. 2006, in Astronomical Society of the Pacific Conference Series, Vol. 351, Astronomical Data Analysis Software and Systems XV, ed. C. Gabriel, C. Arviset, D. Ponz, & S. Enrique, 751–+

Blustin, A. J., et al. 2006, The Astrophysical Journal, 637, 901

Boër, M., Atteia, J. L., Damerdji, Y., Gendre, B., Klotz, A., and Stratta, G. 2006, The Astrophysical Journal, 638, L71

Bonnell, J. T., Norris, J. P., Nemiroff, R. J., and Scargle, J. D. 1997, The Astrophysical Journal, 490, 79

Briggs, M. S., et al. 1999, The Astrophysical Journal, 524, 82

Bromm, V., and Loeb, A. 2006, The Astrophysical Journal, 642, 382

Brown, W. R., Geller, M. J., Kenyon, S. J., and Kurtz, M. J. 2006, The Astrophysical Journal, 647, 303

Burrows, D. N., et al. 2005a, Space Science Reviews, 120, 165

Burrows, D. N., and Racusin, J. 2007, eprint arXiv, (astro-ph/0702.633)

Burrows, D. N., et al. 2005b, Science, 309, 1833

Butler, N. R., Kocevski, D., Bloom, J. S., and Curtis, J. L. 2007, The Astrophysical Journal, 671, 656

Cameron, P. B., and Frail, D. A. 2005, GRB Coordinates Network, 3495, 1

Cardelli, J. A., Clayton, G. C., and Mathis, J. S. 1989, The Astrophysical Journal, 345, 245

Castro, S., Galama, T. J., Harrison, F. A., Holtzman, J. A., Bloom, J. S., Djorgovski, S. G., and Kulkarni, S. R. 2003, The Astrophysical Journal, 586, 128

Cavallo, G., and Rees, M. J. 1978, Monthly Notices of the Royal Astronomical Society, 183, 359

Cenko, S. B., and Fox, D. B. 2005, GRB Circular Network, 3834, 1

—. 2006, GRB Coordinates Network, 5975, 1

—. 2007, GRB Coordinates Network, 6028, 1

Cenko, S. B., et al. 2006a, The Publications of the Astronomical Society of the Pacific, 118, 1396

—. 2008, The Astrophysical Journal, 677, 441

Cenko, S. B., Gezari, S., Small, T., Fox, D. B., and Chornock, R. 2007, GRB Coordinates Network, 6322, 1

Cenko, S. B., et al. 2006b, The Astrophysical Journal, 652, 490

Chandra, P., et al. 2008, eprint arXiv, (astro-ph/0802.2748)

Chavan, A. M., Giannone, G., Silva, D., Krueger, T., and Miller, G. 1998, in Astronomical Society of the Pacific Conference Series, Vol. 145, Astronomical Data Analysis Software and Systems VII, ed. R. Albrecht, R. N. Hook, & H. A. Bushouse, 255–+

Chester, M., Page, M., Roming, P., Marshall, F., Boyd, P., Angelini, L., Greiner, J., and Gehrels, N. 2005, GRB Circular Network, 3838, 1

Chevalier, R. A., and Li, Z.-Y. 2000, The Astrophysical Journal, 536, 195

Chevalier, R. A., Li, Z.-Y., and Fransson, C. 2004, The Astrophysical Journal, 606, 369

Christensen, L., Hjorth, J., and Gorosabel, J. 2004, Astronomy and Astrophysics, 425, 913

Churchill, C. W., Rigby, J. R., Charlton, J. C., and Vogt, S. S. 1999, The Astrophysical Journal Supplement Series, 120, 51

Cordes, J. M., Romani, R. W., and Lundgren, S. C. 1993, Nature, 362, 133

Costa, E., et al. 1997, Nature, 387, 783

Cucchiara, A., Fox, D. B., and Berger, E. 2006a, GRB Coordinates Network, 4729, 1

Cucchiara, A., Fox, D. B., and Cenko, S. B. 2007a, GRB Coordinates Network, 7124, 1

Cucchiara, A., Fox, D. B., Cenko, S. B., and Price, P. A. 2007b, GRB Coordinates Network, 6083, 1

Cucchiara, A., Price, P. A., Fox, D. B., Cenko, S. B., and Schmidt, B. P. 2006b, GRB Coordinates Network, 5052, 1

Cummings, J., et al. 2005a, GRB Circular Network, 3835, 1

—. 2005b, GRB Circular Network, 3858, 1

Cusumano, G., et al. 2006, Nature, 440, 164

Dai, X., et al. 2007, eprint arXiv, (astro-ph/0712.2239)

Dai, Z. G., and Cheng, K. S. 2001, The Astrophysical Journal, 558, L109

Dai, Z. G., Liang, E. W., and Xu, D. 2004, The Astrophysical Journal, 612, L101

Daigne, F., and Mochkovitch, R. 1998, Monthly Notices of the Royal Astronomical Society, 296, 275

de Paz, A. G., et al. 2005, The Astrophysical Journal, 627, L29

Dickey, J. M., and Lockman, F. J. 1990, Annual Review of Astronomy and Astrophysics, 28, 215

Eichler, D., Livio, M., Piran, T., and Schramm, D. N. 1989, Nature, 340, 126

Evans, P. A., et al. 2007, Astronomy and Astrophysics, 469, 379

Falcone, A. D., Barthelmy, S. D., Burrows, D. N., Cummings, J. R., Gehrels, N., Hunsberger, S. D., Kennea, J. A., and Palmer, D. M. 2006a, GRB Coordinates Network, 4966, 1

Falcone, A. D., et al. 2006b, The Astrophysical Journal, 641, 1010

Falcone, A. D., Burrows, D. N., Morris, D., Racusin, J., O'Brien, P. T., Osborne, J. P., and Gehrels, N. 2006c, GRB Coordinates Network, 5009, 1

Falcone, A. D., et al. 2007, The Astrophysical Journal, 671, 1921

Fermi, E. 1949, Physical Review, 75, 1169

Filippenko, A. V. 1997, Annual Review of Astronomy and Astrophysics, 35, 309

Firmani, C., Avila-Reese, V., Ghisellini, G., and Ghirlanda, G. 2006, Monthly Notices of the Royal Astronomical Society, 372, L28

Floc'h, E. L., et al. 2003, Astronomy and Astrophysics, 400, 499

Foley, R. J., Chen, H.-W., Bloom, J. S., and Prochaska, J. X. 2005, GRB Coordinates Network, 3949, 1

Foley, R. J., et al. 2006, The Astrophysical Journal, 645, 450

Ford, L. A., et al. 1995, The Astrophysical Journal, 439, 307

Fox, D. B., and Cenko, S. B. 2005, GRB Circular Network, 3829, 1

Fox, D. B., et al. 2005, Nature, 437, 845

Fox, D. B., and Moon, D.-S. 2004, GRB Coordinates Network, 2734, 1

Fox, D. W., et al. 2003a, The Astrophysical Journal, 586, L5

—. 2003b, Nature, 422, 284

Frail, D. A., et al. 2006, The Astrophysical Journal, 646, L99

Frail, D. A., Kulkarni, S. R., Nicastro, L., Feroci, M., and Taylor, G. B. 1997, Nature, 389, 261

Frail, D. A., et al. 2001, The Astrophysical Journal, 562, L55

Fraser, S., and Steele, I. A. 2004, in Proceedings of the Society of Photo-Optical Instrumentation Engineers (SPIE) Conference, Vol. 5493, Optimizing Scientific Return for Astronomy through Information Technologies, ed. P. J. Quinn & A. Bridger, 331–340

Freedman, D. L., and Waxman, E. 2001, The Astrophysical Journal, 547, 922

Friedman, A. S., and Bloom, J. S. 2005, The Astrophysical Journal, 627, 1

Frontera, F., et al. 2000, The Astrophysical Journal Supplement Series, 127, 59

Fruchter, A. S., and Hook, R. N. 2002, The Publications of the Astronomical Society of the Pacific, 114, 144

Fruchter, A. S., et al. 2006, Nature, 441, 463

Fryer, C. L., Woosley, S. E., and Hartmann, D. H. 1999, The Astrophysical Journal, 526, 152

Fugazza, D., et al. 2005, GRB Coordinates Network, 3948, 1

Fukugita, M., Ichikawa, T., Gunn, J. E., Doi, M., Shimasaku, K., and Schneider, D. P. 1996, Astronomical Journal, 111, 1748

Fukugita, M., Shimasaku, K., and Ichikawa, T. 1995, The Publications of the Astronomical Society of the Pacific, 107, 945

Fynbo, J. P. U., et al. 2002, in Lighthouses of the Universe: The Most Luminous Celestial Objects and Their Use for Cosmology, ed. M. Gilfanov, R. Sunyeav, & E. Churazov, 187–+

Fynbo, J. P. U., et al. 2005, GRB Coordinates Network, 3749, 1

—. 2006, Nature, 444, 1047

Gal-Yam, A., et al. 2006, Nature, 444, 1053

—. 2004, The Astrophysical Journal, 609, L59

Galama, T. J., et al. 1998, Nature, 395, 670

Gehrels, N., et al. 2004, The Astrophysical Journal, 611, 1005

—. 2005, Nature, 437, 851

Genet, R. M., and Hayes, D. S. 1989, Robotic observatories. Remote-access. Personal-Computer astronomy (Mesa, Arizona: AutoScope Corp., 1989)

Ghirlanda, G., Ghisellini, G., and Lazzati, D. 2004a, The Astrophysical Journal, 616, 331

Ghirlanda, G., Ghisellini, G., Lazzati, D., and Firmani, C. 2004b, The Astrophysical Journal, 613, L13

Golenetskii, S., Aptekar, R., Mazets, E., Pal'Shin, V., Frederiks, D., and Cline, T. 2007, GRB Coordinates Network, 6049, 1

Goodman, J. 1986, The Astrophysical Journal, 308, L47

—. 1997, New Astronomy, 2, 449

Granot, J., and Sari, R. 2002, The Astrophysical Journal, 568, 820

Granzer, T., Weber, M., and Strassmeier, K. G. 2001, Astronomische Nachrichten, 322, 295

Grupe, D., Nousek, J. A., Berk, D. E. V., Roming, P. W. A., Burrows, D. N., Godet, O., Osborne, J., and Gehrels, N. 2007, The Astronomical Journal, 133, 2216

Haislip, J. B., et al. 2006, Nature, 440, 181

Hao, H., et al. 2007, The Astrophysical Journal, 659, L99

Harrison, F. A., et al. 1999, The Astrophysical Journal, 523, L121

Heise, J., in't Zand, J., Kippen, R. M., and Woods, P. M. 2001, Gamma-Ray Bursts in the Afterglow Era: Proceedings of the International Workshop Held in Rome, 16

Henden, A. 2005, GRB Circular Network, 3845, 1

Hibbard, J. E., et al. 2005, The Astrophysical Journal, 619, L87

Hjorth, J., et al. 2003a, The Astrophysical Journal, 597, 699

—. 2003b, Nature, 423, 847

—. 2005, Nature, 437, 859

Hogg, D. W., Baldry, I. K., Blanton, M. R., and Eisenstein, D. J. 2002, eprint arXiv, (astro-ph/0210394)

Holland, S. T., et al. 2003, The Astronomical Journal, 125, 2291

Honeycutt, R. K., Vesper, D. N., White, J. C., Turner, G. W., and Adams, B. R. 1990, in CCDs in Astronomy. II. New Methods and Applications of CCD Technology, ed. A. G. D. Philip, D. S. Hayes, & S. J. Adelman, 177–+

Hook, I. M., Jørgensen, I., Allington-Smith, J. R., Davies, R. L., Metcalfe, N., Murowinski, R. G., and Crampton, D. 2004, The Publications of the Astronomical Society of the Pacific, 116, 425

Horne, K. 1986, The Publications of the Astronomical Society of the Pacific, 98, 609

Horváth, I. 2002, Astronomy and Astrophysics, 392, 791

Hu, J. H., Lin, H. C., Huang, K. Y., Urata, Y., Ip, W. H., Tamagawa, T., and Fox, D. B. 2004, GRB Coordinates Network, 2744, 1

Hurley, K., et al. 2007, GRB Coordinates Network, 6024, 1

Jakobsson, P., et al. 2006a, Astronomy and Astrophysics, 460, L13

Jakobsson, P., Hjorth, J., Fynbo, J. P. U., Watson, D., Pedersen, K., Björnsson, G., and Gorosabel, J. 2004, The Astrophysical Journal, 617, L21

Jakobsson, P., et al. 2006b, Astronomy and Astrophysics, 447, 897

Jakobsson, P., Vreeswijk, P. M., Hjorth, J., Malesani, D., Fynbo, J. P. U., and Thoene, C. C. 2007, GRB Coordinates Network, 6952, 1

Jarrett, T. H., et al. 2006, The Astronomical Journal, 131, 261

Jordi, K., Grebel, E. K., and Ammon, K. 2006, Astronomy and Astrophysics, 460, 339

Jørgensen, P. S., Riis, T., Betto, M., and Pickles, A. 2002, in Astronomical Society of the Pacific Conference Series, Vol. 281, Astronomical Data Analysis Software and Systems XI, ed. D. A. Bohlender, D. Durand, & T. H. Handley, 207–+

Kaiser, N., et al. 2002, in Proceedings of the Society of Photo-Optical Instrumentation Engineers (SPIE), Vol. 4836, Survey and Other Telescope Technologies and Discoveries, ed. J. A. Tyson & S. Wolff, 154–164

Kann, D. A., Klose, S., and Zeh, A. 2006, The Astrophysical Journal, 641, 993

Kann, D. A., et al. 2007, eprint arXiv, (astro-ph/0712.2186)

Kasliwal, M. M., et al. 2008, The Astrophysical Journal, 678, 1127

Katz, J. I., and Piran, T. 1997, The Astrophysical Journal, 490, 772

Kawai, N., et al. 2006, Nature, 440, 184

Kennicutt, R. C. 1998, Annual Review of Astronomy and Astrophysics, 36, 189

Kent, S. M. 1985, Publications of the Astronomical Society of the Pacific, 97, 165

Khamitov, I., et al. 2005, GRB Coordinates Network, 3864, 1

—. 2004, GRB Coordinates Network, 2752, 1

Kinney, A. L., Calzetti, D., Bohlin, R. C., McQuade, K., Storchi-Bergmann, T., and Schmitt, H. R. 1996, The Astrophysical Journal, 467, 38

Klebesadel, R. W., Strong, I. B., and Olson, R. A. 1973, The Astrophysical Journal, 182, L85

Klose, S., et al. 2004, The Astronomical Journal, 128, 1942

Klotz, A., Boër, M., Atteia, J. L., Stratta, G., Behrend, R., Malacrino, F., and Damerdji, Y. 2005, Astronomy and Astrophysics, 439, L35

Kobayashi, S. 2000, The Astrophysical Journal, 545, 807

Kobayashi, S., Piran, T., and Sari, R. 1997, The Astrophysical Journal, 490, 92

Kocevski, D., and Butler, N. 2007, eprint arXiv, (astro-ph/0707.4478)

Kouveliotou, C., Meegan, C. A., Fishman, G. J., Bhat, N. P., Briggs, M. S., Koshut, T. M., Paciesas, W. S., and Pendleton, G. N. 1993, The Astrophysical Journal, 413, L101

Kulkarni, S. R., et al. 1999a, Nature, 398, 389

—. 1999b, The Astrophysical Journal, 522, L97

—. 2007, Nature, 447, 458

Kumar, P., and Panaitescu, A. 2000, The Astrophysical Journal, 541, L9

Lamb, D. Q., and Reichart, D. E. 2000, The Astrophysical Journal, 536, 1

Lazzati, D. 2005, Monthly Notices of the Royal Astronomical Society, 357, 722

Leach, R. W., and Low, F. J. 2000, in Proceedings of the Society of Photo-Optical Instrumentation Engineers (SPIE), Vol. 4008, Optical and IR Telescope Instrumentation and Detectors, ed. M. Iye & A. F. Moorwood, 337–343

Ledoux, C., et al. 2005, GRB Coordinates Network, 3860, 1

Li, H., and Dermer, C. D. 1992, Nature, 359, 514

Li, W., Filippenko, A. V., Chornock, R., and Jha, S. 2003, The Astrophysical Journal, 586, L9

—. 2004, GRB Coordinates Network, 2748, 1

Li, W., Jha, S., Filippenko, A. V., Bloom, J. S., Pooley, D., Foley, R. J., and Perley, D. A. 2006, The Publications of the Astronomical Society of the Pacific, 118, 37

Liang, E., and Zhang, B. 2006, The Astrophysical Journal, 638, L67

Liang, E.-W., Racusin, J. L., Zhang, B., Zhang, B.-B., and Burrows, D. N. 2008, The Astrophysical Journal, 675, 528

Liang, E. W., et al. 2006, The Astrophysical Journal, 646, 351

Lyutikov, M., and Blandford, R. 2003, eprint arXiv, (astro-ph/0312347)

Lyutikov, M., and Usov, V. V. 2000, The Astrophysical Journal, 543, L129

MacLeod, C., and Nysewander, M. 2005, GRB Coordinates Network, 3863, 1

Maiorano, E., et al. 2006, Astronomy and Astrophysics, 455, 423

Malesani, D., et al. 2004, The Astrophysical Journal, 609, L5

Matheson, T., Filippenko, A. V., Ho, L. C., Barth, A. J., and Leonard, D. C. 2000, The Astronomical Journal, 120, 1499

McBreen, S., Hanlon, L., McGlynn, S., McBreen, B., Foley, S., Preece, R., von Kienlin, A., and Williams, O. R. 2006, Astronomy and Astrophysics, 455, 433

Meegan, C. A., Fishman, G. J., Wilson, R. B., Horack, J. M., Brock, M. N., Paciesas, W. S., Pendleton, G. N., and Kouveliotou, C. 1992, Nature, 355, 143

Melandri, A., et al. 2008, eprint arXiv, (astro-ph/0804.811)

Mészáros, P., and Rees, M. J. 2000, The Astrophysical Journal, 530, 292

Metzger, B. D., Thompson, T. A., and Quataert, E. 2007, The Astrophysical Journal, 659, 561

Metzger, M. R., Djorgovski, S. G., Kulkarni, S. R., Steidel, C. C., Adelberger, K. L., Frail, D. A., Costa, E., and Frontera, F. 1997, Nature, 387, 878

Michałowski, M. J., Hjorth, J., Cerón, J. M. C., and Watson, D. 2008, The Astrophysical Journal, 672, 817

Mirabal, N., et al. 2002, The Astrophysical Journal, 578, 818

Modjaz, M., et al. 2006, The Astrophysical Journal, 645, L21

Möller, P., et al. 2002, Astronomy and Astrophysics, 396, L21

Morton, D. C. 1991, The Astrophysical Journal Supplement Series, 77, 119

Nakar, E. 2007, Physics Reports, 442, 166

Nakar, E., and Granot, J. 2007, Monthly Notices of the Royal Astronomical Society, 380, 1744

Narayan, R., Paczynski, B., and Piran, T. 1992, The Astrophysical Journal, 395, L83

Narayan, R., Piran, T., and Kumar, P. 2001, The Astrophysical Journal, 557, 949

Nardini, M., Ghisellini, G., Ghirlanda, G., Tavecchio, F., Firmani, C., and Lazzati, D. 2006, Astronomy and Astrophysics, 451, 821

Norris, J. P., Cline, T. L., Desai, U. D., and Teegarden, B. J. 1984, Nature, 308, 434

Nousek, J. A., et al. 2006, The Astrophysical Journal, 642, 389

Ober, W. W., Eid, M. F. E., and Fricke, K. J. 1983, Astronomy and Astrophysics, 119, 61

O'Brien, P. T., et al. 2006, The Astrophysical Journal, 647, 1213

Ofek, E. O., et al. 2007a, The Astrophysical Journal, 659, L13

—. 2007b, The Astrophysical Journal, 662, 1129

Oke, J. B., et al. 1995, Publications of the Astronomical Society of the Pacific, 107, 375

Paciesas, W. S., et al. 1999, The Astrophysical Journal Supplement Series, 122, 465

Paczynski, B. 1986, The Astrophysical Journal, 308, L43

Paczynski, B., and Xu, G. 1994, The Astrophysical Journal, 427, 708

Page, K. L., Beardmore, A. P., Goad, M. R., Kennea, J. A., Burrows, D. N., Marshall, F., and Smale, A. 2005a, GRB Coordinates Network, 3837, 1

Page, M., et al. 2005b, GRB Circular Network, 3830, 1

Pal'shin, V., and Frederiks, D. 2005, GRB Circular Network, 3852, 1

Panaitescu, A. 2006, Monthly Notices of the Royal Astronomical Society, 367, L42

—. 2007, Monthly Notices of the Royal Astronomical Society, 380, 374

Panaitescu, A., and Kumar, P. 2001, The Astrophysical Journal, 554, 667

—. 2002, The Astrophysical Journal, 571, 779

Panaitescu, A., Mészáros, P., Burrows, D., Nousek, J., Gehrels, N., O'Brien, P., and Willingale, R. 2006, Monthly Notices of the Royal Astronomical Society, 369, 2059

Pandey, S. B., et al. 2003, Bulletins of the Astronomical Society of India, 31, 19

Pei, Y. C. 1992, The Astrophysical Journal, 395, 130

Pélangeon, A. 2006, in American Institute of Physics Conference Series, Vol. 836, Gamma-Ray Bursts in the Swift Era, ed. S. S. Holt, N. Gehrels, & J. A. Nousek, 149–152

Pelangeon, A., and Atteia, J.-L. 2007, GRB Coordinates Network, 6059, 1

Penprase, B. E., et al. 2006, The Astrophysical Journal, 646, 358

Perley, D. A., et al. 2008, eprint arXiv, 0805, 2394, (astro-ph/0805.2394)

Perlmutter, S., et al. 1999, The Astrophysical Journal, 517, 565

Perna, R., Sari, R., and Frail, D. 2003, The Astrophysical Journal, 594, 379

Pian, E., et al. 2006, Nature, 442, 1011

Piran, T. 2002, Science, 295, 986

—. 2005, Reviews of Modern Physics, 76, 1143

Price, P. A., et al. 2002, The Astrophysical Journal, 572, L51

—. 2007, The Astrophysical Journal, 663, L57

Prochaska, J. X., Bloom, J. S., Wright, J. T., Butler, R. P., Chen, H. W., Vogt, S. S., and Marcy, G. W. 2005, GRB Circular Network, 3833, 1

Prochaska, J. X., et al. 2007a, The Astrophysical Journal Supplement Series, 168, 231

Prochaska, J. X., Chen, H.-W., Dessauges-Zavadsky, M., and Bloom, J. S. 2007b, The Astrophysical Journal, 666, 267

Prochaska, J. X., Gawiser, E., Wolfe, A. M., Castro, S., and Djorgovski, S. G. 2003, The Astrophysical Journal, 595, L9

Prochaska, J. X., Murphy, M., Malec, A. L., and Miller, K. 2008, GRB Coordinates Network, 7388, 1

Prochaska, J. X., Roelofs, G., Bloom, J., and Steeghs, D. 2007c, GRB Coordinates Network, 6032, 1

Prochter, G. E., et al. 2006, The Astrophysical Journal, 648, L93

Qin, Y.-P., Xie, G.-Z., Xue, S.-J., Liang, E.-W., Zheng, X.-T., and Mei, D.-C. 2000, Publications of the Astronomical Society of Japan, 52, 759

Quimby, R. M., et al. 2006, The Astrophysical Journal, 640, 402

Racusin, J., and Vetere, L. 2007, GRB Coordinates Network, 6030, 1

Ramirez-Ruiz, E., MacFadyen, A. I., and Lazzati, D. 2002, Monthly Notices of the Royal Astronomical Society, 331, 197

Rao, S. M., Turnshek, D. A., and Nestor, D. B. 2006, The Astrophysical Journal, 636, 610

Rees, M. J., and Meszaros, P. 1992, Monthly Notices of the Royal Astronomical Society, 258, 41P

—. 1994, The Astrophysical Journal, 430, L93

—. 1998, The Astrophysical Journal, 496, L1

Rees, M. J., and Mészáros, P. 2000, The Astrophysical Journal, 545, L73

Rhoads, J. 2005, GRB Coordinates Network, 3527, 1

Rhoads, J. E. 1999, The Astrophysical Journal, 525, 737

Riess, A. G., et al. 1998, The Astronomical Journal, 116, 1009

Rol, E., Jakobsson, P., Tanvir, N., and Levan, A. 2006, GRB Coordinates Network, 5555, 1

Romano, P., et al. 2006, Astronomy and Astrophysics, 456, 917

Roming, P. W. A., et al. 2005, Space Science Reviews, 120, 95

—. 2006, The Astrophysical Journal, 652, 1416

Rybicki, G. B., and Lightman, A. P. 1979, Radiative processes in astrophysics (New York, Wiley-Interscience, 1979. 393 p.)

Rykoff, E. S., et al. 2006, The Astrophysical Journal, 638, L5

—. 2004, The Astrophysical Journal, 601, 1013

—. 2005, The Astrophysical Journal, 631, L121

Sari, R., and Esin, A. A. 2001, The Astrophysical Journal, 548, 787

Sari, R., and Mészáros, P. 2000, The Astrophysical Journal, 535, L33

Sari, R., and Piran, T. 1999a, The Astrophysical Journal, 517, L109

—. 1999b, The Astrophysical Journal, 520, 641

Sari, R., Piran, T., and Halpern, J. P. 1999, The Astrophysical Journal, 519, L17

Sari, R., Piran, T., and Narayan, R. 1998, The Astrophysical Journal, 497, L17

Sasaki, T., et al. 2000, in Proceedings of the Society of Photo-Optical Instrumentation
   Engineers (SPIE), Vol. 4009, Advanced Telescope and Instrumentation Control
   Software, ed. H. Lewis, 350–354

Savage, B. D., and Sembach, K. R. 1996, Annual Review of Astronomy and Astro-
   physics, 34, 279

Savaglio, S., Fall, S. M., and Fiore, F. 2003, The Astrophysical Journal, 585, 638

Schlegel, D. J., Finkbeiner, D. P., and Davis, M. 1998, The Astrophysical Journal,
   500, 525

Shao, L., and Dai, Z. G. 2005, The Astrophysical Journal, 633, 1027

Shemi, A., and Piran, T. 1990, The Astrophysical Journal, 365, L55

Shin, M.-S., et al. 2006, eprint arXiv, (astro-ph/0608327)

Silvey, J., et al. 2004, GRB Coordinates Network, 2833, 1

Sirianni, M., et al. 2005, The Publications of the Astronomical Society of the Pacific,
   117, 1049

Skrutskie, M. F., et al. 2006, The Astronomical Journal, 131, 1163

Smith, N., et al. 2007, The Astrophysical Journal, 666, 1116

Soderberg, A. M., et al. 2006a, The Astrophysical Journal, 650, 261

Soderberg, A. M., Chevalier, R. A., Kulkarni, S. R., and Frail, D. A. 2006b, The Astrophysical Journal, 651, 1005

Soderberg, A. M., et al. 2004, Nature, 430, 648

—. 2006c, Nature, 442, 1014

—. 2006d, The Astrophysical Journal, 636, 391

—. 2007, The Astrophysical Journal, 661, 982

Spergel, D. N., et al. 2007, The Astrophysical Journal Supplement Series, 170, 377

Stanek, K. Z., et al. 2007, The Astrophysical Journal, 654, L21

—. 2003, The Astrophysical Journal, 591, L17

Steele, I. A., and Carter, D. 1997, in Proceedings of the Society of Photo-Optical Instrumentation Engineers (SPIE), Vol. 3112, Telescope Control Systems II, ed. H. Lewis, 222–233

Steidel, C. C., and Sargent, W. L. W. 1992, The Astrophysical Journal Supplement Series, 80, 1

Tagliaferri, G., et al. 2005, Astronomy and Astrophysics, 443, L1

Tanvir, N., Levan, A., Jarvis, M., and Wold, T. 2006, GRB Coordinates Network, 5587, 1

Tanvir, N. R., et al. 2004, Monthly Notices of the Royal Astronomical Society, 352, 1073

Thilker, D. A., et al. 2005, The Astrophysical Journal, 619, L79

Thoene, C. C., Fynbo, J. P. U., and Jakobsson, P. 2006, GRB Coordinates Network, 5747, 1

Thuan, T. X., and Gunn, J. E. 1976, The Publications of the Astronomical Society of the Pacific, 88, 543

Tody, D. 1986, in Proceedings of the Society of Photo-Optical Instrumentation Engineers (SPIE), Vol. 627, Instrumentation in astronomy VI, ed. D. L. Crawford, 733–+

Tyson, A. 2005, in Astronomical Society of the Pacific Conference Series, Vol. 339, Observing Dark Energy, ed. S. C. Wolff & T. R. Lauer, 95–+

Tytler, D. 1982, Nature, 298, 427

Usov, V. V. 1992, Nature, 357, 472

Valle, M. D., et al. 2006a, Nature, 444, 1050

—. 2006b, The Astrophysical Journal, 642, L103

van Dokkum, P. G. 2001, The Publications of the Astronomical Society of the Pacific, 113, 1420

van Paradijs, J., et al. 1997, Nature, 386, 686

Vaughan, S., et al. 2006, The Astrophysical Journal, 638, 920

Vestrand, W. T., et al. 2005, Nature, 435, 178

—. 2006, Nature, 442, 172

Vreeswijk, P. M., et al. 2007, Astronomy and Astrophysics, 468, 83

—. 2008, GRB Coordinates Network, 7444, 1

Wade, R. A., and Horne, K. 1988, The Astrophysical Journal, 324, 411

Waxman, E., and Mészáros, P. 2003, The Astrophysical Journal, 584, 390

Wiersema, K., Tanvir, N., Vreeswijk, P., Fynbo, J., Starling, R., Rol, E., and Jakobsson, P. 2008, GRB Coordinates Network, 7517, 1

Wilson, J. C., et al. 2003, in Proceedings of the Society of Photo-Optical Instrumentation Engineers (SPIE), Vol. 4841, Instrument Design and Performance for Optical/Infrared Ground-based Telescopes, ed. M. Iye & A. F. M. Moorwood, 451–458

Wolfe, A. M., Gawiser, E., and Prochaska, J. X. 2005, Annual Review of Astronomy & Astrophysics, 43, 861

Woosley, S. E. 1993, The Astrophysical Journal, 405, 273

Woosley, S. E., and Bloom, J. S. 2006, Annual Review of Astronomy & Astrophysics, 44, 507

Woźniak, P. R., Vestrand, W. T., Wren, J. A., White, R. R., Evans, S. M., and Casperson, D. 2005, The Astrophysical Journal, 627, L13

—. 2006, The Astrophysical Journal, 642, L99

Wren, J., Vestrand, W. T., Wozniak, P., Evans, S., and White, R. 2005, GRB Circular Network, 3836, 1

Yost, S. A., Harrison, F. A., Sari, R., and Frail, D. A. 2003, The Astrophysical Journal, 597, 459

Zeh, A., Klose, S., and Hartmann, D. H. 2004, The Astrophysical Journal, 609, 952

Zeh, A., Klose, S., and Kann, D. A. 2006, The Astrophysical Journal, 637, 889

Zhang, B., Fan, Y. Z., Dyks, J., Kobayashi, S., Mészáros, P., Burrows, D. N., Nousek, J. A., and Gehrels, N. 2006, The Astrophysical Journal, 642, 354

Zhang, Q., Fall, S. M., and Whitmore, B. C. 2001, The Astrophysical Journal, 561, 727